Hybrid polymer/liquid vesicles as new particles for drug delivery and cell mimics

Thi Phuong Tuyen Dao

▶ **To cite this version:**

Thi Phuong Tuyen Dao. Hybrid polymer/liquid vesicles as new particles for drug delivery and cell mimics. Polymers. Université de Bordeaux; Universidade de Lisboa, 2016. English. NNT : 2016BORD0190 . tel-01469562

HAL Id: tel-01469562

https://theses.hal.science/tel-01469562

Submitted on 16 Feb 2017

HAL is a multi-disciplinary open access archive for the deposit and dissemination of scientific research documents, whether they are published or not. The documents may come from teaching and research institutions in France or abroad, or from public or private research centers.

L'archive ouverte pluridisciplinaire **HAL**, est destinée au dépôt et à la diffusion de documents scientifiques de niveau recherche, publiés ou non, émanant des établissements d'enseignement et de recherche français ou étrangers, des laboratoires publics ou privés.

THÈSE EN COTUTELLE PRÉSENTÉE

POUR OBTENIR LE GRADE DE

DOCTEUR DE

L'UNIVERSITÉ DE BORDEAUX

ET DE L'INSTITUTO SUPERIOR TÉCNICO

ÉCOLE DOCTORALE DES SCIENCES CHIMIQUES

SPÉCIALITÉ : POLYMÈRES

Par Thi Phuong Tuyen DAO

HYBRID POLYMER/LIPID VESICLES AS NEW PARTICLES FOR DRUG DELIVERY AND CELL MIMICS

Sous la direction de

M. Jean-François LE MEINS, M. Manuel PRIETO, M. Fábio FERNANDES

Soutenue : le 16 Décembre 2016

Membres du jury :

Mme. LI Min-Hui	Directrice de recherche, CNRS, Chimie Paris Tech	Rapporteur
M. TRIBET Christophe	Directeur de recherche, CNRS, ENS Paris	Rapporteur
M. NASSOY Pierre	Directeur de recherche, CNRS, Université de Bordeaux	Président de jury
Mme. HELLWIG Petra	Professeur, Université de Strasbourg	Examinateur
Mme. BRULET Annie	Ingénieur de recherche, CNRS, CEA-Saclay	Examinateur
M. BERBERAN-SANTOS Mário	Professeur, Instituto Superior Técnico, Lisboa	Examinateur
M. LE MEINS Jean-François	Maître de conférences, Université de Bordeaux	Directeur de thèse
M. PRIETO Manuel	Professeur, Instituto Superior Técnico, Lisboa	Co-directeur de thèse
M. SANDRE Olivier	Directeur de recherche, CNRS, Université de Bordeaux	Membre Invité
M. FERNANDES Fábio	Chercheur FCT, Instituto Superior Técnico, Lisboa	Membre Invité

Acknowledgements

This thesis has been carried out at the Laboratoire de Chimie des Polymères Organiques in Bordeaux and the Centro de Química-Física Molecular in Lisbon from October 2013 to December 2016. I would like to express my acknowledgments to all people who supported me throughout these three years.

I must first express my gratitude towards Dr. Olivier Sandre for introducing me to this new exciting topic. This project has contributed significantly to broadening my knowledge in this challenging field. Also, I thank him for all interesting discussions, ideas and help along my work.

My special acknowledgment I would like to give to Dr. Jean-François Le Meins. He was an amazing supervisor, always active for the discussions. I was able to discuss research plans, results or all of troubles whenever I need. This thesis would not have been possible without his guidance and kind support.

I sincerely thank Prof. Manuel Prieto from CQFM for supervision, guidance and countless encouragements throughout the three years. With his enthusiasm and his inspiration, I can approach to the end of my PhD journey.

Also from CQFM, I will always be grateful to Dr. Fábio Fernandes. I greatly appreciate the scientific knowledge I got from him. For me, Fábio seems knowing everything of every aspect, his depth knowledge has always impressed me. Without his brilliant guidance, this thesis could not be done.

I would like to thank the members of my PhD committee for accepting to go through my work and for fruitful suggestions, comments and questions during my defense.

I thank the International Doctoral School in Functional Materials (IDS-FunMat), Erasmus Mundus Program of the European Union for the financial support, giving me an opportunity to work in two great labs in two different countries.

This project involves collaborations with numerous great people. I would like to thank Mériem Er-Rafik at ICS Strasbourg for performing all of Cryo-TEM experiments, an important part of this work. Many thanks to Annie Brulet from LLB, CEA-Saclay for her strong supports during neutron scattering experiments and data interpretation. Jean-Paul Chapel from CRPP and Hugo Oliveira from INSERM are also kindly acknowledged for their supports in Langmuir and FACs experiments.

I would like to express my gratitude to Aleksander Andreevich who performed a huge number of decays experiments at CQFM, Lisbon.

I especially want to thank Emmanuel Ibarboure who teached me the complex protocol of micropipette aspiration technique. During last years, he spent many hours to teach, discuss, do experiment and solve the occurring problems with me. Outside the work, he has been also a very “cute” friend, staying with him I never had bad mood.

I do not want to forget to thank all the scientific staffs at both LCPO and CQFM. It is great having the opportunity of being part of these two research groups. Many valuable meetings of the teams during these past three years helped me to significantly improve my knowledge.

Regarding the technical matters, I would like to thank all the helpful supports along this thesis from Nico, Anne-Laure, Loïc, Amélie, Cédric, Gérard…

Regarding the administrative staffs, I would like to thank Catherine, Dominique and Corinne, from LCPO; Andreia and Madalena from CQFM; Audrey and Christopher from IDSFunMat for all their helps.

Many thanks to all my friends at LCPO, it was very enjoyable to work at this laboratory, both on personal and professional sides. Especially, I would like to thank Cony and Marie, their supports were not only in the lab but also in my personal life. The moments with them truly helped me refreshed especially during the stressful times.

I'm also really glad for the new friendships gained during my second year at CQFM, Lisbon. My great love with Portugal came from them, very very nice Portuguese persons.

My warmest thanks go to my family: my parents, my sisters and my brother for their love and never ending support.

Finally and most importantly, I would like to dedicate this thesis to my beloved husband, To Van Vinh. He is a powerful emotional support that I can share my burdens, fears and sadness. Thanks for his understanding, help and endless love.

Thi Phuong Tuyen Dao

Pessac, 16/01/2017

TITLE: HYBRID POLYMER/LIPID VESICLES AS NEW PARTICLES FOR DRUG DELIVERY AND CELL MIMICS

Abstract:

Hybrid copolymer/lipid vesicle are recently developed self-assembled structures that could present biocompatibility and biofunctionality of liposomes, as well as robustness, low permeability and functionality variability conferred by the copolymer chains. However, to date, physical and molecular parameters governing copolymer/lipid phase separation in these hybrid membranes are not well understood. In this work, we studied in detail the formation and phase separation in the membranes of both Giant Unilamellar Hybrid Vesicles (GHUVs) and Large Unilamellar Hybrid Vesicles (LHUVs) obtained from the mixture of phospholipids in the fluid (liquid disordered) or gel state (solid ordered) with various copolymers based on poly(dimethylsiloxane) (PDMS) and poly(ethylene glycol) (PEO) with different architectures (grafted, triblock) and molar masses. For GHUVs, phase separation at the micron scale and nanoscale was evaluated through confocal microscopy, and Fluorescence lifetime imaging microscopy technique (FLIM) respectively, whereas a combination of Small angle neutron scattering (SANS), Cryo-transmission electron microscopy (Cryo-TEM) and Time-resolved Förster resonance energy transfer (TR-FRET) techniques was used for LHUVs. We demonstrate that the lipid/polymer fraction, lipid physical state, and the line tension at lipid polymer/lipid boundaries which can be finely modulated by the molar mass and architecture of the copolymer are important factors that govern the formation and structuration of hybrid vesicles. We also evidence that elasticity of the hybrid membrane can be modulated *via* the lipid polymer composition, through the use of micropipettes techniques.

Keywords: hybrid vesicles, hybrid membrane, phase separation, GHUV, LHUV…

TITRE: VESICULES HYBRIDES LIPIDE/POLYMERES COMME NOUVEAUX SYSTEMES DE VECTORISATION ET MODELES DE MEMBRANES CELLULAIRES

Résumé:

Les vésicules hybrides polymère/lipides sont des structures récemment développées dans la littérature. Idéalement, celles-ci peuvent présenter la biocompatibilité et la biofonctionnalité des liposomes, ainsi que la robustesse, la faible perméabilité et la versatilité de fonctionnalisation chimique conférées par les chaînes de copolymères. Cependant, à ce jour, les facteurs régissant la séparation des phases dans ces membranes hybrides ne sont pas bien compris. Dans ce travail, nous avons étudié en détail la formation et la séparation de phases dans les membranes de vésicules géantes (GHUVs) et de taille nanométriques (100nm) (LHUVs) constituées de phospholipides en phase fluide ou gel et de copolymères à base de poly (diméthylsiloxane) et de poly (éthylèneglycol). Différentes architectures (greffée, tribloc) et masses molaires ont été utilisées. La séparation de phase a été étudiée sur les vésicules géantes à l'échelle micrométrique et nanométrique respectivement par microscopie confocale et imagerie de fluorescence résolue en temps (FLIM), tandis que pour les LHUVs, différentes techniques comme la diffusion de neutrons, la Cryo-microscopie et la spectroscopie de fluorescence résolue dans le temps ont été combinées. Nous avons pu montrer que la fraction lipide/polymère, l'état physique du lipide et la tension de la ligne aux interfaces lipide/polymère modulable par la masse molaire et l'architecture du copolymère sont les facteurs importants régissant la formation et la structuration des vésicules hybrides. Enfin, nous avons montré que les propriétés élastiques de la membrane peuvent être modulées *via* la composition polymère lipide.

Mots clés: membrane hybride, hybride vésicule, séparation de phase

Résumé (Français)

Les vésicules hybrides polymère/lipides sont des structures récemment développées dans la littérature. Idéalement, celles-ci pourraient présenter la biocompatibilité et la biofonctionnalité des liposomes, ainsi que la robustesse, la faible perméabilité et la variabilité de fonctionnalité conférées par les chaînes de copolymères. A l'échelle nanométrique, les vésicules unilamellaires hybrides de ~ 100 nm (LHUVs) possèdent un grand intérêt pour les applications biomédicales (système de délivrance des médicaments) alors qu'à l'échelle micrométrique, les vésicules hybrides unilamellaires géantes (GHUVs) peuvent être un outil pour mieux comprendre les mécanismes des membranes cellulaires qui régissent la formation de domaines, la fusion et/ou la fission. Cependant, à ce jour, les facteurs physiques et moléculaires régissant la structuration des vésicules hybrides (répartition des lipides et de chaînes de copolymères dans la membrane hybride) et leurs conséquences sur les propriétés de la membrane ne sont que partiellement compris.

Dans ce contexte, l'objectif de cette thèse est de contrôler la formation et la structuration des vésicules hybrides à l'échelle nanométrique et l'échelle micrométrique. Pour cela, nous avons généré différents systèmes hybrides polymère/lipide en utilisant différents phospholipides (POPC T_m = -2°C et DPPC T_m = 41°C) et divers copolymères de même nature chimique constitué de blocs hydrophobes de poly(diméthylsiloxane) (PDMS) et poly(oxyde d'éthylène) (PEO) comme block hydrophiles. Différentes masses molaires et architectures (greffé, tribloc) ont été utilisées: PEO_8-*b*-$PDMS_{22}$-*b*-PEO_8, PEO_{12}-*b*-$PDMS_{43}$-*b*-PEO_{12}, PEO_{17}-*b*-$PDMS_{67}$-*b*-PEO_{17} et $PDMS_{26}$-*g*-$(PEO_{12})_2$. Ces copolymères s'auto-assemblent en vésicules avec

des épaisseurs de membrane variables (de ~ 5,4 nm à ~ 11,2 nm). Les différents systèmes hybrides ont été examinés avec la même méthodologie et l'effet de la taille des parties hydrophobes, l'architecture du polymère et la fluidité du phospholipide sur la formation des vésicules hybride et la structuration de leur membrane (séparation de phase) ont été étudiés. Les techniques habituellement utilisées pour analyser la séparation de phase dans les vésicules lipidiques à multi-composants ont été exploitées dans cette étude. La séparation de phase a été étudiée sur les vésicules géantes (GHUVs) à l'échelle micrométrique et nanométrique respectivement par microscopie confocale et imagerie de fluorescence résolue en temps (FLIM), tandis que pour les LHUVs, différentes techniques comme la diffusion de neutrons, la Cryo-microscopie et la spectroscopie de fluorescence résolue dans le temps ont été combinées (TR-FRET). La formation de GHUVs obtenues par électroformation a été étudiée dans toute la gamme de composition polymère/lipide (de 0 à 100% en masse de phospholipide) tandis que les LHUVs, obtenue par la technique de réhydratation/extrusion qui est la plus couramment ont été étudiés jusqu'à 30% en masse de lipide.

L'association de différentes techniques (SANS, TR-FRET, Cryo-TEM) nous a permis de montrer que des LHUVs sont bien obtenues, malgré une quantité non-négligeable de liposomes et de polymersomes, en particulier lorsque la différence d'épaisseur de membrane de la phase lipidique et la phase polymère augmente, et peut même conduire à la formation de micelle hybride vermiculaires « worm-like micelles ». La diminution de la masse molaire ou le changement de l'architecture du copolymère, du tribloc au greffé, a abouti à une formation plus efficace de vésicules hybrides. Ceci suggère que la tension de ligne aux interfaces lipides/polymères, qui est un facteur important dans la structuration de

membranes multi-phasées, pourrait être modulée non seulement par la masse molaire, mais également par l'architecture du copolymère.

Concernant les GHUVs, notre étude montre clairement que la masse molaire a une forte influence sur l'obtention et la structuration de membrane des vésicules. Globalement plus la masse molaire augmente plus il est difficile d'obtenir des vésicules hybrides en grande quantités. Les phases lipidiques ont tendance à être éjectées par un procédé de bourgeonnement et fission de domaine micrométrique de lipide. De manière inédite nous avons pu obtenir des systèmes pour lesquels ce phénomène de bourgeonnement est stoppé avant fission, illustrant une parfaite balance entre l'énergie de ligne à l'interface polymère lipide et l'énergie de courbure générée par le bourgeonnement. Cette stabilisation a été observée sur les vésicules de copolymère présentant une épaisseur de membrane proche de ces des liposomes (PEO_8-*b*-$PDMS_{22}$-b-PEO_8/POPC). Avec des copolymères de masse molaire plus élevée, le bourgeonnement et la fission des domaines lipidiques se sont produits rapidement après électroformation (PEO_{12}-*b*-$PDMS_{43}$-*b*-PEO_{12}/POPC). Ce phénomène conduit à la formation de liposomes/polymersomes ou de vésicules hybrides ayant une membrane homogène à l'échelle micrométrique. Nous avons pu montrer que des domaines de lipides nanométriques sont présents dans les GHUVs qui apparaissent comme « homogènes » en utilisant la méthodologie FLIM-FRET.

En ce qui concerne l'architecture du copolymère, comme mentionné ci-dessus, le copolymère greffé conduit à une formation plus efficace des vésicules hybrides à l'échelle nanométrique. Cependant à l'échelle micrométrique, une instabilité des domaines (bourgeonnement et fission) a été observée alors que le bourgeonnement est stabilisé le

tribloc PEO_8-*b*-$PDMS_{22}$-*b*-PEO_8. Cela suggère que la structuration de membrane observées dans les LHUVs ne reflètent pas systématiquement celle des GHUVs (et vice versa).

Dans cette thèse, nous avons exploré aussi les propriétés physiques des vésicules hybrides et les avons liées à la structuration de leur membrane. Nous sous sommes penchés sur La fluidité et l'élasticité dans la mesure où ces propriétés sont d'une grande importance dans de nombreux événements biologiques (résistance des cellules sur choc osmotique, fission et fusion cellulaire, motilité cellulaire ...) ou pour l'administration de médicaments (résistance des membranes vésiculaires dans la circulation sanguine). La technique de Recouvrance de Fluorescence après Photo-blanchiment (FRAP) a été utilisée pour étudier les coefficients de diffusion et la technique de manipulation en micropipette a été utilisée pour mesurer l'élasticité sous étirement. La diffusion des chaînes de polymères dans la membrane hybride semble être perturbée par la présence de nanodomaines alors que la diffusion des molécules lipidiques est similaire à celle des liposomes purs. De plus, le module de compressibilité peut être modulé entre ceux des membranes polymères et lipidiques, et augmente graduellement avec la fraction en lipides.

TABLE OF CONTENTS

ABBREVIATIONS

BSA	Bovine Serum Albumin
Chol	Cholesterol
DHPE	1,2-Dihexadecanoyl-sn-glycero-3-phosphoethanolamine
DLPC	1,2-Dilauroyl-sn-glycero-3-phosphocholine
DOPC	1,2-Dioleoyl-sn-glycero-3-phosphocholine
DOPE	1,2-Dioleoyl-sn-glycero-3-phosphoethanolamine
DPPC	1,2-dipalmitoyl-*sn*-glycero-3-phosphocholine
FITC	Fluorescein
GHUV	Giant Hybrid Unilamellar Vesicle
GUV	Giant Unilamellar Vesicle
HSPC	Hydrogenated soy phosphatidylcholine
LHUV	Large Hybrid Unilamellar Vesicle
LUV	Large Unilamellar Vesicle
MLHV	Multilamellar Hybrid Vesicle
MLV	Multilamellar Vesicle
MWCO	Molecular Weight Cut-Off
NBD	Nitrobenzoxadiazol
NHS	N-hydroxysuccinimide
PBS	Phosphate Buffer Saline
PDI	Polydispersity
PDMS	Poly(dimethylsiloxane)
PEO	Poly(ethylene oxide)
PBd	Poly(butadiene)
PIB	Poly(isobutylene)
PMOXA	Poly(methyloxazoline)
POPC	1-palmitoyl-2-oleoyl-*sn*-glycero-3-phosphocholine
Rhod	Rhodamine
RI	Refractive Index
ROI	Region of Interest

SYMBOLS

D	Lateral diffusion coefficient
IM_f	Immobile fraction
M_f	Mobile fraction
τ	Fluorescence lifetime
d	Membrane thickness measured by Cryo-TEM
K_P	Partition coefficient
f	Hydrophilic fraction (w %)
K_a	Area compressibility modulus
κ	Bending rigidity
τ_c	Lysis tension
α_c	Lysis strain
δ	Hildebrand solubility parameter
R_h	Hydrodynamic radius
R_g	Radius of gyration
T_m	Melting temperature
T_g	Glass transition temperature
λ_{db}	Line tension

GENERAL INTRODUCTION

Mixing phospholipids and amphiphilic copolymers into a single hybrid membrane is a relatively recent approach developed in the past few years [1, 2]. Ideally, these structures could present biocompatibility and biofunctionality of liposomes, as well as robustness, low permeability and functionality variability conferred by the copolymer chains. This is expected to be of great interest in pharmaceutical applications for which only a few formulations based on liposomes are authorised on the drug market despite decades of research (e.g. DaunoXome®, Doxil®/Caelyx®) as well as in personal care. Such moderate use of liposomes in clinics could be due to their lack of mechanical stability in the high shear rate of blood circulation through tiny vessels [3-5]. Liposomal drug delivery system also often exhibits uncontrolled leakage phenomena (seen as a "burst release" effect on their pharmacokinetic profiles) [6]. As a consequence, the controlled release of encapsulated molecules at the pre-determined biological target (e.g. a tumour site), remains a difficult challenge. Besides the obvious interest of the association of lipids and amphiphilic copolymers into a single membrane at the nano scale (forming Large Hybrid Unilamellar Vesicles – LHUVs) for biomedical applications, the Giant Hybrid Unilamellar Vesicles – GHUVs can be also a tool to get more insight into the molecular and macroscopic parameters that govern the cell membrane domain formation, fusion and/or fission.

In order to perfectly exploit the potential of such systems, the membrane structuration must be tuned either towards homogeneous mixing of the components, or on the contrary to lateral phase separation, leading to the presence of domains. Then, the relationship between membrane structure and their physical and bio-functional properties must be understood in detail in order to eventually optimize them and validate their use in future biomedical applications, namely drug delivery, tumour targeting, bio-recognition or bio-adhesion. The literature on the subject is still relatively limited [1, 2], although the scientific output is growing with interest from different scientific communities (biophysicists, biologists, physical-chemists). To date, the physical and molecular factor governing the phase separation in these hybrid polymer/lipid membranes are only partially understood.

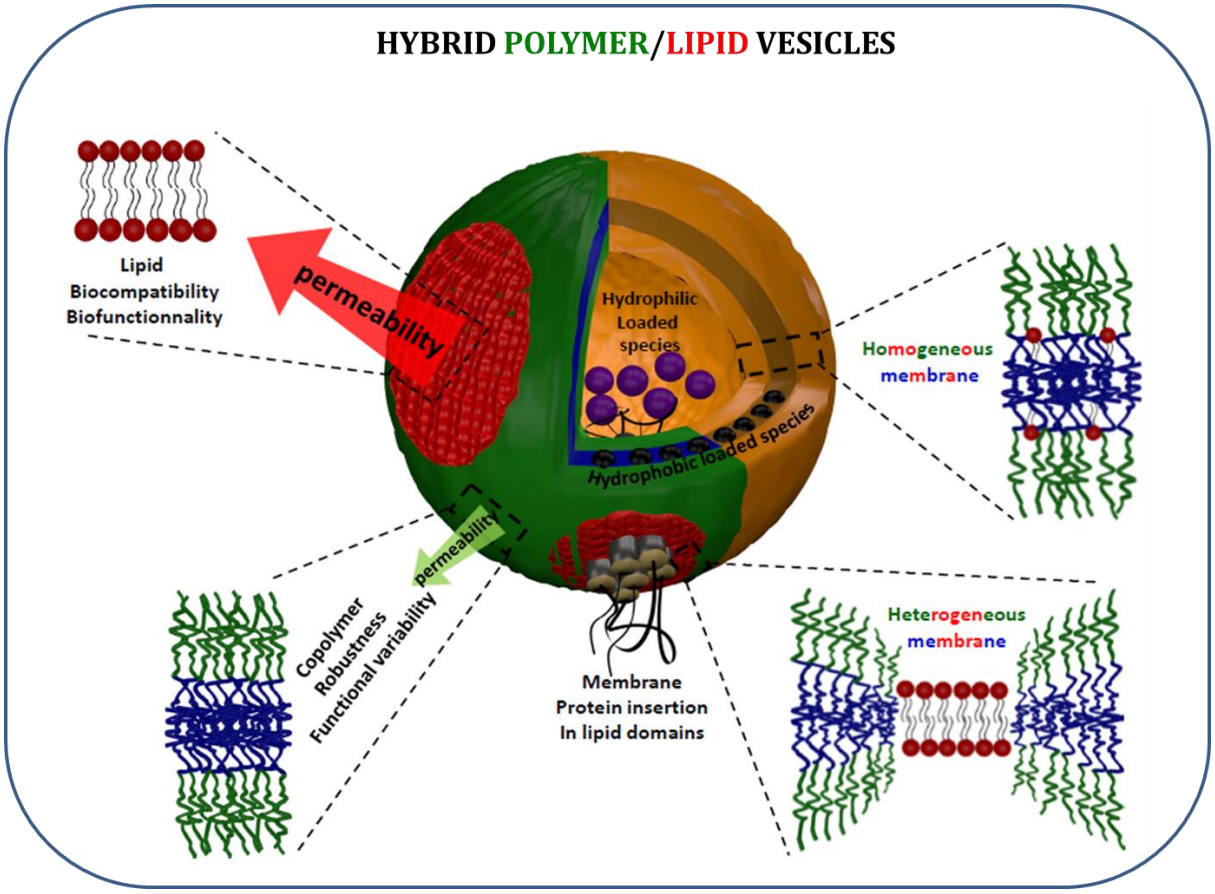

Figure 1. Hybrid polymer/lipid vesicle: the possible membrane structuration (homogeneous mixing of the components or lateral phase separation into domains) and expected characteristics.

Accordingly, the primary aim of this PhD-work is to reach a control of the formation and structuration of hybrid vesicles at both nano and micron scale. For that purpose, we generated different hybrid polymer/lipid systems by blending different phospholipids (fluid and gel state) with various copolymers based on the same chemical nature poly(dimethylsiloxane) (PDMS) and poly(ethylene oxide) (PEO), but varying molar masses and architectures (grafted, triblock). These different hybrid systems were examined with the same methodologies and compared, in order to reveal the effect of hydrophobic mismatch, polymer architecture and fluidity of phospholipid. The second objective is to explore the physical properties of hybrid vesicles and correlate them to the membrane structure. Fluidity and mechanical properties were chosen, as these ones are of high importance in many biological events (resistance of cells upon osmotic shock, cell fission and fusion, cell motility…) [7] or for drug delivery applications.

This thesis manuscript is organized in six chapters. The first chapter is a literature review where we resume basic concepts about self-assembly of amphiphilic molecules: phospholipids and copolymers; fundamental terms of vesicular structures and the current knowledge on hybrid polymer/lipid vesicles. The second chapter introduces the materials and methods relevant for this work. All practical details about apparatus settings, experimental procedures and data analyses are also described.

The results description starts with the third chapter where the synthesis of copolymers and fluorescently labelled copolymer needed for the whole work of this thesis is described, together with the characterisation of their self-assembly.

Chapter 4 is devoted to the formulation of LHUVs and the thorough analysis of their membrane structuration by different techniques: Small angle neutron scattering (SANS), Time-resolved Förster resonance energy transfer (TR-FRET) and Cryo-transmission electron microscopy (Cryo-TEM). Particularly, in this chapter, we introduced a new SANS model entitled “hybrid vesicle form factor” to analyse our specific hybrid polymer/lipid systems.

In the next Chapter 5, different hybrid systems were also investigated systematically but at the micron scale (GHUVs). Herein, fluorescence confocal imaging is the main method to reveal information on the micrometric domains and particularly, an advanced microscopy methodology, FLIM-FRET (Förster resonance energy transfer through fluorescence lifetime imaging microscopy) was a complementary tool to detect nanodomains below the resolution of microscope.

Finally, the last chapter (Chapter 6) deals with the fluidity and mechanical properties measurements *via* Fluorescence recovery after photobleaching (FRAP) and micropipette aspiration respectively. The variation profile of those properties detected on hybrid membranes are interpreted considering the acquired knowledge of membrane structure in order to establish a structure-properties relationship of hybrid formulation.

REFERENCES

1. Le Meins, J.F., et al., *Hybrid polymer/lipid vesicles: state of the art and future perspectives.* Materials Today, 2013. **16**(10): p. 397-402.

2. Schulz, M. and W.H. Binder, *Mixed Hybrid Lipid/Polymer Vesicles as a Novel Membrane Platform.* Macromolecular Rapid Communications, 2015. **36**(23): p. 2031-2041.

3. Allen, T.M. and P.R. Cullis, *Liposomal drug delivery systems: From concept to clinical applications.* Advanced Drug Delivery Reviews, 2013. **65**(1): p. 36-48.

4. Sercombe, L., et al., *Advances and Challenges of Liposome Assisted Drug Delivery.* Frontiers in Pharmacology, 2015. **6**(286).

5. Akbarzadeh, A., et al., *Liposome: classification, preparation, and applications.* Nanoscale Research Letters, 2013. **8**(1): p. 102.

6. Peer, D., et al., *Nanocarriers as an emerging platform for cancer therapy.* Nat Nano, 2007. **2**(12): p. 751-760.

7. Gennis, R.B., *Biomembranes: molecular structure and function*. 2013: Springer Science & Business Media.

CHAPTER 1 - LITERATURE REVIEW

Table of Contents

1.1. AMPHIPHILIC MOLECULES AND THEIR SELF-ASSEMBLIES

1.1.1. Amphiphilic molecules

Phospholipids

Phospholipids are amphiphiles composed of two fatty acid tails, a glycerol unit, a phosphate group and a polar molecule. The phosphate group and polar head molecule form the hydrophilic region and define each type of phospholipid, including zwitterionic groups with zero overall net charge at physiological pH, such as phosphatidylcholine (PC) and phosphatidylethanolamine (PE) or anionic groups with negative net charge such as phosphatidylglycerol (PG), phosphatidylserine (PS) and phosphatidylinositol (PI). The remaining part is a glycerol molecule esterified by two fatty acids, forming hydrophobic region that can be of different lengths (between 12-24 carbons) and degree of saturations. Phospholipids are the main component of biological membranes.

Amphiphilic copolymers

Amphiphilic copolymers are synthetic amphiphiles, composed of a hydrophilic (e.g. polyethylene oxide PEO, polyacrylic acid PAA…) and a hydrophobic segment (e.g. Polybutadiene PBd, Polystyrene PS…). Amphiphilic copolymers can have different architectures, e.g: diblock, triblock, graft… A schematic representation of phospholipid and amphiphilic copolymer is given in Figure 1.1.

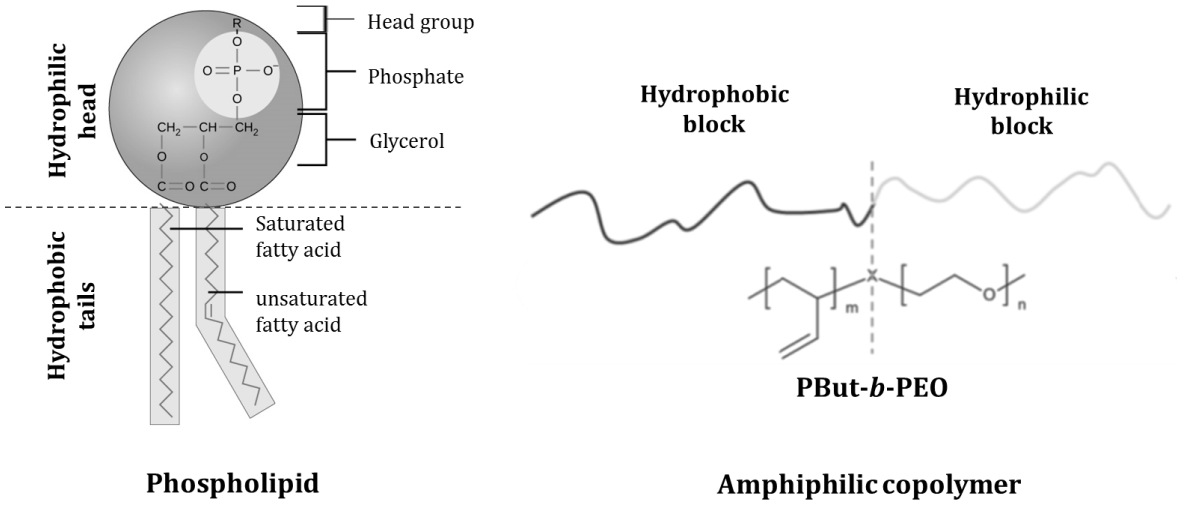

Figure 1.1. Representative amphiphile structures: phospholipid and amphiphilic copolymer.

1.1.2. General aspects of self-assembly of an amphiphile

When dissolved in aqueous solution above the critical micelle concentration (CMC), the amphiphiles self-assemble into diverse structures depending on their geometrical properties in order to minimize the contact area between water molecules and the hydrophobic chain tails.

Critical packing parameter

The first useful parameter to predict which structures can be obtained is the so-called packing parameter *ρ* according to Israelachvili's concept [1]. This parameter is defined as:

$$\rho = \frac{v}{a_o l_c} \qquad \text{(Eq. 1.1)}$$

where v is the volume of the hydrophobic portion of the amphiphile, a_o is the area occupied on average by the polar head group packed in the aggregate and l_c is the length of the hydrophobic tails. The relationship between packing parameter *ρ* and the optimal aggregate structure is illustrated in Table 1.1.

Table 1.1. Israelachvili's concept of the critical packing parameter: schematic representation of the molecular shapes of amphiphilic molecules and their preferred self-assembled structures in aqueous solution. Adapted from [2].

Critical packing parameter	ρ < 1/3	1/3 ≤ ρ ≤ 1/2	1/2 < ρ < 1	ρ ~ 1	ρ > 1
Molecular packing shape	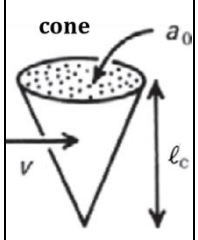	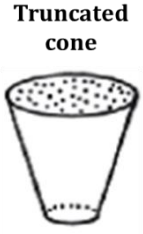			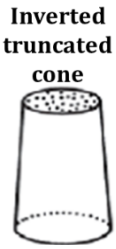
Aggregate structure formed	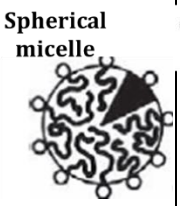	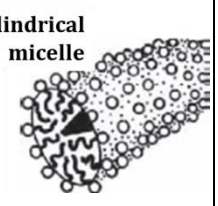	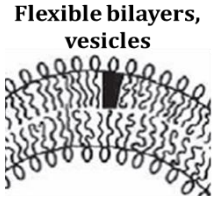	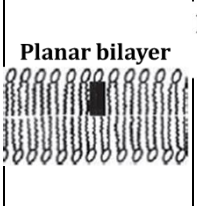	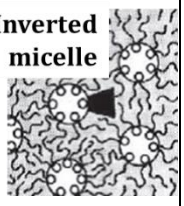

Generally, as displayed in Table 1.1, it is proposed that small ρ (ρ < 1/3) which corresponds to molecules with a relatively large polar head and small hydrocarbon tail imply highly curved aggregates such as spherical micelles. The geometry of molecules with 1/3 ≤ ρ ≤ 1/2 can be approximated to a truncated cone; such molecules are expected to form aggregates of a cylindrical or rod-like shape. Upon a further increase ρ until 1, corresponding to the cylindrical molecule, bilayer or sheet-like structure are formed. Finally, amphiphilic molecules with ρ > 1 form reverse aggregates.

The packing parameter was initially established to describe low molecular weight amphiphilic molecules such as surfactants and lipids but it can be applied also to some extent to block copolymers. The packing parameter can be related to the curvature of the hydrophilic-hydrophobic interface [3], as follows:

$$\rho = \frac{\mathrm{v}}{\alpha \mathrm{l}} = 1 - \mathrm{Hl} + \frac{\mathrm{Kl}^2}{3} \qquad \text{(Eq. 1.2)}$$

Here v is the hydrophobic volume occupied by the amphiphile, α is the interfacial energy and l is the chain length of the hydrophobic chain. The parameters describing the hydrophobic-hydrophilic interface are the mean curvature (H) and the Gaussian curvature (K), and both are given by the two radii of curvature R_1 and R_2. Descriptions of those parameters are displayed in Figure 1.2.

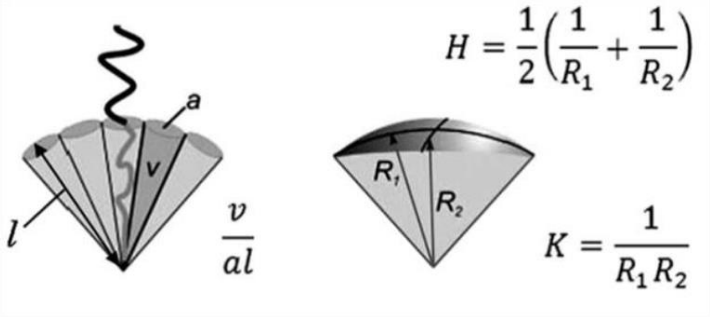

Figure 1.2. Description of the amphiphile shape in terms of the packing parameter ρ and its relation to the interfacial mean curvature (H) and Gaussian curvature (K); reproduced from [3].

Hydrophilic weight fraction

Although the trend of packing parameter is generally followed also for the amphiphilic copolymers, it is more convenient to characterize the preferred aggregate morphology of copolymers by the hydrophilic weight fraction (f) which is synthetically more accessible than ρ as proposed by [4]. Diblock copolymers are expected to form vesicular structures if f ~ 35 ±

10 %. Cylindrical micelles are expected for f-values < 50%, whereas f-values > 50% lead to spherical micelles. Nevertheless, it should be noticed that this relationship between hydrophilic weight fraction and morphologies may not be applicable to all systems as it was just confirmed for molecular weight range of 2 – 20 kDa and only for PEE-PEO and PBut-PEO diblock coil-coil copolymers. An excellent correlation between f and ρ has been found also by Discher et al [5] on the basis of numerous results from both experimental and simulation for various amphiphilic copolymers: $f \approx e^{-\rho/\beta}$, where β = 0.66. The relations between the geometry of the self-assembled structures, molecular curvature, ρ and f are resumed in Figure 1.3.

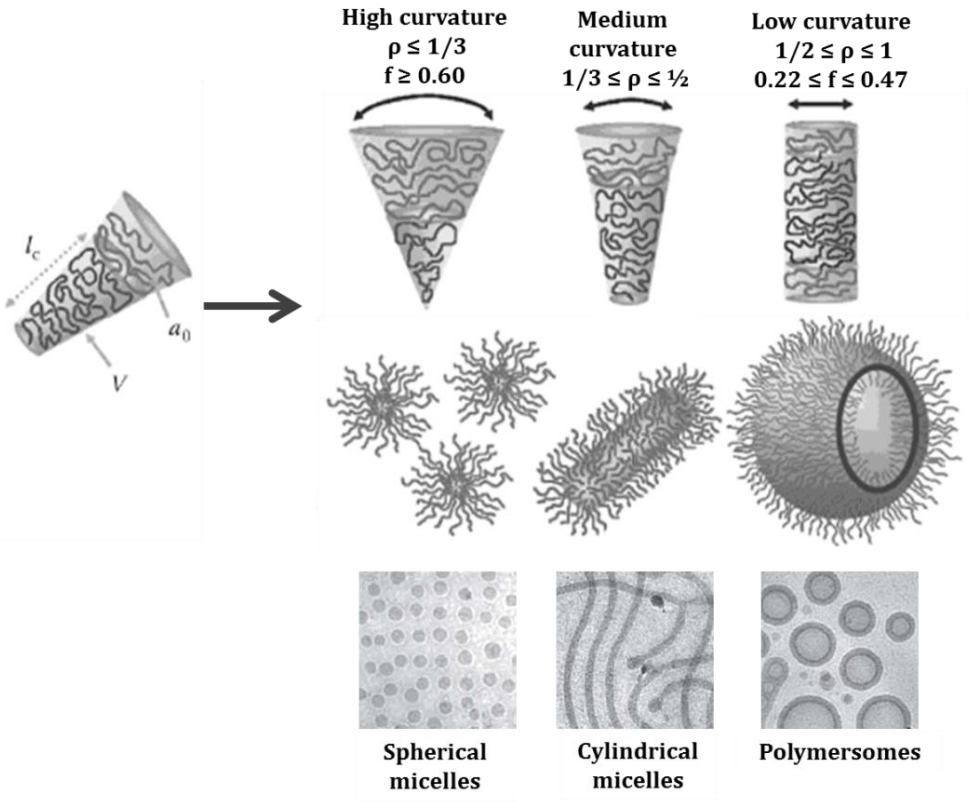

Figure 1.3. Interrelations between the self-assembled structures formed by amphiphilic copolymers in aqueous solution with packing parameter ρ and hydrophilic fraction f; scheme reproduced from Ref [6] and cryo-TEM images extracted from [7].

1.2. VESICLE

1.2.1. General features

Vesicles evolve from bilayer forming amphiphile with 1/2 ≤ ρ ≤ 1 in excess water. Upon hydration, the amphiphiles first self-assemble into a lamellar phase before they transform to unbound flexible bilayer sheets and finally close into spherical bilayers which are called

vesicles [8, 9]. The self-closing of flexible bilayer sheets in dilute aqueous solution is driven by the elimination of the energetically unfavourable contact of the hydrophobic edges with water (Figure 1.4). According to this self-assembly process, the basic vesicle structure is generally described as a hollow sphere that contains an aqueous solution in the core surrounded by a bilayer membrane. With such morphology, the aqueous core of vesicle can be used for the encapsulation of therapeutic molecules such as drugs, proteins and peptides, DNA… while the membrane can integrate hydrophobic drugs. This possibility to load both hydrophilic and hydrophobic drugs is one of the great interests of vesicles for therapeutic applications. Vesicles prepared from phospholipids are generally called liposomes and from amphiphilic copolymers, polymersomes.

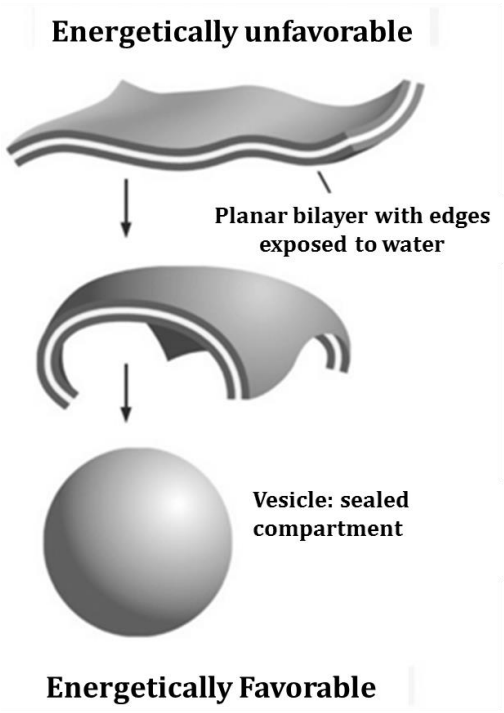

Figure 1.4. Spontaneous closure of a planar bilayer forming vesicle structure, from Ref [10].

Vesicles are most commonly classified by their size and number of bilayers (lamella) as schematically shown in Figure 1.5. Unilamellar vesicles consist of a single bilayer. Based on their mean diameter, they are divided into small unilamellar vesicles (SUVs: 20-100 nm), large unilamellar vesicles (LUVs: 100-500 nm) and giant unilamellar vesicles (GUVs: 0.5 – 100 µm). Multilamellar vesicles (MLVs) have a membrane composed of several bilayer shells and multivesicular vesicles (MVVs) are large or giant vesicles encapsulating smaller vesicles inside.

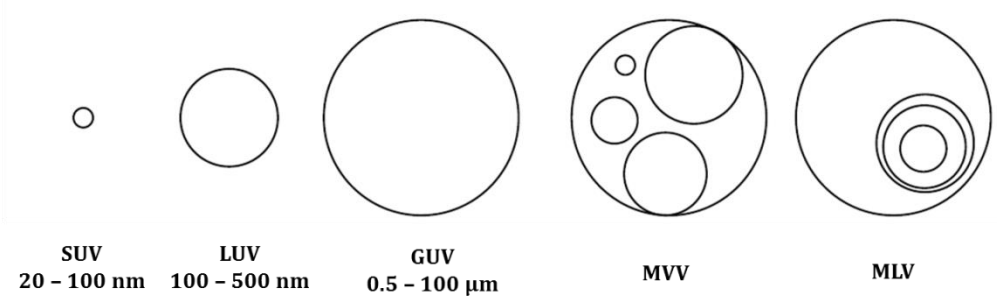

Figure 1.5. The common structural vesicle classes of small unilamellar vesicles (SUV), large unilamellar vesicles (LUV), giant unilamellar vesicles (GUV), multilamellar vesicles (MLV) and multivesicular vesicles (MVV).

1.2.2. Preparation of vesicles

The formation of vesicle in aqueous solution often requires input of external energy [11]. Therefore, the size and lamellarity of the resulting vesicles depend not only on the chemical structure of the amphiphile and on the solution conditions but particularly on the method of vesicle preparation [12]. In general, the methods described for the preparation of lipid vesicles are also applicable for amphiphilic copolymers [13]. However, the formation of polymersomes can be more complex and slower compared to liposomes, depending on T_g and the flexibility of the block copolymer chains [3, 14]. In the following, we introduce some of common methods that will be exploited in this thesis to prepare the GUVs and LUVs.

1.2.2.1. Preparation of giant unilamellar vesicles

Electroformation method

The electroformation method was first presented by Angelova and Dimitrov in 1986 [15] and is currently the most widely used method to prepare the giant unilamellar vesicles. The principle of this method is based on the hydration of a thin amphiphile film in aqueous solution of low ionic strength and in the presence of an alternating current electric field (ac). Generally, the ac electric field and the periodic electroosmotic motion of water molecules (electroosmotic vibration) enhance the swelling kinetics of the amphiphile film and promote bilayer separation (Figure 1.6).

In an electroformation experiment, the amphiphile film is directly deposited from an organic stock solution on the surfaces of two parallel electrodes assembled in an electroformation chamber. The most commonly used electrodes are Pt wires or Indium Tin Oxide (ITO) glass plates. After connecting the electroformation chamber to an external ac supply and filling in the hydration medium at $T > T_m$ or T_g of the amphiphile used, the film swells and GUVs

growth. The growth behaviour of GUVs and the final diameters of electroformed GUVs depend on different experimental conditions, including the amphiphile used, the thickness and homogeneity of the film, the swelling medium, the membrane fluidity and the applied electric field parameters (voltage, frequency, duration). The standard electric field parameters applied to lipid membranes consist of a voltage of 1-2 V (peak to peak), a frequency of 10 Hz and total electroformation time of 60 – 120 min [16, 17]. Polymer GUVs can also be obtained within 60 – 120 min by keeping the frequency at 10 Hz and applying somewhat higher driving voltages in the range of 4 to 10 V depending on the fluidity of the polymer membrane [18, 19]. For extremely viscous polymer membranes, the necessary electroformation time can be extended to several hours or /and temperature of electroformation can be increased [20]

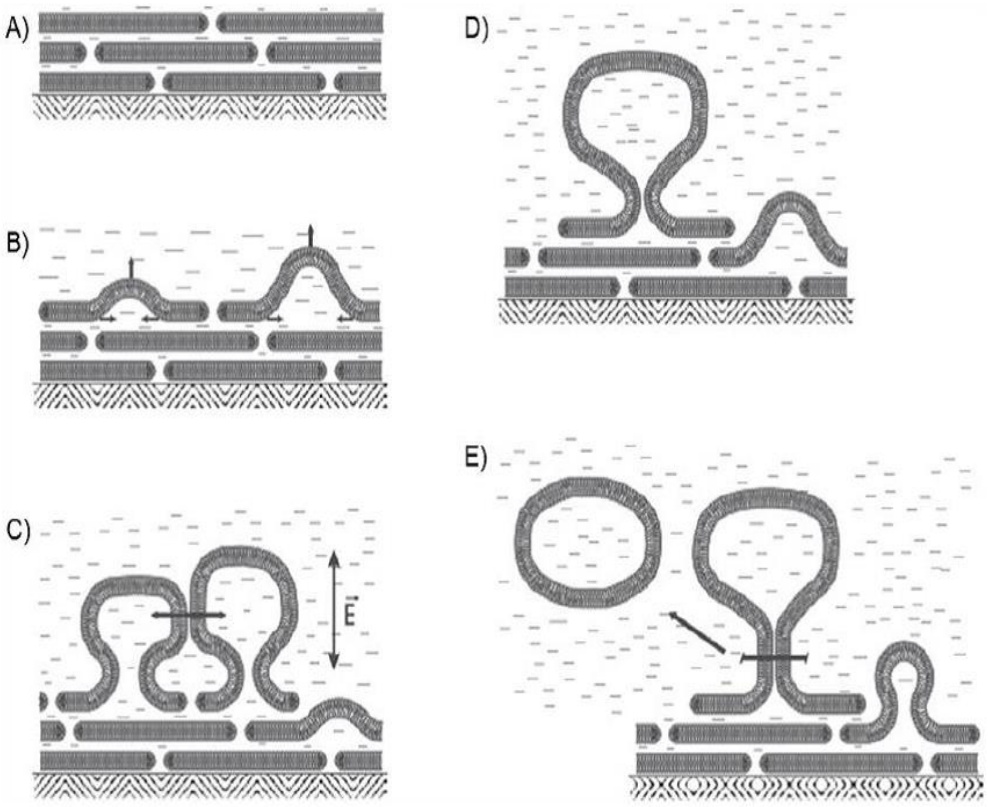

Figure 1.6. Schematic representation of growth of vesicles during electroformation process; adapted from [21].

1.2.2.2. Preparation of large unilamellar vesicles

Film rehydration

Simple hydration of amphiphiles in excess aqueous solution under agitation is the simplest way to prepare vesicle suspensions, generally yielding multilamellar vesicles (MLVs).

In the film rehydration process, the amphiphile is dissolved in a suitable organic solvent, usually chloroform. Then, the solvent is completely removed under vacuum, forming a dry thin film on the glass surface of the flask. The subsequent addition of an aqueous solution (at $T > T_m$ or T_g of the amphiphile used) induces swelling of the dry film. The film swelling process proceeds through the hydration of the hydrophilic domains, formation of a lamellar phase and increasing separation of the lamellae which eventually buckle and unbind to self-close into MLVs [22, 23]. In order to obtain the LUVs, MLVs will be prepared with the extrusion process as introduced in the following.

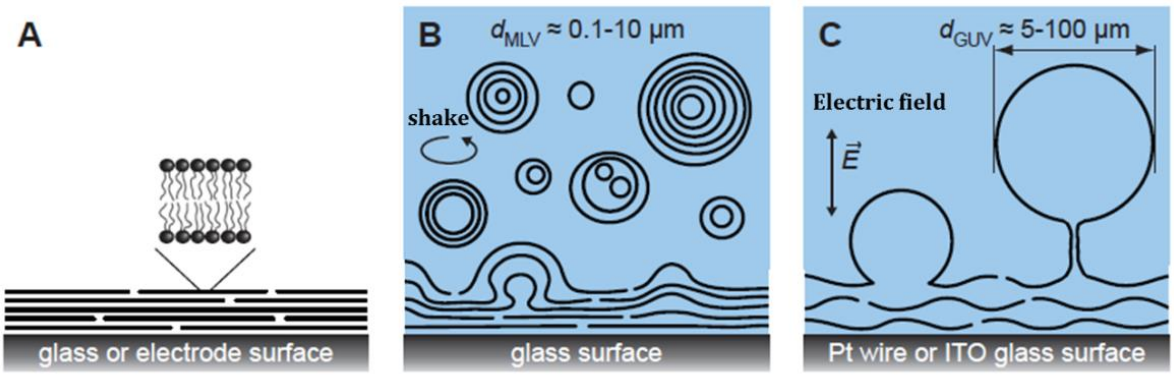

Figure 1.7. Schematic illustration of the formation of MLVs and GUVs through thin film hydration: (A): dried amphiphile thin film deposited onto a solid surface (glass of the flask or the Pt/ITO electrode); (B): MLV formation by hydration of the thin film in aqueous solution under shaking and (C): GUV formation by hydration of the thin film in aqueous solution under an electric field. Adapted from [16].

Extrusion

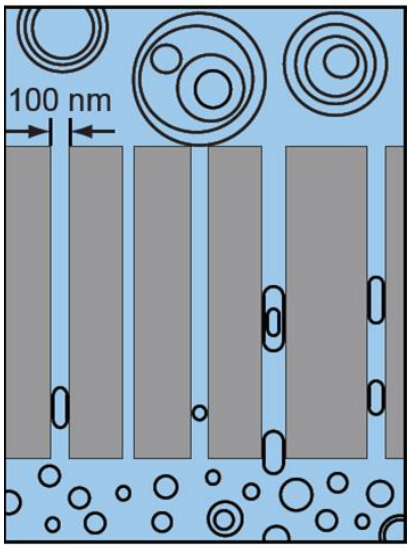

Figure 1.8. Schematic representation of extrusion process; adapted from [12].

The extrusion method was originally developed by Olson et al [24] and is the most popular method to produce homogeneous vesicles with controlled size and lamellarity. This method consists of repetitively force, under moderate pressure, a MLV suspension to go through well-defined, cylindrical pore channels of a polycarbonate filter membrane. The pore diameter range of the membranes used is commonly from 50 – 500 nm. Unilamellar or multilamellar vesicles that are larger than the mean diameter of the pore channels are reduced in size and lamellarity upon passage through the channels as schematically illustrated in Figure 1.8. The resulting mean vesicle size reflects the mean diameter of the pores.

Double emulsion evaporation

For highly hydrophobic copolymers, generally film rehydration process is hard to achieve. In this case, a useful method is the so-called double emulsion evaporation, whose principle is depicted in Figure 1.9. In this method, water is first added directly into an organic solution containing the amphiphiles under mechanical stirring, forming a primary w/o emulsion. This emulsion is subsequently dispersed again into large volume of aqueous solution, producing a w/o/w double emulsion. Vesicles, with relatively high size dispersity, are obtained following the progressive evaporation of organic solvent under probe sonication. In order to obtain the LUVs with narrow size distribution, extrusion is required afterward.

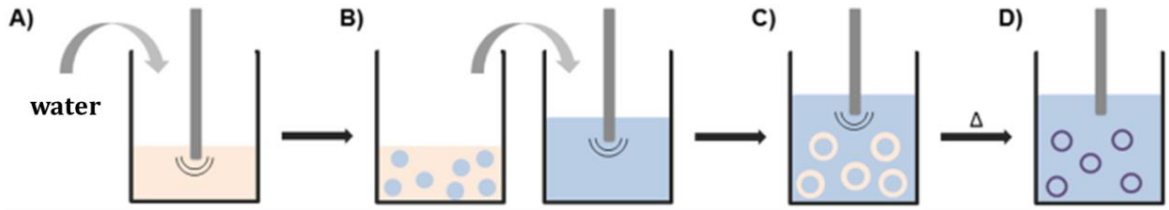

Figure 1.9. Schematic representation for double emulsion evaporation method used to prepare polymersomes; adapted from [25].

1.2.3. Physics of vesicles

1.2.3.1. Equilibrium state: membrane curvature and bending energy

Membrane curvature

The curvature describes the shape of each small membrane element which can be characterized by radii R_1 and R_2 of two arcs lying in the surface plane and oriented in two

principal directions [26]. The inverse radii $c_1 = 1/R_1$ and $c_2 = 1/R_2$ are defined as two principal curvatures (Figure 1.10). To describe the bilayer membrane shapes, the total and Gaussian curvatures that are respectively the sum $J = c_1 + c_2$ and the product $K = c_1 * c_2$ are often used [27]. By this way, a sphere radius R has a total curvature $J = \frac{2}{R}$ and a Gaussian curvature $K = \frac{1}{R^2}$, while for an infinite cylinder with radius R, the total curvature is $\frac{1}{R}$ and Gaussian curvature is null. Hence, J and K are indeed local parameters, which completely describe the shape of the membrane.

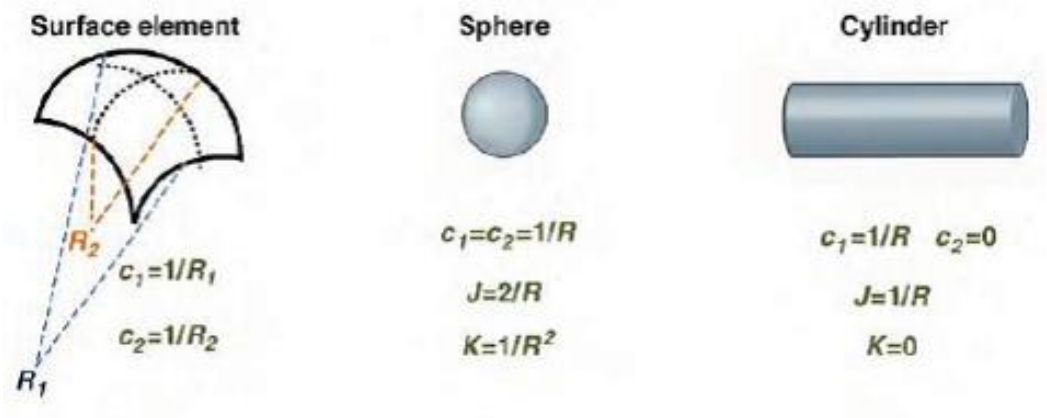

Figure 1.10. Geometric definition of membrane curvature and examples for basic shapes like spherical and cylindrical shape, adapted from [28]

An interface may also have spontaneous curvature (c_O) which corresponds to the relaxed curvature of the membrane. A symmetrical membrane has a zero spontaneous curvature while an asymmetrical membrane has a non-zero spontaneous curvature, because the sum of the spontaneous curvatures of the two leaflets is no longer zero. This asymmetry can be induced by using different molecules for the inner and outer leaflet or by unilateral binding of other molecules to one of the surfaces of the membrane [29, 30].

Bending energy

The energy that is required to curve a membrane into a vesicle is called bending energy (or curvature elastic energy or free energy of bending/curvature). The bending energy is related to the curvature of the membrane by the following equation [27]:

$$E_H = \frac{\kappa}{2}\oint (c_1 + c_2 + c_0)^2 \, dA + \kappa_G \oint c_1 c_2 \, dA \qquad \text{(Eq. 1.3.)}$$

Where κ is the bending rigidity constant, κ_G is the Gaussian bending rigidity. For a symmetric vesicle membrane, this equation is rewritten as:

$$E_H = \frac{\kappa}{2}\oint (c_1 + c_2)^2 \, dA \qquad \text{(Eq. 1.4.)}$$

So then for a vesicle with a radius R: $c_1 = c_2 = 1/R$:

$$E_H = 8\pi\kappa \qquad \text{(Eq. 1.5)}$$

The bending rigidity κ reflects the difficulty to bend a membrane. It is related to many molecular parameters of bilayers (overall shape of vesicle, chemistry of amphiphile…) and macroscopic parameters (temperature…), but the most important parameter that modulates κ is the thickness of the membrane. A thicker membrane should cause greater differential strains between two leaflets, and therefore is more difficultly bended. Bending rigidity is quadratic with the bilayer thickness [31]. That is why for phospholipid bilayers, κ is in the order of 10 – 20 kT, significantly smaller than those of polymer membranes.

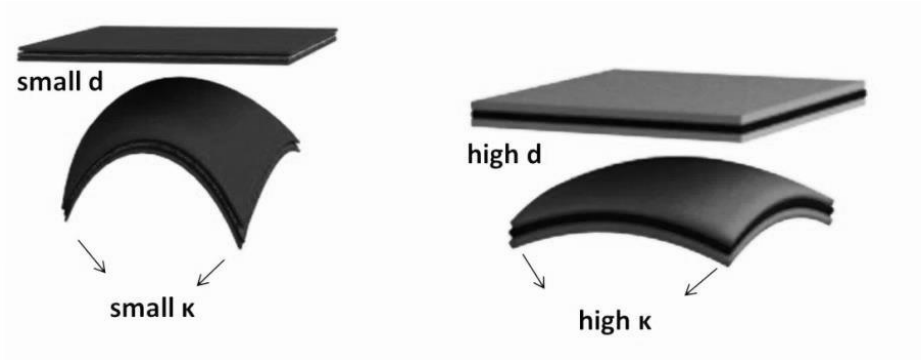

Figure 1.11. The easiness to bend a surface of thinner lipidic membrane giving small κ values while a thicker polymeric membrane usually exhibit a higher κ.

1.2.3.2. Membrane deformation: stretching energy

Stretching is a deformation, which modify the area A of a membrane. This deformation can be described *via* a parameter, namely the "reduced vesicle volume" ϑ as introduced in Eq.1.6. This parameter is defined as the ratio between the vesicle volume V and the volume of a sphere having the same surface area as the vesicle and an equivalent radius R_0 [29].

$$\vartheta = \frac{V}{{}^{4\pi}/_{3}\, {R_0}^3} \qquad \text{(Eq. 1.6)}$$

When the vesicle volume is reduced below the maximum $V_0 = {}^{4\pi}/_{3}\, {R_0}^3$ at a constant surface area, $\vartheta < 1$, the vesicles are deflated and present excess membrane area. On the contrary, when the vesicle volume is larger than V_0 ($\vartheta = 1$), elastic expansion of the membrane is present and under these conditions, the dominant energy is the stretching

energy and a uniform membrane tension σ in the plane of the bilayer appears. The stretching energy can be defined as Eq.1.7 [32]:

$$E_{strech} = \frac{1}{2} K_a \frac{(A - A_0)^2}{A_0} \quad (Eq. 1.7)$$

Here K_a is so-called the stretching modulus or area compressibility modulus, A_0 and A are the membrane area at rest and under tension respectively. The relationship of induced membrane tension and the change in area of vesicle can be given by [33]:

$$\alpha \approx \frac{k_B T}{8\pi\kappa} \ln(\sigma) + \frac{\sigma}{K_a} \quad (Eq. 1.8)$$

Here k_B is the Boltzmann's constant, T is absolute temperature and κ is the bending modulus as mentioned in previous paragraph. This equation is typically used to determine the stretching and bending modulus K_a and κ. At low tension, thermal fluctuation of the membrane dominates and the bending rigidity is accessible whereas at high tension, as mentioned before, stretching elasticity dominates, giving access to K_a.

Modulation of membrane tension

Membrane tension is usually controlled by micropipette aspiration technique or by applying variation of osmotic pressure. The osmotic pressure method is exploited since vesicular membranes are generally semipermeable which allows water diffusing across the membrane due to an osmotic difference between the interior and exterior water regions. In hypotonic condition, where water diffuse inside, vesicles swell and membrane tension increases. On the contrary, hypertonic conditions allow water to diffuse outside and lead to a deflation of the vesicle, decreasing membrane tension. The induced membrane tension by this method can be quantified by the following equation:

$$\sigma = \frac{pr}{2} + \frac{\kappa c_o}{2r}(2 - c_o r) \quad (E.q. 1.9)$$

with p is the osmotic pressure between inner and outer media, r is the radius of vesicle, κ is the bending modulus and c_0 is the spontaneous curvature.

Membrane tension can be induced also by directly applying an external mechanical force to the vesicle, i.e. using micropipette aspiration. This technique consists in aspirating the vesicle with a capillary pipette by a controlled suction pressure. The tension of membrane in this case can be deduced via Laplace equation by:

$$\sigma = \frac{R_p * \Delta_p}{2(1 - \frac{R_p}{R_v})} \qquad (Eq.\ 1.10)$$

R_p and R_v are respectively the radius of pipette and vesicle and Δ_p is the aspiration pressure. By recording the membrane areal strain due to this stretching at each point of membrane tension, this method allows the measurement of stretching and bending modulus according to Eq.1.8.

1.3. MEMBRANE CHARACTERISTICS

1.3.1. Characteristics of lipidic membranes

Thermodynamic state

Lipid membranes can exist in different phase states depending on temperature. Two of them are represented in the figure below:

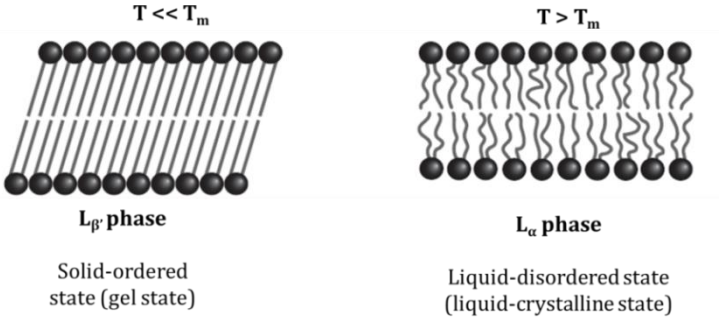

Figure 1.12. Phase states of lipid membranes below and above the main phase transition temperature T_m; adapted from [34].

At temperatures below than T_m, lipid bilayers are in the solid-ordered state (also named gel or crystalline state). The lipid arrangement in the bilayer corresponds to that typically found in the staked bilayers of the lamellar equilibrium phase $L_{\beta'}$. It is characterized by rigid, extended and tilted hydrophobic chains allowing an ordered and dense packing of the lipid molecules in the membranes. As a result, the area occupied by the head group is minimum whereas the thickness is maximum. For instance, pure DPPC membrane in the gel phase has an area per lipid of 0.48 nm² (it is 0.63 nm² per lipid in the fluid phase) and a thickness (head to head distance) of 4.79 nm (which goes down to 3.92 nm in the fluid phase) [35, 36].

Above T_m, lipid bilayers are in the liquid-disordered state (or so-called fluid state). In this case, the hydrophobic chains exist in a flexible and disordered conformation. This leads to the fluid-like behaviour membranes, i.e. the amphiphiles exhibit fast lateral and rotational

diffusions. Most of the dynamic process observed in lipid vesicle systems including their formation by swelling of a lamellar phase, shape fluctuations and shape transformations are restricted to the fluid state of the lipid phase [17, 29].

Molecular dynamic

Lipid membranes in a fluid state are generally highly dynamic. Both the position (i.e. lateral diffusion) and the orientation (i.e. rotation) of a lipid within the membrane bilayers are continuously changing over time. Different diffusion coefficients are used to characterize the lipid dynamic within the membranes. The lateral diffusion coefficient determines the ability of a lipid molecule to laterally exchange with one of its neighbours while the rotational diffusion coefficient defines the angular rotation of a lipid molecule around its axis perpendicular to the plane of the bilayer. The transfer of one lipid molecule from one leaflet of the bilayer to the other one is called transversal diffusion or flip-flop of phospholipids and is generally a very slow process. The possible motion of the individual lipids inside the bilayer are presented in Figure 1.13.

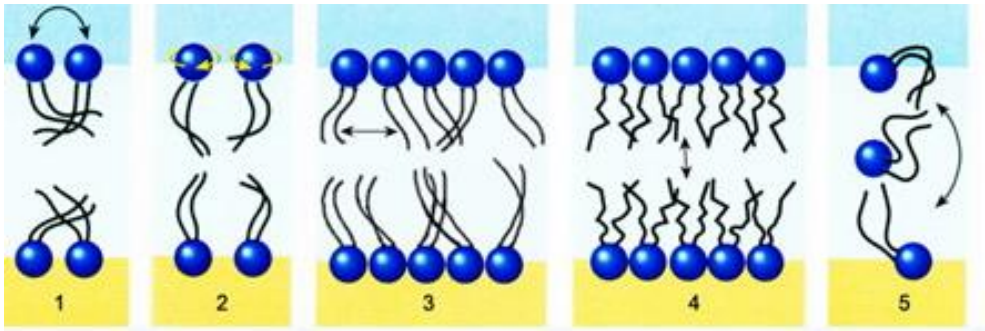

Figure 1.13. The types of motion within bilayer membrane: (1): Lateral diffusion: molecules simply transpose with neighbouring molecules; (2): Rotation: an individual lipid molecule rotates very quickly around its axis; (3): Swing: molecules move from side to side; (4): Flexion: contraction movement; (5): Flip-flop: motion of molecules from one-half of a monolayer to the other, this is an uncommon event for phospholipids. Reproduced from https://animalcellbiology.wordpress.com/chapter3.

Mechanical properties

Mechanical features of the membrane are typically characterized in terms of the stretching modulus K_a, bending modulus κ and the lysis tension as mentioned in the previous sections. As bending modulus κ and the lysis tension are dependent on membrane thickness, the lipid membranes with relatively thin-layer generally suffer a low mechanical stability. This is the major drawback of liposomes for biomedical application. The typical values are given in Table 1.15.

Permeability

Permeability of membranes is reflected by the permeation rate of specific molecules across the membrane. There are many factors that influence the vesicle membrane permeability, but it mostly depends on the membrane thickness, fluidity and the packing density of membrane. Accordingly, lipid membranes possess relatively high permeability (water permeability of liposomes is in the range of 15 – 150 µm.s^{-1} [37]). That's why liposomes used as drug delivery systems often exhibit uncontrolled leakage phenomena, and the controlled release of encapsulated molecules remains a challenge for liposome formulations.

1.3.2. Characteristics of polymeric membranes

Membrane conformation

While liposomes are composed of lipid bilayers, amphiphilic copolymers may present different conformations in the membrane of polymersome. Figure 1.14 [13] illustrates the possible assemblies for AB diblock, ABA, BAB and ABC triblock copolymers where A and C are different hydrophilic polymer blocks and B is a hydrophobic block.

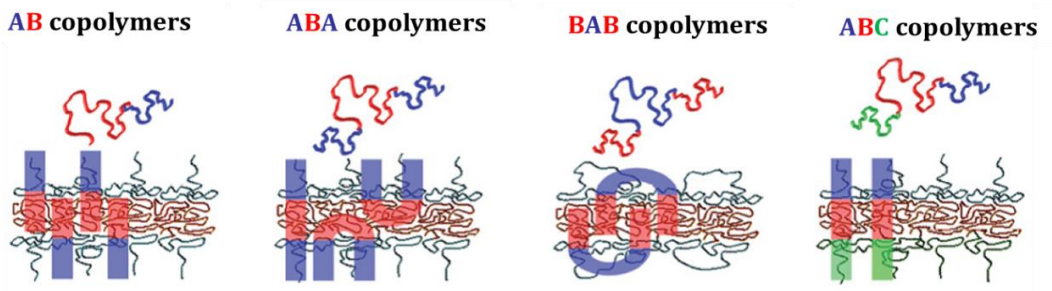

Figure 1.14. Membrane conformation of polymersomes formed by different diblock and triblock copolymers, adapted from [13].

Briefly, AB diblock can self-assemble into a bilayer in analogy with liposomes, while ABA triblock can present two possible conformations: the hydrophobic block can either form a loop in such a way that the hydrophilic chains are on the same side of the membrane (hairpin or U-shape) or they can present an extended conformation, forming a monolayer with the two hydrophilic blocks at the opposite sides of the membrane (I-shape). Alternatively, with BAB triblock, the hydrophobic chain ends must assemble into a membrane and the hydrophilic form a loop (U-shape). Interestingly, the ABC triblock self-assembles into asymmetric membranes e.g., the chemical nature of the internal and external surfaces differs from each other.

Membrane thickness

In polymersomes, the membrane thickness d scales with the molar mass as $d \sim (M_h)^b$ where the scaling exponent b is a parameter describing the folding state of the polymer chain and M_h is the molar mas of the hydrophobic block. Briefly, for polymersomes based on PEE-PEO [38] and PB-PEO [39], b has been found to be equal to 0.55. A value of 0.5 has been reported for for a series of PS-PAA polymersomes [40] while a higher value of the exponent (b = 0.66) has been determined by Battaglia et al for PEO-PBO copolymers, for relatively thin membranes (d < 7 nm) [9] and also for PEE-PEO polymersomes, below a critical DP of the PEE block [38]. The scaling exponent close to 0.83 found by numerical simulation for membrane thickness below 7 nm is also in conformity with the existence of a critical molar mass [38]. At low membrane thickness, the chains are stretched and are characterized by an exponent corresponding to a strong-segregation state that is 2/3. Upon increasing membrane thickness, the repulsion between blocks leading to stretching, decrease and interdigitation of the chains increases, resulting in a gradual reduction of the scaling exponent to a value of 0.5, which corresponds to a non-perturbed state of the chains and seems universal for coil-coil block copolymer-based vesicles. One exception from this rule is the data of Leson et al [41] who have found a scaling exponent of unity, corresponding to fully stretched chains for a series of poly(2-vinylpyridine)-PEO bock copolymers of a relatively limited molar mass range.

Basic physical properties

The basic physical properties of polymer membranes are shown in Table 1.2. Compared to lipid membranes, polymer vesicles possess higher mechanical toughness and lower permeability that can be modulated *via* the molar mass of the copolymer used. Moreover, they present more versatile chemical functionality compared to liposomes.

Table 1.2. Physical and mechanical properties of liposomes and polymersomes and scaling with membrane thickness d and polymer molar mass M_w (Adapted from [42]).

Property	Liposomes	Polymersomes	Scaling
Bending modulus (kT)	11 – 30 [43]	40 – 460 [19, 44]	$\sim d^2$ [44]
Stretching modulus ($mN.m^{-1}$)	250 ± 2 [43]	80 – 100 [39]	$\sim d^0$ [39]

Lysis strain (%)	5 [39]	20 – 50 [39]	~$d^{0.6}$ for $M_w < M_e$ [39]
Membrane surface shear viscosity ($mN.ms^{-1}$)	10^{-5} [45]	15.10^{-3} [19]	-
Water permeability ($\mu m.s^{-1}$)	15 – 150 [37]	0.7 – 10 [37]	~d^{-1} [22]
Lateral diffusion coefficient ($\mu m^2.s^{-1}$)	3.8 [46]	0.12 – 0.024 [46]	~M_w^{-1} (Rouse scaling for $M_w < M_e$) ~M_w^{2-3} (bulk reptation for $M_w > M_e$)

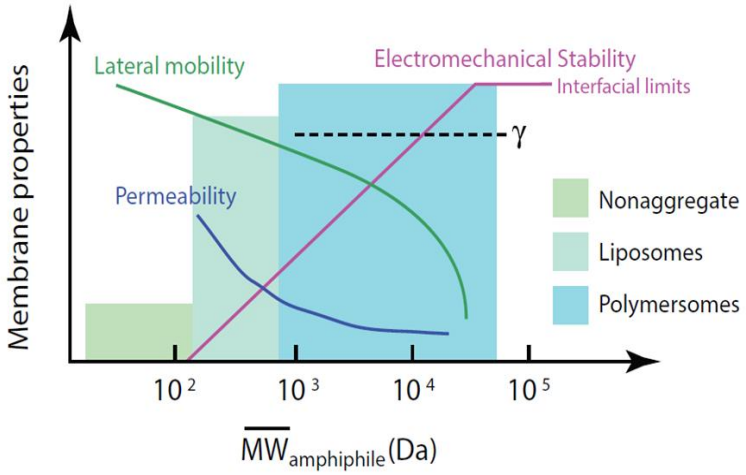

Figure 1.15. Schematic diagram showing changes in membrane properties upon increase in the molar mass of macromolecular amphiphiles. Adapted from Ref [47].

1.4. MULTICOMPONENT MEMBRANES

1.4.1. Biological membranes

Biological membranes are constituted mainly of lipids and proteins [48]. Lipids are organized in a bilayer with a thickness about 3 - 5 nm where proteins are embedded. It was suggested in 1925, that biological membranes were made of two lipid layers [49]. The presence of proteins was later suggested by Danielli and Davson in 1935 [50]. The most accepted model of membrane structure originates from the so-called fluid mosaic model proposed by Singer and Nicolson in 1972 [51] as shown in Figure 1.16. In their model, all lipid and proteins are mixed together to form a homogenous two-dimensional fluid. Nowadays, biomembranes are believed to be heterogeneous structures where lipid exist in different states can form domains and interact with the proteins [52].

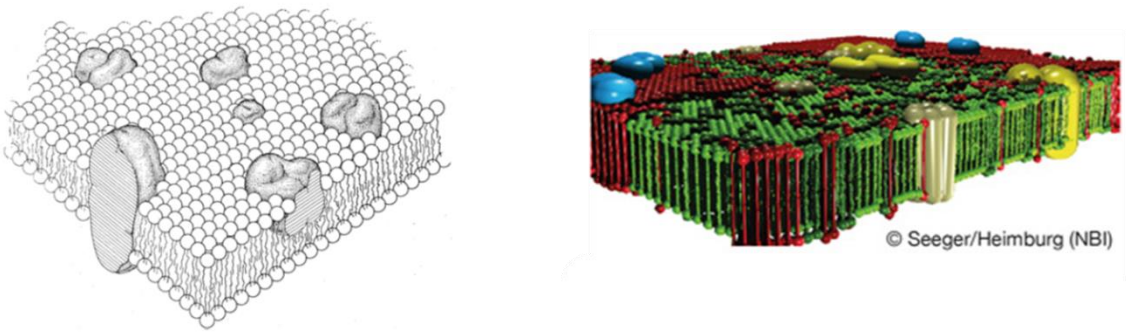

Figure 1.16. Models of biological membranes Left: the fluid mosaic model proposed by [51] and right: membrane proteins, lipids and different species are distributed heterogeneously in the membrane plane, adapted from [48].

1.4.2. Multicomponent lipid membranes

Multicomponent lipid vesicles have been extensively studied to understand the structure-properties relationship of biological membranes. Numerous works have been realized on model GUVs to understand the role of lipid segregation into domains [53, 54]. Basically, two types of phase separation in lipid membrane can occur: lateral phase separation of two lipids into different areas or vertical phase separation between the two leaflets of the lipid bilayer as depicted in Figure 1.17. Vertical phase separation can be triggered via addition of an external compound whereas lateral phase separation can occur due to different interaction energies between lipid components but also by recruiting mobile "binders" among the lipids into the adhesion area with a substrate [55].

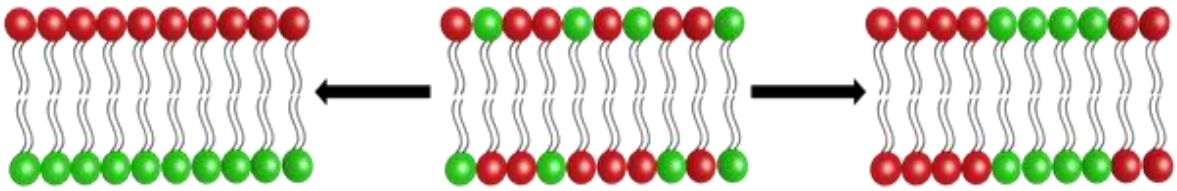

Figure 1.17. Illustration of the two main types of possible phase separations in lipid bilayers: vertical phase separation (left) lateral phase separation (right).

Non-ideal mixing or even de-mixing (phase separation) can occur between lipids with similar structure (e.g. phosphocholine head group with two saturated acyl chains) provided that a sufficient length difference in lipid tails is present (typically four CH_2 groups). In that case, phase separation is obtained below a given temperature of fluid/solid or solid/solid transition. A different nature of the head groups (e.g. charged/neutral) can also lead to phase separation, but in that case the ionic content of the solution is important (e.g. added

Ca^{2+} ions [56]). A strong difference in melting temperatures is generally associated with a strong difference in chemical structures (e.g. sphingolipids and phospholipids) leading to solid/solid or fluid/solid phase separations at certain temperatures. Fluid-fluid phase separation can also occur through weak attractive forces. Cholesterol has been largely employed to modulate the fluidity of membranes and create phase separation above the main transition temperature of a phosphocholine lipid leading to liquid ordered and liquid disordered phase coexistence [57]. Phase separation lead to lipid/lipid boundaries and possibly height mismatch between both phases. Consequently, the membrane elastically deform at the domain interface to minimize the exposure of hydrophobic tails to water. The height mismatch has an energetic cost proportional to the length of the boundary line, thus defining the line tension λ. Thermodynamically, the line tension tends to favour domain coalescence (once a nucleation size is reached) to minimize the boundary length. As a consequence, the lipid domains would grow with time into one single large circular domain in the membrane. However, some distribution of domain sizes can be found in model GUV and biological membranes. This is due to the fact that the line tension is balanced by other mechanisms such as an "entropic trap" stabilizing the domains at a nanometric size [58], the "elastic interaction" between dimpled domains due to deformation of the surrounding membrane [59], the long range electrostatic dipolar interaction [60] and the natural vesicle spontaneous curvature [59, 61, 62] and bending rigidity κ of the membrane.

1.4.3. Hybrid polymer/lipid membranes

Inspired from the previous studies about multicomponent lipid vesicles, hybrid vesicles composed of both amphiphilic copolymer and phospholipid have been developed recently. After the first study introduced in 2005, a relatively limited but continuously growing number of work on these systems has been published. The purpose of this section is to review the current knowledge about their membrane structuration and properties on the Giant Scale (GHUVs) and Nanoscale (LHUVs).

1.4.3.1. Lateral structuration of giant hybrid vesicles

In the case of copolymer and lipid mixtures, a very important parameter controlling the formation of stable hybrid vesicles is the discrepancy of chemical composition and size of hydrophobic segments between polymers and lipids. In the case of lipid mixtures, one must consider interactions between lipid tails, always constituted of saturated or unsaturated

fatty acid chains. However, in the case of polymer/lipid mixture, the nature of monomeric unit may lead to a stronger immiscibility between the hydrophobic copolymer blocks and the lipid tails. In addition, the characteristic thickness of lipid membranes is around 3 to 5nm, well below those commonly observed for polymersomes (~10nm or more, although this parameter is directly controlled by the polymerization degree) and may lead to strong geometric differences between the molecules constituting the membrane and large driving force towards demixing. This most often results in fission, leading to separate populations of liposomes and polymersomes.

A relatively limited number of amphiphilic copolymers have been used so far to form Hybrid Giant Unilamellar Vesicles. Hydrophobic blocks were based on poly(dimethyl siloxane) (PDMS) [63, 64], poly(isobutylene) (PIB) [65-68] or poly(butadiene) (PBd) [69-72], while hydrophilic blocks were either made of poly(ethylene oxide) (PEO) or poly(2-methyl oxazoline) (PMOXA). All these polymer blocks possess a low glass transition temperature (T_g), allowing dynamic exchanges of the chains and leading to the formation of membranes with a structure at thermal equilibrium. The low T_g is a criterion which appeared so far as essential, but not unique, to the successful formation of GHUVs. Concerning the choice of lipids, most studies were performed with phosphatidylethanolamine or phosphatidylcholine head groups like POPC [71] [70, 72], HSPC [69], DOPC, DLPC [65, 66] and the most often used DPPC [63-65, 67, 72]. All the systems used so far are summarized in Table 1.3, together with the corresponding results regarding lateral structuration of Giant hybrid polymer/lipid vesicles.

Table 1.3. Structuration of different giant hybrid polymer/lipid vesicles.

Copolymer	Phospholipid	Lipid mass fraction	Membrane structure	Reference
PMOXA-*b*-PDMS-*b*-PMOXA M_n = 9000 g·mol^{-1} d = 10 nm	PC PE	PC: 1% PE: 1%	Homogeneous	[73]
PBd_{46}-*b*-PEO_{30} M_n = 3800 g·mol^{-1} d = 8 nm	POPC	POPC: 0% - 8%	Homogeneous	[71]
		POPC: 10% - 27%	No GUVs formation.	
		POPC: 32% - 100%	Pure liposomes + pure polymersomes	
	POPC + Biotinyl DSPE	POPC: 6% Biotinyl DSPE: 5%	Heterogeneous with small lipid domains	
		POPC: 28% Biotinyl DSPE: 8%	Heterogeneous with large lipid domains	
	POPC + Chol	POPC: 10.3% Chol: 5.2%	Heterogeneous with large lipid domains	[74]
		POPC: 15.4% Chol: 7.8%		
		POPC: 23.8% Chol: 4.8%		
	DPPC	DPPC: 11.4%	- Heterogeneous at room temperature - Homogeneous at 50°C	
	DPPC + Chol	DPPC: 10% Chol: 3.5%	Heterogeneous at room temperature	
PBd_{22}-*b*-PEO_{14} M_n = 1800 g·mol^{-1} d ~ 6 nm	HSPC	HSPC: 5%	Homogeneous	[75]
		HSPC: 13%		
	POPC	POPC: 30%	Homogeneous	[70]

PIB_{87}-*b*-PEO_{17} M_n = 5350 g·mol^{-1} d : data not shown	DOPC	DOPC: 26%	Homogeneous and stable vesicles	[65]
		DOPC: 37%		
		DOPC: 57%	Homogeneous turning into heterogeneous then budding and fission to pure polymersomes and liposomes	
	DPPC	DPPC: 0%	No GUVs formation	[68]
		DPPC: 0.15% - 26%	Homogeneous	
		DPPC: 26% - 35.4%	Heterogeneous	
		DPPC: 46% - 93%	GUVs with facetted surface and hole defects	
PIB_{37}-*b*-PEO_{48} M_n = 3970 g·mol^{-1} d : data not shown	DPPC	DPPC: 43%	Homogeneous	[68]
		DPPC: 62.4%	Heterogeneous	
Ch-PEG_{30}-*b*-$hbPG_{23}$ M_n = 1100 g·mol.$^{-1}$ d : data not shown	POPC DLPC DOPC	Lipid: 98.5%	Homogeneous	[76]
		Lipid: 93%		
		Lipid: 77%		
		Lipid: 41%		
$PDMS_{22}$-*g*-$(PEO_{12})_2$ M_n = 2750 g·mol^{-1} d = 5.6 nm	POPC	POPC: 3% - 14%	Homogeneous	[77]
		POPC: 22% - 42%	Heterogeneous then budding and fission into pure polymersomes and liposomes	
	DPPC	DPPC: 4%	Homogeneous	
		DPPC: 7% - 41%	Heterogeneous	
		DPPC: 1% - 7%	Homogeneous	[63]
		DPPC > 7%	Heterogeneous membranes	

It is interesting to note that the Hildebrand solubility parameters δ of hydrocarbon moieties in hydrophobic polymer blocks and phospholipids are relatively close, that is δ = 9.1 $cal^{1/2}/cm^{3/2}$ for the fatty acid tail in lipids and δ = 7.3 $cal^{1/2}/ cm^{3/2}$, 7.7 $cal^{1/2}/cm^{3/2}$ and 8.32 $cal^{1/2}/cm^{3/2}$ respectively for PDMS, PIB and PBd blocks [78, 79]. These relatively close values suggest that the chemical compatibility between the components is indeed a parameter of uppermost importance to enable the formation of such hybrid vesicles, even though the lateral phase separation of components inside the membrane still can occur for other reasons, as it will be commented in the following.

In each of the abovementioned contributions, there is no real systematic investigation allowing a clear extraction of molecular and macroscopic parameters necessary to intimately mix the components into stable GHUVs presenting homogeneous distribution of both components, or on the contrary, to induce formation of heterogeneous membranes patterned with domains. Moreover, another difficulty arises from the fact that the molar composition of lipid and copolymer in the final hybrid vesicles can be different from the starting composition, as evidenced by fluorescence microscopy, which complicates the analysis of the results. This is inherent to the experimental procedures used so far for the formation of GHUVs.

The physical state of the lipids, which depends on their main chain transition temperature (from gel state at T<Tm to fluid, liquid-crystalline state at T > Tm) as well as the composition of the lipid / copolymer mixture, are among the most relevant parameters. It seems that at high copolymer content (>70% weight), the formation of homogeneous hybrid vesicles is favoured when using a lipid with phosphocholine as head group and fatty chains in a fluid state at room temperature, [69-72], except in one case where no GUVs were obtained between 90% and 73% weight fraction of a PBd-*b*-PEO copolymer presenting a number average molecular weight of 3800g·mol^{-1} [71].

Above a critical lipid weight fraction, one generally observes the formation of heterogeneous vesicles presenting lipid-rich micrometric domains, that progressively evolve through a budding and fission phenomenon towards separated liposomes and polymersomes [64, 65]. This ultimate phase separation into two pure GUVs occurs for fluid domains in fluid membranes, and is directly linked to a sufficiently high line tension. When λ_{db} is large enough, the energetic barrier induced by the larger curvature energy associated with

membrane budding can be overcome by decreasing the boundary length between the lipid and copolymer domains and the associated excess energy. To get rid of the line energy implies a cost in bending energy as the curvature of membrane will increase trough the formation of the bud. Therefore, line tension between the domains and bending rigidity of the membrane are two parameters of prime importance.

In copolymer/lipid hybrid vesicles, line tension and bending rigidities are probably different to some large extent as compared to their values for lipid/lipid mixtures. The usual membrane (bilayer) thickness is indeed 3–5 nm for liposomes, while it may varies from 5 to 50 nm for polymersomes. In case of a large size gap, the formation of a lipid domain would result in a high line tension at the lipid/copolymer boundaries arising from the exposure of hydrophobic polymer segments to water ("hydrophobic mismatch"). To reduce this exposure and the resulting energetic cost of the boundary lines, the two opposite plausible scenarios can be considered. The first one (i) consists in a conformational adaptation through elastic deformation of the polymer chains at the boundary to decrease the line tension (Figure 1.18-a), in analogy to elastic deformation of membrane at lipid/lipid domain boundary in lipid bilayers [80]. Another possibility (ii) is to decrease the interfacial length and therefore the interfacial energy, by coalescence into fewer domains of larger area.

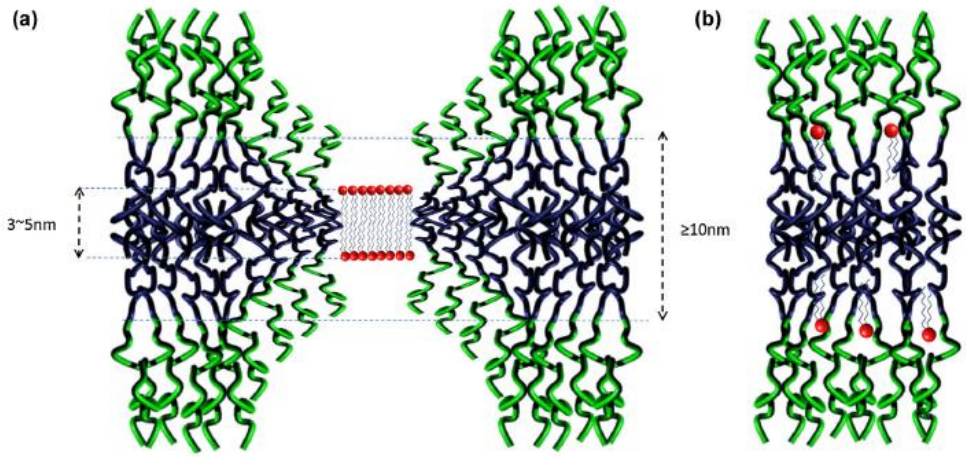

Figure 1.18. (a) Conformational adaptation expected at polymer/lipid domain boundary in hybrid vesicles in case of domain formation; (b) Absence of conformational adaptation between polymer/lipid boundary leading to homogeneous mixture of the components.

The conformational adaptation of the polymer implies a collapse of the hydrophobic polymer chains near the lipidic interface, therefore reducing the total number of conformations and opposing the entropic elasticity of chains. Therefore it is clear that the

molar mass (or chain length) and the rigidity (or Kühn length) of the hydrophobic polymer backbone are also playing a major role. If this adaptation cannot be achieved, then the domain formation is improbable (spontaneously nucleated domains eventually collapse) and a homogeneous mixture of the components is expected Figure 1.18-b.

A large hydrophobic mismatch is met in most of the studies performed so far, as the diblock or triblock copolymers usually used are forming membranes whose thickness is at least 7nm, and line tension, although not yet quantified experimentally, is expected to be high and driving the budding and fission of existing fluid domains. However the hydrophobic mismatch is certainly not the only parameter, as the budding and fission of lipid domains have been observed also in a study in which a grafted copolymer, PDMS-*g*-$(PEO)_2$ well-known to form vesicles with a membrane thickness close to liposomes (~5nm), was used [64]. In addition to the chemical nature of the hydrophobic block which obviously plays a role in the miscibility with the lipid phase and consequently on the interfacial energy, the architecture of the copolymer (*block vs. graft*) may be also an important factor to consider.

The fluidity of the lipid phase is also of significance in the membrane structuration of GHUVs. In the case of lipids in the gel state at room temperature, and using a formation protocol described in section 3, the spontaneous formation of domains at the optical microscope scale was reported only as a rare event. For instance in one of these studies [68], GUVs presenting stable micrometric domains were spontaneously obtained using DPPC and PIB_{87}-*b*-PEO_{17}, but only in a narrow composition range (65%–74 mass% polymer). It is supposed that the large hydrophobic block in that case limited the conformational adaptation at the copolymer–lipid boundary. The large hydrophobic thickness (~10nm) plays in favour of a statistic distribution of the lipid in the copolymer phase as sketched on Figure 1.18-b. Interestingly, homogeneous vesicles at least at the micrometric scale were observed for all copolymer contents larger than 30 mol%, (or 75 mass%). Below 60 w/w %, homogeneous vesicles presenting faceted surfaces were obtained, which is the signature of the DPPC gel phase. As described before, using a copolymer presenting a membrane thickness close to that of liposomes, allows the spontaneous formation of micrometric lipid domains in GHUVs in a large polymer content range (from 10% to 93 mass%). Above 93%, the lipid is apparently dispersed in the polymer phase and homogenous vesicles can be observed microscopically.

1.4.3.1. Lateral structuration in large unilamellar hybrid vesicles

The studies available on LHUVs are less numerous and among these studies, focus is mainly on potential applications (drug delivery [81] and targeting [75] of these systems. It is worth mentioning that the structure characterization at nano size required more complicated and indirect methods and the confirmation of hybrid character of LUVs is a challenge in itself. While with GHUVs, the "hybrid status" is observable under microscope, an indirect proof for LHUVs seems much more difficult. So far in literature, Liedberg and col [70] used the flow cytometry method and concluded to the presence of a large majority of vesicles with hybrid character using PB-PEO/POPC mixture and hydration extrusion process to obtain LUVs of 450 and 200 nm in size. However, no blank samples were considered in their studies (mixture of pure liposomes and polymersomes) to definitely attest the presence of hybrid vesicles. Also, there is no result regarding the membrane structuration of these LUVs. DSC has been used also to check the hybrid character of LUV by analysing the melting transition of lipid phases in hydrated films [82]. Interestingly Wintzen et al. used dual-color fluorescence cross-correlation spectroscopy (DC-FCCS), to evaluate the hybrid character of LUV made from mixtures of PDMS-*b*-PMOXA and DMPC [83].

Globally, at such scale, there is a crucial lack of information about the real hybrid character of the vesicles formed and their membrane structuration (presence of domains). The techniques commonly used to analyse the lipid LUVs, such as: small angle neutron scattering (SANS) and Förster resonance energy transfer (FRET), have not yet been considered for LHUVs up to now and will be considered in this thesis.

1.4.3.2. Physical properties of hybrid vesicles

Depending on their composition and structuration, modulation of membrane physical properties like fluidity, permeability, bending, stretching elasticity is expected for hybrid vesicles. These modulations can be of importance for different applications fields like drug delivery, cell membrane mimics, or as micro- or nano- reactors.

Mechanical properties

As mentioned in section 1.2, the bending rigidity κ, the stretching modulus K_a and the lysis tension are the typical parameters which allow characterizing the membrane toughness.

Although such parameters are well documented for pure liposomes and polymersomes, few data is available for hybrid vesicles.

Regarding the stretching modulus K_a, Cheng and col, in their early work on hybrid vesicles in 2011, reported that when PBd_{22}-*b*-PEO_{14} and HSPC were mixed at a molar ratio 75:25, the resulting vesicles showed no evidence of the macroscopic domains, and exhibited an intermediate elastic modulus between the values of pure lipid and pure polymer vesicles ($K_{a_{polymer}}$ = 72 mN.m^{-1} < $K_{a_{polymer:lipid\ 75:25}}$= 112 mN.m^{-1} < $K_{a_{lipid}}$= 206 mN.m^{-1}) [75]. Similar results for hybrid vesicles composed of PBd_{46}-*b*-PEO_{30} and POPC were also indicated in another work [71]. Although in this study, there was a relatively large composition range where hybrid vesicles could not be formed (between 35 and 65% mol of lipid), in the remaining fractions, homogeneous hybrid vesicles showed a gradual decrease of K_a with increasing copolymer content. Alternatively, measurements performed on heterogeneous vesicles ($PDMS_{26}$-*g*-$(PEO_{12})_2$/DPPC) by [63] indicated that when the stretching was done in the polymer-rich phase of the vesicle, the K_a value was mostly similar to the pure copolymer membrane. Whereas the lysis strain of homogeneous vesicles mentioned previously was always in between the value of lipidic- and polymeric- membrane, the lysis strain in this case was still high and similar to lysis strain of pure polymersomes, despite the potential fragility that could result from the interfaces at the polymer/lipid boundaries.

Regarding the bending modulus, quantitative data reported so far in literature are scarce compared to lipid GUVs that are well documented. There is only one approach using AFM performed for LHUVs of $PDMS_{60}$-b-$PMOXA_{21}$ /DMPC (50: 50 molar ratio or 90: 10 mass ratio) [83]. In this study, an intermediate value between liposomes and polymersomes was reported (62.10^{-19} J or 1500 kT). Interestingly, when using cholesterol instead of DMPC, a large increase of the bending modulus of more than four times that of the pure polymersomes was observed. According to the authors, this was due to an increase of the packing density in the membrane.

Fluidity

Although there are many types of molecular individual and collective motions within membranes, the mobility of molecules inside a membrane has been mostly evaluated through the measurement of the lateral diffusion coefficient, which is directly linked to the

surface shear viscosity of the membrane. Such measurement is commonly made by fluorescence recovery after photo-bleaching (FRAP) experiments. In the case of hybrid membranes, with FRAP, one can access either to the mobility of lipid molecules or copolymer chains depending on the localization of the fluorescent probes. Lateral diffusion coefficients of lipids are very high compared to those observed for copolymer chains in polymersomes (values extracted mainly from polymersomes obtained from PBut-b-PEO block copolymer) as introduced in section 1.1. Huge differences in term of surface shear viscosity have also been reported [19, 45]. Therefore, large variations of such parameters are anticipated depending on the lipid / copolymer composition, but subtle modifications could result also from peculiar membrane lateral structuration (presence of domains) as it was shown in multicomponent lipid membranes. It was indeed observed on POPC/PBd_{46}-*b*-PEO_{30} GHUV by Nam et al. who found that with increasing copolymer content, the diffusion of lipid molecules in hybrid GUVs becomes slower. Since for this system, none of the hybrid vesicles showed macroscopic domains, the homogeneous insertion of copolymer chains into lipid membrane may somewhat hamper the motion of lipid chains. Other authors obtained information about the mobility of lipid molecules in hybrid membranes composed of DPPC in gel state at room temperature and PIB_{87}-*b*-PEO_{17} copolymer [84]. For that purpose, they used Rh-DHPE as a diffusion probe. Whereas no fluorescence recovery was detected for pure DPPC, above a threshold in polymer fraction for GHUVs, the data revealed a clear increase in mobility of Rh-DHPE in the hybrid membranes with the copolymer content. The authors interpreted these observations by the breaking up of the rigid DPPC densely packed phase by the copolymer chains. The interpretation of such data is however not obvious as Rh-DPE is known to exhibit a large preference for disordered phase. It is likely that Rh-DHPE inserts into the polymer phase which presents a higher mobility compared to DPPC gel phase and the signal become visible above a given polymer fraction. In these preliminary results, the authors probed the lipid mobility in the fraction range where there was no evidence of macroscopic domain presence. This does not rule out the existence of domains below the optical resolution, which can act as obstacles hindering the diffusion, in a similar manner as lipid rafts or membrane proteins. Liquid ordered phases within membranes are indeed suspected to have a significant impact on the dynamic of molecules in natural and synthetic membranes.

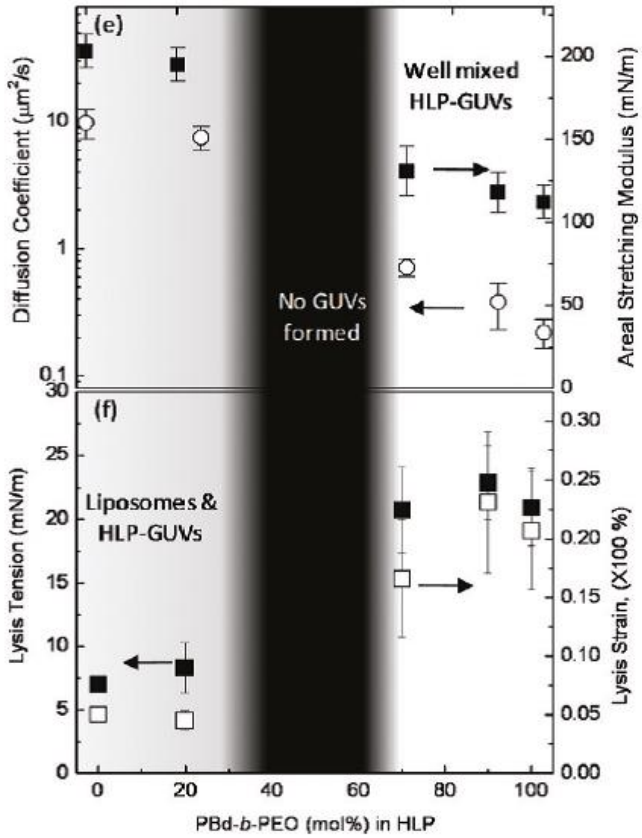

Figure 1.19. Mechanical properties and fluidity results of POPC/ PBd_{46}-*b*-PEO_{30} GHUVs from [71].

Permeability

It is important also to evaluate and control how the soluble molecules can easily pass through the vesicular membrane of GUVs in the presence of osmotic gradients. Permeability is essential for regulation of transmembrane exchange of substances, such as drug release and water transport [85]. The permeability of polymersomes is far below than that of liposomes therefore the hybrid membrane permeability is expected to be tuneable by changing the lipid/copolymer fraction. Currently, there are no quantitative data available on GHUVs. Some information has been obtained on LHUVs whose size was followed *versus* time by dynamic light scattering. Shen et al examined the water permeability of hybrid triblock copolymer PMOXA-*b*-PDMS-*b*-PMOXA/DOPC vesicles with different copolymer/lipid ratios, from 0 to 10 copolymer chains per 100 lipid molecules [86]. By using two copolymers with different molar masses ($PMOXA_6$-*b*-$PDMS_{33}$-*b*-$PMOXA_6$ and $PMOXA_{15}$-*b*-$PDMS_{67}$-*b*-$PMOXA_{15}$), they obtained different variation profiles of the permeability with the copolymer/lipid content. The hybrid system with the shorter triblock copolymer showed a regular decrease of permeability with increasing copolymer ratio while the permeability of the hybrid systems

obtained with the longer triblock copolymer, according to the authors, would decrease up to 5% of copolymer and then re-increase as the polymer ratio was further increased. These results were explained by the incorporation of copolymer chain into the defects and voids existing in DOPC membranes partly due to steric hindrance of unsaturated chains, therefore changing the packing density and decreasing the permeability. In the case of long copolymer chains, due to a large thickness mismatch between the alkyl tails of lipids and the hydrophobic block of the copolymer, an excessive amount of copolymer in the hybrid membranes could cause over-saturated occupation of the filler space and create new void spaces, leading to a reduced packing density again, which would explain the re-increase of permeability at 10 copolymer chains/100 lipids. It is important to mention that according to the error bars of the experiments, this non-monotonous variation is not obvious. Another possible explanation to our opinion is that, the high hydrophobic mismatch in this system plays a role, but different, in the sense that too long copolymer chains could not incorporate in lipid LUVs, because of a high curvature energy of the membrane at such size and a large steric hindrance between the hydrophilic blocks confined in the inner compartment of the LUVs and therefore would not modify significantly permeability. Beside the water permeability, we would like also to mention another work from which the release profile of encapsulated hydrophilic molecules in hybrid LUVs was measured [70]. It was found that the permeability of the hybrid vesicles prepared from PBd_{22}-PEO_{14}/POPC changed clearly with the fraction of copolymer/lipid. The higher the copolymer content introduced, the more significantly delayed molecule release was detected. In Figure 1.19, we reproduced the results in literature mentioned above.

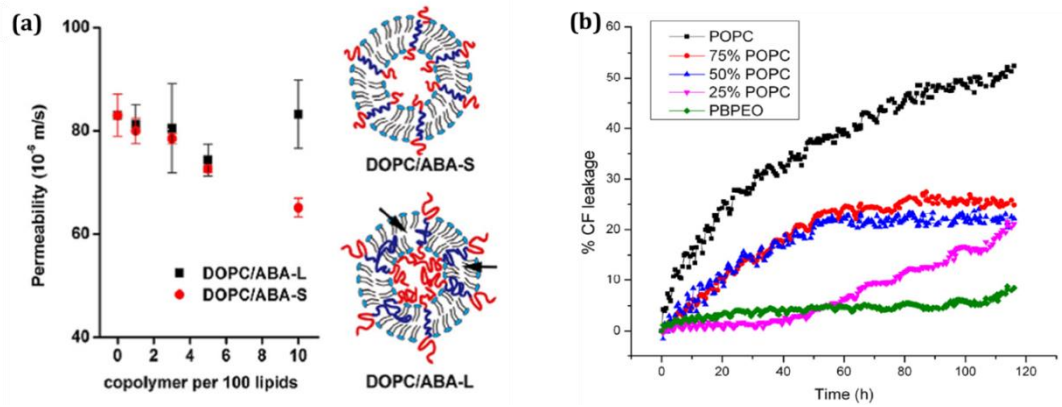

Figure 1.20. (a) Water permeability of hybrid vesicles and schematic of different packing of DOPC/$PMOXA_6$-$PDMS_{33}$-$PMOXA_6$ (ABA-S) and DOPC/ $PMOXA_{15}$-$PDMS_{67}$-$PMOXA_{15}$ (ABA-L) on hybrid vesicles, from [86]. (b) Hydrophilic dye carboxy-fluorescein (CF) release from different vesicles PB-PEO/POPC containing 0%, 25%, 50%, 75%, 100% POPC, from [70]

REFERENCES

1. Israelachvili, J.N., D.J. Mitchell, and B.W. Ninham, *Theory of self-assembly of hydrocarbon amphiphiles into micelles and bilayers.* Journal of the Chemical Society, Faraday Transactions 2: Molecular and Chemical Physics, 1976. **72**(0): p. 1525-1568.
2. Israelachvili, J.N., *20 - Soft and Biological Structures*, in *Intermolecular and Surface Forces (Third Edition)*. 2011, Academic Press: San Diego. p. 535-576.
3. Antonietti, M. and S. Förster, *Vesicles and Liposomes: A Self-Assembly Principle Beyond Lipids.* Advanced Materials, 2003. **15**(16): p. 1323-1333.
4. Discher, D.E. and A. Eisenberg, *Polymer Vesicles.* Science, 2002. **297**(5583): p. 967-973.
5. Discher, D.E., et al., *Emerging Applications of Polymersomes in Delivery: from Molecular Dynamics to Shrinkage of Tumors.* Progress in polymer science, 2007. **32**(8-9): p. 838-857.
6. Rangelov, S. and A. Pispas, *Polymeric Nanoparticles from Pure Block Copolymers*, in *Polymer and Polymer-Hybrid Nanoparticles*. 2013, CRC Press. p. 67-218.
7. Jain, S. and F.S. Bates, *On the Origins of Morphological Complexity in Block Copolymer Surfactants.* Science, 2003. **300**(5618): p. 460-464.
8. Helfrich, W., *Lyotropic lamellar phases.* Journal of Physics: Condensed Matter, 1994. **6**(23A): p. A79.
9. Battaglia, G. and A.J. Ryan, *The evolution of vesicles from bulk lamellar gels.* Nat Mater, 2005. **4**(11): p. 869-876.
10. Alberts, B., et al., *Essential Cell Biology, Fourth Edition*. 2013: Taylor & Francis Group.
11. Lasic, D.D., et al., *Spontaneous vesiculation.* Advances in Colloid and Interface Science, 2001. **89–90**: p. 337-349.
12. Walde, P., *Preparation of vesicles (liposomes)*, in *Encyclopedia of Nanoscience and Nanotechnology*, H.S. In Nalwa, Editor. 2004, American Scientific Publishers: California. p. 43-79.
13. LoPresti, C., et al., *Polymersomes: nature inspired nanometer sized compartments.* Journal of Materials Chemistry, 2009. **19**(22): p. 3576-3590.
14. Meier, W.P. and W. Knoll, *Polymer membranes/biomembranes*. Vol. 224. 2009: Springer Science & Business Media.
15. Angelova, M.I. and D.S. Dimitrov, *Liposome electroformation.* Faraday Discussions of the Chemical Society, 1986. **81**(0): p. 303-311.
16. Shimanouchi, T., H. Umakoshi, and R. Kuboi, *Kinetic Study on Giant Vesicle Formation with Electroformation Method.* Langmuir, 2009. **25**(9): p. 4835-4840.
17. Walde, P., et al., *Giant Vesicles: Preparations and Applications.* ChemBioChem, 2010. **11**(7): p. 848-865.
18. Discher, B.M., et al., *Polymersomes: Tough Vesicles Made from Diblock Copolymers.* Science, 1999. **284**(5417): p. 1143-1146.
19. Dimova, R., et al., *Hyperviscous diblock copolymer vesicles.* Eur. Phys. J. E, 2002. **7**(3): p. 241-250.

20. Vriezema, D.M., et al., *Electroformed Giant Vesicles from Thiophene-Containing Rod−Coil Diblock Copolymers.* Macromolecules, 2004. **37**(12): p. 4736-4739.

21. Angelova, M.I., *Liposome Electroformation*, in *Perspectives in Supramolecular Chemistry*. 2007, John Wiley & Sons, Ltd. p. 26-36.

22. Battaglia, G. and A.J. Ryan, *Pathways of Polymeric Vesicle Formation.* The Journal of Physical Chemistry B, 2006. **110**(21): p. 10272-10279.

23. Kaoui, B., A. Farutin, and C. Misbah, *Vesicles under simple shear flow: Elucidating the role of relevant control parameters.* Physical Review E, 2009. **80**(6): p. 061905.

24. Olson, F., et al., *Preparation of liposomes of defined size distribution by extrusion through polycarbonate membranes.* Biochimica et Biophysica Acta (BBA) - Biomembranes, 1979. **557**(1): p. 9-23.

25. Salva, R., *Modulation des propriétés de membrane des polymersomes: perméabilité et évolution de forme* 2013, University of Bordeaux.

26. Spivak, M., *A comprehensive introduction to differential geometry*. 1999, Publish or Perish, INC: Houston, Texas.

27. Helfrich, W., *Elastic properties of lipid bilayers: theory and possible experiments.* Zeitschrift für Naturforschung. Teil C: Biochemie, Biophysik, Biologie, Virologie, 1973. **28**(11): p. 693-703.

28. Kozlov, M.M., H.T. McMahon, and L.V. Chernomordik, *Protein-driven membrane stresses in fusion and fission.* Trends in biochemical sciences, 2010. **35**(12): p. 699-706.

29. Lipowsky, R. and E. Sackmann, *Structure and Dynamics of Membranes*. 1995, Elsevier: North Holland.

30. Bassereau, P., B. Sorre, and A. Lévy, *Bending lipid membranes: Experiments after W. Helfrich's model.* Advances in Colloid and Interface Science, 2014. **208**: p. 47-57.

31. Evans, E.A., *Bending Resistance and Chemically Induced Moments in Membrane Bilayers.* Biophysical Journal, 1974. **14**(12): p. 923-931.

32. Deserno, M., *Fluid lipid membranes: From differential geometry to curvature stresses.* Chemistry and Physics of Lipids, 2015. **185**: p. 11-45.

33. Evans, E. and W. Rawicz, *Entropy-driven tension and bending elasticity in condensed-fluid membranes.* Physical Review Letters, 1990. **64**(17): p. 2094-2097.

34. Walde, P. and S. Ichikawa, *Enzymes inside lipid vesicles: preparation, reactivity and applications.* Biomolecular Engineering, 2001. **18**(4): p. 143-177.

35. Heimburg, T., *Mechanical aspects of membrane thermodynamics. Estimation of the mechanical properties of lipid membranes close to the chain melting transition from calorimetry.* Biochimica et Biophysica Acta (BBA) - Biomembranes, 1998. **1415**(1): p. 147-162.

36. Tristram-Nagle, S., H.I. Petrache, and J.F. Nagle, *Structure and interactions of fully hydrated dioleoylphosphatidylcholine bilayers.* Biophysical Journal, 1998. **75**(2): p. 917-925.

37. Lorenceau, E., et al., *Generation of Polymerosomes from Double-Emulsions.* Langmuir, 2005. **21**(20): p. 9183-9186.

38. Srinivas, G., D.E. Discher, and M.L. Klein, *Self-assembly and properties of diblock copolymers by coarse-grain molecular dynamics.* Nat Mater, 2004. **3**(9): p. 638-644.

39. Bermudez, H., et al., *Molecular Weight Dependence of Polymersome Membrane Structure, Elasticity, and Stability.* Macromolecules, 2002. **35**(21): p. 8203-8208.

40. Chen, Q., H. Schonherr, and G.J. Vancso, *Mechanical properties of block copolymer vesicle membranes by atomic force microscopy.* Soft Matter, 2009. **5**(24): p. 4944-4950.

41. Leson, A., et al., *Molecular Exchange through Membranes of Poly(2-vinylpyridine-block-ethylene oxide) Vesicles.* Small, 2007. **3**(6): p. 1074-1083.

42. Le Meins, J.-F., O. Sandre, and S. Lecommandoux, *Recent trends in the tuning of polymersomes' membrane properties.* The European Physical Journal E, 2011. **34**(2): p. 14.

43. Rawicz, W., et al., *Effect of chain length and unsaturation on elasticity of lipid bilayers.* Biophysical Journal, 2000. **79**(1): p. 328-339.

44. Bermúdez, H., D.A. Hammer, and D.E. Discher, *Effect of Bilayer Thickness on Membrane Bending Rigidity.* Langmuir, 2004. **20**(3): p. 540-543.

45. Evans, E., et al., *Dynamic Tension Spectroscopy and Strength of Biomembranes.* Biophysical Journal, 2003. **85**(4): p. 2342-2350.

46. Lee, J.C.M., et al., *From Membranes to Melts, Rouse to Reptation: Diffusion in Polymersome versus Lipid Bilayers.* Macromolecules, 2002. **35**(2): p. 323-326.

47. Discher, D.E. and F. Ahmed, *POLYMERSOMES.* Annual Review of Biomedical Engineering, 2006. **8**(1): p. 323-341.

48. Heimburg, T., *Thermal biophysics of membranes*. 2008, John Wiley & Sons.

49. Gorter, E. and F. Grendel, *ON BIMOLECULAR LAYERS OF LIPOIDS ON THE CHROMOCYTES OF THE BLOOD.* The Journal of Experimental Medicine, 1925. **41**(4): p. 439-443.

50. Danielli, J.F. and H. Davson, *A contribution to the theory of permeability of thin films.* Journal of Cellular and Comparative Physiology, 1935. **5**(4): p. 495-508.

51. Singer, S.J. and G.L. Nicolson, *The Fluid Mosaic Model of the Structure of Cell Membranes.* Science, 1972. **175**(4023): p. 720-731.

52. Mouritsen, O.G., *Life-as a matter of fat*. 2005: Springer.

53. Binder, W.H., V. Barragan, and F.M. Menger, *Domains and Rafts in Lipid Membranes.* Angewandte Chemie International Edition, 2003. **42**(47): p. 5802-5827.

54. Lipowsky, R. and R. Dimova, *Domains in membranes and vesicles.* Journal of Physics: Condensed Matter, 2002. **15**(1): p. S31.

55. Brochard-Wyart, F. and P.G. de Gennes, *Adhesion induced by mobile binders: Dynamics.* Proceedings of the National Academy of Sciences of the United States of America, 2002. **99**(12): p. 7854-7859.

56. Cevc, G. and H. Richardsen, *Lipid vesicles and membrane fusion.* Advanced Drug Delivery Reviews, 1999. **38**(3): p. 207-232.

57. García-Sáez, A.J. and P. Schwille, *Stability of lipid domains.* FEBS Letters, 2010. **584**(9): p. 1653-1658.

58. Frolov, V.A.J., et al., *"Entropic Traps" in the Kinetics of Phase Separation in Multicomponent Membranes Stabilize Nanodomains.* Biophysical Journal, 2006. **91**(1): p. 189-205.

59. Ursell, T.S., W.S. Klug, and R. Phillips, *Morphology and interaction between lipid domains.* Proceedings of the National Academy of Sciences, 2009. **106**(32): p. 13301-13306.

60. Travesset, A., *Effect of dipolar moments in domain sizes of lipid bilayers and monolayers.* The Journal of Chemical Physics, 2006. **125**(8): p. 084905.

61. Hu, J., T. Weikl, and R. Lipowsky, *Vesicles with multiple membrane domains.* Soft Matter, 2011. **7**(13): p. 6092-6102.

62. Semrau, S., et al., *Membrane-mediated interactions measured using membrane domains.* Biophysical journal, 2009. **96**(12): p. 4906-4915.

63. Chen, D. and M.M. Santore, *Hybrid copolymer-phospholipid vesicles: Phase separation resembling mixed phospholipid lamellae, but with mechanical stability and control.* Soft Matter, 2015. **11**(13): p. 2617-2626.

64. Chemin, M., et al., *Hybrid polymer/lipid vesicles: fine control of the lipid and polymer distribution in the binary membrane.* Soft Matter, 2012. **8**: p. 2867-2874.

65. Schulz, M., et al., *Lateral surface engineering of hybrid lipid-BCP vesicles and selective nanoparticle embedding.* Soft Matter, 2014. **10**(6): p. 831-839.

66. Olubummo, A., et al., *Phase Changes in Mixed Lipid/Polymer Membranes by Multivalent Nanoparticle Recognition.* Langmuir, 2014. **30**(1): p. 259-267.

67. Schulz, M., et al., *Controlling molecular recognition with lipid/polymer domains in vesicle membranes.* Angewandte Chemie - International Edition, 2013. **52**(6): p. 1829-1833.

68. Schulz, M., et al., *Hybrid lipid/polymer giant unilamellar vesicles: Effects of incorporated biocompatible PIB-PEO block copolymers on vesicle properties.* Soft Matter, 2011. **7**(18): p. 8100-8110.

69. Cheng, Z., et al., *Improved Tumor Targeting of Polymer-based Nanovesicles Using Polymer-Lipid Blends.* Bioconjugate Chemistry, 2011. **22**(10): p. 2021-2029.

70. Lim, S., et al., *Hybrid, Nanoscale Phospholipid/Block Copolymer Vesicles.* Polymers, 2013. **5**(3): p. 1102.

71. Nam, J., P.A. Beales, and T.K. Vanderlick, *Giant Phospholipid/Block Copolymer Hybrid Vesicles: Mixing Behavior and Domain Formation.* Langmuir, 2011. **27**(1): p. 1-6.

72. Nam, J., T.K. Vanderlick, and P.A. Beales, *Formation and dissolution of phospholipid domains with varying textures in hybrid lipo-polymersomes.* Soft Matter, 2012. **8**: p. 7982–7988.

73. Ruysschaert, T., et al., *Hybrid Nanocapsules: Interactions of ABA Block Copolymers with Liposomes.* Journal of the American Chemical Society, 2005. **127**(17): p. 6242-6247.

74. Nam, J., T.K. Vanderlick, and P.A. Beales, *Formation and dissolution of phospholipid domains with varying textures in hybrid lipo-polymersomes.* Soft Matter, 2012. **8**(30): p. 7982-7988.

75. Cheng, Z., et al., *Improved Tumor Targeting of Polymer-Based Nanovesicles Using Polymer–Lipid Blends.* Bioconjugate Chemistry, 2011. **22**(10): p. 2021-2029.

76. Scholtysek, P., et al., *Unusual triskelion patterns and dye-labelled GUVs: consequences of the interaction of cholesterol-containing linear-hyperbranched block copolymers with phospholipids.* Soft Matter, 2015. **11**(30): p. 6106-6117.

77. Chemin, M., et al., *Hybrid polymer/lipid vesicles: fine control of the lipid and polymer distribution in the binary membrane.* Soft Matter, 2012. **8**(10): p. 2867-2874.

78. Roth, M., *Solubility parameter of poly(dimethyl siloxane) as a function of temperature and chain length.* Journal of polymer science. Part B. Polymer physics, 1990. **28**(13): p. 2719.

79. King, J.W., *Supercritical fluid technology for lipid extraction, fractionation and reactions*, in *Lipid biotechnology*, T.M. Kuo and H.W. Gardner, Editors. 2002, Marcel Dekker: New York. p. 663-687.

80. Kuzmin, P.I., et al., *Line tension and interaction energies of membrane rafts calculated from lipid splay and tilt.* Biophys J, 2005. **88**(2): p. 1120-33.

81. Pippa, N., et al., *PEO-b-PCL-DPPC chimeric nanocarriers: self-assembly aspects in aqueous and biological media and drug incorporation.* Soft Matter, 2013. **9**(15): p. 4073-4082.

82. Pippa, N., et al., *Chimeric lipid/block copolymer nanovesicles: Physico-chemical and bio-compatibility evaluation.* European Journal of Pharmaceutics and Biopharmaceutics, 2016. **107**: p. 295-309.

83. Winzen, S., et al., *Submicron hybrid vesicles consisting of polymer-lipid and polymer-cholesterol blends.* Soft Matter, 2013. **9**(25): p. 5883-5890.

84. Schulz, M., et al., *Controlling Molecular Recognition with Lipid/Polymer Domains in Vesicle Membranes.* Angewandte Chemie International Edition, 2013. **52**(6): p. 1829-1833.

85. Lodish H, B.A., Zipursky SL, , *Molecular Cell Biology. 4th edition - Chapter 15, Transport across Cell Membranes*. 2000, New York.

86. Shen, W., J. Hu, and X. Hu, *Impact of amphiphilic triblock copolymers on stability and permeability of phospholipid/polymer hybrid vesicles.* Chemical Physics Letters, 2014. **600**: p. 56-61.

CHAPTER 2

MATERIALS AND METHODS

Table of Contents

OUTLINE

This chapter describes all materials and methodology applied in this thesis. Beside the methods used to prepare hybrid unilamellar vesicles at all sizes, we present the characterization techniques used for each scale. While the large hybrid unilamellar vesicles (LHUVs) were characterized by a wide range of techniques such as: light scattering, neutron scattering, cryo-transmission electron microscopy and different fluorescence spectroscopy techniques; the giant hybrid unilamellar vesicles (GHUVs) were studied by confocal microscopy, fluorescence lifetime imaging microscopy, fluorescence recovery after photobleaching and micropipette aspiration. For each method, we mainly focus on introducing how it is usually exploited for the study of vesicle in general and for our hybrid polymer/lipid systems particularly. All experimental procedures are also included in details.

2.1. COMMERCIAL MATERIALS

2.1.1. Phospholipids

All phospholipids were purchased from Avanti Polar Lipids, Inc. as powder and dissolved in 2/1 chloroform/methanol solvent (v/v) to make stock solutions. This solvent mixture was chosen because of its higher polarity and lower volatility than pure chloroform. The exact concentration of each stock solution was re-quantified by phosphorus titration method (Annex A.2.1) or by gravimetric analysis and then stored at -20°C in glass vials closed with teflon caps. Details of phospholipids used in this thesis are given in Table 2.1:

Table 2.1. List of phospholipids used in this thesis.

Common Name	Abbreviation	Molecular Formula	M_w ($g.mol^{-1}$)
1-palmitoyl-2-oleoyl-*sn*-glycero-3-phosphocholine	POPC	$C_{42}H_{82}NO_8P$	760.076
1,2-dipalmitoyl-*sn*-glycero-3-phosphocholine	DPPC	$C_{40}H_{80}NO_8P$	734.039
Deuterated 1,2-dipalmitoyl-d62-*sn*-glycero-3-phosphocholine	DPPC-d62	$C_{40}H_{18}NO_8PD_{62}$	796.421
1,2-dioleoyl-*sn*-glycero-3-phosphoethanolamine-N-(cap biotinyl)	PE-biotinyl	$C_{57}H_{102}N_4O_{11}PNaS$	1105.469

i) POPC and DPPC were chosen as model phospholipids at fluid and gel state at room temperature respectively. The transition temperature (T_m) of POPC and DPPC are around -2°C and 41°C respectively.

ii) DPPC-d62 was used in small angle neutron scattering experiments (SANS) as its coherent neutron scattering lengths density is greatly enhanced. It has to be noted that its transition is slightly lower than DPPC (about 37°C).

iii) PE-biotinyl, a biotinylated phospholipid which strongly interacts with avidin coated surface was used to immobilize the vesicles for Fluorescence recovery after photobleaching (FRAP) experiments.

The molecular structures of all phospholipids mentioned above are presented in Figure 2.1.

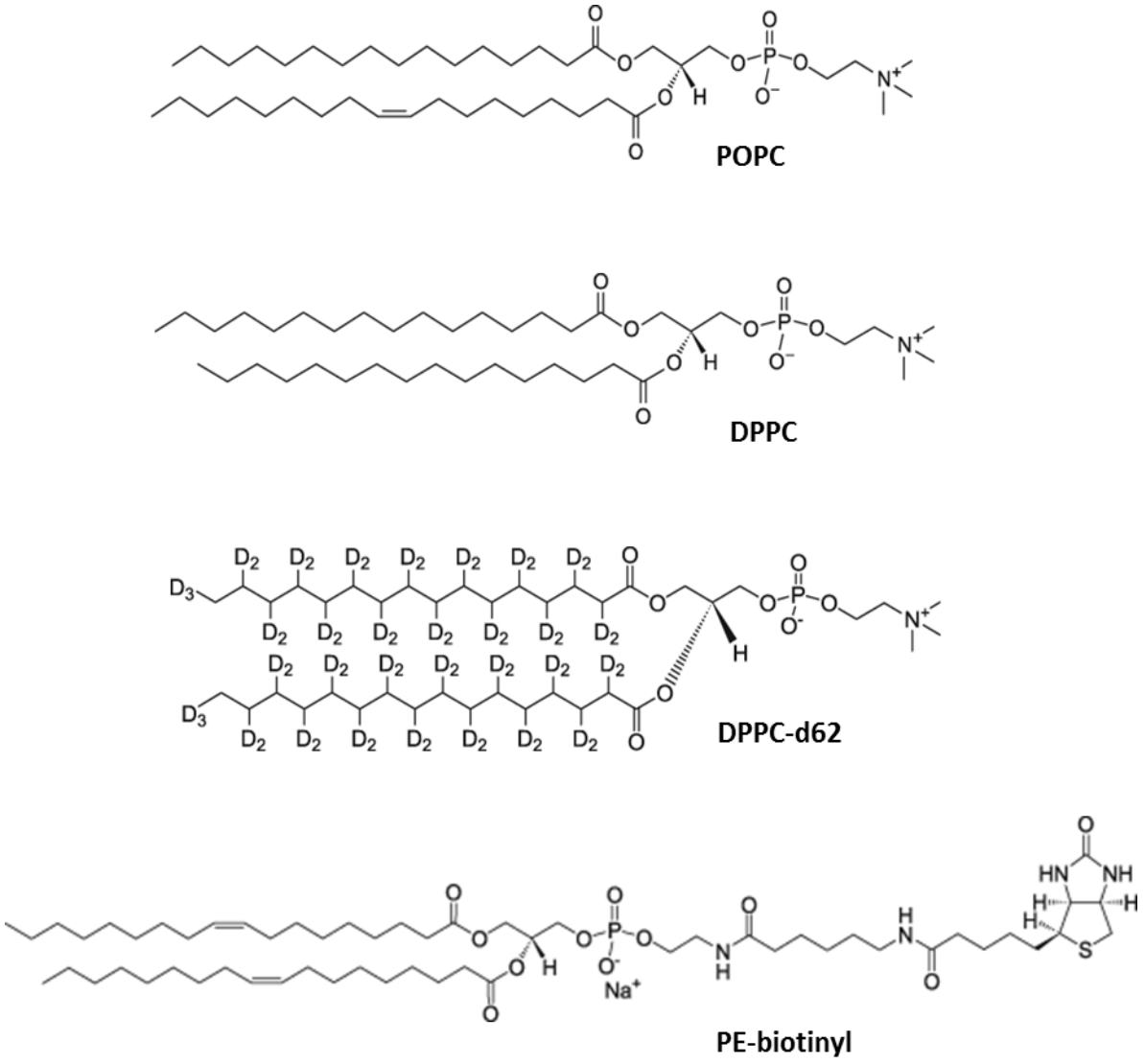

Figure 2.1. Molecular structures of phospholipids used in this thesis.

2.1.2. Functionalized homopolymers and amphiphilic copolymer

While phospholipids used are all commercial products, amphiphilic copolymers were synthesized to obtain a series of products forming vesicles with different membrane thicknesses. The synthesis reaction consists in a coupling of an amine terminated poly(dimethylsiloxane) with a succinimidyl-functionalized poly(ethylene oxide). The synthesis of these copolymers and the characterisation of their self-assembled structure will be described in Chapter 3. All reactive homopolymers used for the synthesis are presented in Table 2.2.

Table 2.2. Reactive homopolymers of PDMS and PEO at different molar masses used to synthesize different amphiphilic triblock copolymers PEO-*b*-PDMS-*b*-PEO.

IUPAC Name	Abbreviated Name	Approximate M_w (g/mol)	Supplier
α, ω-bisaminopropyl-terminated poly(dimethylsiloxane)	NH_2-$PDMS_{22}$-NH_2	1500	ABCR, Germany
	NH_2-$PDMS_{43}$-NH_2	3000	
	NH_2-$PDMS_{67}$-NH_2	5000	
Succinimidyl-((N-methyl)-poly(ethylene oxide) ester	$(PEO)_4$-NHS	333	Thermo Fisher Scientific, France
	$(PEO)_8$-NHS	509	
	$(PEO)_{12}$-NHS	685	
α-Methoxy-ω-N-hydroxysuccinimide ester poly(ethylene oxide)	$(PEO)_{17}$-NHS	750	Rapp Polymer, Germany

In addition to the different synthesized amphiphilic triblock copolymers, we also studied one commercial amphiphilic graft copolymer PDMS-*g*-PEO which is a gift from Dow Corning, Inc. It is composed of a PDMS chain decorated with two arms of PEO on average. According to literature, it is composed of 22 units of PDMS [1, 2] and PEO degree of polymerisation is 12. We found a number of repeating units of PDMS chain of 26, determined by ^{1}H NMR assuming 24 units for PEO chains. The average number molar mass is equal to 2700 g/mol and viscosimetric molar mass is equal to 3000 g/mol. The molar mass dispersity is Đ = 1.32 [3].

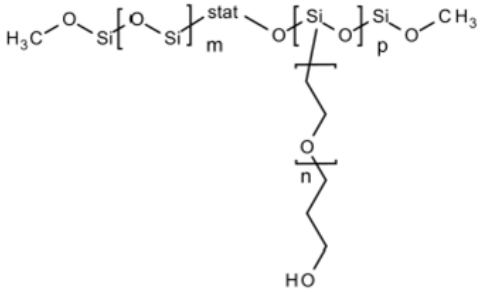

Figure 2.2. Molecular structure of amphiphilic graft copolymer PDMS-*g*-PEO obtained from DOW Corning, Inc.

2.1.3. Reactive fluorophores and fluorophore labelled amphiphile

In this thesis, fluorophore labelled phospholipid and copolymer were used for various fluorescence techniques. While fluorescent labelled phospholipid used was a commercial product from Avanti Polar Lipids, Inc, named DOPE-Rhod (1,2-dioleoyl-sn-glycero-3-phosphoethanolamine-N-(lissamine rhodamine B sulfonyl), fluorescent labelled copolymer

on the contrary, were synthesized using amine-reactive probes (Succinimidyl 6-(N-(7-nitrobenz-2-oxa-1,3-diazol-4-yl)amino) hexanoate (NBD-NHS) and 5-(and 6-) carboxyfluorescein, succinimidyl ester (FITC-NHS)) which were purchased from Thermo Fisher Scientific. Molecular structures, Excitation/Emission spectral profiles of DOPE-Rhod, NBD-NHS and FITC-NHS mentioned above are given in Figure 2.3.

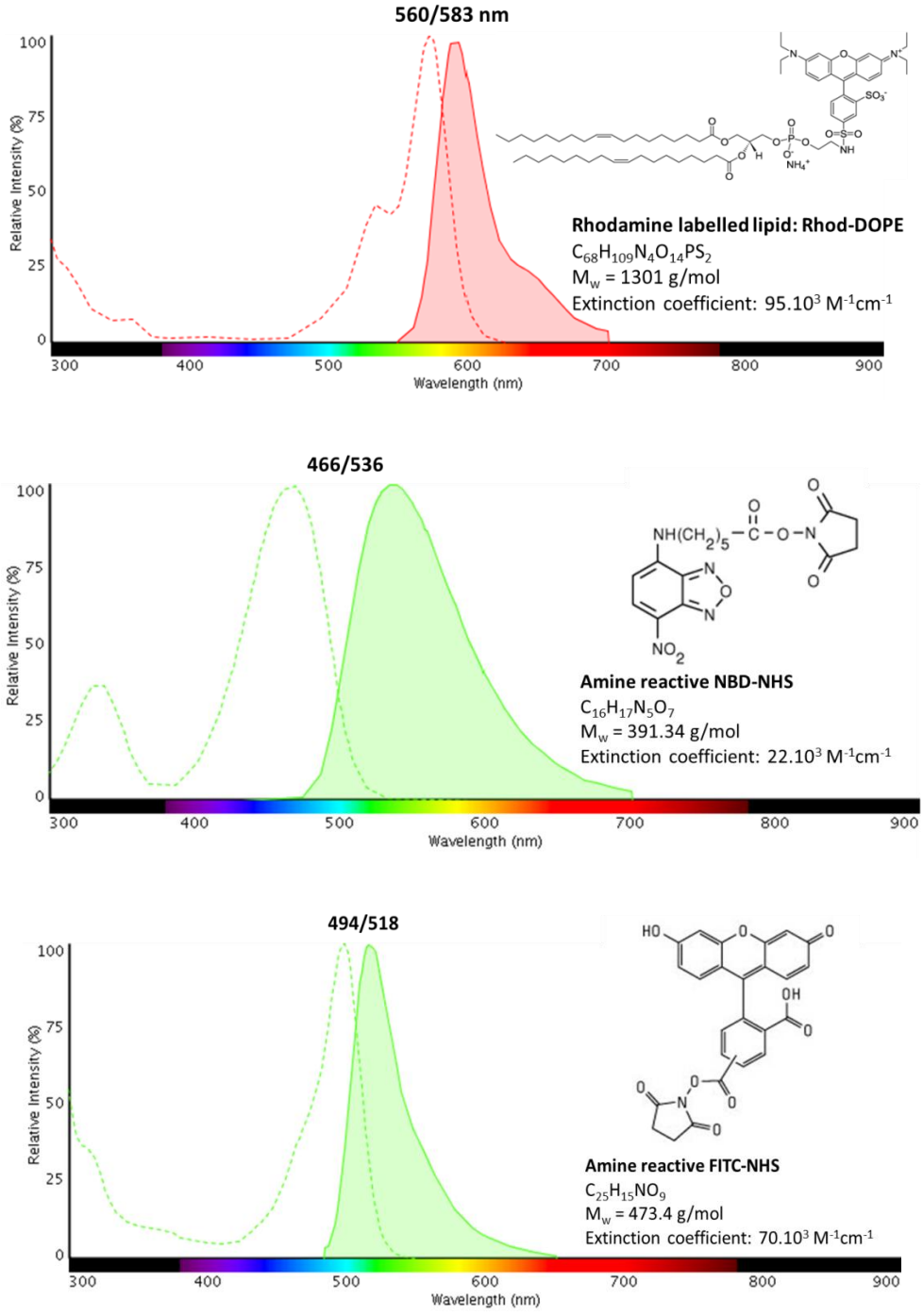

Figure 2.3. Details of Rhod labelled phospholipid and amine-reactive fluorophore used to tag copolymer (Spectra exported from https://www.thermofisher.com, Extinction coefficient values given by [4] or by supplier).

2.1.4. Other commercial chemicals

Beside the principal products mentioned above, all other chemicals and solvents used are listed in Table 2.3.

Table 2.3. The general chemicals used in this thesis.

Product	Formula	M_w	Supplier
Ammonia	NH_3	17.03	Sigma-Aldrich
Ammonium heptamolybdate	$(NH_4)_6Mo_7O_{24}.4H_2O$	1235.86	Merck
Ascorbic acid	$C_6H_8O_6$	176.12	Merck
Avidin from egg white	Glycoprotein	~ 66000	Sigma-Aldrich
Bovine serum albumin	Protein	~ 66000	Sigma-Aldrich
Chloroform	$CHCl_3$	119.38	Sigma-Aldrich
Cyclohexane	C_6H_{12}	84.16	Sigma-Aldrich
Deuterated chloroform	$CDCl_3$	120.38	Eurisotop
Deuterium oxide	D_2O	20.03	Eurisotop
Dichloromethane	CH_2Cl_2	84.93	Sigma-Aldrich
Diisopropylethylamine	$C_8H_{19}N$	129.25	Acros Organics
Dipotassium phosphate	KH_2PO_4	174.18	Merck
Disodium phosphate	Na_2HPO_4	141.96	Sigma-Aldrich
Glucose	$C_6H_{12}O_6$	180.16	Sigma-Aldrich
Anhydrous magnesium sulphate	$MgSO_4$	120.36	Alfa Aesar
Methanol	CH_4O	32.04	Sigma-Aldrich
Monosodium phosphate	NaH_2PO_4	119.98	Sigma-Aldrich
Perchloric acid	$HClO_4$	100.46	Sigma-Aldrich
Sodium bicarbonate	$NaHCO_3$	84.01	Sigma-Aldrich
Sodium chloride	NaCl	58.44	Sigma-Aldrich
Sucrose	$C_{12}H_{22}O_{11}$	342.30	Sigma-Aldrich
Tetrahydrofuran	C_4H_8O	72.10	Sigma-Aldrich
Triethylamine	$C_6H_{15}N$	101.19	Fisher

2.2. PREPARATION OF UNILAMELLAR HYBRID VESICLES

2.2.1. Methodology

Methods for preparation of Giant Hybrid Unilamellar Vesicles (GHUVs: 20-50 μm) and Large Hybrid Unilamellar Vesicles (LHUVs: ~ 100 nm) were basically the same as those used for preparation of liposomes and polymersomes in literature. They were based on two main experimental protocols: (i) hydration of a dry polymer/lipid film and (ii) emulsion evaporation methods. The methods relying on film hydration were used to prepare either GHUVs or LHUVs while the emulsification method was used to prepare the LHUVs, as described below:

i) Methods based on hydration process are based on the swelling of well-mixed polymer/lipid dry film in an aqueous solution. The swelling is due to the diffusion of water into the film layers, inducing formation of vesicles. The size and lamellarity of hybrid vesicles depend on the hydration condition, as indicated in literature for polymersomes and liposomes [5]. For instance, to obtain GHUVs, the hydration is carried out under a controlled oscillating electric field (electroswelling mechanism reported by Angelova [6]). To obtain LHUVs, the hydration is classically carried out on glass surface under gentle shaking. In this condition, multilamellar hybrid vesicles (MLHVs) of different sizes from few hundred of nanometers to several microns are obtained. LHUVs of controlled and low size dispersity can be further obtained by extrusion using polycarbonate filter with a defined pore size.

ii) Another way to prepare the LHUVs in this work is based on the double emulsion evaporation technique. In this process, water is added directly into organic solution containing the solubilized polymer and lipid and under mechanical stirring (probe sonication) forming a primary w/o emulsion. This emulsion is subsequently dispersed again into large volume of aqueous solution, producing a w/o/w double emulsion. Vesicles, probably heterogeneous in size, are obtained following the progressive evaporation of organic solvent during the probe sonication. In order to obtain the LHUVs with narrow size distribution, extrusion must be done afterward.

Figure 2.4 illustrates the formation schematic of unilamellar hybrid vesicles applied in this thesis; the details of experimental conditions are described in the following part.

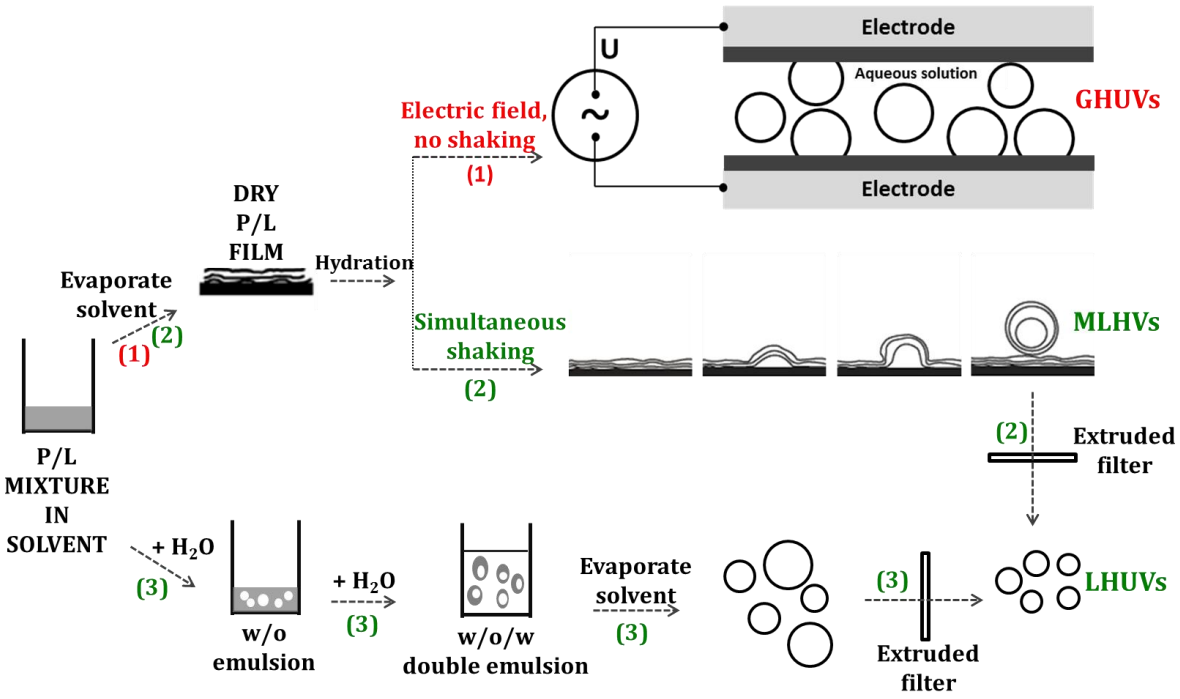

Figure 2.4. Scheme of processes used to prepare GHUVs and LHUVs in this thesis: (1) Hydration of dry polymer/lipid films deposited on platinum wires under oscillating electric field giving GHUVs (2) Hydration of dry polymer/lipid films under mechanical shaking, followed by an extrusion process, giving LHUVs and (3) Emulsion evaporation method followed by an extrusion process giving LHUVs. Part of the scheme is adapted from [7].

2.2.2. Experimental procedures

In this section, experimental details of all preparation processes as presented in Figure 2.4 are described.

GHUVs preparation by electroformation on Platinum (Pt) electrode

With this method, all the components were first well-mixed in chloroform/methanol solvent 2/1 (v/v) at a total concentration of 1 mM. Depending on experiments, other components such as fluorescent probes, biotinylated lipid were also added in this primary solution at given amount precised in Table 2.4. 3 µL of the solution was spread on all sides of Platinum wires with a 10 µL gas-tight syringe. This small volume syringe should be used to control a slow spreading to achieve a thin and homogeneous film. With only 3 µL of solution, the traces of organic solvent can be removed simply by natural evaporation in 3 – 5 minutes. The electrode were then submerged in 1 mL sucrose solution 100 mM and immediately connected to an AC voltage to avoid any spontaneous swelling. A sinusoidal tension (2V, 10Hz) was applied for hybrid samples made with amphiphilic copolymer having molecular weight below 5000 $g.mol^{-1}$. For larger copolymer, a higher sinusoidal tension (10V, 7Hz) had

to be used to enhance the driving forces for the growth of vesicles. All hybrid samples containing POPC were electroformed at room temperature while all hybrid samples containing DPPC were electroformed at 50°C. The vesicles were collected after 75 minutes by gently shaking the electrode in solution and kept at room temperature until being used.

Table 2.4. Molar proportion (regarding the molar total) of the fluorescent labelled lipid, fluorescent labelled copolymer and biotinylated lipid used to prepare the GHUVs depending on each specific characterization technique.

Characterization technique	Fluorescent labelled copolymer	Fluorescent labelled lipid	Biotinylated lipid
Confocal imaging	1.5%	0.2%	0%
Fluorescent lifetime imaging microscopy	1.5%	0% or 0.5%	0%
Fluorescence recovery after photobleaching	1.5%	0.2%	0.0001%
Micropipette aspiration	1.5%	0.2%	0%

LHUVs preparation by film rehydration-extrusion

In this technique, once again, the desired quantities of copolymer and phospholipid (with an additional of fluorescent probes if necessary) were mixed in chloroform/methanol (2/1 v/v) and vacuum-dried until complete solvent evaporation to produce a thin hybrid film. Subsequently, it was re-suspended in an adequate aqueous solution (phosphate buffer saline (PBS) with pH = 7.4 except samples for neutron scattering where D_2O/H_2O mixtures were used as explained in section 2.3.1.2) under gentle agitation at temperature above the T_m of the lipid component during few hours. This suspension was then extruded 21 times (Mini-extruder from Avanti Polar Lipids, Inc.) through polycarbonate filters (100 nm pore size, Millipore™) at the temperature of the hydration step. All LHUVs samples were stored at 4°C after preparation.

LHUVs preparation by double-emulsion evaporation

With this technique, mixtures of copolymer and phospholipid were first prepared in small volume of chloroform (about 200 µL). Afterward, about 20 µL of adequate aqueous solution (D_2O/H_2O mixture for neutron scattering samples and PBS for the others) was added and followed by 20s of probe sonication programmed at 60% power (Vibra-cell™ VCX 130W),

cycle 2s on, 1s off to form the primary w/o emulsion. The entire resulting emulsion was added drop-wise to the corresponding aqueous solution used at previous step and probe-sonicated again during 120s. As such, the organic solvent is removed by natural heating of the solution. Finally, the obtained suspension was extruded through polycarbonate filters (100 nm pore size, 21 times) above the T_m of phospholipids.

2.3. METHODOLOGY FOR LUVs and LHUVs CHARACTERIZATION

2.3.1. Scattering techniques

Scattering techniques such as light, neutron and X-ray scattering are useful methods for obtaining quantitative information about size, shape and structure of submicron objects. The general principle of scattering experiments is illustrated in Figure 2.5.

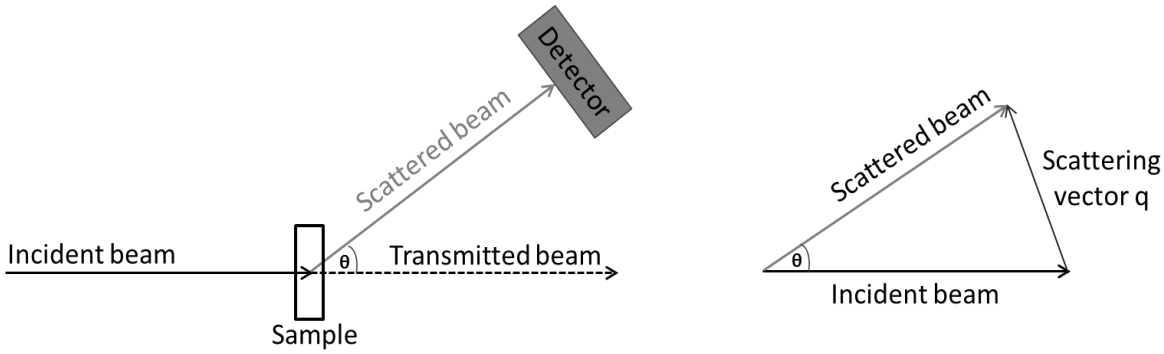

Figure 2.5. Principle of scattering techniques: an incident beam of single wavelength λ is scattered by the sample and the scattered beam is detected at the scattering angle θ relative to the transmitted beam. Adapted from [8].

It basically consists in illuminating the sample with a monochromatic incident beam of single wavelength λ and detecting the intensity scattered at a given angle θ with respect to the transmitted beam. Scattering results from the variations within the sample of refractive index in case of light, electron density in case of X-rays, and of nuclear density in case of neutrons. An important variable of scattering experiments is the scattering vector q whose magnitude is given by Eq.2.1. For light scattering n represents the refractive index of the medium whereas for neutron and X-ray scattering, n is not considered.

$$q = \frac{4\pi \sin\frac{\theta}{2}}{\lambda} \quad \text{with } \lambda = \frac{\lambda_0}{n} \quad (\lambda_0 \text{ wavelength in vacum}) \qquad (\text{Eq. 2.1})$$

The spatial resolution of a scattering experiment is given by the inverse of the scattering vector q. This means that the higher the vector q, the smaller the structure that can be

investigated. As the wavelength vary depending on the scattering techniques (4000 Å < λ < 7000 Å for light, 1 Å < λ < 20 Å for neutrons and 0,2 Å < λ < 2 Å for X-rays), a large range a scattering vector q can be investigated (5.10^{-5} Å^{-1} < *q* < 3.10^{-3} Å^{-1} for light scattering, 2.10^{-3} Å^{-1} < *q* < 5.10^{-1} Å^{-1}for neutrons and X-ray scattering).

The scattering intensity can be described with the simplified following equation:

$$I_{th}(q) = \text{Contrast} \times P(q) \times S(q) \qquad \text{(Eq. 2.2)}$$

The contrast represent the differences in scattering power between the studied system and the environment (suspending medium..), $P(q)$ is the form factor of the particles studies (shape, size) and $S(q)$ is the structure factor (particle-particle interactions). In our studies, this last parameter equal to 1 as we will work on diluted systems, interactions are neglected. This is the shape of the Curve $I(q)$ which allows to obtain geometrical parameters of the studied particles through the form factor $P(q)$.

In this thesis work, both light and neutron scattering were used to characterize the Large Unilamellar Vesicles. While dynamic and static light scattering could deliver the global information on either LUVs or LHUVs about their whole size, shape and average weight; Small Angle Neutron scattering enabled to make a full structural characterization. In the following, each technique is basically summarized and the most important equations used in the interpretation of data are introduced. The instrumentation and experimental procedures are also subsequently described.

2.3.1.1. Dynamic light scattering

In a dynamic light scattering (DLS) measurement, sample is illuminated by an incident laser beam and the scattered light is recorded as a function of the time. Fluctuation of scattered intensity, due to the Brownian motion gives information relative to the dynamic. In order to extract those quantitative values, an intensity autocorrelation function is constructed as described in Eq.2.3 [9]:

$$G(\tau) = \langle I(q,t)I(q,t+\tau)\rangle = \lim_{\tau\to\infty} \frac{1}{T}\int_0^T I(q,t)I(q,t+\tau)dt \qquad \text{(Eq. 2.3)}$$

$I(t)$ and $I(t+\tau)$ are the intensities of the scattered light measured at two times, t and t + τ respectively. The normalized function can be treated then by different mathematical

approaches such as: CONTIN [10] or CUMULANT methods [11, 12], to extract the decay rate Γ and relate it to translational diffusion coefficient D by:

$$D = \frac{\Gamma}{q^2} \qquad \text{(Eq. 2.4)}$$

with q is the magnitude of the scattering wave vector q as given above. This translational diffusion coefficient value related to the hydrodynamic radius of particle according to the Stokes-Einstein law:

$$R_h = \frac{kT}{6\pi\eta D} \qquad \text{(Eq. 2.5)}$$

where, k is the Boltzmann's constant, T is the temperature (K) and η is solvent viscosity (Pa.s). It has to be noted that this hydrodynamic radius R_h reported by DLS just reflects the theoretical radius of a sphere particle (Stokes Radius R_s) which moves with the same translational diffusion coefficient D.

For polydisperse samples, the size dispersity can be investigated through the polydispersity index (PDI) when the autocorrelation function is fitted with cumulant method. It is based on expanding the logarithm of the autocorrelation function in terms of the cumulants $\kappa_i(\Gamma)$ of the distribution giving a polynomial in the delay time τ [11, 12]:

$$\ln\big(G(t)\big) = -\bar{\Gamma}\tau + \frac{\kappa_2}{2!}\tau^2 - \frac{\kappa_3}{3!}\tau^3 + \frac{\kappa_4}{4!}\tau^4 - \cdots \qquad \text{(Eq. 2.6)}$$

In this equation, the first two coefficients represent the average decay rate $\bar{\Gamma}$ and its variance respectively. The second cumulant commonly referred as PDI parameter:

$$PDI = \frac{\kappa_2}{\bar{\Gamma}^2} \qquad \text{(Eq. 2.7)}$$

In this thesis work, all LUVs and LHUVs were characterized by DLS to measure the vesicle size distribution and verify the absence of aggregation. All measurements were carried out with a Malvern Zetasizer Nano ZS90 using disposable single-used polystyrene cuvettes, typically two repeats for each measurement.

2.3.1.2. Static light scattering

SLS focus on the average value of the scattered light intensity and allow the measurement of the average weight ($\bar{M}_w$) as well as the radius of gyration R_g of the nanoparticle. Those

parameters obtained from SLS are typically determined by a plot proposed by Zimm [13] based on the equation:

$$\frac{KC}{R_\theta} = (1 + \frac{q^2 {R_g}^2}{3}) \frac{1}{\overline{M_w}} + 2A_2C \qquad (Eq.\,2.8)$$

Here K is the constant defined from refractive index of the solvent (n); the refractive index increment (dn/dc) and the wavelength of the incident light (λ_0):

$$K = 4\pi^2 n^2 (\frac{dn}{dc})^2 {N_A}^{-1} {\lambda_0}^{-4} \qquad (Eq.\,2.9)$$

C is the concentration, A_2 is the second virial coefficient and R_θ is the Rayleigh ratio of the scattered to incident light intensity given by:

$$R_\theta = \frac{I_{sample} - I_{solvent}}{I_{standard}} . R_{\theta,standard} \qquad (Eq.\,2.10)$$

Suggested by Zimm, the simplest way of solving Eq.2.7 is to plot the scattering intensity at different angles and at different concentrations as illustrated in Figure 2.6. From a double extrapolation ($\theta \rightarrow 0$, C constant and θ constant, $C \rightarrow 0$) one can determine $\overline{M}_w$, A_2 and R_g from the intercept with the ordinate and the initial slopes, respectively.

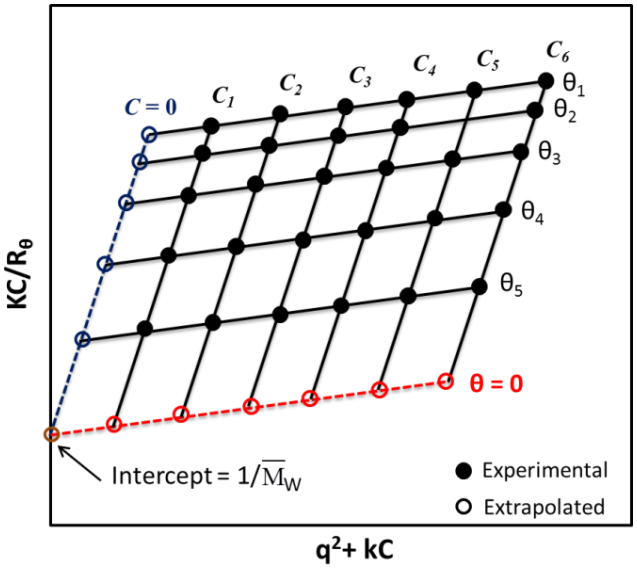

Figure 2.6. A typical Zimm plot of SLS measurements where the data is extrapolated to θ = 0 (red line) and to C = 0 (blue line) to extract the average molecular weight $\overline{M}_w$.

In addition, a simple plot of the logarithmic of measured scattered intensity ln(I(q)) *vs* the scattering vector q^2 [14] also allows the determination of R_g. The advantage is that neither

value of dn/dc nor concentration is needed. This plot yields a straight line and R_g is obtained from its slope according to Eq.2.11:

$$\ln\big(I(q)\big) = \ln\big(I(0)\big) - \frac{{R_g}^2}{3}q^2 \qquad \text{(Eq. 2.11)}$$

However, it should be known that the Guinier equation is acceptable only where R_g is in the range of ≤ 1/q.

Unlike R_h obtained from a calculation where a perfect hard sphere is assumed to move with the same translational diffusion coefficient, R_g obtained from SLS as described above is independent on any shape assumptions. Basically, this radius represents the mean distance from the center of mass of the object to each mass element in the object. In Figure 2.7, we illustrated R_g and R_h for different morphologies. Depending on the morphology, different ratio R_g/R_h can be found.

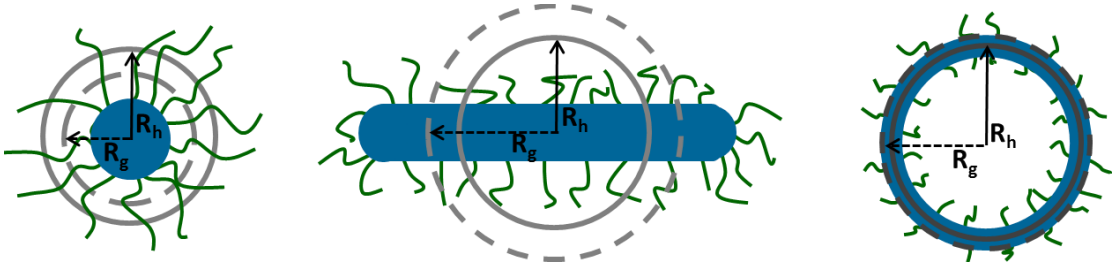

Figure 2.7. Illustration of R_g and R_h in different morphologies: R_g is the radius indicated by the dashed grey line and R_h is the radius indicated by the solid black line. Adapted from [15].

In this thesis, we used SLS to characterize the self-assembled structures formed from the synthesized triblock copolymers. In addition to check their morphology *via* the R_g/R_h ratio, the area per polymer chain $\bar{A}$ in a vesicle membrane (if its morphology was determined as vesicle) was estimated. This parameter is very important for our simulation works that will be described in chapter 4. This value was achieved by a series of calculation as shown in Eq.2.12 - 2.14.

$$N_{agg} = \frac{\bar{M}_w}{M_n} \qquad \text{(Eq. 2.12)}$$

$$\bar{A} = \frac{4\pi R^2}{N_{agg}} \qquad \text{(Eq. 2.13)}$$

$$\bar{A} = \frac{8\pi R^2}{N_{agg}} \qquad \text{(Eq. 2.14)}$$

Where $\bar{M}_w$ is the average weight of vesicle; M_n is average molar mass in number of the copolymer, R is the vesicle radius and N_{agg} is the aggregation number which is calculated by Eq.2.12. It is important to note that the copolymer chains within polymersome can be arranged into either monolayer or bilayer conformation depending on its architecture; therefore Eq.2.13 illustrates the case of monolayer while Eq.2.14 illustrates the case of bilayer.

All SLS analyses in this work were performed with an ALV/CG-3 laser compact goniometer which consists of a 22mW He Ne linear polarized laser operating at a wavelength of λ = 632.8 nm. The goniometer covers a scattering angle range from θ = 30° to 150°. The concentration range of the vesicular suspensions was in between 0.2 mg/ml to 1 mg/ml.

2.3.1.3. Small angle neutron scattering

We used small angle neutron scattering (SANS) not only to probe the global size of vesicle in a q-range where $qR_g < 1$, but also to study the local organization of polymer and lipid chains within nano-hybrid vesicles at higher q values. Our methodology was based on the contrast variation method in order to detect selectively polymer or lipid phase or both in hybrid vesicles as illustrated in Figure 2.8. The principle of this method is detailed in the following.

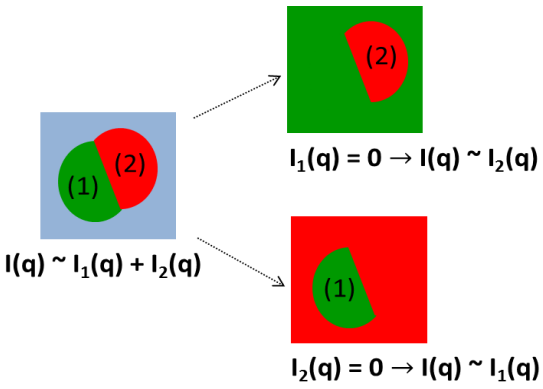

Figure 2.8. The principal idea of contrast variation method in our SANS experiment: "kill" part of system and enhance another part by changing the suspending medium used.

Neutrons are scattered by the nucleus and the strength of the interaction between the neutron and nucleus is characterized by the coherent scattering length of the nucleus (b_{coh}). This value depends on the type, spin state of the nucleus and seems varying randomly across the periodic table based on quantum mechanical Eigen state [16]. The coherent scattering lengths of atoms and isotopes considered in this study are given in Table 2.5. Special attention should be given to the values of hydrogen and its isotope deuterium.

Table 2.5. Scattering length for some of common atoms [16]

Atom	b_{coh} (10^{-4} Å)
Hydrogen	-0.374
Deuterium	0.667
Carbon	0.664
Oxygen	0.580
Silicon	0.41
Phosphorus	0.513

In a SANS experiment, the scattering length of a molecule correspond to the sum of each scattering length of its constituting atom. Contrast in SANS is related to the difference of scattering length density (SLD) between the molecule studied and its suspending medium. The SLD can be defined for a molecule as the sum of the all coherent length of its constitutive atoms divided by its molar volume. The SLD for a molecule can be calculated by:

$$\rho = \frac{\sum b_{i,coh}}{V_m} = \frac{\sum b_{i,coh}}{M_w} dN_A \qquad (Eq.\ 2.15)$$

where b_i is the scattering length of the atom i in the molecule having density d, molar mass M_w and molar volume V_m.

The scattered intensity measured is expressed by:

$$I(q) = \phi V \Delta\rho^2 P(q) S(q) \qquad (Eq.\ 2.16)$$

where ϕ is the volume fraction, V is the volume, P(q) is the form factor and S(q) is the structure factor (1 in our case). Δρ is called the contrast factor which represents the SLD difference between the scatterer and medium. This factor can be easily altered due to the fact that the scattering lengths of deuterium and hydrogen are significantly different as shown in Table 2.5. For instance, the SLD of aqueous medium can be tuned from the minimum value of $-0.56.10^{-06}$ Å^{-2} (100% H_2O) to the maximum value of $6.40.10^{-06}$ Å^{-2} (100% D_2O) by simply adjusting the ratio of D_2O and H_2O. Therefore we are able to match either the lipid signal or polymer signal playing on of D_2O and H_2O mixtures. This is the principal idea of contrast variation method used in most of our SANS experiments.

Part of the measurements were carried out at the Léon Brillouin laboratory (CEA Saclay, France) on the PACE and PAXY spectrometers. Three configurations were used to cover

overlapping *q* ranges respectively of 2.4×10^{-3} – 2.6×10^{-2}, 1.1×10^{-2} – 1.2×10^{-1} $Å^{-1}$ and 3.6×10^{-2} – 0.37 $Å^{-1}$, with following values of the sample-to-detector distance *D* and neutron wavelength *λ*: *D* = 4.57 m and *λ* = 17 Å, *D* = 2.86 m and *λ* = 6 Å, *D* = 0.87 m and *λ* = 6 Å. The main part of the experiments was done at D11 at Institute Laue Langevin (ILL), Grenoble, France. A range of moduli of scattering vectors, q, from 0.0019 to 0.32 Å-1 was covered by three sample-to-detector distances (d = 1.2; 8 and 34 m) at the neutron wavelength λ = 6 Å (with a full width at half-maximum value 10%). The samples were kept in quartz Hellma© cells with 1 or 2 mm path lengths. Thermalization for the samples with accuracy ± 1°C was achieved by a thermalized fluid circulated throughout the sample holder. The raw spectrum were corrected from the empty cell and other sources by conventional procedures using LAM¨ program in order to obtain the SANS curves in absolute units (cm^{-1}). Different models were used to analyse the scattered intensity curves of the samples. Various fits to the form factor of vesicles, disks or core-shell cylinders were achieved using SasView program (http://www.sasview.org/). To describe the scattering of phase separated polymer/lipid vesicles, we developed a new model based on the holey shell form factor introduced by Bergstrom et al [17]: this model is detailed in section 4.1 of Chapter 4. We also used different standard plots (Guinier, Porod…) used to get some preliminary information about vesicle size and membrane thickness of the vesicles.

2.3.2. Fluorescence spectroscopy techniques

In addition to scattering experiments, fluorescence spectroscopy techniques were the other main tools used to characterize the LHUVs in this work. They were performed both as steady-state and time-resolved measurements. In the following, we do not provide an exhaustive introduction but merely focus on the principal fundamentals and the photophysical processes relevant to this work such as resonance energy transfer.

2.3.2.1. Steady-state fluorescence measurements

Steady-state fluorescence measurements are performed with constant illumination and observation. Sample is illuminated with a continuous beam of light and the data obtained is plotted on a graph of fluorescence intensity or photon counts *vs* registered wavelength. Due to the nanosecond time scale of fluorescence, the sample attains a steady-state almost instantaneously [18]. Steady-state measurement is fast and simple but it only gives an average intensity, the detailed molecular information available from fluorescence is lost

during the time averaging process. In addition to fluorescence intensity, selected samples in this thesis were also characterized by steady-state fluorescence anisotropy.

Steady-state fluorescence anisotropy

Based on the principle of photoselective excitation of fluorophore by a polarized light [19], steady-state fluorescence anisotropy measurements generally investigate the rate of rotation of fluorophores. Briefly, the anisotropy (r) describes the depolarization of the fluorophore emission after its excitation with polarized light and is given by:

$$r = \frac{I_{VV} - GI_{VH}}{I_{VV} + 2GI_{VH}} \qquad (Eq.\ 2.17)$$

where I_{VV}, I_{VH} are respectively the vertically and horizontally polarized components of the fluorescence emission with the excitation polarized vertically. G is a correction factor for the different sensitivity of the optics in the spectrofluorimeter to polarized light, defined as:

$$G = \frac{I_{HV}}{I_{HH}} \qquad (Eq.\ 2.18)$$

Basically, high anisotropy indicates a slow rotation while low anisotropy indicates a fast rotation of fluorophore. This value therefore can be used to evaluate the rigidity of membranes as shown in many previous studies [20-22].

All steady-state fluorescence measurements in this thesis were performed with a SLM Aminco 8100 Series 2 spectrofluorimeter (Rochester, NY) with double excitation and emission monochromators (MC-400), in right angle geometry. The light source was a 450-W Xe arc lamp and the reference was a Rhodamine B quantum counter solution. The temperature was controlled by a Julabo F25 circulating water bath controlled with 0.1°C precision directly inside the cuvette with a type-K thermocouple (Electrical Electronic Corp., Taipei, Taiwan). For steady-state fluorescence anisotropy measurements, polarization of excitation and emission light was obtained by rotation of Glan-Thompson polarizers. Table 2.6 summarized the excitation and emission wavelengths typically used in all steady-state experiments.

Table 2.6. The excitation and emission wavelengths typically used in the steady-state for samples labelled with NBD and Rhod.

Probe	Steady-state fluorescence emission		Steady-state fluorescence anisotropy	
	λ_{Exc} (nm)	λ_{Em} (nm)	λ_{Exc} (nm)	λ_{Em} (nm)

NBD	460	480 - 600	460	520
Rhod	540	550 - 650	540	590

2.3.2.2. Time-resolved fluorescence measurements

In time-resolved measurements, the sample is usually excited with a very short pulse of light (time-domain methodologies) and the fluorescence intensity is monitored as a function of time with a high-speed detection system that permits the intensity to be measured on the ns timescale [18]. The principle of time-resolved measurements is shown in Figure 2.9.

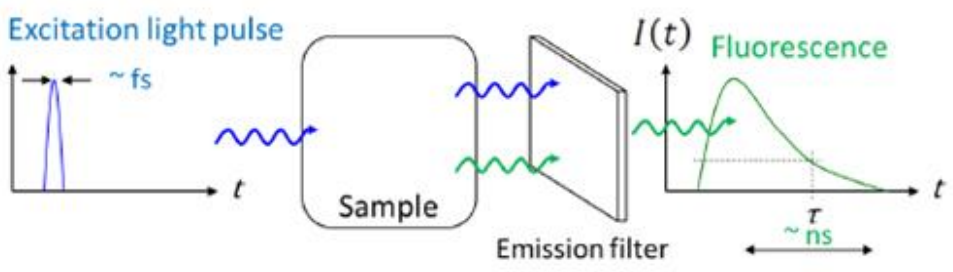

Figure 2.9. Principle of a time-resolved fluorescence measurement; adapted from [23]

In addition, single photon timing methodologies are also possible, and these were the ones used in this thesis [24]. While steady-state fluorescence spectroscopy is facile to operate, the time-resolved spectroscopy typically requires more complex and expensive instrumentation. Nevertheless, on the contrary with the average representation of steady-state measurements (which is an integration of the intensity decay over time), the time-resolved analyses provides a dynamic picture of the fluorescence, enabling to develop complex models for the molecular interaction. Notice that time-resolved measurements can be employed in spectroscopy as well as in microscopy, which will be introduced more thoroughly in the next section.

Fluorescence lifetime and intensity decay laws

The fluorescence lifetime τ of a molecule is defined as the average duration a molecule spends in the excited state after absorbing an excitation photon. Typically τ values range from less than 1ns to more than 1ms depending on the fluorescent molecules and are defined as:

$$\tau = \frac{1}{k_r + k_{nr}} \qquad \text{(Eq. 2.19)}$$

Here k_r is the radiative decay rate, which mostly depends on the chemical structure of the fluorophore and k_{nr} is the non-radiative decay rate which is also dependent on the environment of the fluorophore.

The relationship between the fluorescence intensity decay $I(t)$ and fluorescence lifetime is described by a mono-exponential curve as illustrated in Figure 2.10 and Eq.2.20:

$$I(t) = I_0 e^{-t/\tau} \qquad \text{(Eq. 2.20)}$$

where I_0 is the initial intensity at t = 0.

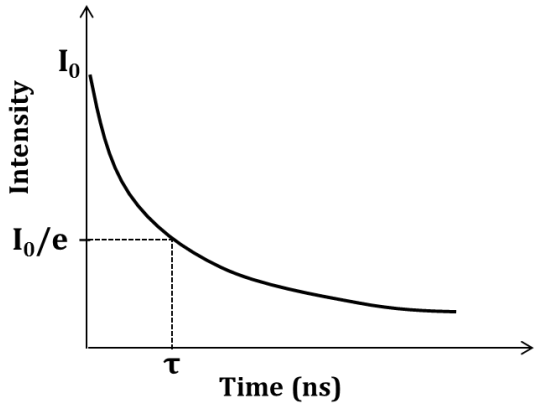

Figure 2.10. An illustration for a single fluorescence decay process

In case of more complex decays, the fluorescence intensity can be described by the sum of individual single exponential decays:

$$I(t) = \sum_{i=1}^{n} \alpha_i \exp(-t/\tau_i) \qquad \text{(Eq. 2.21)}$$

Here τ_i and α_i represent the decay time and the amplitude of the component i respectively, n is the number of decays. In this case the average lifetime is determined by:

$$\bar{\tau} = \frac{\sum_{i=1}^{n} \alpha_i \tau_i^2}{\sum_{i=1}^{n} \alpha_i \tau_i} \qquad \text{(Eq. 2.22)}$$

It is important to note that, in some occasions, another term called the amplitude-weighted lifetime or lifetime-weighted quantum yield which is given in Eq.2.23 should be used. For instance, it is used in this work to calculate the energy transfer efficiency, which will be discussed thoroughly in the next part.

$$\langle \tau \rangle = \sum_{i=1}^{n} \alpha_i \tau_i \qquad \text{(Eq. 2.23)}$$

Time-resolved Förster resonance energy transfer

As represented on a Jablonski diagram in Figure 2.11, Förster resonance energy transfer (FRET) is a non-radiative process where the energy is transferred between a fluorophore called the donor and a molecule called the acceptor, through a long-range dipole-dipole coupling mechanism [25, 26].

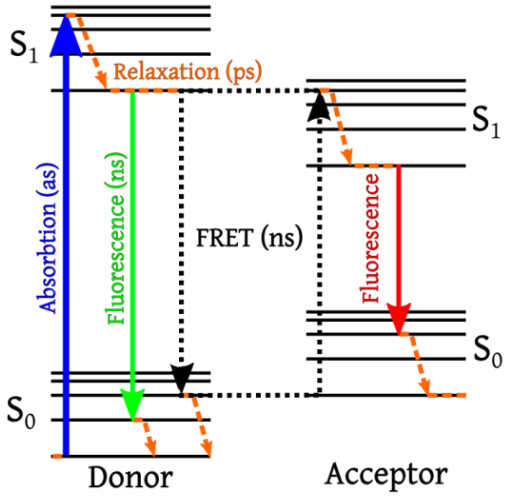

Figure 2.11. Jablonski diagram of the energy transfer occurring during FRET.

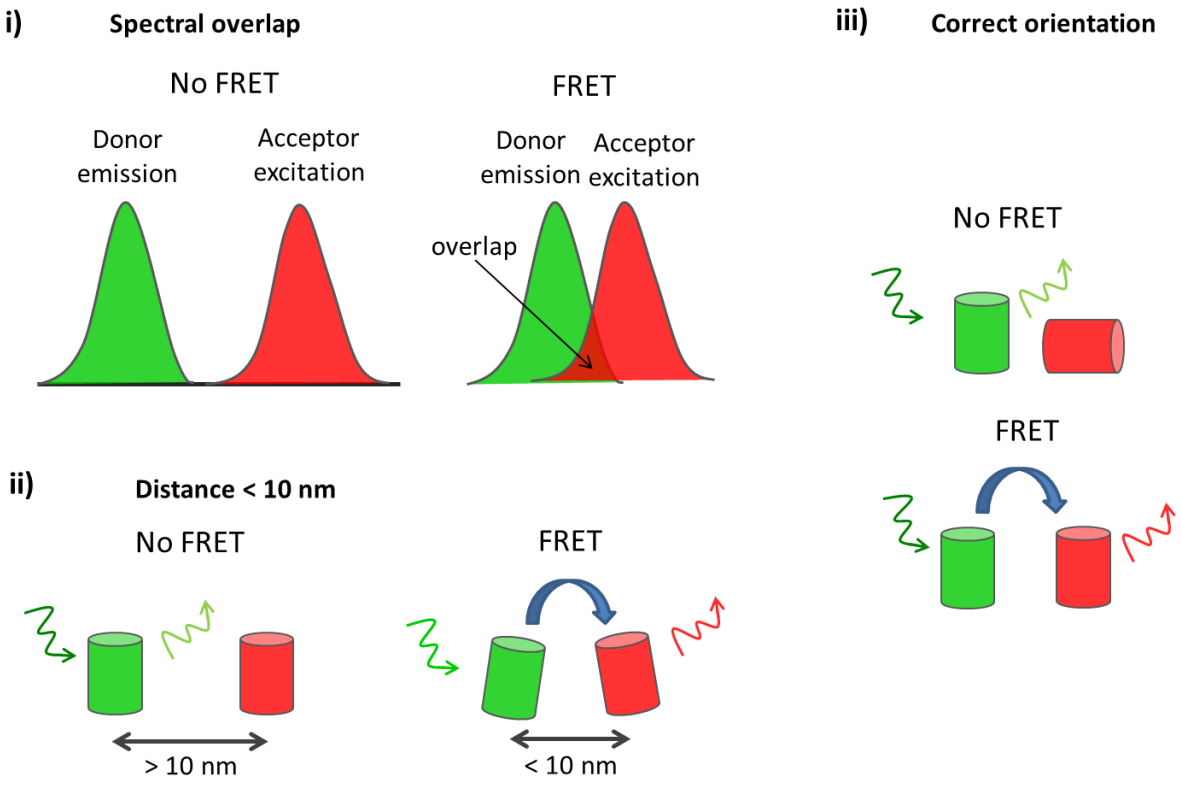

Figure 2.12. Schematic diagrams depicting the three conditions that must be met for efficient FRET; adapted from [27]

The required conditions for occurrence of FRET, as illustrated in Figure 2.12, are: i) the emission spectrum of donor must sufficiently overlap the absorption spectrum of acceptor, ii) the distance between two fluorophores must be within about 10 nm and, iii) the absorption transition dipole moment of the acceptor is not perpendicular to the emission transition moment of the donor.

FRET efficiency is determined *via* the changes in photophysical properties of donors with and without the presence of acceptors. Those properties could be either the fluorescence intensity (I) determined by steady-state measurement, or fluorescence lifetime (τ) obtained from time-resolved measurements:

$$E = 1 - \frac{I_{DA}}{I_D} = 1 - \frac{\tau_{DA}}{\tau_D} \qquad (Eq.\ 2.24)$$

Here E is the FRET efficiency, the subscript D and DA refer for the property of the donor in the absence and presence of the acceptor, respectively. FRET efficiency is inversely proportional to the sixth power of the distance between donor and acceptor, making that is a very sensitive technique to probe molecular organization at distances on the nanometer scale:

$$E = \frac{1}{1 + (\frac{r}{R_0})^6} \qquad (Eq.\ 2.25)$$

where r is the distance between donor and acceptor molecules and R_0 is the distance at which FRET efficiency is 50%. R_0 is characteristic of each donor-acceptor pair, and is called Förster distance (or radius).

In this thesis, the motivation to use FRET is to study the organization of polymer and lipid chains within LHUVs *via* investigation of distance distribution functions between the polymer fluorescent analogues and derivative fluorescent lipids. Briefly, the NBD-tagged copolymer acts as FRET donor and the Rhod-labelled phospholipid is the FRET acceptor. Their spectrums satisfy the requirement for FRET as shown in Figure 2.13.

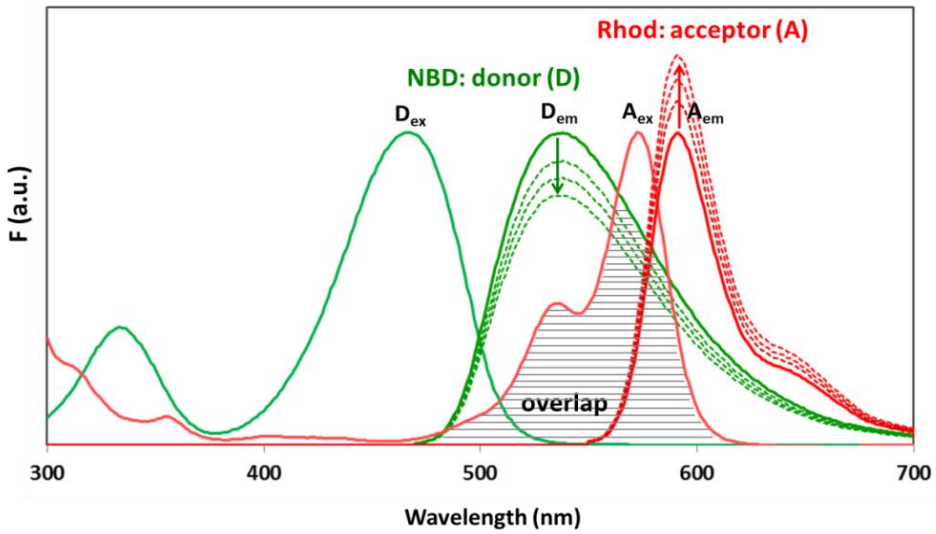

Figure 2.13. Overlap of the NBD emission spectrum and the excitation spectrum of Rhod. In case of occurrence of FRET, the donor emission (D_{em}) is reduced while the acceptor emission (A_{em}) increases.

All FRET efficiency values in this work were quantified by time-resolved measurements. One of the major advantages of using the fluorescence lifetime instead of steady state intensity is that the measurement is independent of either concentration or incident power of the excitation source, as it is based on an intrinsic molecular property of the excited state of fluorophore. This means that changes in concentration whether caused by photobleaching or diluting/concentrating the sample, would not affect the lifetime value.

Considering the experimental procedures, all time-resolved fluorescence intensity data acquisition was carried out through the Time-Correlated Single-Photon Timing technique (TCSPT) by Aleksander Fedorov at Centro de Química-Física Molecular, Lisboa, Portugal. The procedures were exactly the same as described in previous studies [24]. With NBD, measurements were performed at λ_{Exc} = 335 and λ_{Em} = 520 nm. The decays were analysed using TRFA software (Scientific Software Technologies Center, Minsk, Belarus).

2.3.3. Cryo-Transmission electron microscopy

Cryogenic transmission electron microscopy (cryo-TEM) is a technique where transmission electron microscopy is used to image cryogenically cooled samples [28, 29]. The idea of cryo-TEM is to avoid sample dehydration - a mandatory treatment process in TEM but may cause unpredictable alterations to the sample. Instead, samples are frozen by rapid cooling into cryogenic liquids and viewed in vitreous ice in cryo-TEM. It allows the visualisation of the trapped structure in solution very close to their native state. As such, cryo-TEM has proven

to be an extremely powerful technique to analyse self-assembled nanostructures (morphology, membrane thickness of vesicles) [30-32]. In this thesis work, cryo-TEM was used at first to characterize the nanostructures resulting from the self-assembly of all synthesized triblock copolymers. Many important aspects like size, morphology and the polymersomes membrane thicknesses could be revealed. Moreover, it was used also to complement the analyses obtained from scattering and fluorescence spectroscopy techniques on LHUVs.

All cryo-TEM experiments were performed by Er-Rafik Meriem at Institute Charles Sadron, Strasbourg, France. Briefly, the vitrification of the samples was carried out in a homemade vitrification system. The chamber was held at 22°C and the relative humidity at 80%. 5 µL drop of the sample was deposited onto a lacey carbon film covered grid (Ted Pella) rendered hydrophilic using an ELMO glow discharge unit (Cordouan Technologies). The grid is automatically blotted to form a thin film which is plunged in liquid ethane hold at -190°C by liquid nitrogen. In that way, a vitrified film is obtained in which the native structure of the vesicles is preserved. The grid was mounted onto a cryo holder (Gatan 626) and observed under low dose conditions in a Tecnai G2 microscope (FEI) at 200 kV. Images were acquired using an Eagle slow scan CCD camera (FEI).

2.4. METHODOLOGY FOR GUVs and GHUVs CHARACTERIZATION

2.4.1. Imaging by confocal laser scanning microscopy

Whereas the characterization of vesicles at nanometer scale often requires complex analyses of FRET data, the study of giant vesicles is based on a simpler approach: direct visualization by microscopy. In this way, to characterize the giant hybrid vesicles, we used fluorescence microscopy which can reveal directly the organization of polymer and lipid chains through the localization of their corresponding fluorescent analogues. Moreover, instead of using the wide-field epifluorescence microscopy, confocal laser scanning microscopy (CLSM) was considered. There are a number of advantages to using CLSM over the conventional fluorescence microscope, including: i) the elimination of out-of-focus light, ii) the ability to control depth of field and, iii) the capability to collect serial optical sections from thick specimens to reveal its three dimensional structure. They are all achieved due to the presence of a small pinhole aperture before the detector, as illustrated in Figure 2.14 [33].

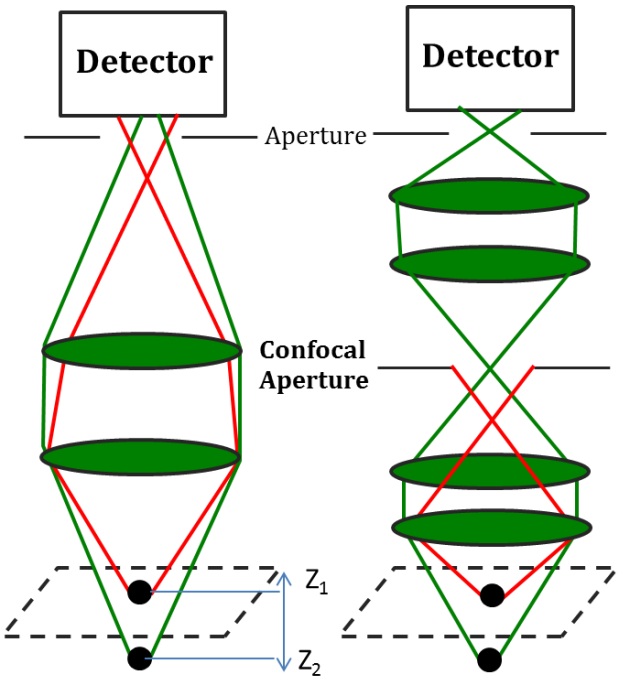

Figure 2.14. Schema illustrating the differences in wide-field epifluorescence and confocal microscopy

The CLSM used in this thesis work is the Leica TCS SP5 (Leica Microsystems CMS GmbH, Mannheim, Germany) inverted confocal microscope (DMI6000). A 63x apochromatic water immersion objective with a NA of 1.2 (Zeiss, Jena Germany) was used for all experiments. Fluorescein and Rhodamine excitation were achieved with the 488 nm and 514 nm lines respectively from an argon laser, while the emission was collected in the 500-530 nm range for FITC and in 600-700 nm range for Rhod. Temperature control was achieved using a thermostated plate (Linkman).

2.4.2. Fluorescence lifetime imaging microscopy

In section 2.3.2, fluorescence lifetime, FRET and time-resolved measurement in spectroscopy were described. Time-resolved methodologies can also be performed under the microscope, and this is known as fluorescence lifetime imaging microscopy (FLIM). Introduced the first time in 1989 [34], FLIM is a technique in which the mean fluorescence lifetime of a fluorophore is measured at each spatially resolvable element of a microscope image. Since the fluorescence lifetime τ can be used to investigate energy transfer as mentioned above, measuring the lifetime *via* FLIM provides essential information on FRET at micrometric scale. This FLIM-FRET approach was also used in this thesis. The FRET efficiency values in different GHUVs were interpreted similarly to the measurements in LHUVs; just the FLIM-FRET

additionally allows mapping the lifetime distribution. Because of photobleaching problem, FLIM-FRET in GHUVs was performed using FITC-Rhod as the FRET pair (Fig. 2.15).

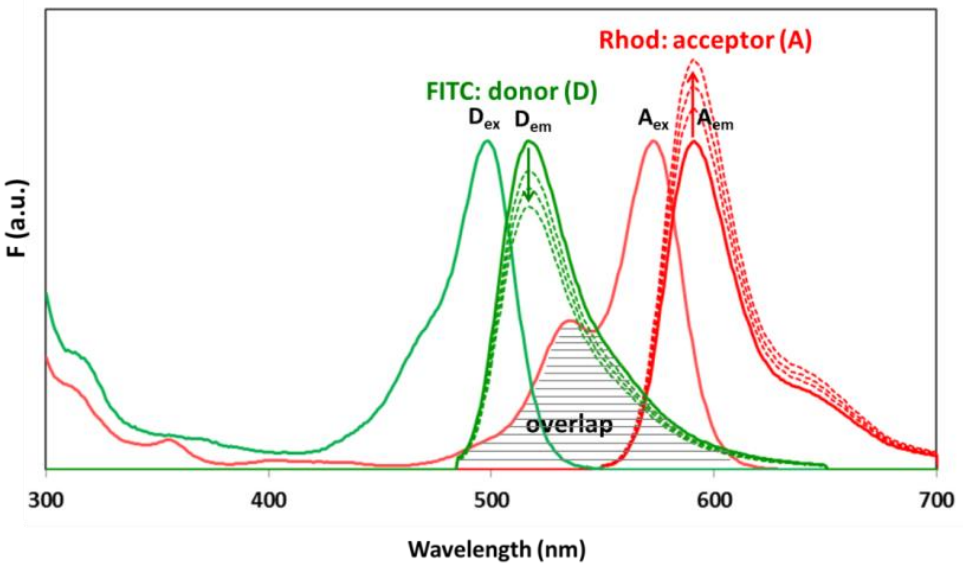

Figure 2.15. Overlap of the FITC emission spectrum and the excitation spectrum of Rhod. As a result of FRET, the donor emission (D_{em}) is reduced while the acceptor emission (A_{em}) increases.

FLIM measurements were performed using the same setup confocal microscope as previously described, coupled to a multiphoton Titanium: Sapphire laser (Spectra-Physics Mai Tai BB, Darmstadt, Germany, 710-990 nm, 100 femtoseconds, 80 MHz) as the excitation source. A photomultiplier tube was coupled to the X-port of the microscope, and the emitted photons were processed by an SPC board that addresses simultaneously the xy location of the collected photons (Becker and Hickl, GmbH, PMC-100-4 SPC-830). The laser power was adjusted to give an average photon counting rate higher than 5.10^4 photon/s and images were acquired during 60 seconds to achieve reasonable photon statistics. The excitation wavelength was set to 820 nm, and emission light was selected with a dichroic beam splitter with an excitation SP700 short-pass filter and an emission 530 band-pass filter inserted in front of the photomultiplier. Images were acquired using a Becker and Hickl SPC 830 module. Fluorescence lifetimes were obtained by analysing the fluorescence decays through a least square iterative re-convolution of decay functions with the instrument response function (IRF) using the software SPC Image (Becker and Hickl, Berlin, Germany).

2.4.3. Fluorescence recovery after photobleaching

Established in the seventies by Axelrod and coworkers [35], fluorescence recovery after photobleaching (FRAP) is one of the advanced fluorescence microscopy techniques that

allows obtaining information on the dynamics of mobile fluorescent molecules at the micrometer scale. Specifically, FRAP can be used to study the diffusion process, transient-binding events and directed transport [36]. In this thesis, FRAP was used to investigate the lateral motion of both lipid and polymer molecules within hybrid vesicles. The diffusion coefficient values were measured as a function of GHUVs constitution and composition, in order to establish the correlation between membrane structuration and mobility of the components.

As implied in the acronym, FRAP basically measures the kinetics of recovery of fluorescence intensity in an area of the membrane where the fluorophores have been bleached by a powerful laser pulse. A schematic representation of a FRAP experiment is described in Figure 2.16 and the corresponding typical FRAP curve is illustrated in Figure 2.17.

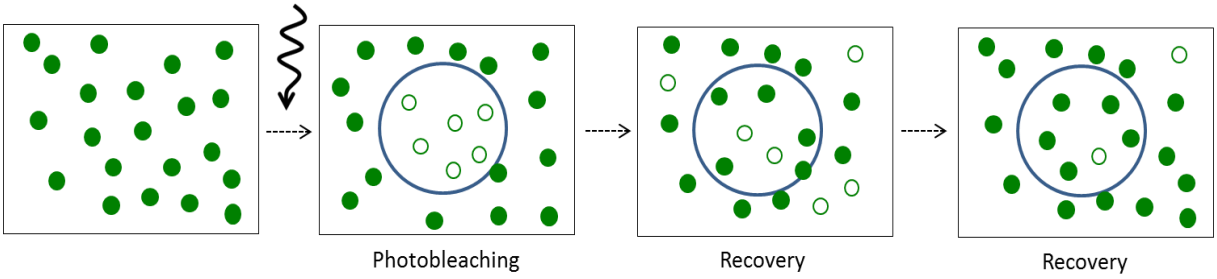

Figure 2.16. Schematic representation of a FRAP experiment: a region of interest (ROI) is photobleached by an intense laser beam and the fluorescence recovery in the ROI is measured over time.

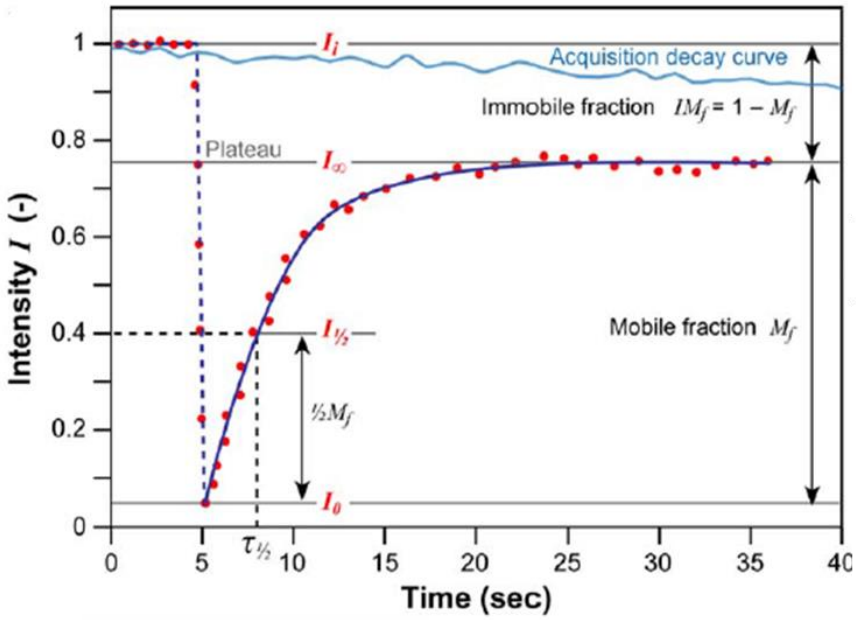

Figure 2.17. Anatomy of a typical FRAP curve: from the initial fluorescence intensity (I_i), the signal drops to a particular value (I_0) as the high intensity laser beam bleaches fluorophores in the ROI. Overtime the signal recovers from the post-bleach intensity (I_0) to a maximal plateau value (I_∞). Adapted from [33]

Briefly, in a FRAP measurement; an intense laser light is first used to photobleach an area of the sample which is called region of interest (ROI), leading to a local reduction of fluorescence intensity in this ROI. Subsequently, a low intensity laser light is used to follow the recovery of fluorescence. Since the photobleaching is an irreversible process, this recovery is a result of diffusion of unbleached molecules from areas of membrane unaffected by the bleaching pulse. As such, fitting the recovery curve with an appropriate FRAP model can yield the physical quantities describing the local diffusion in the sample, such as diffusion time τ and the diffusion coefficient D [37] which are related *via*:

$$D = \frac{\omega^2}{\tau} \qquad \text{Eq. 2.26}$$

where ω is the size of the bleaching spot. Additionally, FRAP can also report the presence of immobile fluorescent molecules that cannot participate in the exchange between bleached and unbleached regions, and results in an incomplete recovery of the fluorescence signal. This is referred as the immobile fraction (IM_f) and is calculated by:

$$IM_f = \frac{I_i - I_\infty}{I_i - I_0} \qquad (\text{Eq. 2.27})$$

where I_i, I_0 and I_∞ are the fluorescence intensity at initial pre-bleached time, bleached time and at maximal recovery respectively. The fraction of fluorescent molecules that can participate in this exchange is called the mobile fraction (M_f) and is defined by:

$$M_f = 1 - IM_f \qquad (\text{Eq. 2.28})$$

In this work, FRAP experiments were performed on the same confocal microscopy setup as described in section 2.4.1. The microscope settings were controlled by the FRAP-Wizard of LAS-AF microscope software version 15.1 that allowed defining the scanning conditions, the time-lapsed between the images and the number of frames in each phase (pre-bleach, photo-bleach and post-bleach phases respectively). FITC was excited and bleached with 488 nm laser line of the argon laser and the fluorescence emission was collected between 500-600 nm using a PMT detector. Otherwise, Rhod was excited and bleached with 514 nm line and the emission was collected in 600-700 nm range. FRAP acquisition was started with 10 images scan, at low laser intensity (80% Argon laser, 2-5% 488 nm laser line). Then FITC was bleached locally inside the ROI sized 5 µm, using a scan of 3 frames at high laser intensity (80% Argon laser, 100% 488 nm laser line). Finally, the fluorescence redistribution was

monitored by the acquisition of a series of 150 images with the same low laser intensity as pre-bleach phase (80% Argon laser, 2-5% 488 nm laser line). In all steps, the images were acquired using a frame size of 256 x 256 pixels and bidirectional scan at a 1400 Hz line frequency scan speed, which gave a time-lapse of 0.113 s. The pinhole was set to 222.92 µm (2 Airy) and a zoom of 6x was employed. All measurements were made at T = 20°C ± 1°C.

To fully immobilize the vesicles during acquisition, samples were transferred to the wells of an eight-well µ-Slide from Ibidi (Munich, Germany) coated avidin at 15 minutes before measurement. The avidin coating was realised by incubating the well with 200 µL of avidin solution at 0.1 mg/ml during at least 1h at 4°C, and subsequently washing with MiliQ-water to remove all the non-attached avidin [38].

Quantitative interpretation of FRAP data was performed using the FRAP Analyser software version 1.0.5 developed by A. Halavatyi, M. Yatskou and E. Friederich. This software allows normalizing the data, fitting different models to the normalized data and considering different ROI geometries. The FRAP data were normalized first to remove variations due to differences in the absolute amount of fluorescent molecules between samples. In this way, the relative fluorescence changes after photobleaching become proportional to the initial values and independent of fluorophores concentration. The method used in this work was double normalization:

$$I_{Norm}(t) = \frac{I_{Ref\_pre}}{I_{Ref}(t) - I_{Bck}(t)} \cdot \frac{I_{Frap}(t) - I_{Bck}(t)}{I_{Frap_{pre}}} \qquad \text{(Eq. 2.29)}$$

where $I_{Norm}(t)$: normalized intensity, $I_{Frap}(t)$: measured average intensity inside the bleached spot, $I_{Ref}(t)$: measured average reference intensity and $I_{Bck}(t)$: measured average background intensity outside. Subscript $_{pre}$ means the averaging of intensity in the corresponding ROI immediately before bleaching and after subtraction of background intensity.

All experimental data were fitted with the circular spot model in 2D diffusion, whose equation is:

$$I_{Norm}(t) = a_0 + a_1 . e^{\frac{\tau}{2(t - t_{bleach})}} . \left(I_0 \left(\frac{\tau}{2(t - t_{bleach})} \right) + I_1 \left(\frac{\tau}{2(t - t_{bleach})} \right) \right) \qquad \text{(Eq. 2.30)}$$

2.4.4. Micropipette aspiration

Micropipette aspiration (MPA) technique is a widely used methodology to measure the mechanical properties of both model and biological membranes. This technique, pioneered by Evans and Kwok [39] consists in capturing a giant vesicle into a small glass capillary and evaluating its deformation upon pressure suction, which produces a uniform membrane tension. Typical procedure of a micropipette aspiration experiment is summarized in Figure 2.18.

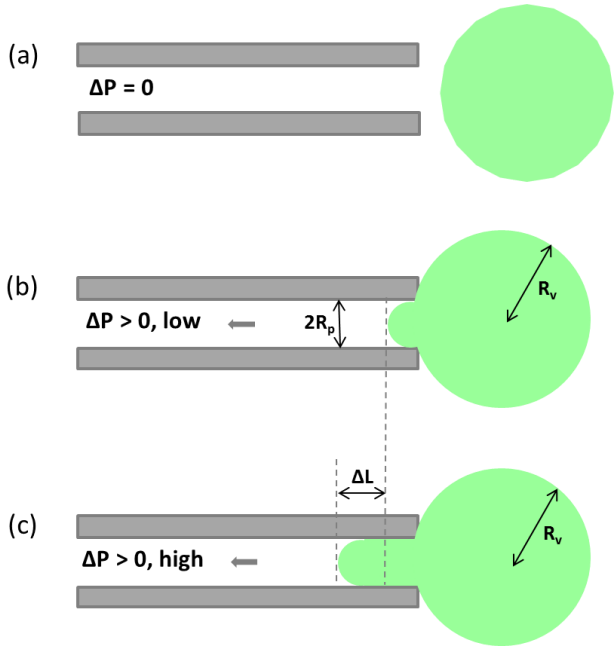

Figure 2.18. Micropipette aspiration methodology: (a) a floppy vesicle before aspirating (b) aspirating with a low suction pressure (c) aspirating with a high suction pressure

Suction pressure can be controlled by moving upward or downward a water reservoir which is connected to the upper outlet of the capillary. The suction pressure exerted over the membrane therefore is calculated by following equation:

$$\Delta P = (h - h_0)\rho_w g \qquad \text{(Eq. 2.31)}$$

where ρ_w is the density water (ρ = 1 g.cm^{-3}), g is the gravitational acceleration (9.8 m.s^{-2}), h is the position of the water reservoir and h_0 is the initial position where the pressure is zero. This suction pressure applied to a fluid membrane yields a uniform membrane tension σ over the entire surface whose magnitude is given by Eq.2.32:

$$\sigma = \frac{\Delta P \times R_p}{2(1 - \frac{R_p}{R_v})} \qquad \text{(Eq. 2.32)}$$

where R_p and R_v are the capillary and vesicle radius respectively. Under tension, the membrane area will change. A relative area change of the membrane (α) can be defined as:

$$\alpha = \frac{A - A_0}{A_0} \qquad (Eq.\ 2.33)$$

A_0 being the membrane area of the vesicle at the lower suction pressure. α can be estimated from the increase in projection length ΔL of vesicle inside the capillary tip according to Eq.2.34:

$$\alpha = \frac{1}{2} \times \frac{R_p}{{R_v}^2} \times \Delta L \times \left(1 - \frac{R_p}{R_v}\right) \qquad (Eq.\ 2.34)$$

Under very low tension regime, the apparent expansion is dominated by smoothing of thermal bending undulations. Plotting ln(σ) *vs* α at low-σ values (typically 0.001 – 0.5 mN.m^{-1} [40]) give a straight line whose slope is related to bending modulus (Eq.2.34). Under higher tensions (> 0.5 mN.m^{-1}), membrane undulations are totally suppressed and membrane area increases as the result of increasing the spacing of the molecules. In this regime, the rate of membrane area increase with tension can be used to calculate stretching or area compressibility modulus K_a according to Eq.2.35 approximated by [41]:

$$\alpha \approx \frac{k_B T}{8\pi\kappa} \ln(\sigma) + \frac{\sigma}{K_a} \qquad (Eq.\ 2.35)$$

with k_B is the Boltzmann's constant and T is absolute temperature.

Additionally, the other mechanical parameters that can be quantified are lysis tension and lysis strain. They represents the tension and area expansion at which the vesicle rupture.

The practical details of each sequential step in MPA experiments are described by the following:

i) Preparation of micropipettes:

Micropipettes were obtained by stretching Borosilicate capillaries (1mmOD, 0.58mmID) from WPI, with a pipette puller (Sutter Instrument P-97). The pulled pipets were then forged to the desired diameter using a micro-forge Narishige MF-900. The typical inner diameters of pipette tips are between 6 and 8 µm, suitable for the general size range of the vesicles of 20 – 25 µm. Micropipettes were coated with BSA to prevent vesicle adhesion using different protocols that will be described in chapter 6.

ii) Connecting micropipette into system:

After being coated with BSA solution, micropipette was connected to the water reservoir *via* flexible tubing that was fitted into the micropipette holder (Figure 2.19). During connection, great care has to be taken to prevent the presence of air microbubbles, which will completely perturb the control of the pressure. The micropipette holder was then fixed to the micromanipulator (Eppendorf, Patchman NP2) allowing precise control of the positioning of pipette in 3D. The overall picture of system can be seen in Figure 2.19.

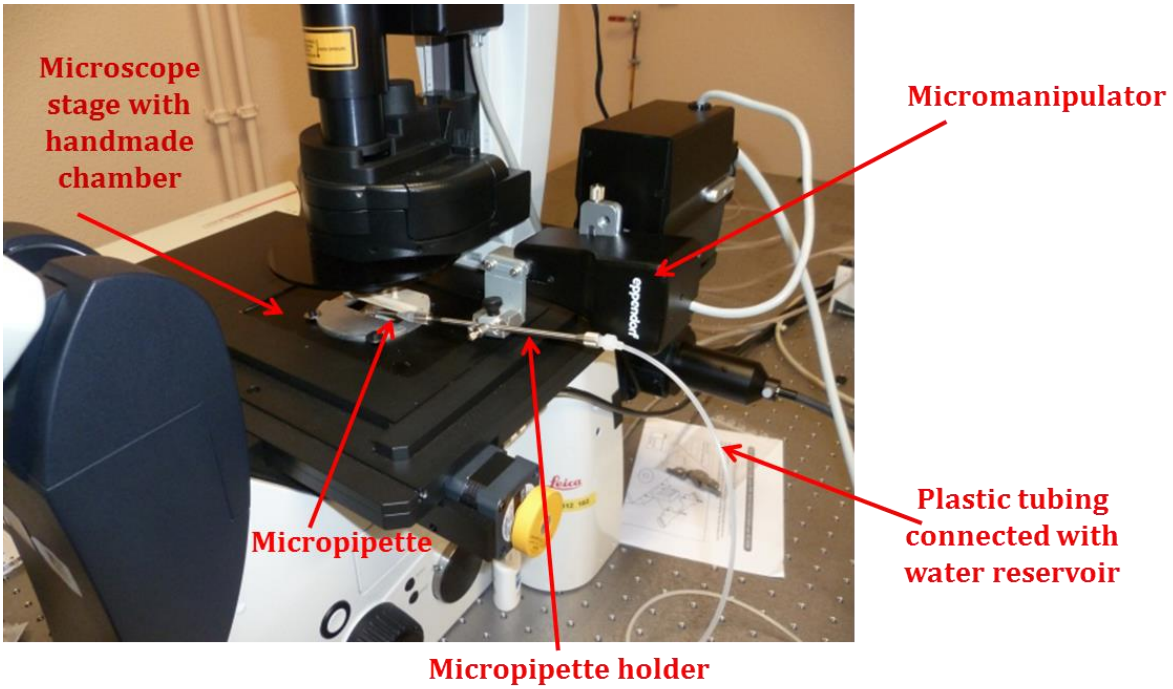

Figure 2.19. Setting up micropipette into system

iii) Setting up the MPA chamber:

A handmade open chamber made of two small cut coverslip (2 x 1 cm) separated by ~ 0.5 cm, fixed by vacuum grease was inserted on the microscope stage plate as illustrated in Figure 2.20.

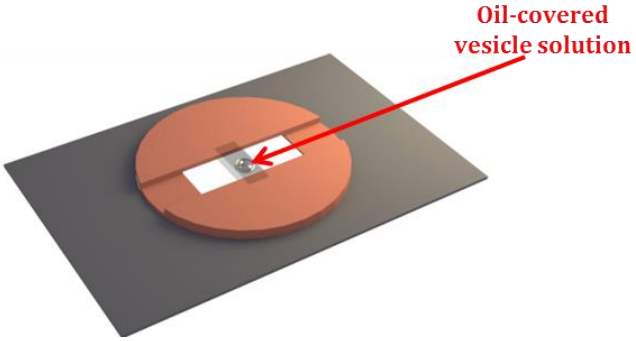

Figure 2.20. Handmade MPA chamber wherein the GUVs containing suspension is filled

This open chamber allows the horizontal insertion of the micropipette on one side. One drop of sample is placed on the center of chamber with a syringe. The micropipette is then positioned for the experiments using the micromanipulator. A drop of oil is then added in order to cover sample and limit the evaporation.

iv) Performing measurements:

The first step of an experiment consists in defining the "zero pressure". For that purpose, small negative and positive pressures were applied until the smaller vesicle or any fluorescent object in the suspension that are always present and observable, do not move under the water flux created by the micropipettes. The height of the water reservoir was noted as the "zero" pressure at this point. A little suction was then applied in order to capture the vesicle with the desired diameter, which is between 20 - 25 µm. The vesicle must not present any inhomogeneity inside the aqueous compartment (smaller vesicle tubes aggregates, or smaller vesicles attached to the membrane). First, the suction was increased quickly to draw out any wrinkles and tethers in the membrane, this is called pre-stress step. Afterward, the pressure was decreased to nearly zero and pressure was then increased stepwise (1cm step of the position of water reservoir) and deformation of vesicle recorded, until lysis strain was reached (rupture the vesicle).

Miscropipette aspiration experiments in this work were performed with the strong support of Emmanuel Ibarboure (Ingénieur d'étude in the lab)

ANNEX

A.2.1. Determination of phospholipid concentration by phosphorus titration

Phospholipid concentration was determined *via* phosphorus titration method [42]. The phospholipid is acidic digested to inorganic phosphate and the released inorganic phosphate is reacted with ammonium molybdate, forming a strong blue color which can be spectrophotometrically quantified at 825 nm.

Briefly, a set of KH_2PO_4 standard solutions at various concentrations: 0.2 mM, 0.4 mM, 0.8 mM, 1.2 mM, 1.6 mM and 2mM were prepared for a calibration curve. 100 µl of these standard solutions as well as phospholipid sample were transferred into glass tubes. 500 µL of $HClO_4$ were subsequently added to each tube and the tubes (without sealing) were placed in a heated block at 200°C for 1 hour. After cooling the tubes to room temperature, 9.5 mL of reagent solution (5g of ammonium molybdate, 1g of ascorbic acid and 40 mL of $HClO_4$ in 500 mL MiliQ water) was added. The tubes were kept in a water bath at 50°C during 1 hour for the color to develop. Afterward, they were cooled down and the spectral-photometric analyses were carried out, recording the absorbance at 825 nm. The determined phosphate concentration is equal to the phospholipid concentration, since the phospholipid generally contains only one phosphate group.

A.2.2. Spectral-photometric analysis

All absorption measurements were performed at room temperature using a Shimadzu UV-3101PC UV-Vis-NIR Spectrophotometer.

A.2.3. Size exclusion chromatography (SEC)

The SEC analyses to investigate the average molar masses and polydispersity index of the polymers were carried out with PL-GPC 50 Plus (Agilent Technologies) with both refractive index and UV detectors, TOSOH TSK gel columns (G4000HXL, G3000HXL and G2000HXL). Analyses were done with THF as eluent (1 $mL.min^{-1}$) and tricholorobenzene as flow marker.

A.2.4. Nuclear Magnetic Resonance (^{1}H NMR)

All ^{1}H NMR spectra were recorded on a Bruker Avance AC 400 spectrometer using deuterated chloroform as solvent.

REFERENCES

1. Lin, Z., et al., *Cryo transmission electron microscopy study of vesicles and micelles in siloxane surfactant aqueous solutions.* Langmuir, 1994. **10**(4): p. 1008-1011.
2. Nam, J. and M.M. Santore, *Adhesion Plaque Formation Dynamics between Polymer Vesicles in the Limit of Highly Concentrated Binding Sites.* Langmuir, 2007. **23**(13): p. 7216-7224.
3. Chemin, M., et al., *Hybrid polymer/lipid vesicles: fine control of the lipid and polymer distribution in the binary membrane.* Soft Matter, 2012. **8**(10): p. 2867-2874.
4. Haugland, R.P., *Handbook of fluorescence probes and research chemicals*. 1996: Molecular Probes
5. Walde, P., et al., *Giant Vesicles: Preparations and Applications.* ChemBioChem, 2010. **11**(7): p. 848-865.
6. Angelova, M.I. and D.S. Dimitrov, *Liposome electroformation.* Faraday Discussions of the Chemical Society, 1986. **81**(0): p. 303-311.
7. Shimanouchi, T., H. Umakoshi, and R. Kuboi, *Kinetic Study on Giant Vesicle Formation with Electroformation Method.* Langmuir, 2009. **25**(9): p. 4835-4840.
8. Richardson, R., *Scattering and Reflection Techniques*, in *Colloid Science*. 2009, Blackwell Publishing Ltd. p. 228-254.
9. Berne, B.J. and R. Pecora, *Dynamic light scattering: with applications to chemistry, biology, and physics*. 1976: Courier Corporation.
10. Provencher, S., *CONTIN: A general purpose constrained regularization program for inverting noisy linear algebraic and integral equations.* Computer Physics Communications, 1982. **27**(3): p. 229-242.
11. Koppel, D.E., *Analysis of Macromolecular Polydispersity in Intensity Correlation Spectroscopy: The Method of Cumulants.* The Journal of Chemical Physics, 1972. **57**(11): p. 4814-4820.
12. Frisken, B.J., *Revisiting the method of cumulants for the analysis of dynamic light-scattering data.* Applied Optics, 2001. **40**(24): p. 4087-4091.
13. Zimm, B.H., *Apparatus and methods for measurement and interpretation of the angular variation of light scattering; preliminary results on polystyrene solutions.* The Journal of Chemical Physics, 1948. **16**(12): p. 1099-1116.
14. Guimer, A. and G. Fournet, *Small angle scattering of X-rays.* J. Wiley & Sons, New York, 1955.
15. Patterson, J.P., et al., *The analysis of solution self-assembled polymeric nanomaterials.* Chemical Society Reviews, 2014. **43**(8): p. 2412-2425.
16. Koester, L., H. Rauch, and E. Seymann, *Neutron scattering lengths: A survey of experimental data and methods.* Atomic Data and Nuclear Data Tables, 1991. **49**(1): p. 65-120.
17. Bergström, L.M., et al., *Spontaneous Transformations between Surfactant Bilayers of Different Topologies Observed in Mixtures of Sodium Octyl Sulfate and Hexadecyltrimethylammonium Bromide.* Langmuir, 2014. **30**(14): p. 3928-3938.
18. Lakowicz, J.R., *Principles of Fluorescence Spectroscopy*. 2007: Springer US.
19. Kawski, A., *Fluorescence Anisotropy: Theory and Applications of Rotational Depolarization.* Critical Reviews in Analytical Chemistry, 1993. **23**(6): p. 459-529.

20. Pinto, S.N., et al., *A combined fluorescence spectroscopy, confocal and 2-photon microscopy approach to re-evaluate the properties of sphingolipid domains.* Biochimica et Biophysica Acta (BBA) - Biomembranes, 2013. **1828**(9): p. 2099-2110.

21. Lentz, B.R., Y. Barenholz, and T.E. Thompson, *Fluorescence depolarization studies of phase transitions and fluidity in phospholipid bilayers. 2. Two-component phosphatidylcholine liposomes.* Biochemistry, 1976. **15**(20): p. 4529-4537.

22. Castro, B.M., et al., *Formation of Ceramide/Sphingomyelin Gel Domains in the Presence of an Unsaturated Phospholipid: A Quantitative Multiprobe Approach.* Biophysical Journal, 2007. **93**(5): p. 1639-1650.

23. Romain, L., *Fluorescence lifetime spectroscopy and imaging of FRET probes for the study of cell signalling*. 2013, Imperial college London.

24. Pinto, S., et al. *Fluorescence spectroscopy and microscopy to re-evaluate the properties of sphingolipids domains*. in *European Biophysics Journal with Biophysics Letters*. 2013. Springer 233 Spring st, New York, NY 10013 USA.

25. Förster, T., *Zwischenmolekulare Energiewanderung und Fluoreszenz.* Annalen der Physik, 1948. **437**(1-2): p. 55-75.

26. Forster, T., *Energiewanderung und Fluoreszenz.* Naturwissenschaften, 1946. **33**(6): p. 166-175.

27. Broussard, J.A., et al., *Fluorescence resonance energy transfer microscopy as demonstrated by measuring the activation of the serine/threonine kinase Akt.* Nat. Protocols, 2013. **8**(2): p. 265-281.

28. Dubochet, J., et al., *Cryo-electron microscopy of vitrified specimens.* Quarterly Reviews of Biophysics, 1988. **21**(02): p. 129-228.

29. Bellare, J.R., et al., *Controlled environment vitrification system: An improved sample preparation technique.* Journal of Electron Microscopy Technique, 1988. **10**(1): p. 87-111.

30. Tahara, Y. and Y. Fujiyoshi, *A new method to measure bilayer thickness: Cryo-electron microscopy of frozen hydrated liposomes and image simulation.* Micron, 1994. **25**(2): p. 141-149.

31. Kuntsche, J., J.C. Horst, and H. Bunjes, *Cryogenic transmission electron microscopy (cryo-TEM) for studying the morphology of colloidal drug delivery systems.* International Journal of Pharmaceutics, 2011. **417**(1–2): p. 120-137.

32. Almgren, M., K. Edwards, and G. Karlsson, *Cryo transmission electron microscopy of liposomes and related structures.* Colloids and Surfaces A: Physicochemical and Engineering Aspects, 2000. **174**(1–2): p. 3-21.

33. Ishikawa-Ankerhold, H.C., R. Ankerhold, and G.P.C. Drummen, *Advanced Fluorescence Microscopy Techniques—FRAP, FLIP, FLAP, FRET and FLIM.* Molecules, 2012. **17**(4): p. 4047.

34. Bugiel, I., K. König, and H. Wabnitz, *Investigation of cells by fluorescence laser scanning microscopy with subnanosecond time resolution.* Lasers Life Sci, 1989. **3**(1): p. 47-53.

35. Axelrod, D., et al., *Mobility measurement by analysis of fluorescence photobleaching recovery kinetics.* Biophysical Journal, 1976. **16**(9): p. 1055-1069.

36. Lorén, N., et al., *Fluorescence recovery after photobleaching in material and life sciences: putting theory into practice.* Quarterly Reviews of Biophysics, 2015. **48**(03): p. 323-387.

37. Soumpasis, D.M., *Theoretical analysis of fluorescence photobleaching recovery experiments.* Biophysical Journal, 1983. **41**(1): p. 95-97.

38. Sarmento, M.J., M. Prieto, and F. Fernandes, *Reorganization of lipid domain distribution in giant unilamellar vesicles upon immobilization with different membrane tethers.* Biochimica et Biophysica Acta (BBA) - Biomembranes, 2012. **1818**(11): p. 2605-2615.

39. Kwok, R. and E. Evans, *Thermoelasticity of large lecithin bilayer vesicles.* Biophysical Journal, 1981. **35**(3): p. 637-652.

40. Rawicz, W., et al., *Effect of chain length and unsaturation on elasticity of lipid bilayers.* Biophysical Journal, 2000. **79**(1): p. 328-339.

41. Evans, E. and W. Rawicz, *Entropy-driven tension and bending elasticity in condensed-fluid membranes.* Physical Review Letters, 1990. **64**(17): p. 2094-2097.

42. McClare, C., *An accurate and convenient organic phosphorus assay.* Anal. Biochem, 1971. **39**(2).

CHAPTER 3

SYNTHESIS OF AMPHIPHILIC COPOLYMERS AND CHEMICAL MODIFICATION WITH FLUORESCENT PROBE

Table of Contents

3.1. SYNTHESIS OF AMPHIPHILIC COPOLYMERS

3.1.1. Objective and synthetic strategy

In order to decipher the influence of hydrophobic mismatch on the membrane structuration of hybrid vesicles, we needed a series of copolymers which can self-assemble into vesicle of various membrane thicknesses. In that purpose, we chose to synthesize triblock amphiphilic copolymer, with poly(ethylene oxide) (PEO) as hydrophilic blocks and poly(dimethylsiloxane) (PDMS) of different molar masses as the central block. This architecture is expected to help the formation of vesicle in a larger range of hydrophilic ratio compared to classical coil/coil diblock copolymer [1, 2]. PDMS was chosen because of its low glass transition temperature, allowing dynamic exchanges of the chains and leading to the formation of membrane with a structure at thermal equilibrium. Moreover, PDMS has been quite often used in the field to develop hybrid membranes [3-5]. It is worth mentioning that among the different hydrophobic blocks used for the formation of hybrid vesicles (Polyisobutylene [6-8], Polybutadiene [9-12]); PDMS presents the lower Hildebrand solubility parameters (δ = 7.3 $cal^{1/2}/cm^{3/2}$) and would be therefore the less compatible with fatty acid tails in lipids (δ = 9.1 $cal^{1/2}/cm^{3/2}$). Both polymers (PDMS and PEO) are biocompatible. The triblock copolymer will be codified as PEO_m-*b*-$PDMS_n$-*b*-PEO_m in the manuscript, with n and m designing the number of repetitive units of DMS and EO chains respectively.

The synthetic route applied to generate these copolymers is based on the coupling reaction of N-hydroxysuccinimide (NHS) ester derivative and primary amine. In physiologic to slightly alkaline conditions (pH 7 – 9), NHS ester spontaneously react with primary amines by nucleophilic attack, forming stable amide bonds and releasing NHS group as depicted in Figure 3.1 [13].

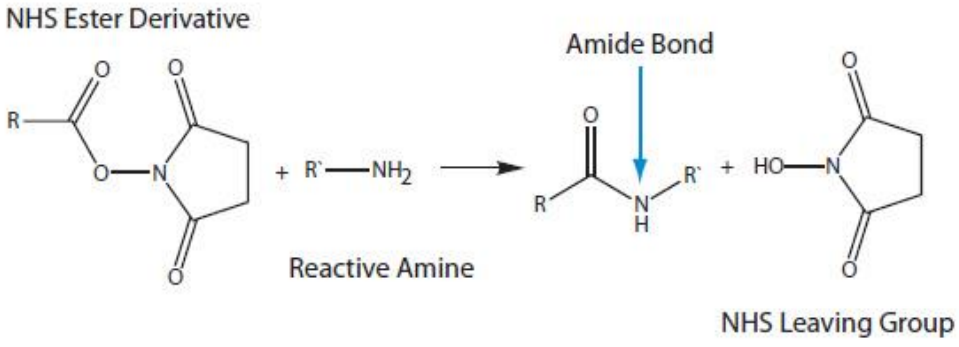

Figure 3.1. NHS-ester reaction scheme for chemical conjugation to a primary amine [13].

It is important to know that reaction of NHS esters with primary amines is strongly pH-dependent. At low pH, the amino group is protonated and no coupling occurs while at higher pH, hydrolysis of NHS ester occurs quickly and thus, the yield of coupling is significantly reduced. When the reaction is conducted in organic solvent, a weak base is added such as triethylamine or N, N-Diisopropylethylamine (DIPEA) to keep amine in its unprotonated, nucleophilic form.

Triblock copolymers PEO_m-*b*-$PDMS_n$-*b*-PEO_m were prepared *via* the coupling of two corresponding blocks: succinimidyl ester-functionalized PEO (PEO_m-NHS) and α, ω-bisaminopropyl-terminated PDMS (H_2N-$PDMS_n$-NH_2) commercially available (Thermo Fisher Scientific, Rapp Polymer and ABCR – see details in Chapter 2). The synthetic pathway is the scheme shown in Figure 3.2.

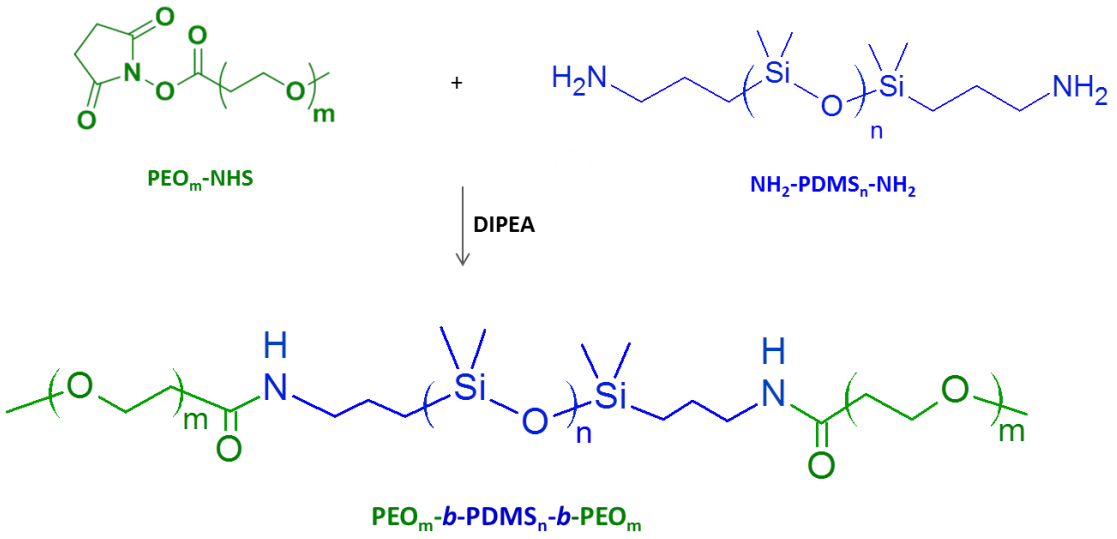

Figure 3.2. Synthetic pathway for PEO_m-*b*-$PDMS_n$-*b*-PEO_m triblock copolymers.

Different pairs of PEO_m-NHS and H_2N-$PDMS_n$-NH_2 blocks were screened, first, in order to find molar masses and hydrophilic fraction of triblock copolymers necessary to generate vesicles and secondly, to modulate their membrane thicknesses from comparable to significantly thicker than liposomal membrane. Previous works of the group on vesicles obtained from a commercial grafted copolymer $PDMS_{26}$-*g*-$(PEO_{12})_2$ [4, 14, 15] have shown that their membrane thickness is 5.6 ± 0.6 nm. In such copolymer, PDMS block has molar mass of 1500 $g.mol^{-1}$ (1900 $g.mol^{-1}$ from our ^1H NMR measurements, annex A.3.1) assuming 2 chains of PEO of 12 units each. Therefore, we decided to investigate H_2N-$PDMS_n$-NH_2 blocks with a number average molar mass of approximately 1500, 3000, 5000 $g.mol^{-1}$ corresponding

respectively to n = 22, 43 and 67. Subsequently, with each H_2N-$PDMS_n$-NH_2 block, an appropriate PEO_m-NHS block was used, based on the empirical law established on coil-coil diblock copolymers by Discher [1], in order to obtain hydrophilic weight fraction of resulting triblock copolymer that would maximize the probability to form vesicles (35±10% hydrophilic weight fraction for diblock) . Finally, PEO_4-NHS, PEO_8-NHS, PEO_{12}-NHS and PEO_{17}-NHS were picked out to react respectively with H_2N-$PDMS_{22}$-NH_2, H_2N-$PDMS_{43}$-NH_2 and H_2N-$PDMS_{67}$-NH_2. Structure and chain-end functionalization rate of all these homopolymers were confirmed by ^1H NMR as shown in Annex A.3.2. The different block copolymers synthesized are summarized in Table 3.1.

Table 3.1. The homopolymer reagents, corresponding target products and their hydrophilic weight fraction (f%)

PDMS block	PEO block	Target product	f (%)
NH_2-$PDMS_{22}$-NH_2	PEO_4-NHS	PEO_4-*b*-$PDMS_{22}$-*b*-PEO_4	18%
NH_2-$PDMS_{22}$-NH_2	PEO_8-NHS	PEO_8-*b*-$PDMS_{22}$-*b*-PEO_8	30%
NH_2-$PDMS_{43}$-NH_2	PEO_8-NHS	PEO_8-*b*-$PDMS_{43}$-*b*-PEO_8	18%
NH_2-$PDMS_{43}$-NH_2	PEO_{12}-NHS	PEO_{12}-*b*-$PDMS_{43}$-*b*-PEO_{12}	25%
NH_2-$PDMS_{67}$-NH_2	PEO_{17}-NHS	PEO_{17}-*b*-$PDMS_{67}$-*b*-PEO_{17}	23%

3.1.2. Synthetic procedure

In the following, the general synthetic protocol used for all coupling reactions is described. Organic solvent was distilled and all glasswares were flamed dried before use.

i) Deprotonation of α, ω-bisaminopropyl-terminated PDMS

This step was to ensure that all the amine group of α, ω-bisaminopropyl-terminated PDMS were deprotonated during coupling. Briefly, the H_2N-PDMS-NH_2 was first dissolved in cyclohexane at concentration about 50 mg/ml and mixed subsequently to an equal volume of 0.1M $NaHCO_3$ solution. After one night under agitation, the organic phase containing deprotonated polymer was recovered using a separation funnel. The traces of water were removed by adding anhydrous $MgSO_4$ and stirring the solution during 1h. This solution was collected afterward *via* filtration and was dried by rotary evaporation to obtain final deprotonated polymer material.

ii) Coupling reaction

A given amount of deprotonated polymer obtained from the first step was transferred into a first Schlenk flask equipped with a magnetic stirring bar. A complementary lyophilisation step was carried out to remove the last traces of solvent and water. The Schlenk flask was sealed with a rubber septum and was flushed with nitrogen several times. Cryo-distilled dichloromethane was subsequently added under nitrogen to reach a concentration of polymer around 100 mg/ml. In a second Schlenk flask, a necessary amount of PEO-NHS (1.2 molar equivalents per amine function of H_2N-PDMS-NH_2) was added. Thereafter, it was solubilized in cryo-distilled dichloromethane containing DIPEA, with one equivalent of DIPEA per amine function. When PEO-NHS was totally dissolved, the solution was injected into first flask containing the deprotonated H_2N-PDMS-NH_2. The resulting reaction mixture was run in 24h at room temperature and the crude product was obtained afterward by removing all organic solvent under dynamic vacuum.

iii) Purification

To remove unreacted reagents and byproduct NHS, the crude product was dispersed in MilliQ water and dialysed against MilliQ water using a membrane MWCO of 50 kDa during at least 2 days. Suspension was then lyophilised, yielding the final dried purified product.

3.1.3. Molecular structure characterizations

3.1.3.1. Proton nuclear magnetic resonance spectroscopy (^{1}H NMR)

All products obtained were first characterized with ^{1}H NMR in $CDCl_3$ to verify the success of coupling. Representative spectra of reagents and achieved products are given in Figure 3.3. The signal of proton of the carbon in α position of the amine groups ($H_2NC\boldsymbol{H_2}CH_2$-) of α, ω-bisaminopropyl-terminated PDMS molecule is positioned at δ = 2.6 ppm. After reaction, this signal is well-shifted to δ = 3.1 ppm corresponding to proton in α position of the amide groups (RCONH$\boldsymbol{CH_2}CH_2$-) with a similar integration value. It demonstrates that all primary amine containing PDMS reacted with PEO-NHS. Additionally, the characteristic signal of NHS group at 2.8 ppm is not visible after reaction, confirming the success of purification process. All remaining peaks on spectra are well-identified as shown in Figure 3.3: δ 0 (m, $Si(C\boldsymbol{H_3})_2O$); δ 0.50 - 0.42 (m, $CH_2C\boldsymbol{H_2}Si$); δ 1.49 - 1.38 (m, $CH_2C\boldsymbol{H_2}CH_2Si$); δ 2.39 (t, $CH_2C\boldsymbol{H_2}CONH$); δ 3.31 (s, $C\boldsymbol{H_3}OCH_2$) and δ 3.7 – 3.42 (m, $C\boldsymbol{H_2}O$).

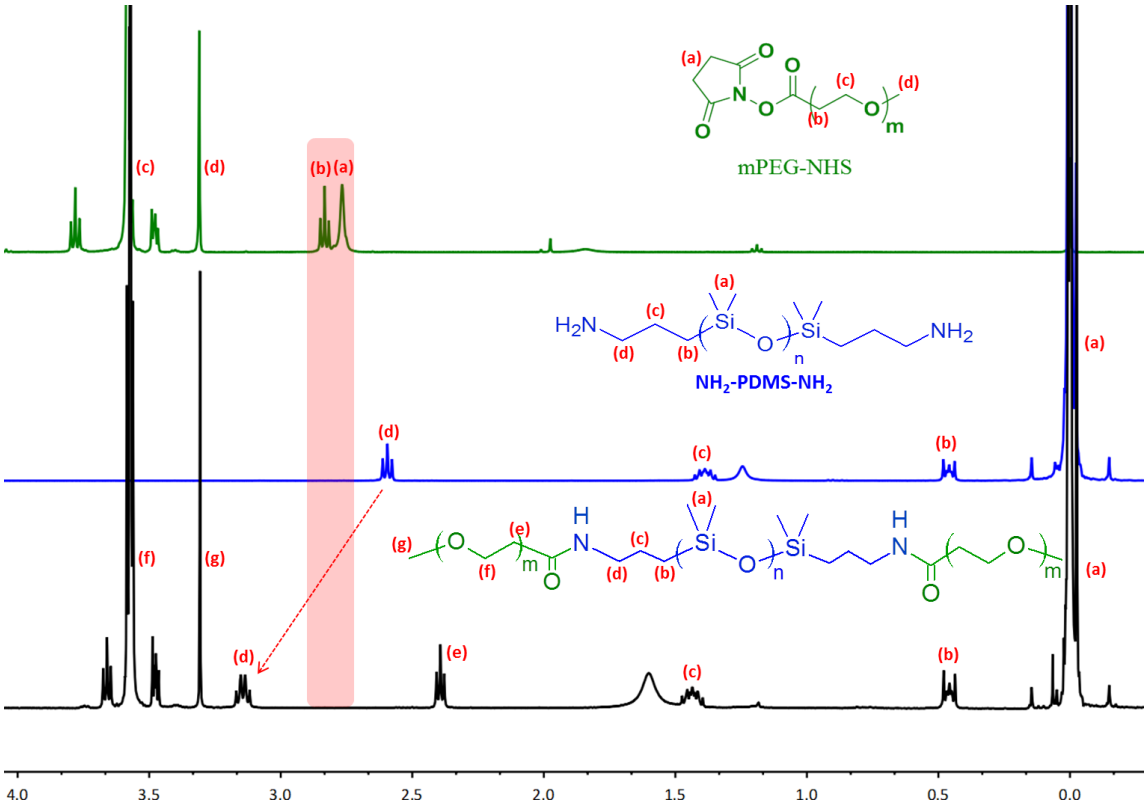

Figure 3.3. Representative ^{1}H NMR spectra in $CDCl_3$ of the homopolymer reagents: PEO_m-NHS (green), H_2N-$PDMS_n$-NH_2 (blue) and triblock PEO_m-*b*-$PDMS_n$-*b*-PEO_n (black).

The integrated ^{1}H NMR spectrum for each triblock copolymer is illustrated in Figure 3.4.

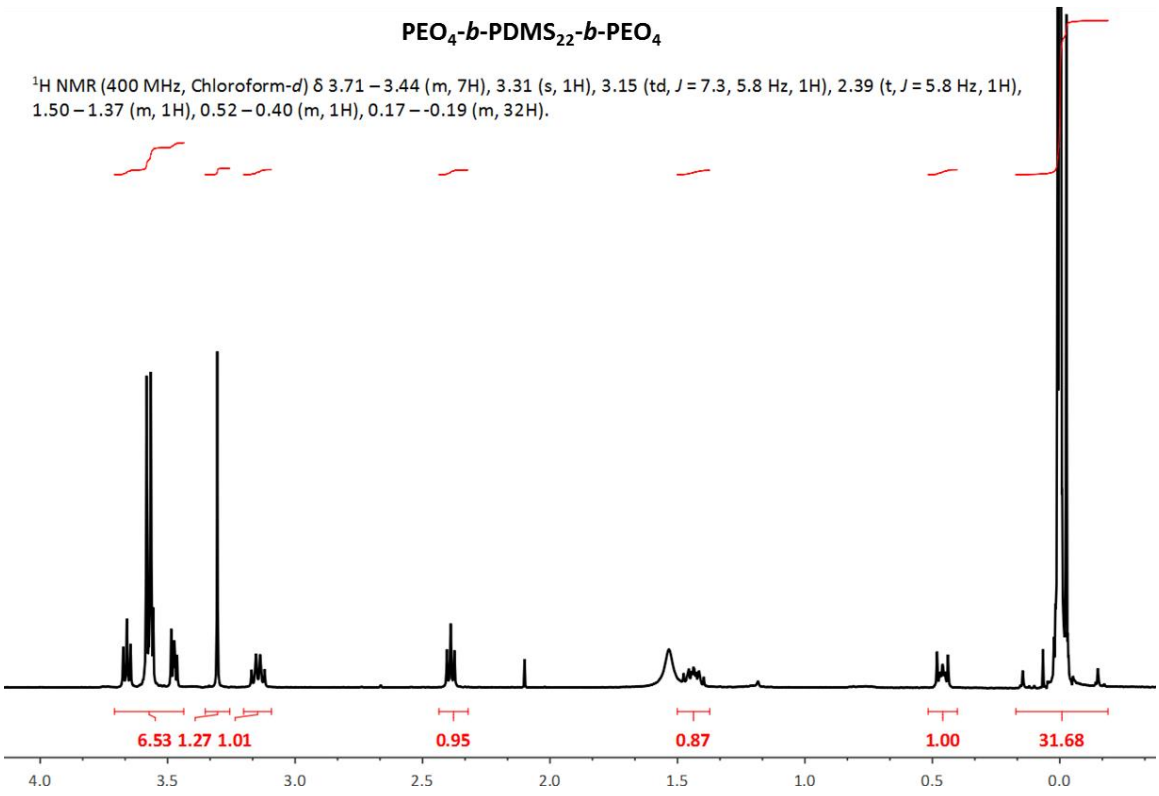

PEO_8-*b*-$PDMS_{22}$-*b*-PEO_8

^{1}H NMR (400 MHz, Chloroform-*d*) δ 3.70 – 3.42 (m, 14H), 3.31 (s, 1H), 3.14 (td, *J* = 7.2, 5.8 Hz, 1H), 2.39 (t, *J* = 5.8 Hz, 1H), 1.49 – 1.38 (m, 1H), 0.50 – 0.42 (m, 1H), 0.13 – -0.11 (m, 33H).

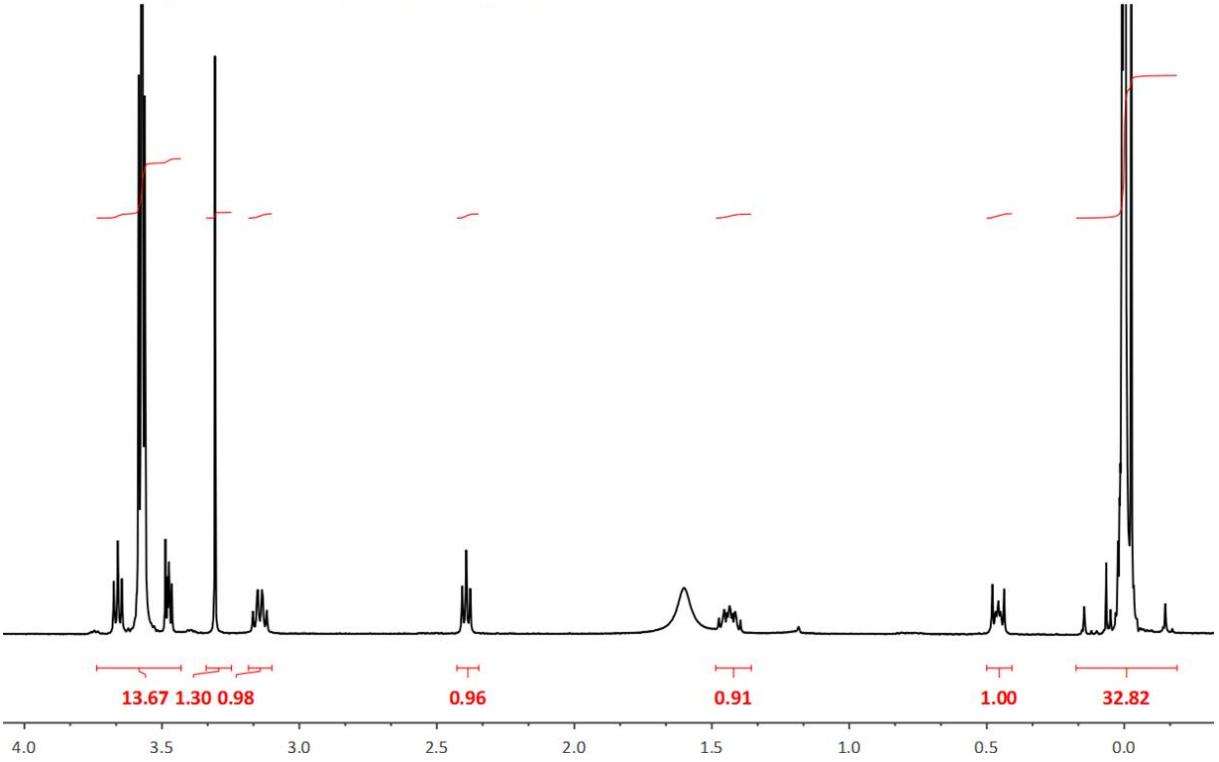

PEO_8-*b*-$PDMS_{43}$-*b*-PEO_8

^{1}H NMR (400 MHz, Chloroform-*d*) δ 3.68 – 3.48 (m, 14H), 3.31 (s, 1H), 3.14 (td, *J* = 7.3, 5.9 Hz, 1H), 2.39 (t, *J* = 5.8 Hz, 1H), 1.50 – 1.29 (m, 1H), 0.50 – 0.40 (m, 1H), 0.18 – -0.21 (m, 61H).

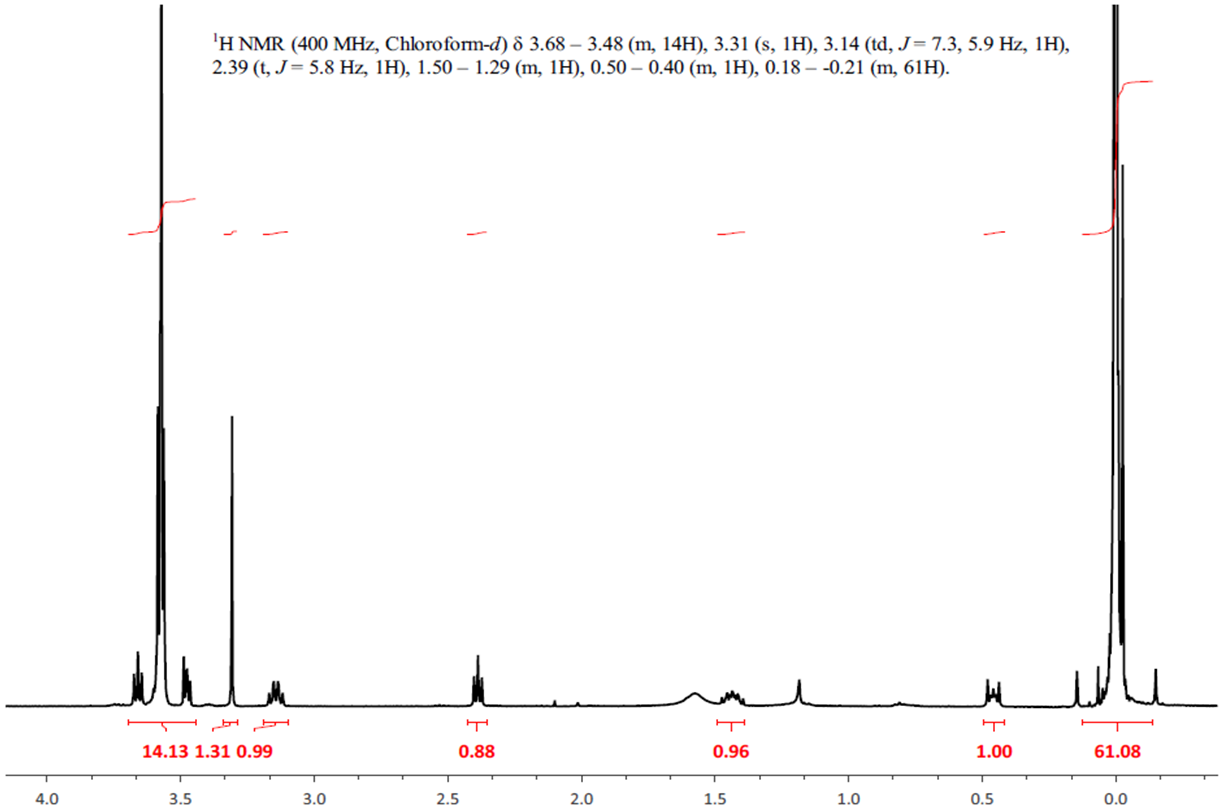

PEO_{12}-*b*-$PDMS_{43}$-*b*-PEO_{12}

^{1}H NMR (400 MHz, Chloroform-*d*) δ 3.78 – 3.38 (m, 22H), 3.31 (s, 1H), 3.19 – 3.10 (m, 1H), 2.39 (t, *J* = 5.9 Hz, 1H), 1.50 – 1.37 (m, 1H), 0.50 – 0.42 (m, 1H), 0.00 (s, 67H).

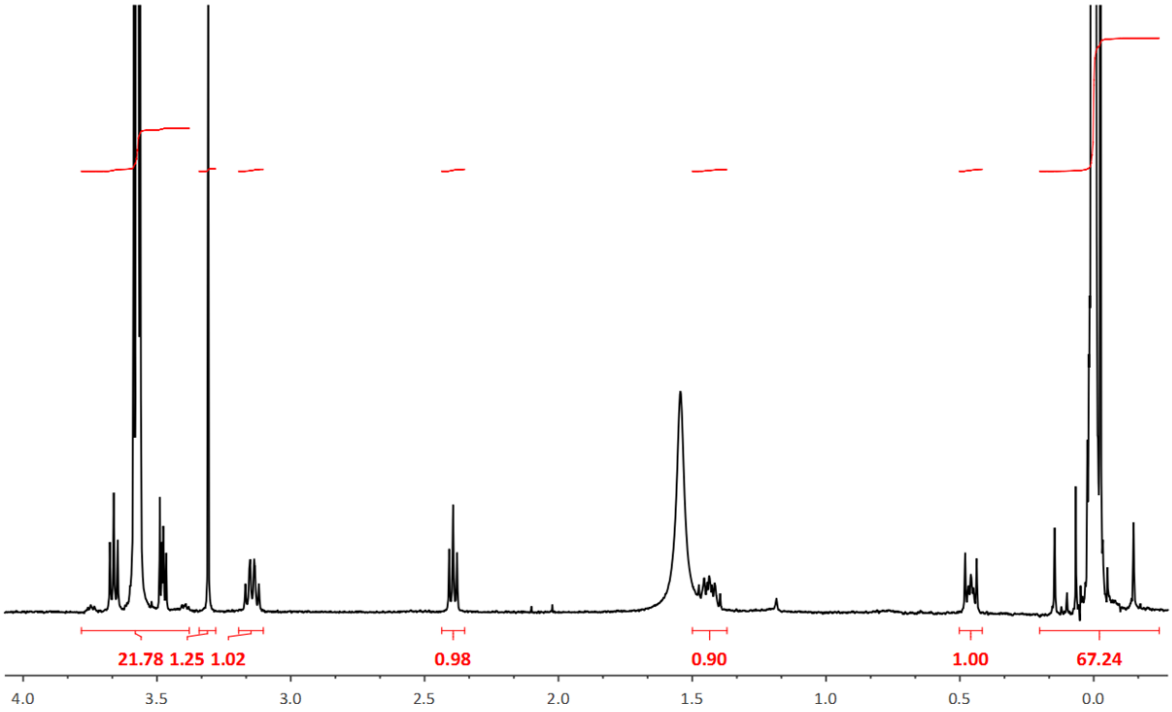

PEO_{17}-*b*-$PDMS_{67}$-*b*-PEO_{17}

^{1}H NMR (400 MHz, Chloroform-*d*) δ 3.71 – 3.32 (m, 33H), 3.31 (s, 1H), 3.14 (q, J = 6.8 Hz, 1H), 2.46 (s, 2H), 1.44 (p, J = 7.6 Hz, 1H), 0.51 – 0.41 (m, 1H), 0.00 (s, 97H).

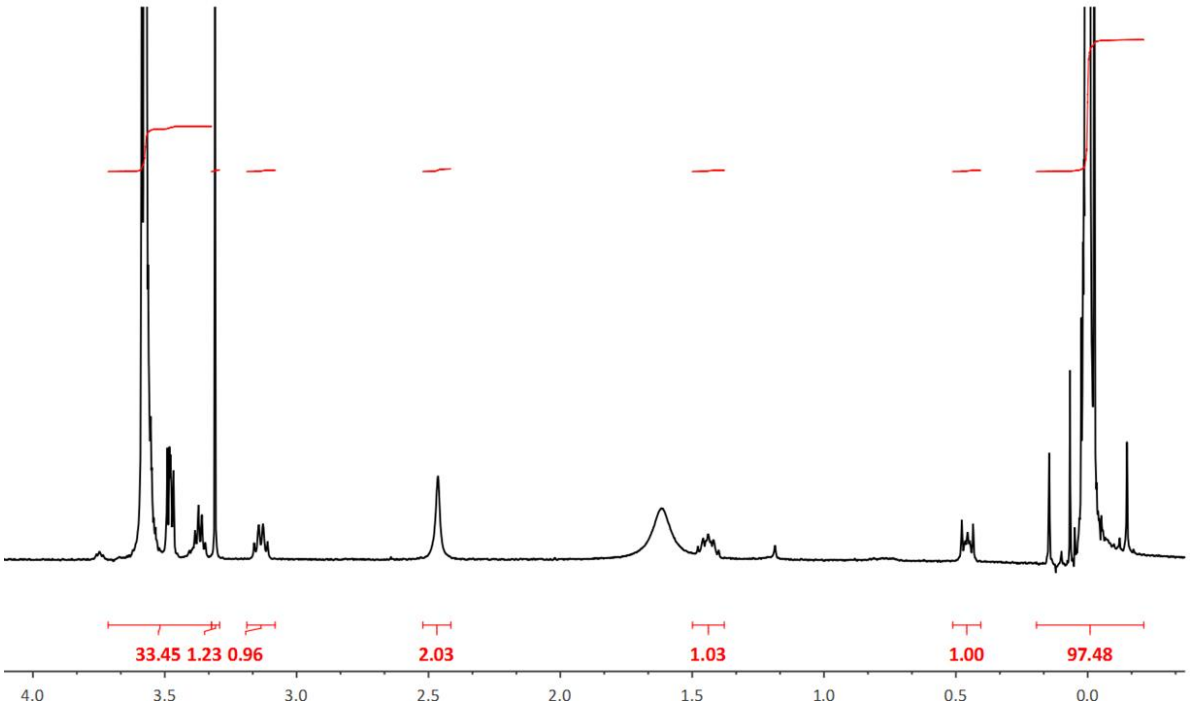

Figure 3.4. ^{1}H NMR spectra of PEO_4-*b*-$PDMS_{22}$-*b*-PEO_4, PEO_8-*b*-$PDMS_{22}$-*b*-PEO_8, PEO_8-*b*-$PDMS_{43}$-*b*-PEO_8, PEO_{12}-*b*-$PDMS_{43}$-*b*-PEO_{12} and PEO_{17}-*b*-$PDMS_{67}$-*b*-PEO_{17} in $CDCl_3$.

3.1.3.2. Size exclusion chromatography (SEC)

To investigate the average molar masses and polydispersity index of the copolymers, the SEC analyses were carried out using refractive index (RI) detector and THF as eluent, with a calibration using PS standards. The SEC chromatograms of part of the triblock copolymers synthesized as well as PEO-NHS are shown in Figure 3.5. Homo-PDMS reagent cannot be characterized since its refractive index is very close to the one of THF. It is clear from the chromatograms that the PEO-NHS unreacted was totally removed during purification process.

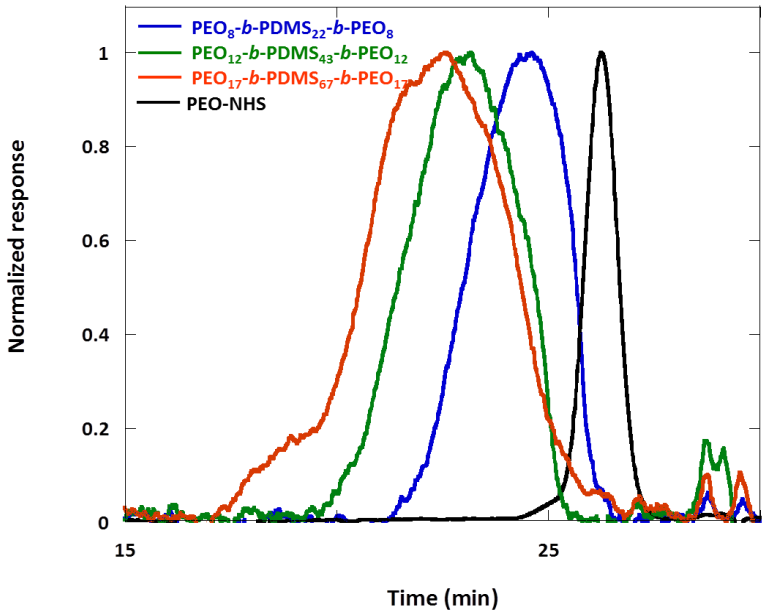

Figure 3.5. Normalized SEC chromatograms of some triblock copolymers and PEO_{17}-NHS reagent.

The average molar mass values achieved via SEC and ^{1}H NMR spectroscopy for all copolymer products are summarized in Table 3.2.

Table 3.2. Average molar masses obtained from SEC and ^{1}H NMR for all copolymer (M_n: Number-average molar mass (g.mol^{-1}); M_w: weight-average molar mass (g.mol^{-1}) and Đ: polydispersity index).

Product	SEC			^{1}H NMR	Yield (%)
	M_n	M_w	Đ	M_n	
PEO_4-*b*-$PDMS_{22}$-*b*-PEO_4	1849	2398	1.29	2238	93.4
PEO_8-*b*-$PDMS_{22}$-*b*-PEO_8	2387	2836	1.18	2668	95.7
PEO_8-*b*-$PDMS_{43}$-*b*-PEO_8	3325	4781	1.43	4158	89.8
PEO_{12}-*b*-$PDMS_{43}$-*b*-PEO_{12}	3877	4995	1.28	4816	91.2
PEO_{17}-*b*-$PDMS_{67}$-*b*-PEO_{17}	6391	7860	1.23	6726	85.6

3.1.4. Self-assembly characterizations

In the following, the ability of the synthesized triblock copolymers to self-assemble into vesicles in an aqueous environment was checked. When vesicular structure was obtained, the main structural parameters were estimated, such as: membrane thickness, vesicle average weight and cross-sectional area (surface area per polymer chain in the vesicle membrane). Film rehydration – extrusion protocol was used to prepare the self-assembled structures from copolymers with rather high hydrophilic fraction such as PEO_8-*b*-$PDMS_{22}$-*b*-PEO_8 and PEO_{12}-*b*-$PDMS_{43}$-*b*-PEO_{12} whereas the self-assembly of copolymers with low hydrophilic fraction as PEO_4-*b*-$PDMS_{22}$-*b*-PEO_4, PEO_8-*b*-$PDMS_{43}$-*b*-PEO_8 and PEO_{17}-*b*-$PDMS_{67}$-*b*-PEO_{17} was formed through double emulsion evaporation, followed by extrusion process. All samples were then characterized with the same methods including static and dynamic light scattering, small angle neutron scattering (SANS) and cryo-TEM. Concentration range of the vesicular suspensions were in between 0.2 mg/ml to 1 mg/ml for light scattering, 10 mg/ml for SANS and 1 mg/ml for cryo-TEM. The characterization of vesicles of commercial copolymer $PDMS_{26}$-*g*-$(PEO_{12})_2$ were also done in parallel.

3.1.4.1. Light scattering

First of all, the self-assembly of copolymers were analysed through both dynamic and static light scattering measurements. All data are summarized in Table 3.3.

Table 3.3. Characteristics of copolymer self-assemblies obtained *via* DLS and SLS measurements (a: R_h determined from relaxation frequency *vs* q^2; b: R_h determined by cumulant analysis at 90°).

Triblock copolymer	Multi-angle		DLS at 90°		R_g/R_h
	R_g (nm)	$R_h^{(a)}$ (nm)	$R_h^{(b)}$ (nm)	PDI	
PEO_4-*b*-$PDMS_{22}$-*b*-PEO_4	60.6	65.2	61.4	0.164	0.93
PEO_8-*b*-$PDMS_{22}$-*b*-PEO_8	43.7	41.6	49.7	0.054	1.05
PEO_8-*b*-$PDMS_{43}$-*b*-PEO_8	68.2	70.4	78.9	0.047	0.97
PEO_{12}-*b*-$PDMS_{43}$-*b*-PEO_{12}	62.8	60.4	61.6	0.077	1.03
PEO_{17}-*b*-$PDMS_{67}$-*b*-PEO_{17}	62.0	51.5	54.0	0.138	1.20
$PDMS_{26}$-*g*-$(PEO_{12})_2$	56.4	54.8	57.5	0.056	1.03

In this Table, gyration radii (R_g) were determined through the Guinier plots and hydrodynamic radii (R_h) were estimated from the apparent diffusion coefficients (D) which were measured from the slope of the q^2 dependence of relaxation rate. The mean

hydrodynamic radii and PDI indexes obtained from the cumulants analyses of the autocorrelation functions measured at 90° were also represented. Figure 3.6 displays the graphs obtained for suspension of PEO_8-*b*-$PDMS_{22}$-*b*-PEO_8, chosen as an example.

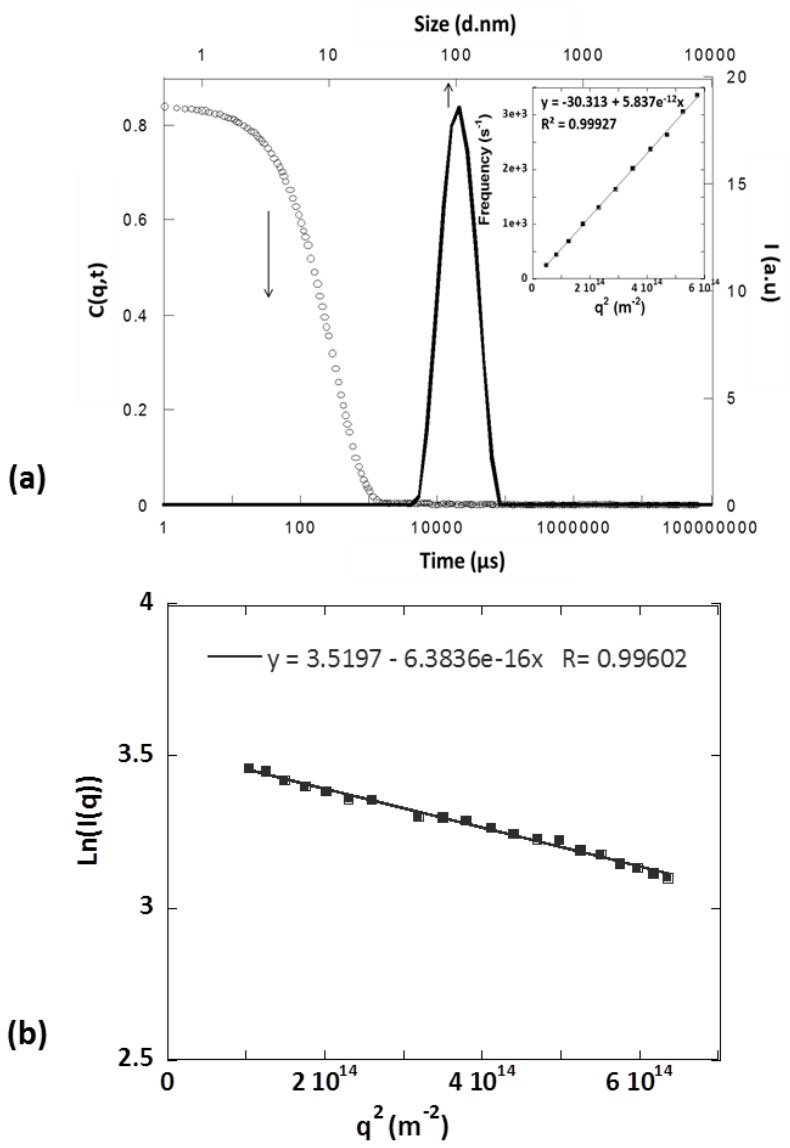

Figure 3.6. Light scattering results obtained for self-assembly of PEO_8-*b*-$PDMS_{22}$-*b*-PEO_8: (a) autocorrelation function at 90° and time distribution function by CONTIN analysis and the insets: relaxation rate *vs* q^2, slope of linear equations is D value; (b): Guinier plot lnI(q) *vs* q^2, slope of linear equation is $-R_g^2/3$.

For all triblock copolymers, the self-assembled aggregates present a narrow size distribution with diameters around 100 nm, close to the pore size of the polycarbonate membrane used for extrusion. In term of morphology, according to R_g/R_h ratio as shown in Table 3.3, we expect vesicular morphologies for PEO_8-*b*-$PDMS_{22}$-*b*-PEO_8, PEO_8-*b*-$PDMS_{43}$-*b*-PEO_8 and PEO_{12}-*b*-$PDMS_{43}$-*b*-PEO_{12} copolymers. The R_g/R_h ratio is higher than 1 in case of PEO_{17}-*b*-$PDMS_{67}$-*b*-PEO_{17} suggesting slightly anisotropic structure.

3.1.4.2. Cryo-TEM

In order to confirm or infirm morphologies suggested by light scattering, cryo-TEM experiments were performed. Examples of images for each sample are presented in Figure 3.7. As expected, samples prepared from PEO_8-*b*-$PDMS_{22}$-*b*-PEO_8 and PEO_{12}-*b*-$PDMS_{43}$-*b*-PEO_{12} copolymers show unilamellar vesicles with the diameter close to the pore size used, 100 nm. PEO_{17}-*b*-$PDMS_{67}$-*b*-PEO_{17} has been already synthesized and studied in the lab by cryo-TEM, this system present 67% of unilamellar vesicles, 23% of wormlike micelles and 5% of double layered vesicles [15]. For PEO_8-*b*-$PDMS_{43}$-*b*-PEO_8, although membrane like structures seems to be observed, the morphologies are irregular and complex. For PEO_4-*b*-$PDMS_{22}$-*b*-PEO_4, aggregates with rounded shape were observed.

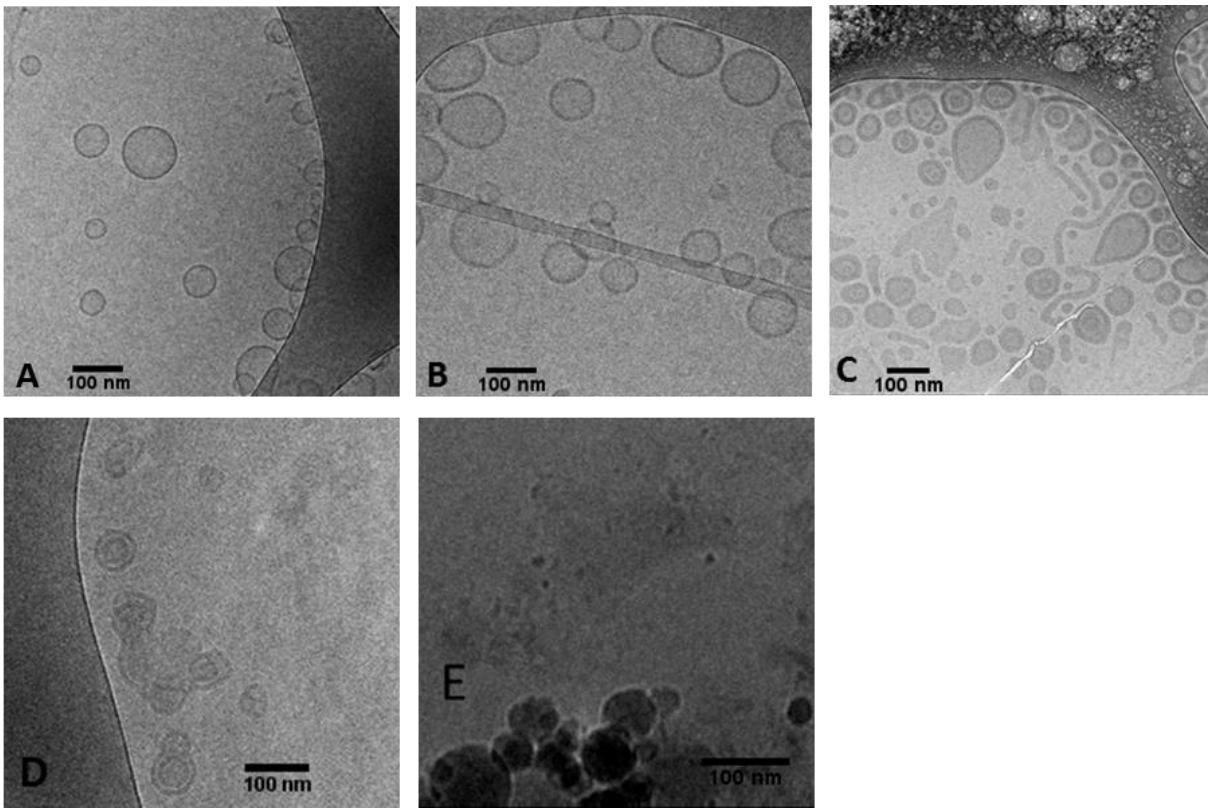

Figure 3.7. Cryo-TEM images for self-assembly of (A): PEO_8-*b*-$PDMS_{22}$-*b*-PEO_8, (B): PEO_{12}-*b*-$PDMS_{43}$-*b*-PEO_{12}, (C): PEO_{17}-*b*-$PDMS_{67}$-*b*-PEO_{17}, (D): PEO_8-*b*-$PDMS_{43}$-*b*-PEO_8 and (E): PEO_4-*b*-$PDMS_{22}$-*b*-PEO_4.

For the copolymers giving vesicular morphologies (PEO_8-*b*-$PDMS_{22}$-*b*-PEO_8, PEO_{12}-*b*-$PDMS_{43}$-*b*-PEO_{12} and PEO_{17}-*b*-$PDMS_{67}$-*b*-PEO_{17}), membrane thicknesses have been characterized. This have been previously evaluated at 11.2 ± 1.2 nm for PEO_{17}-*b*-$PDMS_{67}$-*b*-PEO_{17} in the previous work of the team [15] from an average on 50 vesicles. Histograms are illustrated in Figure 3.8 for PEO_8-*b*-$PDMS_{22}$-*b*-PEO_8 and PEO_{12}-*b*-$PDMS_{43}$-*b*-PEO_{12}.

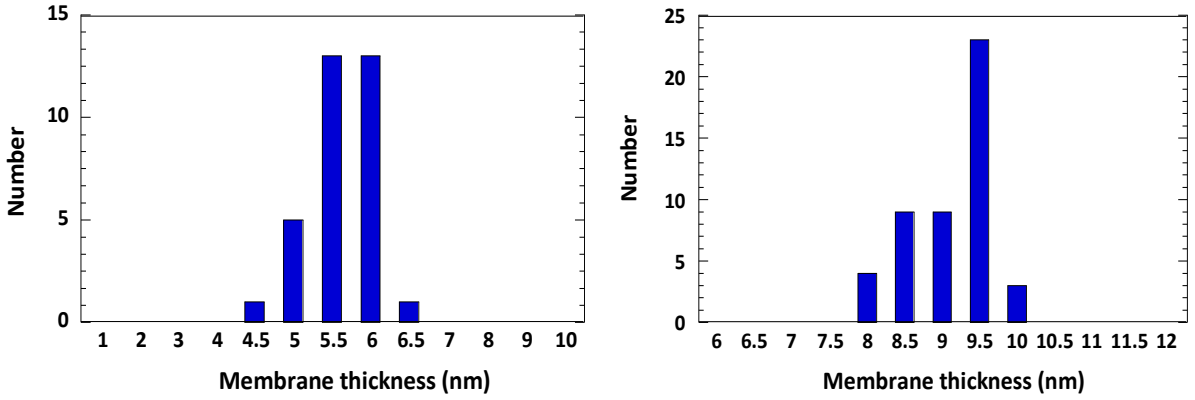

Figure 3.8. Histograms of membrane thicknesses obtained from a set of 35 vesicles PEO_8-*b*-$PDMS_{22}$-*b*-PEO_8 (left) and 50 vesicles PEO_{12}-*b*-$PDMS_{43}$-*b*-PEO_{12} (right).

The values of membrane thicknesses are: 5.4 ± 0.4 nm for PEO_8-*b*-$PDMS_{22}$-*b*-PEO_8 and 8.8 ± 0.5 nm for PEO_{12}-*b*-$PDMS_{43}$-*b*-PEO_{12}. It increases with the number of DMS units and scales with $M^{0.66}$, in good agreement with results obtained for PMOXA-*b*-PDMS-*b*-PMOXA triblock copolymers [2].

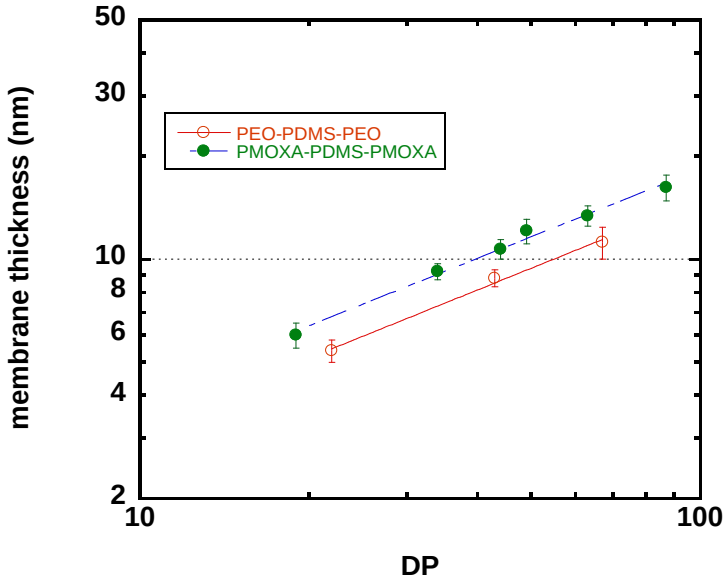

Figure 3.9. Membrane thickness *vs* degree of polymerisation DP for PEO-*b*-PDMS-*b*-PEO synthesized and comparison with results obtained for PMOXA-*b*-PDMS-*b*-PMOXA from [2].

3.1.4.3. Small angle neutron scattering

The self-assembly of copolymers were also investigated by SANS in order to obtain more detailed information on the membrane characteristics. Experiments were only done for copolymers giving vesicular morphologies confirmed by cryo-TEM. Figure 3.10 shows SANS curves (I(q) *vs* q) obtained for these samples. Interestingly, the characteristic q^{-2} dependence

in the intermediate q range which is a signature of scattering from vesicles was observed for all samples.

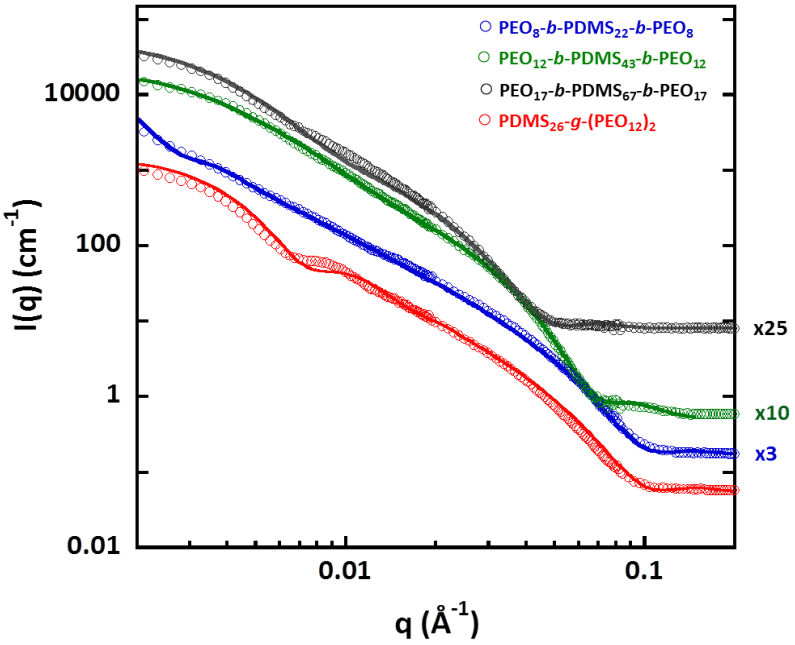

Figure 3.10. Experimentally measured SANS curves for different triblcok copolymers and commercial grafted copolymer. Lines are the best fits with the vesicle model. Somes curves are shifted for the sake of clarity.

As such, they were treated with the polydisperse vesicle form factor ("spherical shell" model) using SasView program with a log-normal distribution law for the core radius and a Gaussian law for the membrane thickness. The fit works well with the relatively high dispersity in radius of vesicle for samples of $PDMS_{26}$-*g*-$(PEO_{12})_2$, PEO_8-*b*-$PDMS_{22}$-*b*-PEO_8 and PEO_{12}-*b*-$PDMS_{43}$-*b*-PEO_{12}. With PEO_{17}-*b*-$PDMS_{67}$-*b*-PEO_{17}, probably because of the existence of various morphologies as seen by cryo-TEM, the fitted radius value seemed not reliable (data not shown). Despite this fact, the membrane thickness is accurately determined for all copolymers. The best fit results (the median inner radius of vesicles R_ϑ, its lognormal distribution width parameter σ_{R_ϑ}, median membrane thickness δ_ϑ and its lognormal distribution $\sigma_{\delta_\vartheta}$) are listed in Table 3.4:

Table 3.4. Parameters obtained by fitting SANS curves with the vesicle model.

Copolymer	R_ϑ (nm)	σ_{R_ϑ}	δ_ϑ (nm)	$\sigma_{\delta_\vartheta}$
$PDMS_{26}$-*g*-$(PEO_{12})_2$	36.5	0.3	5.6	0.18
PEO_8-*b*-$PDMS_{22}$-*b*-PEO_8	30	0.4	5.6	0.14
PEO_{12}-*b*-$PDMS_{43}$-*b*-PEO_{12}	45	0.3	8.8	0.16
PEO_{17}-*b*-$PDMS_{67}$-*b*-PEO_{17}	-	-	11.7	0.15

3.1.4.4. Static light scattering

Static light scattering experiments at multiple angles and concentrations were carried out to determine the aggregation number of the vesicles and access the cross-sectional area per chain which is a parameter of prime importance for the FRET simulation works that will be described in the next chapter. Measurements were conducted at either room temperature or 50°C, corresponding with temperatures used for FRET experiments. For that, we measured refractive index increments of vesicular suspensions at various concentrations from 0.1 to 1 mg/ml. Measurements were conducted at room temperature and 50°C using a differential refractometer from WYATT Technology (Optilab reX and HELEOS-II). The dn/dc values were determined also from one concentration using a differential refractive index detector (WYATT, Optilab rEX) operating at λ = 658 nm in flow mode at 25°C. A defined volume of vesicle suspension was injected at a flow rate of 0.6 mg/ml and dn/dc was obtained from the integration of the corresponding peak area by considering the total polymer mass concentration. Measurements were replicated 2 or 3 times for repeatability. Data were then analysed with Guinier formalism, as illustrated in Figure 3.11.

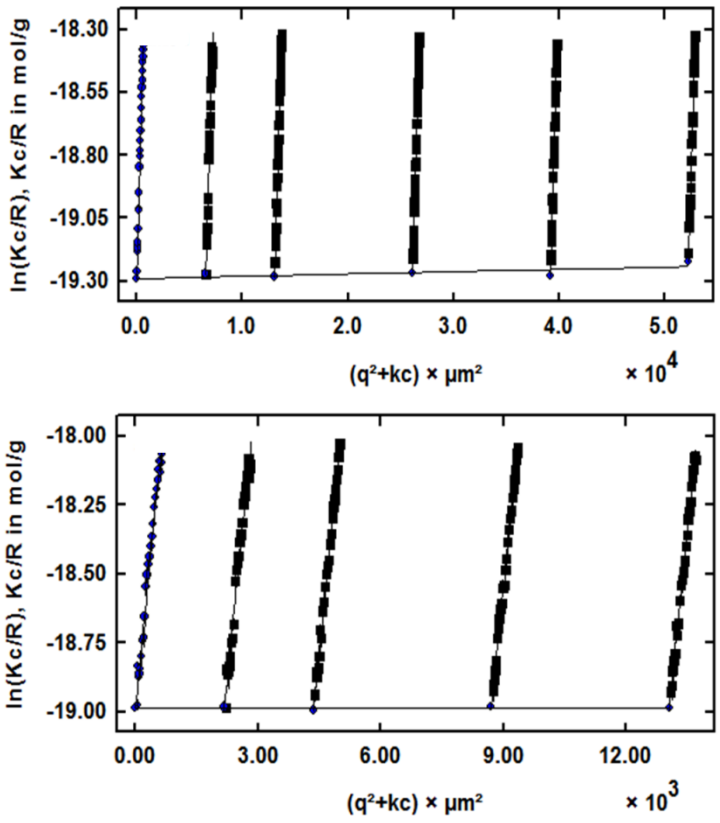

Figure 3.11. Guinier plots obtained for PEO_8-*b*-$PDMS_{22}$-*b*-PEO_8 and PEO_{12}-*b*-$PDMS_{43}$-*b*-PEO_{12} at 50°C.

It was observed that the concentration did not have significant influence on the ln(KC/R) extrapolated at q → 0. Therefore, for repeatability measurement, each sample was replicated two or three times and measurement were made at one concentration (c = 0.2 mg/ml) and different angles. From values of molar masses obtained, area per chain values were calculated and gathered in Table 3.5 (assuming a monolayer in the membrane for the triblock as explained in chapter 2). In this table, the characteristics of grafted copolymer $PDMS_{26}$-*g*-$(PEO_{12})_2$ are also given. Regarding the previous results obtained in our group and from literature, this copolymer is probably organized as a bilayer in analogy to phospholipids [15].

Table 3.5. Characteristics of PEO_8-*b*-$PDMS_{22}$-*b*-PEO_8, PEO_{12}-*b*-$PDMS_{43}$-*b*-PEO_{12}, PEO_{17}-*b*-$PDMS_{67}$-*b*-PEO_{17} vesicles analysed by SLS at 25°C and 50°C ($\bar{A}$ was calculated in assuming the polymer arrange into monolayer conformation) and of $PDMS_{26}$-*g*-$(PEO_{12})_2$ ($\bar{A}$ was calculated for bilayer conformation).

PEO_8-*b*-$PDMS_{22}$-*b*-PEO_8						
	t°	**R_h (nm)**	**dn/dc**	**$\overline{M_n}$ (g/mol)**	**N_{agg}**	**$\bar{A}$ (nm^2)**
	25°C	41.6	0.102	$4.72.10^7$	$1.7.10^4$	1.23
			0.086	$7.15.10^7$	$2.7.10^4$	0.81
Average	*25°C*	*41.6*	*0.094 ± 0.012*	*$(5.9 \pm 1.8).10^7$*	*$(2.2 \pm 0.7).10^4$*	*1.02 ± 0.3*
	50°C	84	0.1137	$3.33.10^8$	$1.25.10^5$	0.71
			0.1273	$2.84.10^8$	$1.06.10^5$	0.83
			0.1372	$2.44.10^8$	$0.91.10^5$	0.97
		73	0.1137	$3.33.10^8$	$1.25.10^5$	0.60
			0.1273	$2.84.10^8$	$1.06.10^5$	0.70
			0.1372	$2.44.10^8$	$0.91.10^5$	0.82
Average	*50°C*	*80 ± 3.5*	*0.127 ± 0.010*	*$(2.87 \pm 0.36).10^8$*	*$(1.1 \pm 0.1).10^5$*	*0.77 ± 0.12*
PEO_{12}-*b*-$PDMS_{43}$-*b*-PEO_{12}						
	t°	**R_h (nm)**	**dn/dc**	**$\overline{M_n}$ (g/mol)**	**N_{agg}**	**$\bar{A}$ (nm^2)**
	25°C	60.4	0.0866	$2.39.10^8$	$5.0.10^4$	0.92
			0.112	$1.72.10^8$	$3.6.10^4$	1.28
Average	*25°C*	*60.4*	*0.099 ± 0.017*	*$(2.06 \pm 0.47).10^8$*	*$(4.3 \pm 0.9).10^4$*	*1.1 ± 0.2*
	50°C	70	0.1137	$2.13.10^8$	$4.4.10^4$	1.39
			0.1200	$1.76.10^8$	$3.7.10^4$	1.68

			0.0980	$2.64.10^8$	$5.5.\ 10^4$	1.12
Average	*50°C*	*70*	*0.109 ± 0.010*	*$(2.18 \pm 0.36).10^8$*	*$(4.5 \pm 0.8).10^4$*	*1.40 ± 0.23*
PEO_{17}-*b*-$PDMS_{67}$-*b*-PEO_{17}						
	25°C	51.5	0.085	$1.45.10^8$	$1.8.10^4$	1.81
			0.080	$1.69.10^8$	$2.2.\ 10^4$	1.55
Average	25°C	51.5	0.082 ±0.003	*$(1.57 \pm 0.17).10^8$*	*$(2.0 \pm 0.2).10^4$*	*1.68 ± 0.18*
$PDMS_{26}$-*g*-$(PEO_{12})_2$						
	25°C	56.4	0.0979	$7.48.10^7$	$2.5.\ 10^4$	2.88

3.1.5. Conclusion

We have successfully synthesized three triblock copolymers based on the same chemical nature and in different molar masses: PEO_8-*b*-$PDMS_{22}$-*b*-PEO_8, PEO_{12}-*b*-$PDMS_{43}$-*b*-PEO_{12} and PEO_{17}-*b*-$PDMS_{67}$-*b*-PEO_{17}. According to the characterization of their self-assemblies, PEO_8-*b*-$PDMS_{22}$-*b*-PEO_8 and PEO_{12}-*b*-$PDMS_{43}$-*b*-PEO_{12} organize into unilamellar vesicles in water with membrane thickness varying from 5.4 nm to 8.8 nm. As mentioned before, in the case of copolymer PEO_{17}-*b*-$PDMS_{67}$-*b*-PEO_{17}, around 20% of wormlike micelles were reported. This set of synthesized triblock copolymer along with the commercial grafted copolymer from Dow Corning, will help us to decipher the influence of molar mass (hydrophobic mismatch) and architecture effect (grafted and triblock forming vesicle with same membrane thickness) on the formation and membrane structuration of GHUV and LHUV.

3.2. TAGGING COPOLYMER WITH FLUORESCENT PROBES

3.2.1. Objective and synthetic strategy

This section aims to describe the synthesis of the fluorescently labelled amphiphilic copolymer which are necessary for the fluorescence methodologies used within this thesis (confocal imaging, FRAP, FLIM, FRET). Similar to lipid probes, these fluorescent polymer analogues are tools to estimate the organization and dynamics of polymer molecules in hybrid polymer/lipid membranes. We decided to use two different polymer probes. One was the commercial grafted $PDMS_{26}$-*g*-$(PEO_{12})_2$ chemically modified with fluorescein and was already available in the lab. This copolymer was used for imaging, FLIM and FRAP experiments. The same copolymer was chemically modified with nitrobenzoxadiazole (NBD) in the framework of this thesis and used for FRET experiments. The amphiphilic copolymer

$PDMS_{26}$-*g*-$(PEO_{12})_2$ possesses hydroxyl groups at the end of the PEO chains from which a conjugation process can be performed. NBD and fluorescein were chosen since they present the suitable properties for both spectroscopic measurements and observation under epifluorescence or confocal microscopy. Particularly, both NBD and fluorescein, in association with Rhodamine B are good FRET pairs as their emission spectra do overlap with absorption spectrum of Rhod, as described in Chapter 2.

The chemical modification of the copolymer by the fluorescent probe is once again based on the coupling chemistry of NHS and primary amine as introduced in previous section. In this case, NHS ester derivative is the NHS functionalized probe and the primary amine is the amine end groups on copolymer molecules.

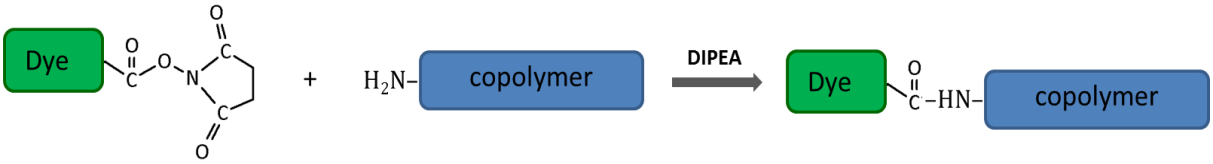

Figure 3.12. Tagging copolymer with fluorescent probe *via* coupling reaction between NHS functionalized fluorescent probe and primary amine functionalized copolymer.

The hydroxyl group of the PEO chains were first converted into amine groups. This was realized by converting the alcohols to sulfonates groups which are very good leaving groups and can further react with nucleophiles. For this step, we used mesyl chloride (MsCl) in presence of a weak base (triethylamine) to neutralize the HCl generated. Schema of this step is displayed in Figure 3.13.

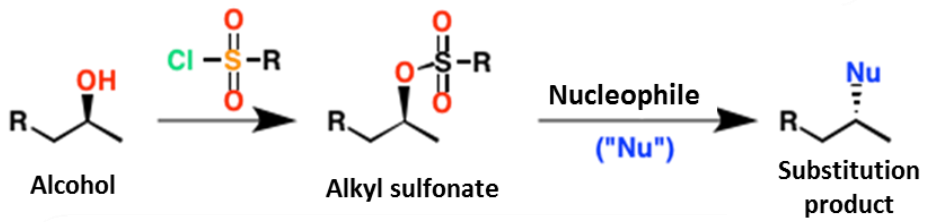

Figure 3.13. Converting of alcohols to good leaving group sulfonate which can react further with nucleophile.

Then, amination was performed using ammonium hydroxide to obtain the amino functionalized copolymer which can be therefore chemically modified with NHS-NBD. The

overall synthetic pathway applied to generate NBD-tagged copolymer is depicted in Figure 3.14.

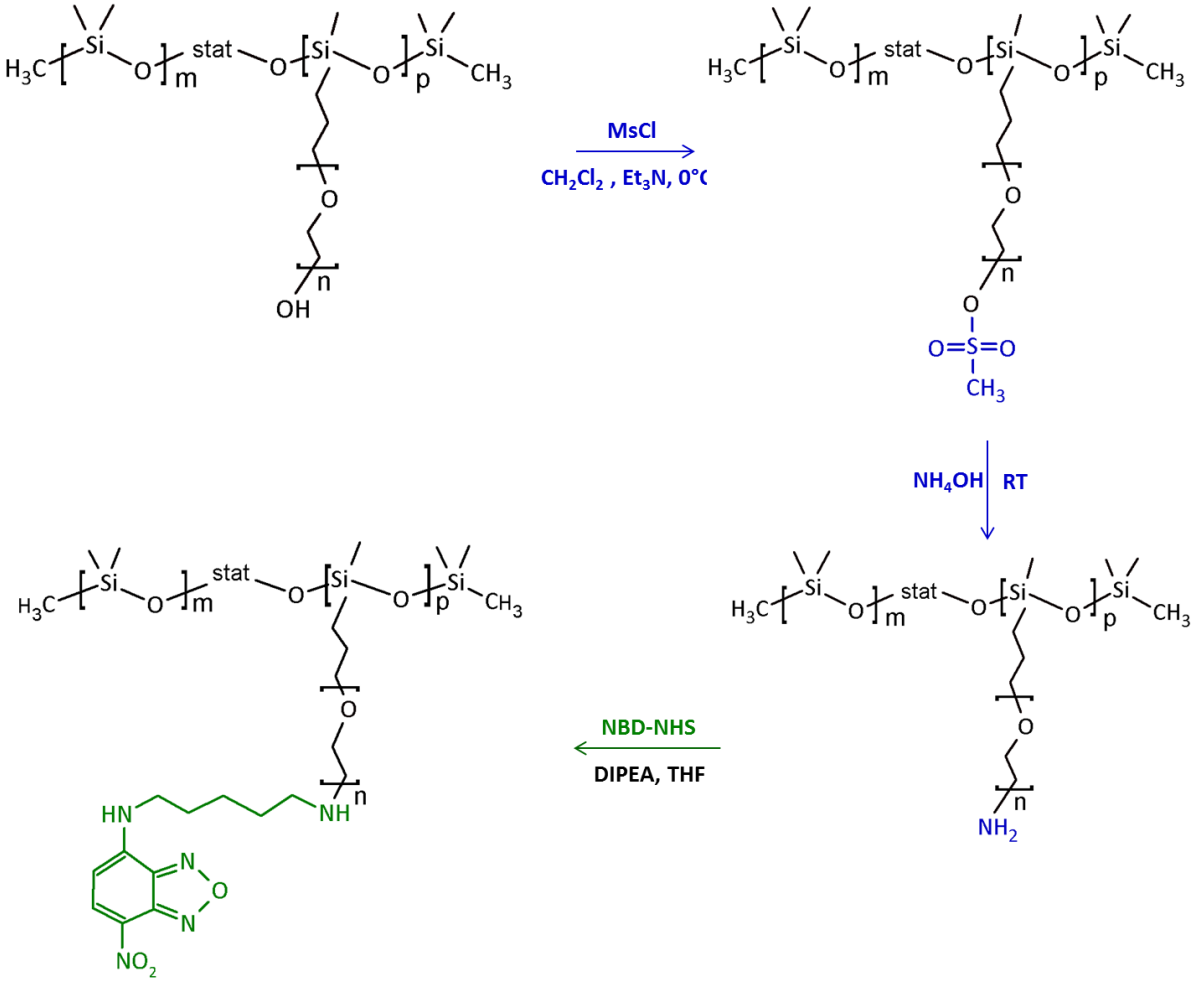

Figure 3.14. Synthetic pathway applied to generate NBD labelled copolymer $PDMS_{26}$-*g*-$(PEO_{12})_2$.

3.2.2. Experimental procedure

i) Mesylation of hydroxyl end group in $PDMS_{26}$-*g*-$(PEO_{12})_2$ copolymer

1g of $PDMS_{26}$-*g*-$(PEO_{12})_2$ corresponding to $3.7.10^{-4}$ mol was dissolved in 20 mL of dichloromethane (DCM) and refrigerated at 0°C. Under magnetic stirring, triethylamine (2 molar equivalents per OH- group) was added immediately with MsCl (1.2 molar equivalents per OH- group). Reaction was run overnight, afterwards, solvent as well as MsCl in excess were removed under vacuum at 60°C.

ii) Amination of $PDMS_{26}$-*g*-$(PEO_{12})_2$ copolymer

A large amount of concentrated ammonia (28%) was added directly to the flask containing mesylated $PDMS_{26}$-*g*-$(PEO_{12})_2$. Reaction was run at room temperature during 5 days under

vigorous magnetic stirring. The crude product was purified by dialysis against water (membrane MWCO 25 kDa) and dried under vacuum. The final yield was 66.4% (w/w). Amine content was checked by non-aqueous titration using hydro bromic acid. Briefly, the polymer was dissolved in a mixture of chloroform/glacial acetic acid and one drop of crystal violet was used as colorimetric indicator. According to the titration, there was 1 amine group per copolymer chain.

iii) Coupling with amine-reactive fluorescent probe

Aminated copolymer was dissolved in THF at a concentration of 50 mg/ml. Subsequently, mixture of DIPEA (1 equivalent per amine groups) and NHS functionalized NBD (1.2 equivalents per amine group) were dissolved in THF and added to the reaction flask. The reaction was performed under gentle agitation during one day.

iv) Purification

Purification was performed first by dialysis using membrane MWCO 25 kDa against basic water (pH ~ 10) in order to facilitate the solubilisation of NBD in excess and therefore its removal. After 4 days, a slight yellow colour was still visible in the dialysis bath. The polymer was then dried under vacuum, re-suspended in basic water and purified using a Sephadex^{TM} G25 column. Finally, the product was lyophilized, giving a viscous orange product. The final yield was evaluated at 62% (w/w) regarding the initial amount of aminated copolymer $PDMS_{26}$-*g*-$(PEO_{12})_2$ used.

3.2.3. Molecular structure characterization

3.2.3.1. Proton nuclear magnetic resonance

The coupling efficiency was first monitored by ^{1}H NMR. Figure 3.15 shows the ^{1}H NMR spectra of copolymer before tagging, NHS fluorescent probe and the resulting tagged copolymer. The characteristic signal at 8.4 ppm of aromatic proton of NBD, is clearly visible on the polymer chain while the signal of proton of NHS group at 2.8 ppm has disappeared. These two information confirm the introduction of NBD onto polymer chain and the success of purification process. It is important to mention that the resulting product must be extremely well purified since the presence of free fluorophore can affect the interpretation of FRET experiment data. The absence of free NBD was checked also by Thin layer chromatography as shown in Annex A.3.4.

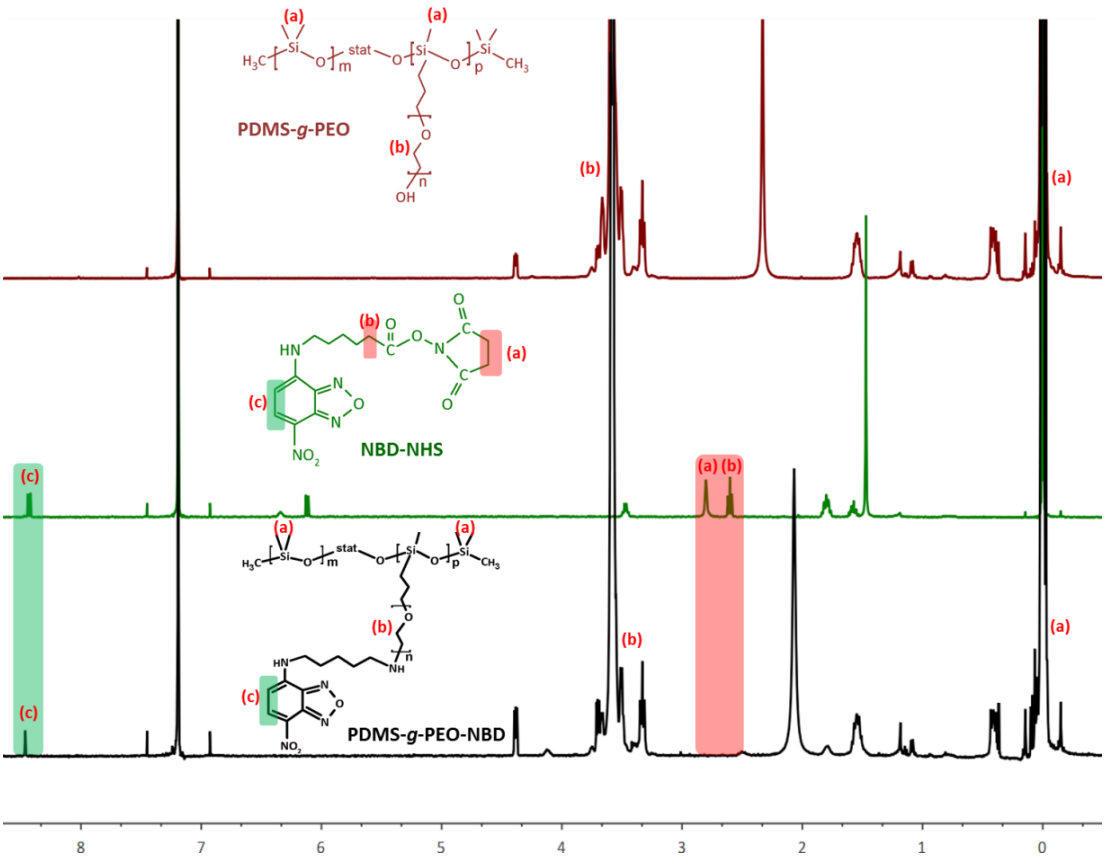

Figure 3.15. ^{1}H NMR of initial copolymer $PDMS_{26}$-*g*-$(PEO_{12})_2$; fluorescent probe NBD-NHS and resulting fluorescent tagged copolymer $PDMS_{26}$-*g*-$(PEO_{12})_2$-NBD.

3.2.3.2. Size exclusion chromatography

The average molar masses of tagged copolymer was investigated by SEC in THF using UV detector and calibration with polystyrene standards. The chromatogram is shown in Figure 3.16. Molar masses obtained are: M_n = 4065 g.mol^{-1}; M_w = 5846 g.mol$^{-1;}$ Đ = 1.43.

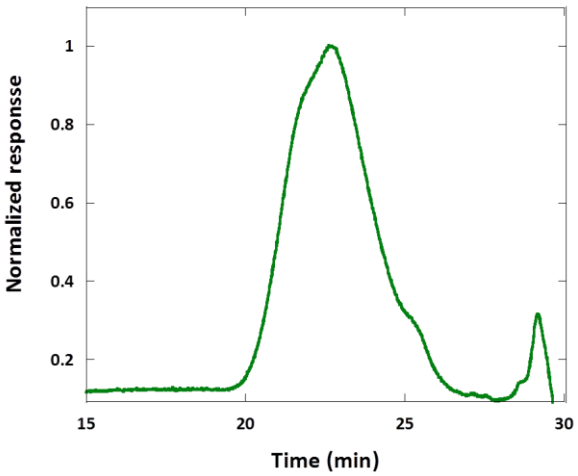

Figure 3.16. SEC chromatogram of $PDMS_{26}$-*g*-$(PEO_{12})_2$-NBD.

3.2.3.3. Spectrophotometric analysis

The fluorescence properties of the resulting products were verified *via* its absorption and fluorescence spectra as shown in Figure 3.17.

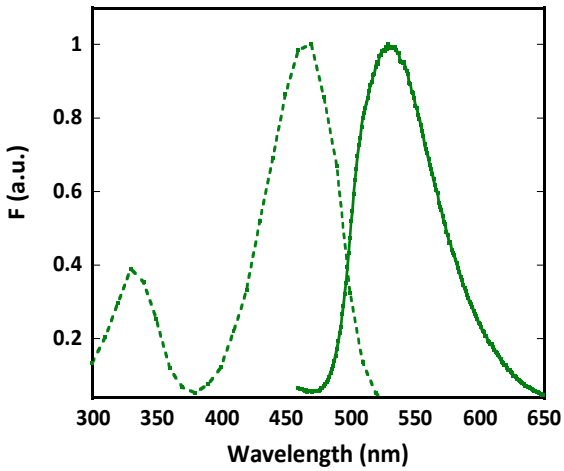

Figure 3.17. Absorption (dash) and fluorescence (solid) spectra of $PDMS_{26}$-*g*-$(PEO_{12})_2$-NBD.

The extent of modification by NBD was also quantified with the NBD absorption spectra. Briefly, we determined the NBD amount in a defined weight of product *via* a calibration curve prepared from a set of pure NBD-X solutions in methanol at various concentrations. All the details of spectra, calibration curve and calculation are given in Figure 3.18, 3.19 and Table 3.6. According to this quantification, each copolymer chain was modified by 0.65 NBD molecules on average.

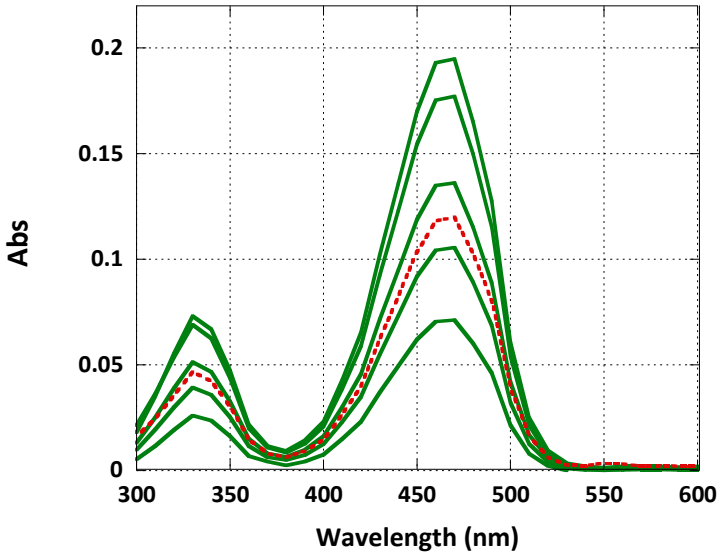

Figure 3.18. Absorption spectra recorded for a set of NBD-X solution at various concentrations (the green solid lines) and for a solution of product $PDMS_{26}$-*g*-$(PEO_{12})_2$-NBD (the red dash line). All solutions were prepared in methanol.

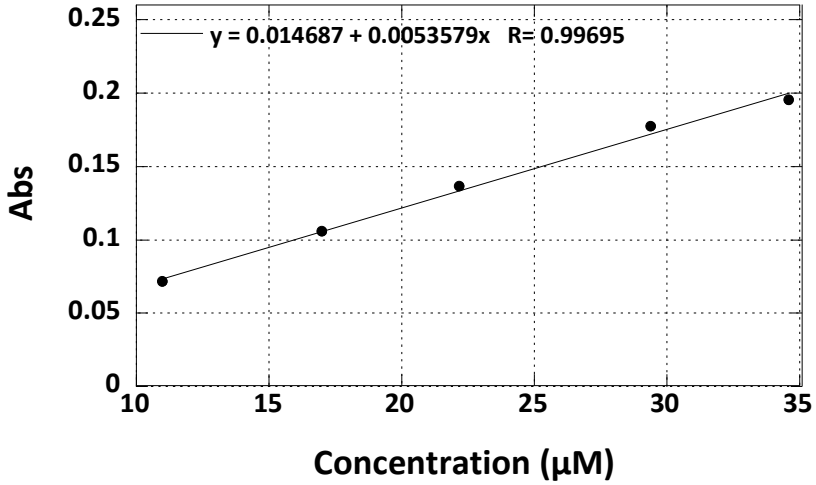

Figure 3.19. Calibration curve established with data from the spectra shown in Figure 3.18.

Table 3.6. Quantification of % NBD modification of product $PDMS_{26}$-*g*-$(PEO_{12})_2$-NBD.

Abs	C_{NBD} (µM)	$m_{polymer(mg)}$	$C_{polymer}$ (µM)	% modification
0.12	19.66 µM	2.07 mg	30.1 µM	65.3%

3.2.4. Conclusion

We have successfully labelled, purified and characterized the amphiphilic graft copolymer: $PDMS_{26}$-*g*-$(PEO_{12})_2$-NBD with 0.65 NBD molecules per chain. This copolymer will be thoroughly used as the donor probe in the Time-resolved Förster resonance energy transfer (TR-FRET) experiments. This copolymer will be inserted in the polymer phases (grafted or triblock copolymer) at low molar amount depending on the experiments.

ANNEX

A.3.1. ^{1}H NMR spectrum of commercial grafted copolymer PDMS$_{26}$-*g*-(PEO$_{12}$)$_2$

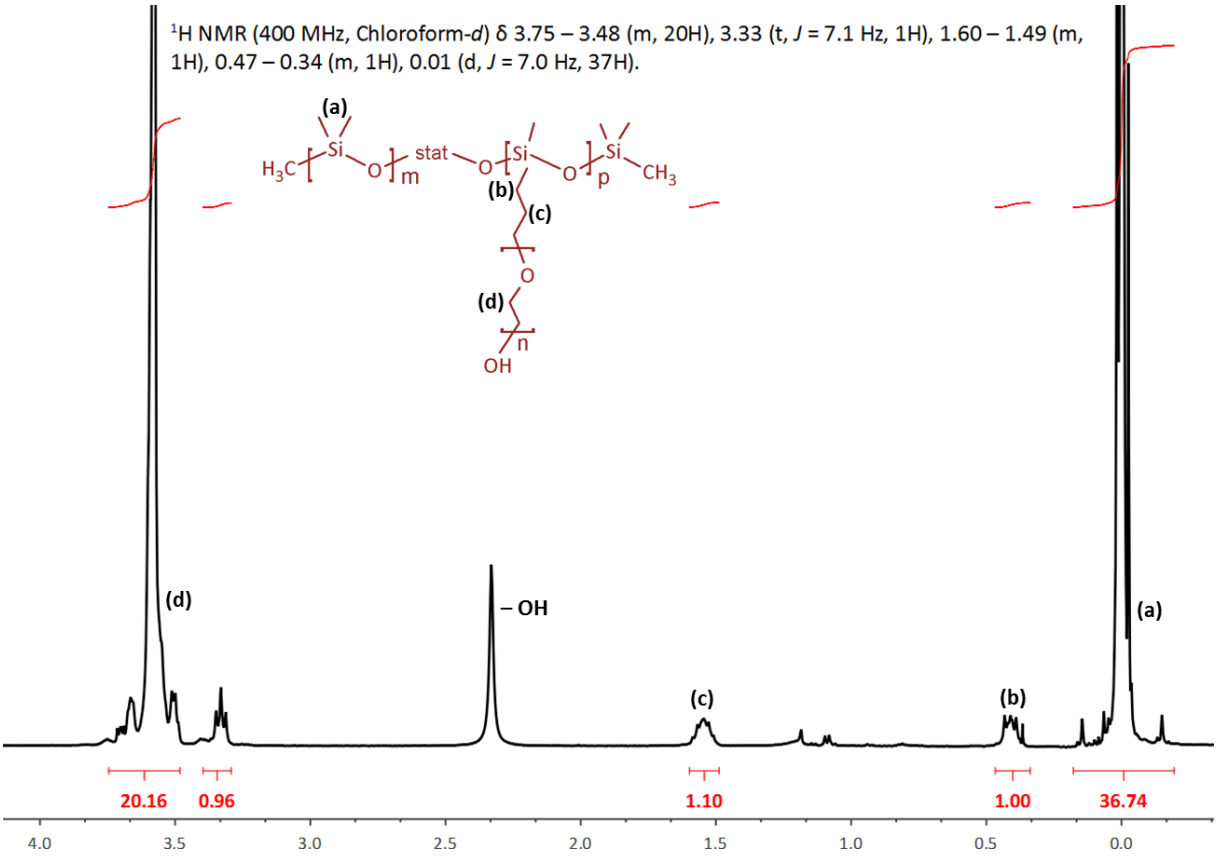

Figure A.3.1. ^{1}H NMR spectrum of PDMS$_{26}$-g-(PEO$_{12}$)$_2$ in $CDCl_3$.

A.3.2. Characterization of functionalized commercial homopolymers

Chain-end functionalization rate of α, ω-bisaminopropyl-terminated PDMS (H_2N-PDMS$_n$-NH_2) were verified by ^{1}H NMR using the integration ratio of the PDMS main chain signal (Si(C***H*****$_3$**)$_2$O, (6xDP$_{PDMS}$)H, δ = 0 ppm) and the proton from the carbon in α position of the amine groups (H_2NC***H*****$_2$**CH_2, 4H, δ = 2.6 ppm). According to molar mass given by manufacturer, it is almost 100% for all these PDMS reagents. The spectrum of H_2N-PDMS$_{43}$-NH_2 is detailed in Figure A.3.2 as an example.

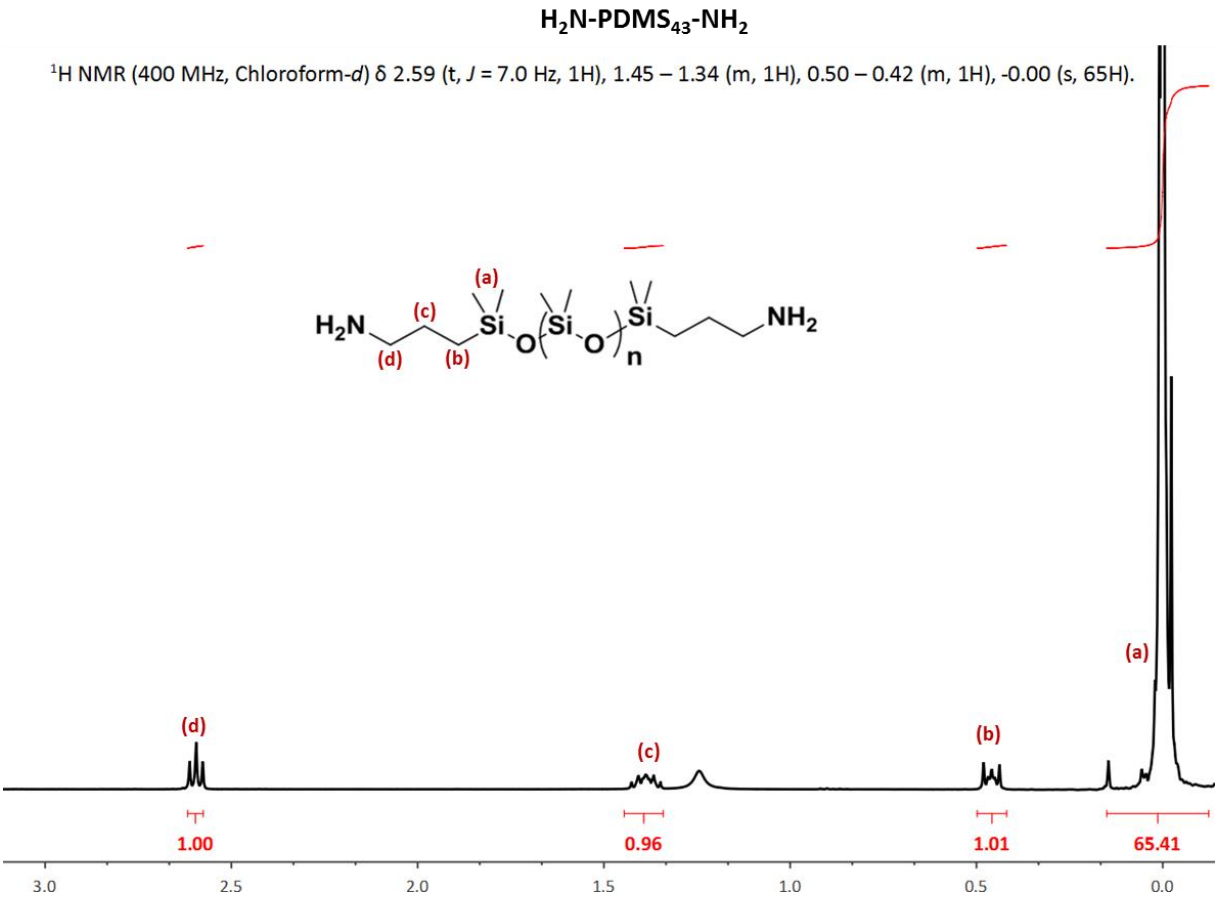

Figure A.3.2. ^{1}H NMR spectrum of commercial homopolymer H_2N-$PDMS_{43}$-NH_2 in $CDCl_3$.

Similarly, by ^{1}H NMR, chain-end functionalization rate of succinimidyl ester-functionalized PEO (PEO_m-NHS) was confirmed through the integration ratio of the methoxy group (C***H***$_3$O-PEO, 3H, δ = 3.3 ppm), the NHS group (C(O)C***H***$_2$C***H***$_2$C(O), 4H, δ = 2.8 ppm and PEO main chain signal (C***H***$_2$C***H***$_2$O, (4xDP_{PEO})H, δ = 3.6 ppm). Some spectra of PEO_m-NHS are shown in Figure A.3.3 as examples. It should be noted that PEO_4-NHS, PEO_8-NHS and PEO_{12}-NHS possess the same structure whereas PEO_{17}-NHS has structure slightly different as also seen in this Figure.

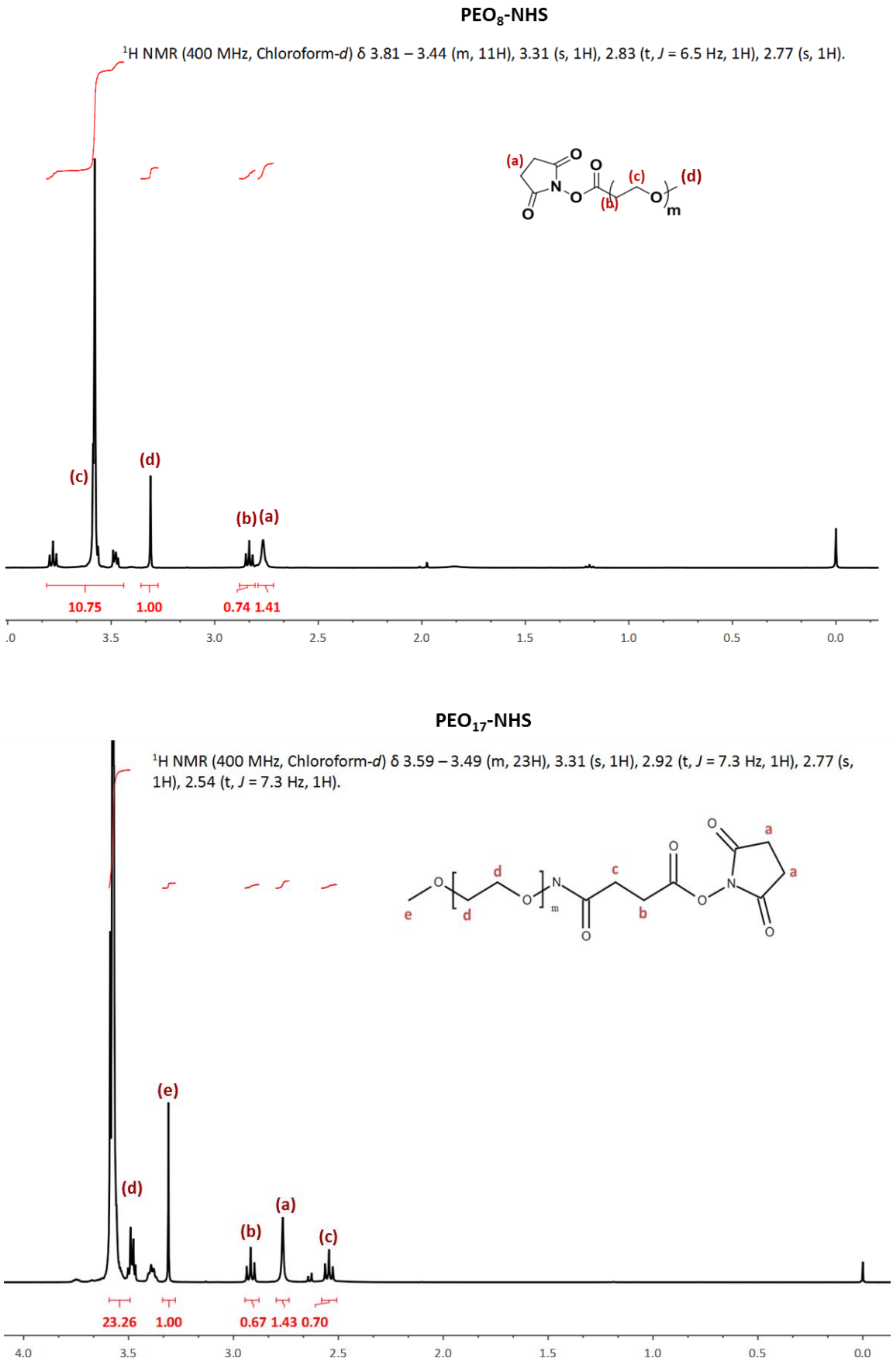

Figure A.3.3. ^{1}H NMR spectrum of commercial homopolymer PEO_m-NHS in $CDCl_3$.

A.3.3 Thin layer chromatography experiment

The absence of free NBD in obtained product was check by thin layer chromatography. As evidenced in Figure A.3.4, the signal of product (left) is large (because of high molecular weight of polymer molecule) and positioned obviously different with the pure NBD (right).

Figure A.3.4. Thin layer chromatography experiment: left: $PDMS_{26}$-*g*-$(PEO_{12})_2$-NBD and right: free NBD.

REFERENCES

1. Discher, D.E. and A. Eisenberg, *Polymer Vesicles.* Science, 2002. **297**(5583): p. 967-973.
2. Itel, F., et al., *Molecular organization and dynamics in polymersome membranes: A lateral diffusion study.* Macromolecules, 2014. **47**(21): p. 7588-7596.
3. Ruysschaert, T., et al., *Hybrid Nanocapsules: Interactions of ABA Block Copolymers with Liposomes.* Journal of the American Chemical Society, 2005. **127**(17): p. 6242-6247.
4. Chemin, M., et al., *Hybrid polymer/lipid vesicles: fine control of the lipid and polymer distribution in the binary membrane.* Soft Matter, 2012. **8**(10): p. 2867-2874.
5. Chen, D. and M.M. Santore, *Hybrid copolymer-phospholipid vesicles: phase separation resembling mixed phospholipid lamellae, but with mechanical stability and control.* Soft Matter, 2015. **11**(13): p. 2617-2626.
6. Schulz, M., et al., *Hybrid lipid/polymer giant unilamellar vesicles: effects of incorporated biocompatible PIB-PEO block copolymers on vesicle properties.* Soft Matter, 2011. **7**(18): p. 8100-8110.
7. Olubummo, A., et al., *Controlling the Localization of Polymer-Functionalized Nanoparticles in Mixed Lipid/Polymer Membranes.* ACS Nano, 2012. **6**(10): p. 8713-8727.
8. Schulz, M., et al., *Controlling Molecular Recognition with Lipid/Polymer Domains in Vesicle Membranes.* Angewandte Chemie International Edition, 2013. **52**(6): p. 1829-1833.
9. Nam, J., P.A. Beales, and T.K. Vanderlick, *Giant Phospholipid/Block Copolymer Hybrid Vesicles: Mixing Behavior and Domain Formation.* Langmuir, 2011. **27**(1): p. 1-6.
10. Cheng, Z. and A. Tsourkas, *Paramagnetic Porous Polymersomes.* Langmuir, 2008. **24**(15): p. 8169-8173.
11. Nam, J., T.K. Vanderlick, and P.A. Beales, *Formation and dissolution of phospholipid domains with varying textures in hybrid lipo-polymersomes.* Soft Matter, 2012. **8**(30): p. 7982-7988.
12. Lim, S., et al., *Hybrid, Nanoscale Phospholipid/Block Copolymer Vesicles.* Polymers, 2013. **5**(3): p. 1102.
13. Hermanson, G.T., *Chapter 2 - The Chemistry of Reactive Groups*, in *Bioconjugate Techniques (Second Edition)*. 2008, Academic Press: New York. p. 169-212.
14. Carlsen, A., et al., *Block Copolymer Vesicle Permeability Measured by Osmotic Swelling and Shrinking.* Langmuir, 2011. **27**(8): p. 4884-4890.
15. Salva, R., et al., *Polymersome Shape Transformation at the Nanoscale.* ACS Nano, 2013. **7**(10): p. 9298-9311.

CHAPTER 4

PHASE SEPARATION IN LARGE HYBRID POLYMER/LIPID UNILAMELLAR VESICLES

Table of Contents

OUTLINE

This chapter is devoted to the formulation of Large Hybrid Unilamellar vesicles (LHUVs) and the thorough analysis of their membrane structuration. The different triblock copolymers whose synthesis and self-assembly have been described in Chapter 3, as well as the grafted copolymers based on PDMS and PEO, were associated with phospholipid and individually analysed to reveal the effect of hydrophobic mismatch and polymer architecture. DPPC was used as the phospholipid component and studies were performed below and above its main chain melting temperature (20°C and 47°C respectively), allowing the evaluation of the effect of phospholipid fluidity. For each mixture, different information about nanostructures in term of morphology, hybrid character and distribution of the components within the membrane were acquired through common techniques to study phase separation at the nanoscale in lipid LUVs: Small angle neutron scattering (SANS), Cryo-transmission electron microscopy (Cryo-TEM) and Time-resolved Förster resonance energy transfer (TR-FRET). The first part of the chapter (section 4.1) will focus on the formalism used to interpret experimental data of SANS and TR-FRET, then the results for each system will be described in section 4.2.

4.1. FORMALISM AND MODEL USED

4.1.1. Interpretation for small angle neutron scattering experiments

In order to interpret the scattered intensity curves of the various systems analysed in this work, different models were used. Besides the common form factors such as vesicles, disks or core-shell cylinders which have been reviewed [1] and for which fitting routines are available (SasView, http://www.sasview.org/), a new model based on the holey shell form factor introduced by Bergstrom et al [2] was developed in this work with the strong support of Annie Brulet (Ingénieur de recherche, CNRS, CEA-Saclay) to describe the scattering of phase separated polymer/lipid vesicles. This new model will be entitled “hybrid vesicle” form factor and is detailed in the following.

Hybrid vesicle form factor

None of the previously mentioned form factors (core-shell particles, multiple layers or single layer vesicles …) is suitable for (polymer) vesicles with (lipid) patches. So far in literature, a model of scattering by lipids vesicles with lateral heterogeneities in the membrane has been developed by using Monte Carlo modelling with a modified coarse-graining method [3]. This structural model approach is very powerful since it provides important qualitative information about lipid mixing. However, it is computationally expensive and time limiting since it does not lead to an analytical form factor for multi-domain vesicles. Therefore, in order to overcome this lack of analytical expressions, the same group utilized a spherical harmonic expansion of the vesicle form factor to obtain an analytical solution for the scattering from vesicles containing a single round domain [4]. Very recently, they extended their model with a general theory for scattering from laterally heterogeneous vesicles of arbitrary size and spatial configuration [5]. They obtained analytical expressions of the form factor and scattering intensity that they compared to corresponding Monte-Carlo calculations. While this approach is very promising, these expressions are not enough simplified and together with problems of sizes distributions and fitting routines methods to implement, it was not feasible to use them to fit our SANS data. Instead, we have developed a simplified approach to try to describe the scattering of hybrid vesicles of polymers with lipid domains, using only classical expressions of scattering amplitudes and form factors that can be easily processed with proven fitting methods. We derived a model recently proposed by Bergstrom et al [2] to describe mixtures of surfactants bilayers with salt creating holes

inside the bilayers. In this simplified model of perforated vesicles, several assumptions were made:

i) the vesicles were considered as infinitely thin circular shells with radius R of form factor:

$$P_\vartheta(q,R) = [F_\vartheta(q,R)]^2 = \left[\frac{\sin(qR)}{qR}\right]^2 \qquad \text{(Eq. 4.1)}$$

the holes being considered as symmetrical disks with radius R_h and amplitude:

$$F_h = \left(\frac{2\left[1-\frac{B_1(2qR_h)}{qR_h}\right]}{qR_h}\right)^{\frac{1}{2}} \qquad \text{(Eq. 4.2)}$$

where $B_1(x)$ is the Bessel function of the first order. The form factor of perforated bilayer vesicles was obtained by subtracting the contribution from the holes to the one of a bilayer vesicle with an appropriate weighting of the areas (equivalent to volume for infinitely thin vesicles), i.e.:

$$S_{per} = \left(\frac{A_{bil}F_{bil} - N_hA_hF_h}{A_{bil} - N_hA_h}\right)^2 \qquad \text{(Eq. 4.3)}$$

Where $A_h = \pi {R_h}^2$ is the area per hole; N_h is the number of holes and $A_{bil} = 4\pi {R_\vartheta}^2$ is the area of the infinitely thin bilayer vesicle.

Hybrid vesicles are slightly different from perforated vesicles since the holes filled with solvent in the vesicles are replaced by disk-like domains filled with lipids. In addition, we also wished to account for the different thicknesses of the polymer and of the lipid membranes. Therefore, we considered a model of hybrid vesicles composed of a bilayer polymer vesicle with bilayer "disks" of lipids as shown in Figure 4.1: a vesicle with inner radius R_ϑ and thickness δ_ϑ containing N_d disks of radius R_d and thickness δ_d.

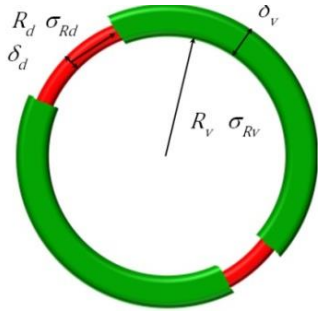

Figure 4.1. Scheme of the "hybrid vesicle" model: a vesicle with inner radius R_ϑ (distribution σ_{R_ϑ}) and thickness δ_ϑ, containing N_d disks of radius R_d (distributionσ_{R_d}) and thickness δ_d.

In order to account for the disk/vesicle thickness, we introduced the scattering amplitude of a bilayer cross-section [2] given by:

$$F_{b,\xi} = \frac{\sin q\xi}{q\xi} \qquad \text{(Eq. 4.4)}$$

Here **ξ** is half the bilayer thickness ($\xi = \frac{\delta}{2}$) and in our case of either the polymer or of the lipid membrane.

The analytical expression of the form factor employed is indicated in Eq.4.5:

$$S_{\text{hybrid vesicle}} = \left(\frac{(\rho_\vartheta - \rho_o)\, V_\vartheta\, F_{b,\delta_\vartheta}\, F_\vartheta\left(q, R_\vartheta + \frac{\delta_\vartheta}{2}\right) - (\rho_\vartheta - \rho_o) N_d \left(\pi {R_d}^2 \delta_\vartheta\, F_{b,\delta_\vartheta}\, F_{h,R_d}\right) + (\rho_d - \rho_o)\, N_d\, V_d\, F_{b,\delta_d}\, F_{h,R_d}}{V_\vartheta - N_d \left(\pi R_d^2\, \delta_d\right) + N_d\, V_d} \right)^2$$

(Eq. 4.5)

where ρ_ϑ, ρ_d, ρ_O are the neutron scattering length densities of the vesicle (polymer), of disks (lipid) and of the solvent. δ_ϑ and δ_d correspond respectively to the membrane thickness of polymer vesicle and of the lipid disks. $F_\vartheta(q,\ R_\vartheta + \delta_\vartheta/2)$ is the scattering amplitude of an infinitely thin circular shell with radius $R_\vartheta + \frac{\delta_\vartheta}{2}$ (Eq.4.1). F_{h,R_d} is the scattering amplitude of symmetrical circles with radius R_d (Eq.4.2); F_{b,δ_ϑ}(respectively F_{b,δ_d}) is the scattering amplitude of a bilayer cross-section of thickness δ_ϑ (respectively δ_d) (Eq.4.4). V_d is the volume of one disk geometrically approximated by $V_d = \pi {R_d}^2 \delta_d$ and V_ϑ is the volume of a vesicle membrane geometrically approximated by $V_\vartheta = 4\pi(R_\vartheta + \delta_\vartheta/2)^2 \delta_\vartheta$.

As in Bergström et al [2], we subtracted the scattering amplitude of N_d disks of thickness δ_ϑ but in order to account for the scattering of full disks instead of holes, we have added a contribution of disks of thickness δ_d, with their own scattering length density ρ_d. For all these contributions, the thicknesses have been taken into account according to Eq.4.4. Moreover, the scattering amplitudes of the different contributions were weighted by the corresponding volumes, instead of the areas in the work of Bergström et al.

As a result, the "hybrid vesicle" model has several parameters: R_ϑ, δ_ϑ, R_d, δ_d and possibly a (log-normal) distribution for each of these parameters, as well as the number of disks N_d. The scattering length densities ρ_ϑ, ρ_d can also be different from the ones of the pure compounds if we assume that a phase separation between lipids and polymers occurs within

the vesicle membrane. Finally, for polydisperse hybrid vesicles, this model has eleven fit parameters. Considering our recorded data, up to a *q* value about 0.12 $Å^{-1}$ where the scattering generally reaches the incoherent background, the number of data points N ≈ 150. Therefore, in order to reasonably describe the main tendencies governing the phase separation occurring in our systems, we reduced the number of fit parameters by using the following assumptions: the scattering length densities are those of pure compounds, the bilayer thickness of polymers and of lipids (δ_ϑ, δ_d) are fixed to the values measured for the pure compound vesicles. No size distribution is used for these two parameters since the fitted distributions obtained on pure compounds are weak (0.12-0.18 assuming a log-normal distribution) and accounting for the *q* resolution of SANS experiments, they will affect the scattering curves at very large *q* values, not very informative here. Thus, five parameters only allow us to describe the phase separation occurring in the hybrid vesicles: those are R_ϑ, σ_{R_ϑ}, N_d, R_d, σ_{R_d}.

Data fitting was performed by writing a Matlab® function according to Eq.4.5 and using Matlab® methods for nonlinear least square curve-fit. Throughout all the fits with Matlab® and SasView programs, corrections were made for instrumental smearing [6, 7].

4.1.2. Förster resonance energy transfer experiments: model and formalism

4.1.2.1. Determination of partition coefficient of donor and acceptor probes

One of important parameters to interpret the FRET data is the partition coefficient (K_P) of both donor and acceptor probes between coexisting phases at the hybrid membranes. Those values were determined spectroscopically through changes in either fluorescence intensity or anisotropy depending on which was most sensitive to the environmental differences between polymer and lipid phases. Temperature used in each study was chosen to maintain the lipid phase in the liquid disordered state, thus 46°C for samples containing DPPC and 25°C for samples containing POPC.

Partition coefficient of donor $PDMS_{26}$-g-$(PEO_{12})_2$-NBD in polymer/lipid mixtures

The partition coefficient of the donor $PDMS_{26}$-*g*-$(PEO_{12})_2$-NBD was determined from the differences in $PDMS_{26}$-*g*-$(PEO_{12})_2$-NBD fluorescence anisotropy in each phase, respectively lipid and copolymer. The values $K_{P_{polymer/lipid}}$ are recovered from the fit of Eq.4.6:

$$< r >= \frac{< r >_{polymer} . F_{polymer} . K_{P_{polymer/lipid}} + \frac{\Phi_{lipid}}{\Phi_{polymer}} < r >_{lipid} . F_{lipid}}{F_{polymer} . K_{P_{polymer/lipid}} + \frac{\Phi_{lipid}}{\Phi_{polymer}} F_{lipid}} \quad \text{(Eq. 4.6)}$$

Here $< r >$ is the experimental fluorescence anisotropy; $< r >_{polymer}$ and $< r >_{lipid}$ are the fluorescence anisotropies in the polymer-rich and lipid-rich phases respectively; $\frac{\Phi_{lipid}}{\Phi_{polymer}}$ is the ratio of quantum yield of $PDMS_{26}$-*g*-$(PEO_{12})_2$–NBD in 100% lipid and 100% polymer.

The dependence of $PDMS_{26}$-*g*-$(PEO_{12})_2$-NBD fluorescence anisotropy with polymer content for mixtures of PEO_8-*b*-$PDMS_{22}$-*b*-PEO_8 with either POPC or DPPC is shown in Fig. 4.2.

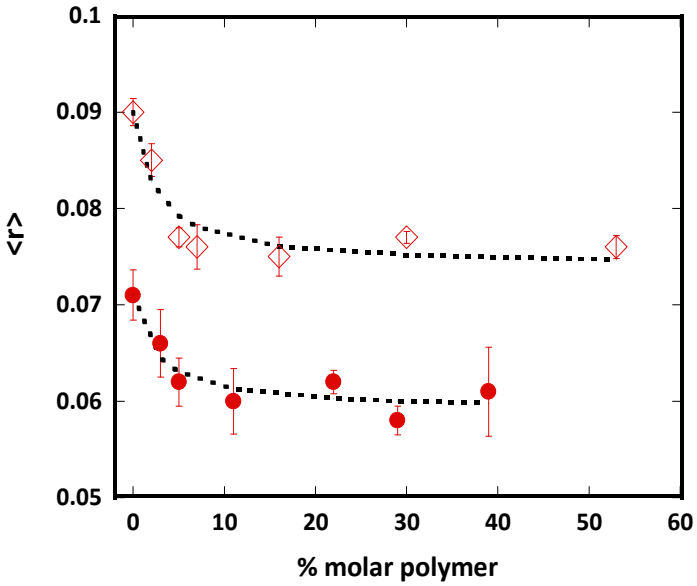

Figure 4.2. Fluorescence anisotropy of $PDMS_{26}$-*g*-$(PEO_{12})_2$-NBD in mixtures of PEO_8-*b*-$PDMS_{22}$-*b*-PEO_8/DPPC (●) and PEO_8-*b*-$PDMS_{22}$-*b*-PEO_8/POPC (◊) at 46°C; the curves correspond to the fit of the data with Eq.4.6.

The shape of the curves is strongly indicative of a drastic preference of $PDMS_{26}$-*g*-$(PEO_{12})_2$-NBD for partition to of PEO_8-*b*-$PDMS_{22}$-*b*-PEO_8-enriched phase, independently of the lipid chosen. Given this result and for estimation of the partition coefficient, the fraction of polymer-rich phase can be anticipated to correspond approximately to the polymer content. Table 4.1 lists all recovered K_P values of the different polymer/lipid mixtures. The fraction of $PDMS_{26}$-*g*-$(PEO_{12})_2$-NBD in the polymer phase for the equimolar mixture is about 98-99 % for all of the studied polymer/lipid systems, so, we can conclude that the polymer fluorescent probe $PDMS_{26}$-*g*-$(PEO_{12})_2$-NBD does not incorporate into the lipid phase. The low solubility of labelled $PDMS_{26}$-*g*-$(PEO_{12})_2$ in lipid-rich phases is corroborated for this and for other copolymers by imaging of $PDMS_{26}$-*g*-$(PEO_{12})_2$-FITC in giant hybrid vesicles showing phase coexistence (see Chapter 5).

Table 4.1. Molar partition coefficients of $PDMS_{26}$-*g*-$(PEO_{12})_2$–NBD in different polymer/lipid mixtures. Lipid was either DPPC or POPC. Measurements were carried out at 46°C for mixtures containing DPPC and at 25°C for mixtures containing POPC.

Mixture	$K_{P_{polymer/lipid}}$	
	Lipid DPPC	Lipid POPC
$PDMS_{26}$-*g*-$(PEO_{12})_2$/lipid	46.4	45.8
PEO_8-*b*-$PDMS_{22}$-*b*-PEO_8/lipid	41.3	42.0
PEO_{12}-*b*-$PDMS_{43}$-*b*-PEO_{12}/lipid	42.5	39.5

Partition coefficient of acceptor DOPE-Rhod in polymer/lipid mixtures

Considering the evidence for poor solubility of copolymer in lipid-rich membranes and phase separation, partition coefficients for the distribution of fluorescent phospholipid analogues between polymer-rich and lipid-rich phases can also be recovered using similar methodologies. The partition coefficient of DOPE-Rhod was determined from the differences in quantum yield of the labelled lipid in each phase. Figure 4.3 shows the fluorescence intensity of DOPE-Rhod in different PEO_8-*b*-$PDMS_{22}$-*b*-PEO_8/lipid, PEO_{12}-*b*-$PDMS_{43}$-*b*-PEO_{12}/lipid and $PDMS_{26}$-*g*-$(PEO_{12})_2$/lipid mixtures.

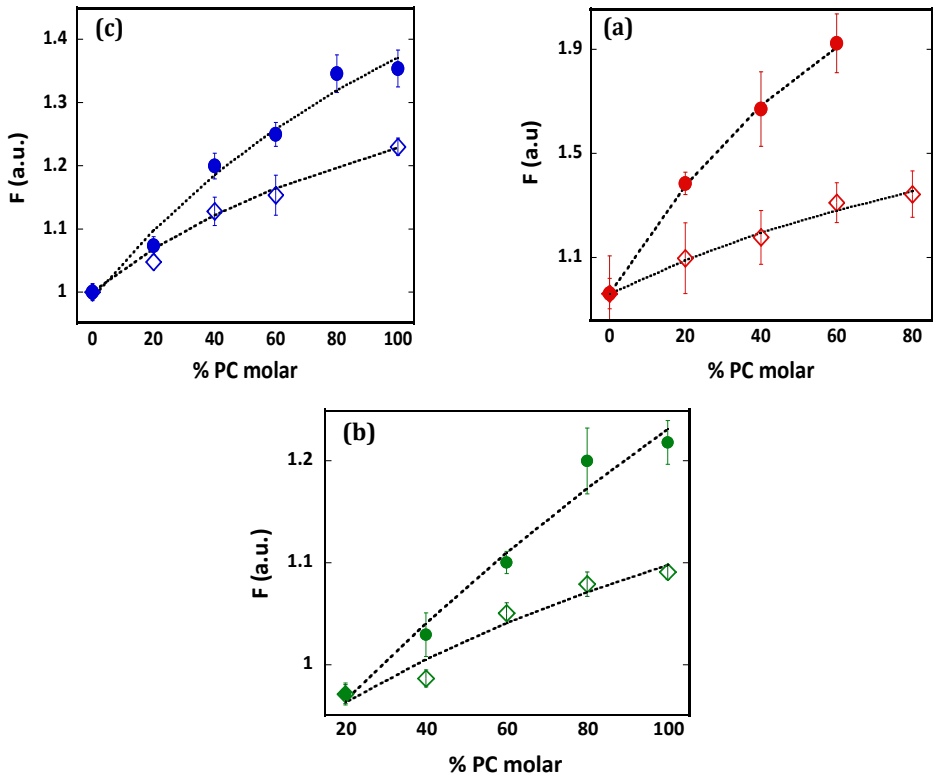

Figure 4.3. Fluorescence intensity of DOPE-Rhod in different mixtures: (a): $PDMS_{26}$-*g*-$(PEO_{12})_2$/DPPC (●) and $PDMS_{26}$-*g*-$(PEO_{12})_2$/POPC (◊); (b) PEO_8-*b*-$PDMS_{22}$-*b*-PEO_8/DPPC (●) and PEO_8-*b*-$PDMS_{22}$-*b*-PEO_8/POPC (◊); (c): PEO_{12}-*b*-$PDMS_{43}$-*b*-PEO_{12}/DPPC (●) and PEO_{12}-*b*-$PDMS_{43}$-*b*-PEO_{12}/POPC (◊); the curves correspond to the fit of the data with Eq.4.7. All recovered partition coefficients for each mixture are shown on Table 4.2.

For all of copolymers, with either POPC or DPPC-fluid state, the shapes of the curves are indicative of a preference of the labelled phospholipid for lipid-rich phases, as expected. The K_P values in molar for each copolymer/lipid mixture were then recovered from the fit of Eq.4.7 to the data:

$$I = \frac{I_{polymer} \cdot F_{polymer} \cdot K_{P_{polymer/lipid}} + I_{lipid} \cdot F_{lipid}}{F_{polymer} \cdot K_{P_{polymer/lipid}} + F_{lipid}} \qquad (Eq.\ 4.7)$$

Here I is the experimental fluorescence intensity; $I_{polymer}$ and I_{lipid} are the fluorescence intensity in the polymer-rich and lipid-rich phases respectively; $F_{polymer}$ and F_{lipid} are the molar fractions of polymer and lipid phases respectively. The quality of the fits was estimated with the coefficient of determination (R^2). Recovered values of $K_{P_{polymer/lipid}}$ for DOPE-Rhod in each system are summarized in Table 4.2.

Table 4.2. Molar partition coefficients of acceptor DOPE-Rhod in different polymer/lipid mixtures. Lipid was either DPPC or POPC. Measurements were carried out at 46°C for mixtures containing DPPC and at 25°C for mixtures containing POPC.

Mixture	$\mathbf{K_{P_{polymer/lipid}}}$	
	Lipid DPPC	**Lipid POPC**
$PDMS_{26}$-*g*-$(PEO_{12})_2$/lipid	0.64	0.59
PEO_8-*b*-$PDMS_{22}$-*b*-PEO_8/lipid	0.51	0.61
PEO_{12}-*b*-$PDMS_{43}$-*b*-PEO_{12}/lipid	0.79	0.66

The molar partition coefficient $K_{P_{polymer/lipid}}$ reflects the ratio of the probe in each membrane phase for an equimolar mixture. According to values shown in Table 4.2, we can conclude that the labelled lipid DOPE-Rhod partitions preferentially to the lipid phase and incorporates into the polymer phase to some extent. From those partition coefficient values, the fraction of DOPE-Rhod within the polymer phase can be quantified for each specific composition. In Table 4.3, we present the values calculated for mixtures at three lipid weight fractions: 15%, 21% and 30% as those fractions will be focused in this thesis.

Table 4.3. Fraction of acceptor within polymer phase for each specific polymer/lipid mixtures.

Mixtures	**% mass DPPC**		
	15%	**21%**	**30%**
$PDMS_{26}$-*g*-$(PEO_{12})_2$/DPPC	0.49	0.39	0.28
PEO_8-*b*-$PDMS_{22}$-*b*-PEO_8/DPPC	0.44	0.34	0.25
PEO_{12}-*b*-$PDMS_{43}$-*b*-PEO_{12}/DPPC	0.40	0.30	0.21

4.1.2.2. FRET model and formalism

Experimental FRET efficiencies were compared with simulated values of FRET from the following model and formalisms.

Theoretical FRET efficiency values in case of a homogeneous or near-homogeneous distribution of polymer and lipid (no phase separation or domains smaller than 5 nm (R_O of NBD-Rhod FRET pair), were obtained from the available analytical solutions to the problem of FRET between donor and acceptor molecules in a membrane environment [8, 9]. Given the large Förster radius (R_O) of the NBD-Rhod FRET pair, FRET occurs not only within the same leaflet but also between the donors and acceptors in opposing leaflets of the membrane. The FRET contribution from acceptors in different planes than the donor has to be considered and can be found from:

$$i_{DA}(t) = i_D(t)\rho_{FRET} \qquad \text{(Eq. 4.8)}$$

$$\rho_{FRET} = \exp\left\{-2\sigma_A \pi {l_1}^2 \int_0^1 \frac{1-\exp(-tb^3\alpha^6)}{\alpha^3} d\alpha\right\}.\exp\left\{-2\sigma_A \pi {l_2}^2 \int_0^1 \frac{1-\exp(-tb^3\alpha^6)}{\alpha^3} d\alpha\right\} \qquad \text{(Eq. 4.9)}$$

$$b = \left(\frac{{R_0}^2}{l}\right)^2 {\tau_D}^{1/3} \qquad \text{(Eq. 4.10)}$$

Where $i_{DA}(t)$ and $i_D(t)$ are the donor decays in the presence and absence of acceptor respectively. σ_A is the acceptor density, τ_D is the donor's lifetime and l_i are the distances between donor and acceptor planes. In case acceptor molecules are excluded from the immediate vicinity of the donor fluorophore by steric exclusion, an acceptor exclusion distance R_{exc} has to be considered and the integration in Eq.4.9 is carried out only up to $\frac{l}{\sqrt{l^2+R^2}}$ (Figure 4.4).

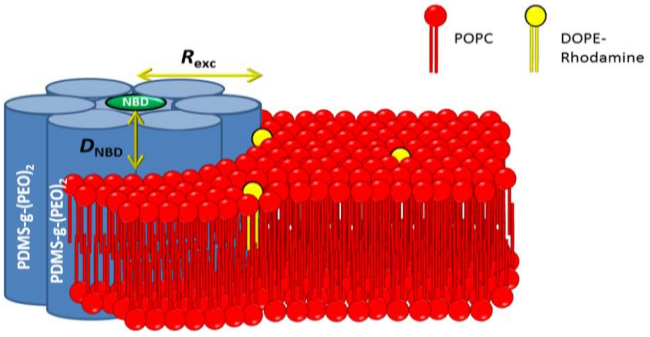

Figure 4.4. Scheme illustrating polymer-lipid segregation in the membrane and characteristic lengths considered in the FRET analysis.

The distribution of DOPE-Rhod (FRET acceptor) is known to be homogeneous in fluid P-rich phases [10] and the position of the Rhodamine fluorophore in the bilayer surface is also well characterized [11]. The uncertainty in molecular areas of polymer as presented in chapter 3 propagates to the acceptor densities in the membrane and therefore to the expected FRET efficiencies. This uncertainty will be taken into account when interpreting data.

Since the molecular area of the lipid is well-know, the only undefined variable in this calculation is the average inter-planar distance of NBD to the closest Rhodamine plane (D_{NBD}). This value was estimated from FRET measurements of $PDMS_{26}$-*g*-$(PEO_{12})_2$)-NBD chains dispersed at a very low fraction in POPC liposomes (1% molar) in the presence of DOPE-Rhod (0.5% molar). The experimental FRET efficiency for $PDMS_{26}$-*g*-$(PEO_{12})_2$)-NBD/POPC/DOPE-Rhod (1/98.5/0.5 mol/mol/mol) is 52% and simulated FRET efficiency in this system for different values of D_{NBD} and R_{exc} are shown in Figure 4.5. It has to be noted that we also assume that the NBD molecule is centered in the PDMS-*g*-$(PEO)_2$ aggregate (axial symmetry, Figure 4.4) and that there is no energy migration (homotransfer within PDMS-*g*-$(PEO)_2$-NBD molecules).

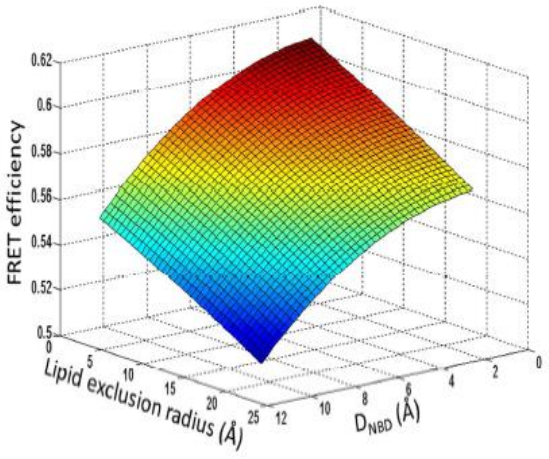

Figure 4.5. Simulation of FRET efficiency for different lipid exclusion radius and D_{NBD}, defined on Figure 4.4 for POPC liposomes labelled with 0.5% molar DOPE-Rhod and in the presence of only 1% molar of $PDMS_{26}$-*g*-$(PEO_{12})_2$)-NBD.

Comparison of the experimental FRET value (*E* = 52%) and results obtained from simulations, indicates that both a significant D_{NBD} value (~ 10 Å) and a R_{exc} ~ 18 Å must be present in this system. A significant D_{NBD} value implies that the NBD moiety is mostly found away from the bilayer surface in a somewhat exposed position (the NBD molecules are grafted on the PEO chains). This result is supported by the value of the wavelength of maximum emission in

these liposomes (λ_{max} = 530 nm) which is typical of a more polar environment than the one at the membrane surface. This is evidenced from the comparison with the fluorescence emission spectra of a NBD-labelled phospholipid (DPPE-NBD) and a NBD-labelled bile acid (DCA-NBD) (Figure 4.6). They exhibit a superficial location in the lipid bilayer but display a more blue-shifted fluorescence emission, as expected from a less solvent-exposed fluorophore [12, 13].

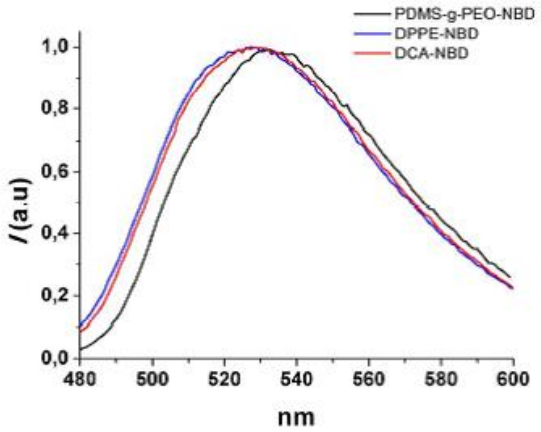

Figure 4.6. $PDMS_{26}$-*g*-$(PEO_{12})_2$)-NBD fluorescence spectra in POPC; the fluorescence emission spectra of $PDMS_{26}$-*g*-$(PEO_{12})_2$)-NBD in a $PDMS_{26}$-*g*-$(PEO_{12})_2$)-NBD/POPC 1/99 (mol/mol) mixture was obtained at 25°C. Wavelength of excitation was 460 nm. The fluorescence emission spectra of NBD labelled phospholipid (DPPE-NBD) and bile acid (DCA-NBD) obtained in POPC liposomes in the same conditions are shown for comparison.

The minimum acceptor exclusion radius for this system (absence of PDMS-*g*-$(PEO)_2$ aggregation) is approximately the sum of the axial radius of PDMS-PEO and of Rhod-PE. Since the molecular superficial area of PDMS-*g*-$(PEO)_2$ is 288 $Å^2$ (Table 3.5, Chapter 3), its axial radius is approximately 9.9 Å, while that of the lipid (POPC) is 4.9 Å. As the summation of these values (14.8 Å) is below the apparent R_{exc} of 18Å, the results are consistent with PDMS-*g*-$(PEO)_2$ aggregation (*i.e.* phase separation), even at 1% molar fraction, which is in agreement with the very high partition coefficient of PDMS-*g*-$(PEO)_2$-NBD (99% in the polymer phase). In brief, for the simulations of all systems presented in this work, the D_{NBD} was generally set to 10 Å.

The case of infinite phase separation (phase separation into domains larger than 5 – 10 times of R_O, hence, 25 – 50 nm and FRET becomes insensitive to further increases in domains size) was also considered. The theoretical FRET efficiency value in this case is defined with the concentration of acceptor-Rhod within the polymer-enriched phase and this value can be determined from the partition coefficients of DOPE-Rhod as shown in Table 4.2.

4.2. EXPERIMENTAL RESULTS

In the following, we will present the results for the different triblock copolymer synthesised, which form vesicles, starting with the triblock forming membrane with a thickness close to those of liposomes (5nm). Then, results obtained for copolymers forming thicker membrane will be described. Finally, the effect of architecture of the copolymer will be evaluated by the study of hybrid structures obtained with grafted PDMS-*g*-PEO and lipid. Three lipid weight fractions: 15%, 21% and 30% were analysed with different techniques: SANS, cryo-TEM and TR-FRET. Globally the aim of this chapter is to evaluate the effect of hydrophobic mismatch tuned by the molar mass of the copolymer, polymer architecture and lipid fluidity on the extent of mixing (hybrid character of the vesicles), morphology and phase separation in these hybrid vesicles.

4.2.1. Results for PEO_8-*b*-$PDMS_{22}$-*b*-PEO_8/lipid LHUVs

4.2.1.1. Small angle neutron scattering measurements

For each studied lipid fraction, in order to separate the contribution to the scattering of the lipid and of the copolymer components, different D_2O/H_2O mixtures were used according to contrast matching method. Briefly, based on the scattering length densities as listed in Table 4.4, the 9% v/v D_2O/H_2O mixture, 81% v/v D_2O/H_2O mixture and 100% D_2O were used to detect respectively lipid phases, polymer phases or both.

Table 4.4. Scattering length density (ρ) of sample components calculated with the molecular volume indicated *Ref [14]

	Density d ($g.cm^{-3}$)	**Scattering length density ρ (10^{10} cm^{-2})**	**Molecular volume* ($Å^3$)**
PDMS	0.965	0.064	127.4
DPPC-d_{62} 20°C	1.154	5.840	1144
DPPC-d_{62} 50°C	1.072	5.420	1232
H_2O	1.000	-0.560	2.99
D_2O	1.107	6.400	2.99
D_2O/H_2O 9% v/v	1.010	0.066	2.99
D_2O/H_2O 81% v/v	1.080	5.030	2.99

General features of scattering curves.

At first, Figure 4.7 shows typical curves obtained for PEO_8-*b*-$PDMS_{22}$-*b*-PEO_8/DPPC-d_{62} mixture in all three contrast conditions at 20°C. Obviously, all of the curves display the q^{-2} scaling law over intermediate q wave vector, characteristic of vesicular structure. Polymer and full contrast give almost similar curves, slightly higher for full contrast due to moderate amount of DPPC-d62 and scattering length density close to the one of D_2O.

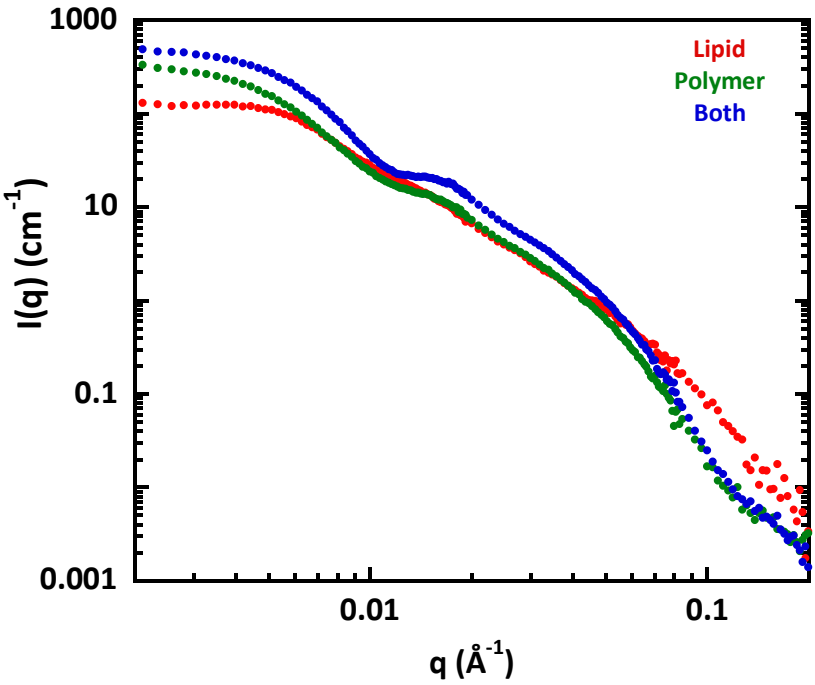

Figure 4.7. SANS curves recorded at 20°C for PEO_8-*b*-$PDMS_{22}$-*b*-PEO_8/DPPC-d_{62} mixture with lipid weight fraction f_d = 0.15 in different contrast conditions: lipid contrast (●), polymer contrast (●) and full contrast (●). In this figure, the incoherent signal at high q has been subtracted.

As clearly seen in Figure 4.8-b, upon temperature increase from 20°C to 47°C, the curve in lipid contrast is significantly changed, while the effects on the curves in polymer contrast is less pronounced although clearly present. Concretely, differences are visible at low q, in the Guinier regime and in the intermediate *q* range where an oscillation is visible up to 5.10^{-2} $Å^{-1}$ (Figure 4.8-d). While the changes in lipid contrast when temperature increase are expected because of the change of lipid state from gel phase to fluid phase, the structural changes observed in polymer contrast are particularly interesting. Indeed, since the vesicular structures obtained from the copolymer are not sensitive to temperature (Figure 4.8-c), the alterations prove that polymers and lipids are somehow mixed within the vesicular structures. It is important to note that the changes observed in those mixtures are

completely reversible as the scattering curves at 25°C obtained before and after experiments at 47°C are completely superimposed whatever the contrast chosen. This reversibility confirms that the structures formed are stable enough to follow the local changes induced by the main chain melting transition of the lipid phase with temperature.

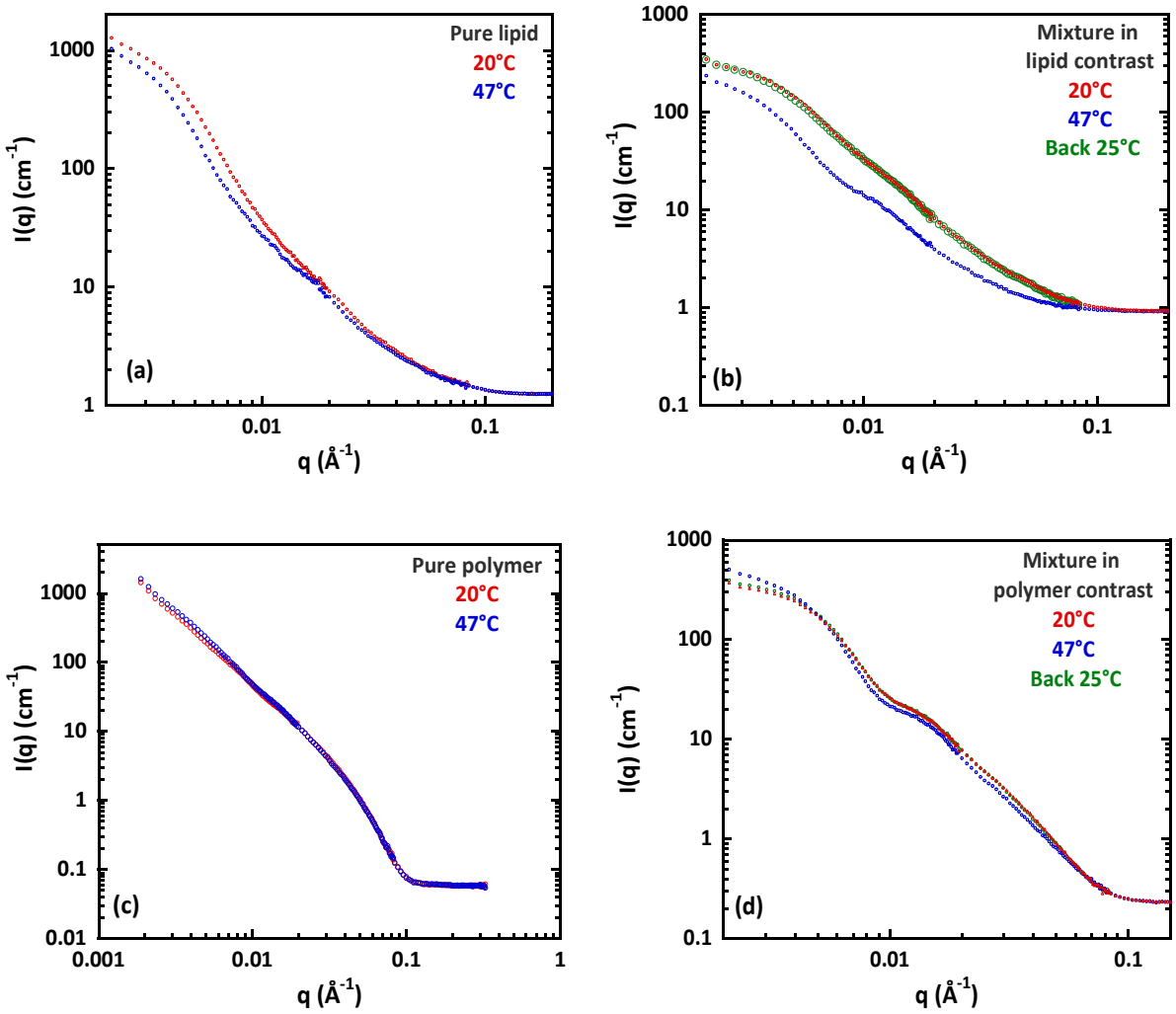

Figure 4.8. SANS curves recorded at different temperatures: 20°C (●), 47°C (●) and back to 25°C (●) for pure DPPC (a), pure PEO_8-*b*-$PDMS_{22}$-*b*-PEO_8 (c) and PEO_8-*b*-$PDMS_{22}$-*b*-PEO_8/DPPC-d_{62} mixture with lipid fraction f_d = 0.21 in both lipid contrast (b) and in polymer contrast (d).

Quantitative analysis of the data

At first, the new model of hybrid vesicles described above was used to fit the curves of samples in polymer contrast. In such case, lipid domains are accounted as holes. Best fits parameters are reported in Table 4.5 and the typical curves are presented in Figure 4.9. Generally, the fits work reasonably well with about 8 to 12 disks of lipids of 2 – 4 nm diameters but with very high dispersity σ_{R_d}. The size of vesicles obtained (R_ϑ) by this fitting

procedure is also low, presenting very high dispersity σ_{R_ϑ}. Taking into account this dispersity, the weight-average radius R_w which can be obtained from the radius of the fit R_o and the dispersion width ($R_w = R_o e^{7/2\sigma^2}$), becomes close to the radius of gyration R_g obtained *via* Guinier plot. Some Guinier plots are presented in annex A.4.3. However, such high dispersity does not allow detection of a possible effect of temperature or lipid fraction on the evolution of the number (N_d) or of the size (R_d) of the lipid domains.

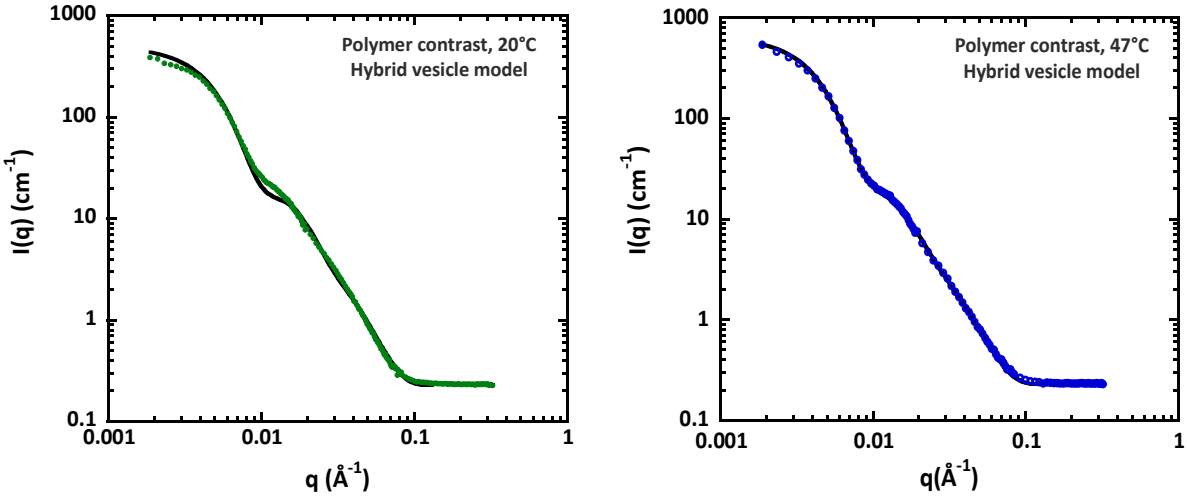

Figure 4.9. SANS curves obtained for mixture of PEO_8-*b*-$PDMS_{22}$-*b*-PEO_8/DPPC-d_{62} with lipid weight fraction f_d = 0.21 at 20°C, 47°C in polymer contrast. Solid lines are the best fits with hybrid vesicle model.

Table 4.5. Radius of gyration and best fit parameters with the hybrid vesicle model deduced from SANS curves of PEO_8-*b*-$PDMS_{22}$-*b*-PEO_8/DPPC-d_{62} mixtures at polymer contrast. (*: fixed parameters).

Lipid fraction f_d	T°C	Guinier	Hybrid vesicle model						
		R_g (nm)	R_ϑ (nm)	σ_{R_ϑ}	N_d	R_d (nm)	σ_{R_d}	δ_ϑ *	δ_d *
0.15	20°C	32.5	20.5	0.32	8.9	1.6	0.9	5.5	4.3
	47°C	36.5	23.7	0.32	12	1	0.1	5.5	3.2
0.21	20°C	33.5	22.0	0.32	7.9	1.9	0.9	5.5	4.3
	47°C	39.0	25.3	0.32	12	1.4	0.38	5.5	3.2
0.30	20°C	33.8	21.5	0.38	7.5	2.0	0.9	5.5	4.3
	47°C	35.8	25.6	0.34	12	1.4	0.28	5.5	3.2

In lipid contrast, the scattering curves were reasonably fitted with a vesicle form factor. The corresponding fit parameters are indicated in Table 4.6 and the typical curves are displayed in Figure 4.10. Again, vesicle radii are rather low with high dispersity, but as previously

mentioned, when taking into account size dispersity σ_{R_ϑ}, they are in good agreement with the radii of gyration obtained by a Guinier plot. Lipid membrane thickness interestingly is well-defined with a good precision (σ ~ 0.1 – 0.2) and decreases slightly with temperature in agreement with what is expected for DPPC membranes [14, 15]. However, values at both temperatures seems lower compared to values obtained for pure lipid vesicles (4.3/3.1 nm at 25°C/47°C – see annex A.4.1). This could be a sign of dispersion of lipids in polymer membranes.

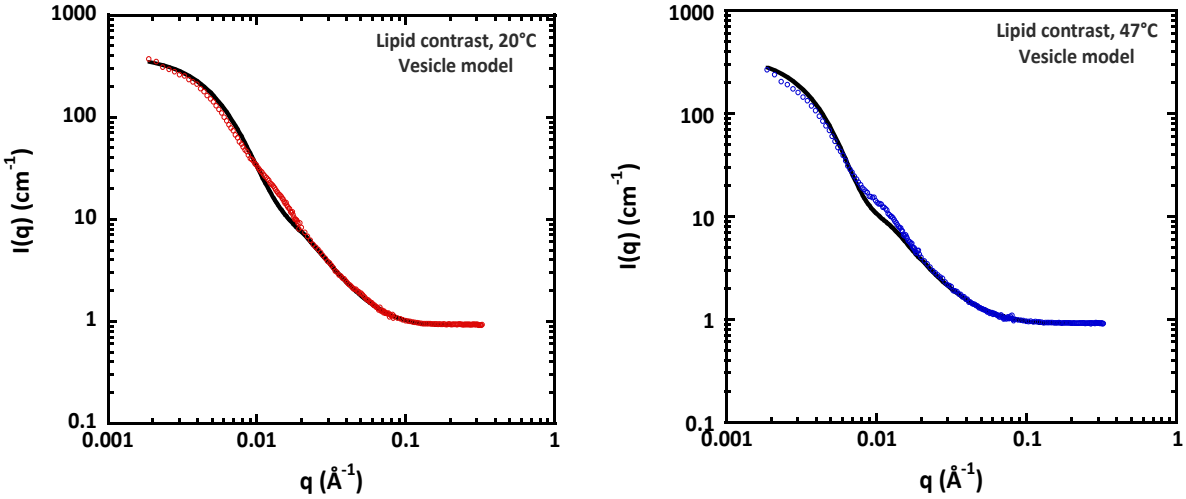

Figure 4.10. SANS curves obtained for mixture of PEO_8-*b*-$PDMS_{22}$-*b*-PEO_8/DPPC-d_{62} with lipid weight fraction f_d = 0.21 at 20°C, 47°C in lipid contrast. Solid lines are the best fits with vesicle model.

Table 4.6. Radius of gyration and best fit parameters with the vesicle model deduced from SANS curves of PEO_8-*b*-$PDMS_{22}$-*b*-PEO_8/DPPC-d_{62} mixtures at lipid contrast.

Lipid fraction f_d	T°C	Guinier	Vesicle model			
		R_g (nm)	R_ϑ (nm)	σ_{R_ϑ}	δ_ϑ (nm)	$\sigma_{\delta_\vartheta}$
0.15	20°C	31.9	Visible oscillation not fitted			
	47°C	36.4	Visible oscillation not fitted			
0.21	20°C	33.3	16	0.4	3.2	0.19
	47°C	41.6	28	0.33	3.0	0.11
0.30	20°C	-	-	-	3.5	0.16
	47°C	-	30	0.4	2.9	0.15

4.2.1.2. Cryo-TEM measurements

Generally, cryo-TEM images of PEO_8-*b*-$PDMS_{22}$-*b*-PEO_8/DPPC mixtures reveal three different morphologies: rounded, rounded and faceted (R/F) with smooth angles, and faceted

vesicles. Rounded vesicles are likely typical of polymersomes either pure or in which a low amount of DPPC is dispersed and faceted vesicles are typical of DPPC rich vesicles [16]. While facetted vesicles illustrate the incomplete mixing of the components, the R/F vesicle is interpreted as a sign of the presence of hybrid polymersome-lipid vesicles, as this morphology is never observed neither for pure polymersomes nor pure DPPC liposomes.

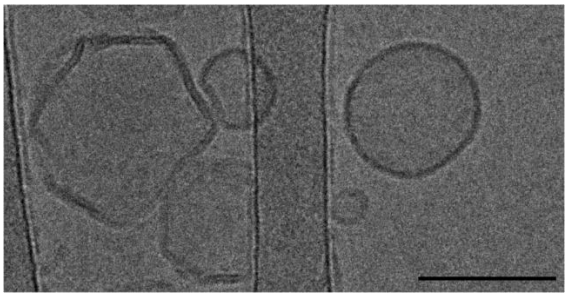

Figure 4.11. Cryo-TEM image of vesicles prepared from the 79/21 w/w % PEO_8-*b*-$PDMS_{22}$-*b*-PEO_8/DPPC mixture quenched from room temperature. Scale bar length is 100 nm.

The statistics performed for the sample of vesicles prepared from PEO_8-*b*-$PDMS_{22}$-*b*-PEO_8/DPPC 79/21 w/w % and frozen from either 20°C and 46°C are displayed in Figure 4.12. It is clear that increasing temperature results into a decrease of the faceted vesicle population (due to the typical behaviour of pure DPPC becoming fluid at 46°C) but also of the R/F vesicle fraction, accompanied by an increase of the population of rounded vesicles.

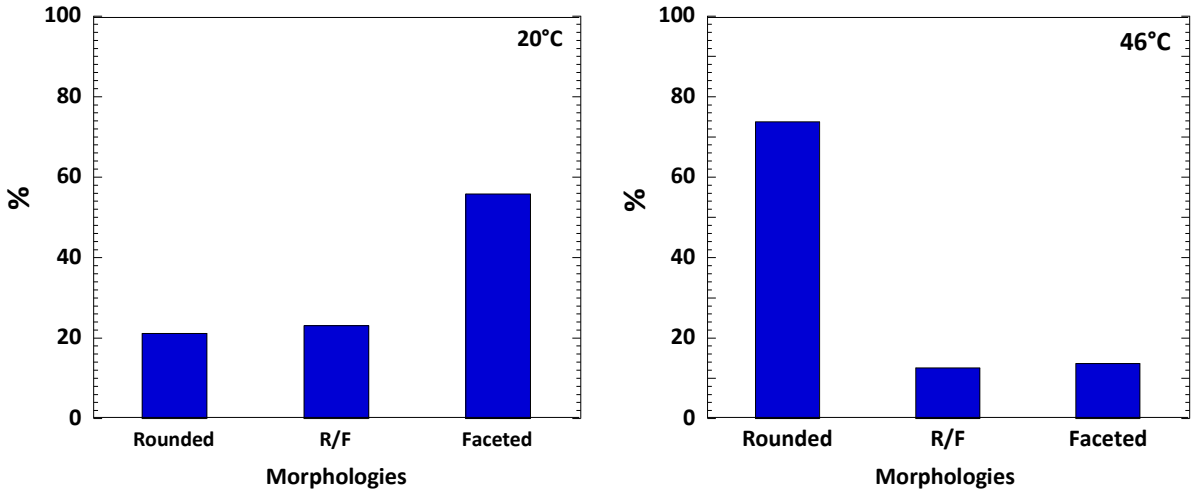

Figure 4.12. Morphology distribution of PEO_8-*b*-$PDMS_{22}$-*b*-PEO_8/DPPC LHUVs containing 21% DPPC determined by Cryo-TEM observation. Left: sample was frozen from 20°C; right: sample was frozen from 46°C.

Regarding membrane thickness, at 20°C it seems that two populations appear (Figure 4.13). One is centred between 5 and 5.5 nm, which corresponds to the membrane thickness of pure PEO_8-*b*-$PDMS_{22}$-*b*-PEO_8 vesicles. Another one is between 7 and 7.5 nm, closer to the 6.2

± 0.4 nm apparent thickness observed for pure DPPC vesicles by Cryo-TEM (annex A.4.2). When temperature increases, the membrane thickness values seem to become more uniformly distributed around a similar average value, with a strong decrease of the population of vesicles with membrane thickness between 5 and 5.5 nm. As the membrane thickness of pure polymersomes does not change with temperature, this is again a good indication of the presence of hybrid vesicles.

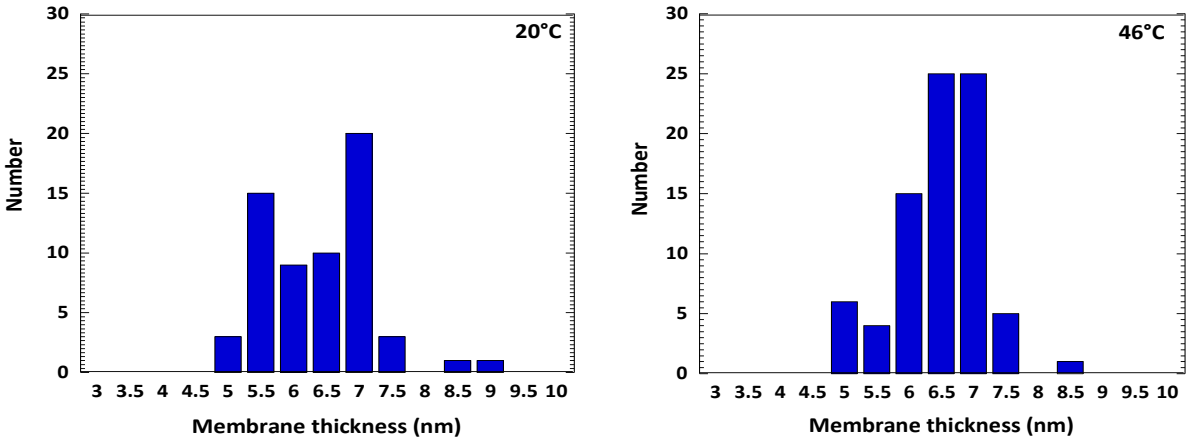

Figure 4.13. Membrane thickness distribution of PEO_8-*b*-$PDMS_{22}$-*b*-PEO_8/DPPC LHUVs containing 21% DPPC determined by Cryo-TEM observation. Left: sample was frozen from 20°C; right: sample was frozen from 46°C.

Globally, although cryo-TEM suggest the presence to a given extent of hybrid vesicles for this copolymer/lipid mixture, no presence of domains could be evidenced since silicium and phosphorus electronic contrast are similar. In addition, the comparable membrane thickness between PEO_8-*b*-$PDMS_{22}$-*b*-PEO_8 and DPPC also makes the domain observation extremely difficult.

4.2.1.3. Time-resolved Förster resonance energy transfer measurements

To get more information regarding lateral organization of lipid and copolymer in the membrane, time-resolved Förster energy transfer experiments were performed. FRET efficiencies versus the molar % of acceptor were measured on LHUVs suspensions and compared with predicted FRET values following the theoretical formalism described in section 4.1.2.

The detection of FRET phenomenon between donor-labelled copolymer and acceptor-labelled lipid, confirms the presence of hybrid vesicles (no energy transfer would occur in a mixture or pure polymersomes and liposomes). However, the recovered FRET values are

below the theoretically determined values for the case of a homogeneous distribution of copolymers and DPPC for both of mixtures containing 15% and 21% lipid (Figure 4.14). In fact, their FRET efficiencies also fall within the infinite phase separation FRET limit. This strongly suggests a significant heterogeneity in copolymer and lipid mixing. This drop in FRET efficiencies can only be rationalized by phase separation into structures of at least 25 – 50 nm size. Since SANS measurements did not detect domains within these large dimensions, the measured FRET efficiencies must reflect the formation of pure liposomes and polymersomes along with hybrid vesicles, which results in a decrease of lipid acceptors in hybrid vesicles.

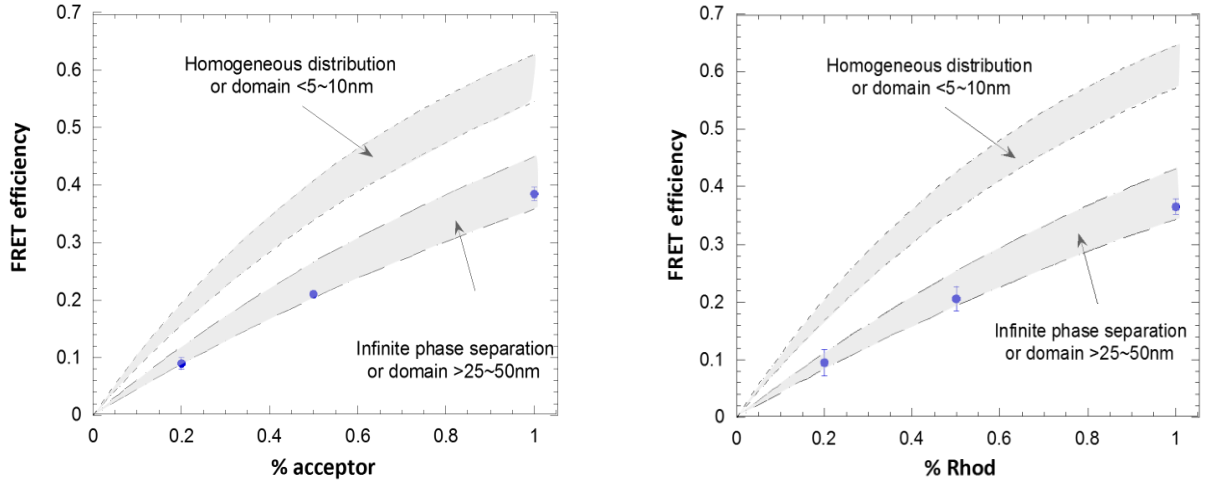

Figure 4.14. FRET efficiencies *vs* content of lipid labelled acceptor (molar %) for PEO_8-*b*-$PDMS_{22}$-*b*-PEO_8/DPPC mixtures containing 15% lipid weight fraction (left) and 21% lipid weight fraction (right). Theoretical expectation for the case of homogeneous distribution and infinite phase separation taking into account experimental uncertainty in the area per polymer chain determination are delimited by shaded areas.

In brief, considering all of three approaches used (SANS, Cryo-TEM and TR-FRET), it can be concluded that for the PEO_8-*b*-$PDMS_{22}$-*b*-PEO_8/DPPC mixture, a significant part of the lipid is dispersed in the polymer phase, leading to the formation of hybrid vesicles. However, pure liposomes are also formed and lead to a global decrease of the FRET efficiency. It is difficult to estimate the relative amount of hybrid vesicles but the homogenization of membrane thickness with temperature and the good quality of the fit obtained using the "hybrid vesicle" form factor in polymer contrast suggest that pure single component vesicles are not the main population.

4.2.2. Results for PEO_{12}-*b*-$PDMS_{43}$-*b*-PEO_{12}/lipid LHUVs

We followed exactly the same methodology for mixtures of triblock copolymer PEO_{12}-*b*-$PDMS_{43}$-*b*-PEO_{12} forming vesicles with slightly higher membrane thickness (~ 8nm).

4.2.2.1. Small angle neutron scattering measurements

General features of scattering curves

With this copolymer, a q^{-2} dependence classically observed in vesicular structure is also obtained for all matching conditions as shown in Figure 4.15.

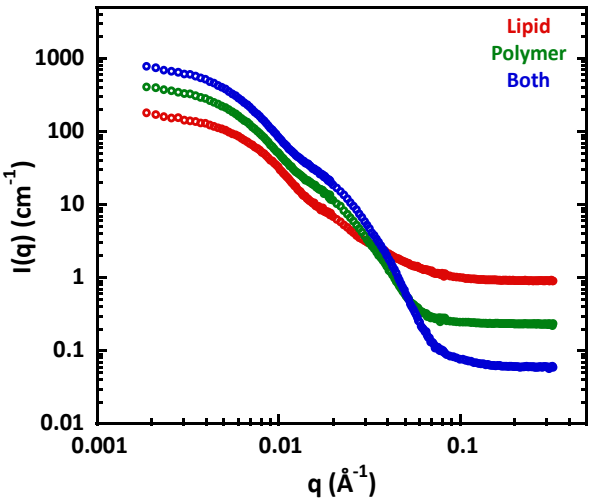

Figure 4.15. SANS curves recorded at 20°C for PEO_{12}-*b*-$PDMS_{43}$-*b*-PEO_{12}/DPPC-d_{62} mixture with lipid fraction f_d = 0.21 (in mass) in three different contrast conditions: lipid contrast (●), polymer contrast (●) and full contrast (●).

Once again, the reversible structural changes upon temperature increase were observed for either lipid or polymer contrast (Figure 4.16). The modification of scattering profile in polymer contrast proves that polymers and lipid are somehow mixed within vesicular structures.

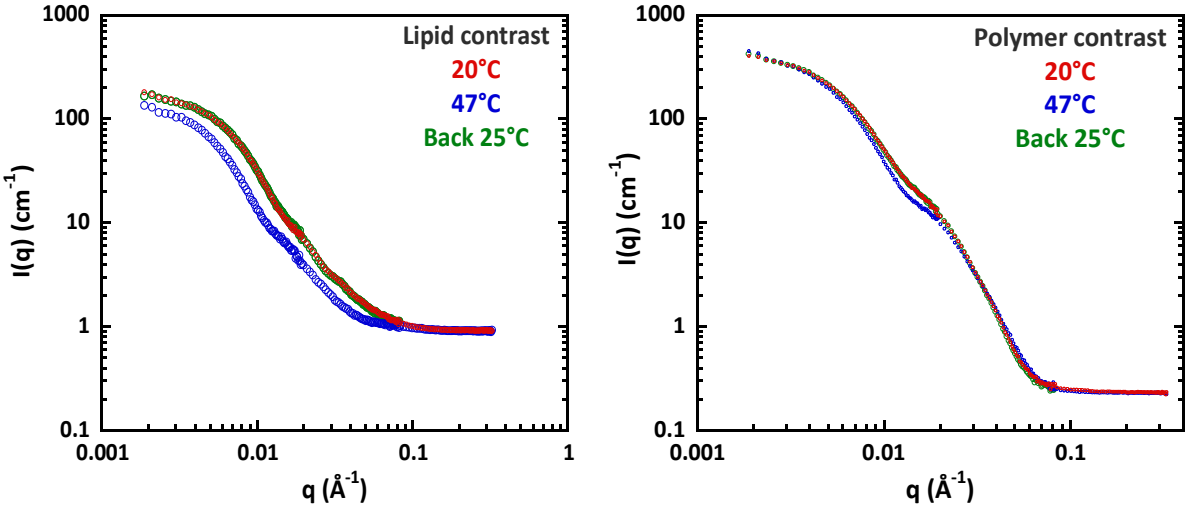

Figure 4.16. SANS curves recorded at different temperatures: 20°C (●), 47°C (●) and back to 25°C (●) for PEO_{12}-*b*-$PDMS_{43}$-*b*-PEO_{12}/DPPC-d_{62} mixtures with lipid fraction f_d = 0.21 (weight fraction): in lipid contrast (left) and in polymer contrast (right).

Quantitative analysis of the data

Following the procedure employed for the previous system, the hybrid vesicle model was first used to fit the scattering curves obtained in polymer contrast. The fit generally works well but the parameters obtained were not physically realistic: hole sizes close to 1 nm with huge size dispersity. Better results were obtained using a simple vesicle form factor. The corresponding parameters can be consulted in Table 4.7 and the representative fitting curves for mixture with lipid weight fraction 0.21 are illustrated in Figure 4.17.

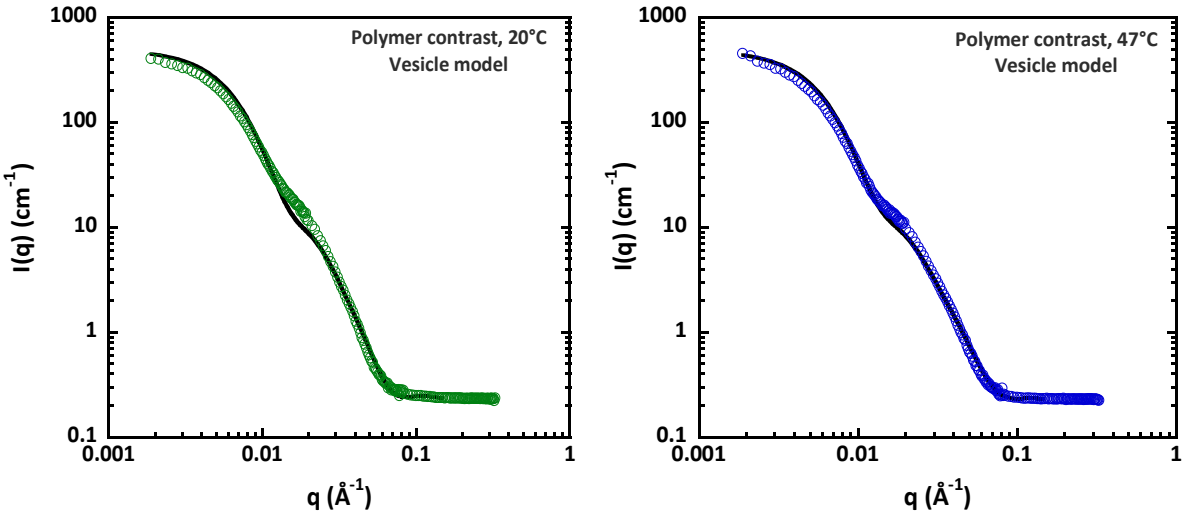

Figure 4.17. SANS curves obtained for mixture of PEO_{12}-*b*-$PDMS_{43}$-*b*-PEO_{12}/DPPC-d_{62} with lipid weight fraction f_d = 0.21 at 20°C, 47°C in lipid and polymer contrast. Solid lines are the best fits with vesicle model.

Table 4.7. Best fit parameters obtained from vesicle form factor fitting of PEO_{12}-*b*-$PDMS_{43}$-*b*-PEO_{12}/DPPC-d_{62} mixtures.

Lipid fraction f_d	T°C	Polymer contrast					Lipid contrast				
		Guinier	Vesicle model				Guinier	Vesicle model			
		R_g (nm)	R_ϑ (nm)	σ_{R_ϑ}	δ_ϑ (nm)	$\sigma_{\delta_\vartheta}$	R_g (nm)	R_ϑ (nm)	σ_{R_ϑ}	δ_ϑ (nm)	$\sigma_{\delta_\vartheta}$
0.15	20°C	32.0	15.4	0.39	7.9	0.13	23.5	13.8	0.32	4.2	0.1
	47°C	34.0	17.9	0.38	6.9	0.12	30.4	21.0	0.27	3.2	0.2
0.20	20°C	28.4	13.2	0.4	7.6	0.1	24.6	13.2	0.35	4.2	0.1
	47°C	31.0	15.7	0.36	6.6	0.13	29.9	18.0	0.3	3.2	0.2
0.30	20°C	27.6	8.0	0.55	7.2	0.12	28.3	13.4	0.36	4.2	0.1
	47°C	29.9	11.2	0.45	6.3	0.1	33.0	17.0	0.35	3.1	0.2

Globally, the vesicle radius obtained by the fit is rather low with important size dispersity and the weight average radius taking into account σ_{R_θ}, is in excellent agreement with Rg obtained via Guinier plot. Values of membrane thickness are however well defined with a rather low dispersity. A slight thinning of the membrane is observed when temperature increases and also when lipid fraction increases, revealing that lipids are mixed to some extent with the copolymers inside the membrane.

Regarding the scattering curves in lipid contrast, good fits are also obtained with the vesicle form factor, with similar vesicle radius presenting high dispersity but again with well-defined membrane thicknesses (~ 4 nm). Thickness values decreases with temperature, typical character of DPPC as previously mentioned. Although the polymer and lipid may not be totally mixed, it seems from the SANS results that there is no clear phase separation inside the membrane and that existing hybrid vesicles present a homogeneous distribution of their components.

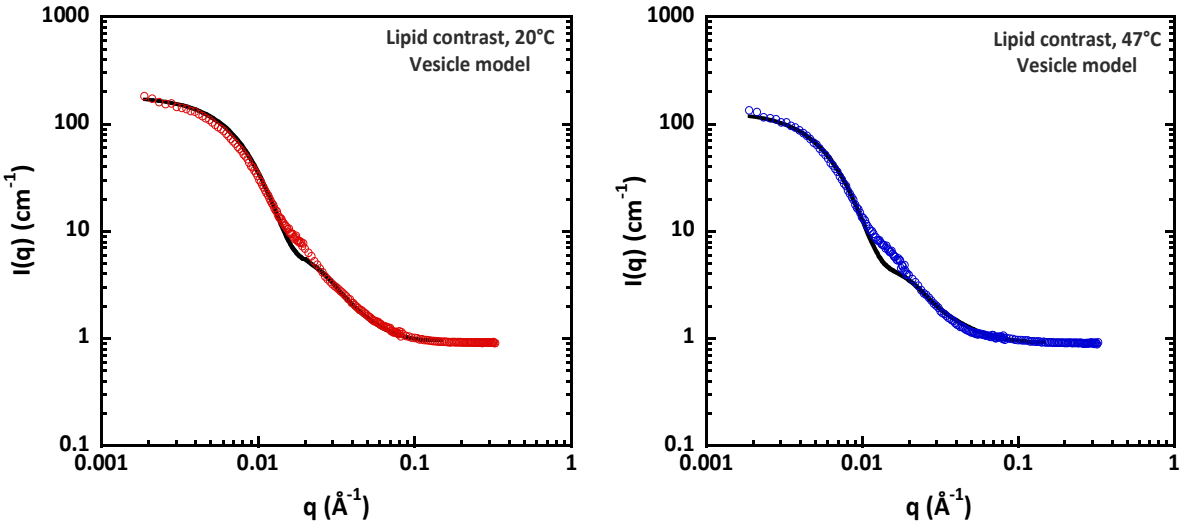

Figure 4.18. SANS curves obtained for mixture of PEO_{12}-*b*-$PDMS_{43}$-*b*-PEO_{12}/DPPC-d_{62} with lipid weight fraction f_d = 0.21 at 20°C, 47°C in lipid and polymer contrast. Solid lines are the best fits. Polymer contrast curves were fitted with hybrid vesicle model and lipid contrast curves were fitted with vesicle model.

4.2.2.2. Cryo-TEM measurements

Cryo-TEM experiment performed on PEO_{12}-*b*-$PDMS_{43}$-*b*-PEO_{12}/DPPC (79/21 w/w %) also reveals the presence of different types of vesicles: 25% are faceted, 65% are rounded vesicles and a few percentages are multilamellar or present R/F morphology. Faceted vesicles once again illustrate the incomplete mixing of the components. Interestingly, observations on a suspension frozen from 46°C revealed a strong increase of R/F population

accompanied by a decrease of faceted vesicles. This strong increase of the fraction of R/F vesicles is interpreted as a sign of the presence of hybrid polymer/lipid vesicles. Details of statistics can be consulted in distribution histograms in Figure 4.19.

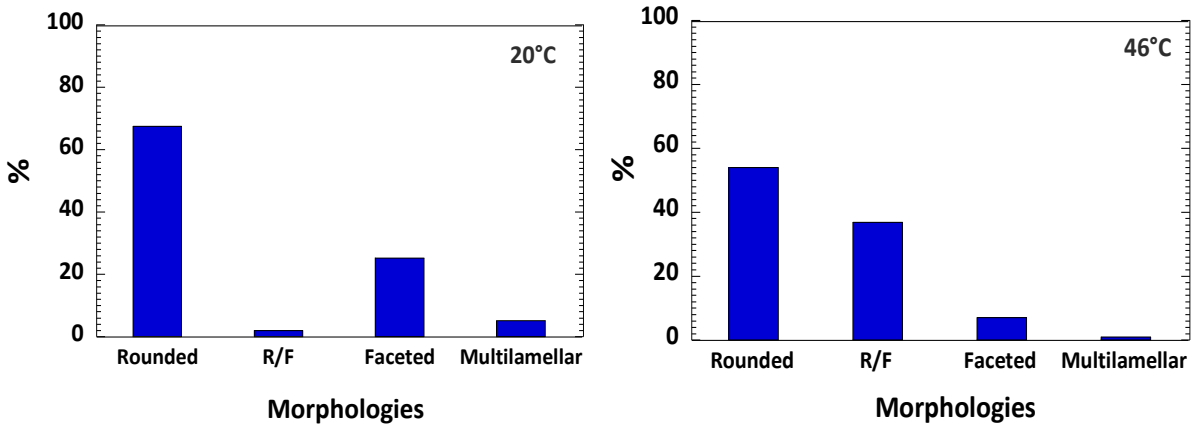

Figure 4.19. Morphology distribution of PEO_{12}-*b*-$PDMS_{43}$-*b*-PEO_{12}/DPPC LHUVs containing 21% DPPC determined by Cryo-TEM observation. Left: sample was frozen from 20°C; right: sample was frozen from 46°C.

Additional signs of the presence of hybrid vesicles can be detected from the statistics on membrane thickness displayed in Figure 4.20. Indeed, for the sample at 20°C, the average membrane thickness distribution is shifted to slightly lower values compared to pure polymersomes (7.3 ± 1.0 instead of 8.8 ± 0.5 nm). At 46°C, another population appears at 5 – 6 nm, a membrane thickness typically observed for pure DPPC vesicles at such temperature by Cryo-TEM. This may result from the simple decrease of membrane thickness of DPPC vesicles expected when temperature increases, making them more visible compared to the polymer membrane thickness, or can be the result of fission of pure DPPC membranes from hybrid vesicles.

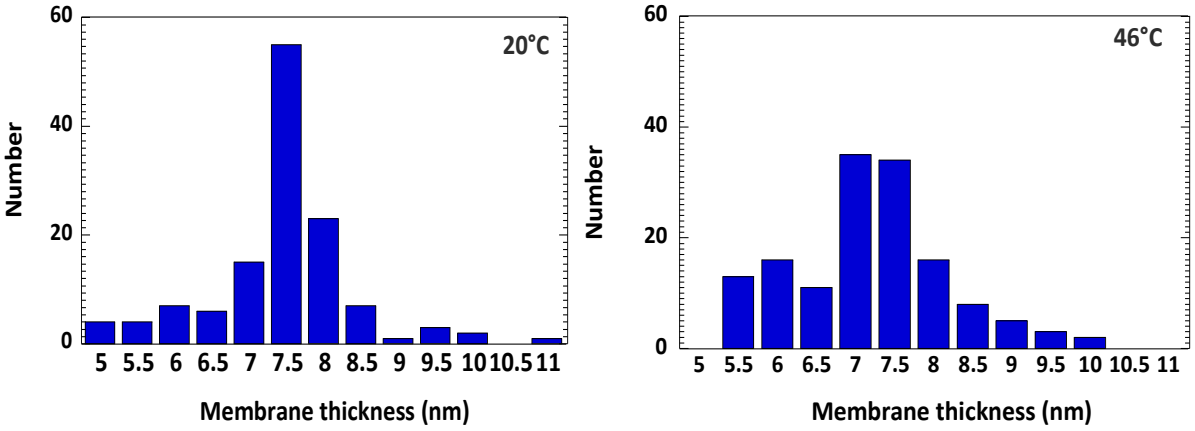

Figure 4.20. Membrane thickness distribution of PEO_{12}-*b*-$PDMS_{43}$-*b*-PEO_{12}/DPPC LHUVs containing 21% DPPC determined by Cryo-TEM observation. Left: sample was frozen from 20°C; right: sample was frozen from 46°C.

Very interestingly, due to a significant difference in membrane thickness of this copolymer and lipid, it was possible to observe the signature of a lipid domain in the surrounding polymer-rich membrane as illustrated in Figure 4.21.

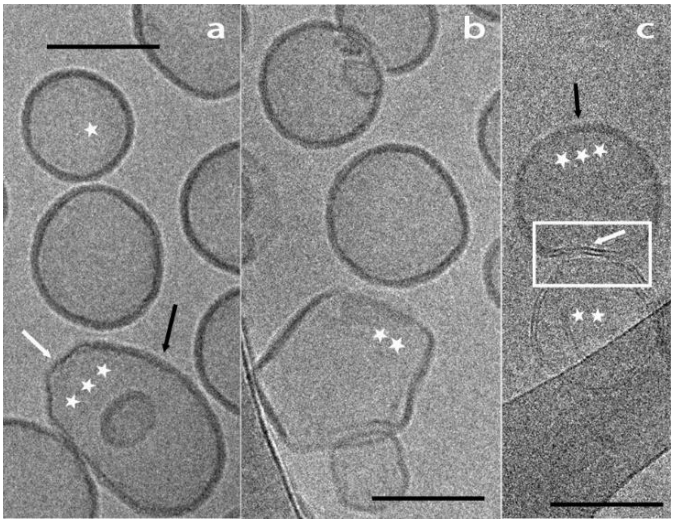

Figure 4.21. Cryo-TEM image of vesicles prepared from the 79/21 (w/w %) PEO_{12}-*b*-$PDMS_{43}$-*b*-PEO_{12}/DPPC mixture quenched from room temperature. The vesicle with one white star corresponds to a pure polymersome. The vesicle with two white stars represents a typical pure DPPC faceted vesicle (insert b). The vesicles with three white stars are hybrid vesicles, the white arrow points to the thinner membrane corresponding to the lipid part and the black arrow points to thicker membrane corresponding to the polymer part. The insert c illustrates nicely the Cryo-TEM signature of lipid domains (bilayer, pointed by the white arrow) in polymer membrane (pointed by the black arrow) obtained on a sample quenched from 46°C. All scale bars represent 100 nm.

4.2.2.3. Time-resolved Förster energy transfer experiments

Similar with the study on the previous system, the TR-FRET experiments were performed to evaluate the distribution of polymer and lipid molecules within the membranes.

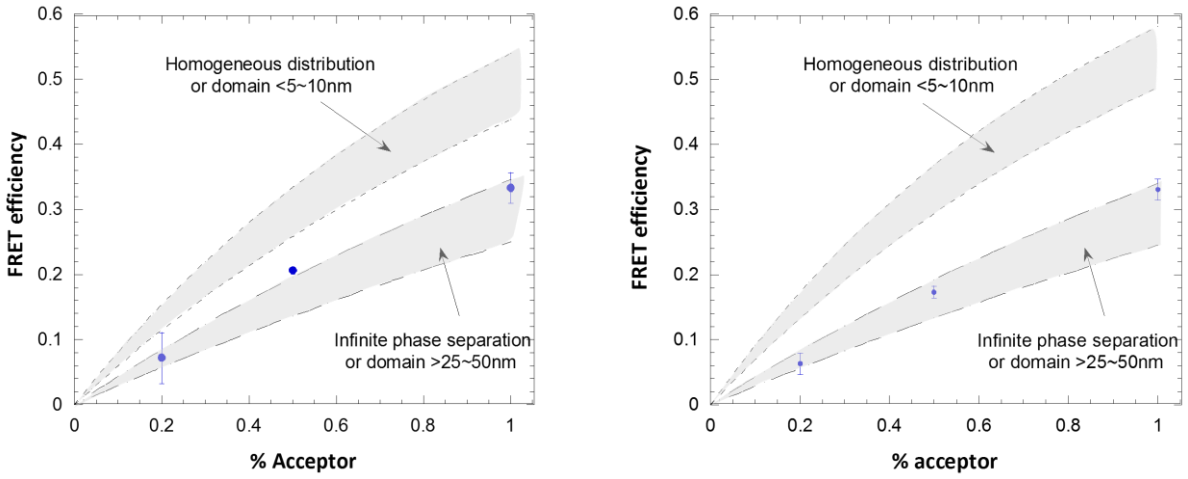

Figure 4.22. FRET efficiencies *vs* content of lipid labelled acceptor (molar %) for PEO_{12}-*b*-$PDMS_{43}$-*b*-PEO_{12}/DPPC mixtures at 46°C with 15% lipid weight fraction (left) and 21% lipid weight fraction (right). Theoretical expectation for the case of homogeneous distribution and infinite phase separation taking into account experimental uncertainty in the area per polymer chain determination are delimited by shaded areas.

The non-zero values of FRET efficiency again confirm the presence of hybrid vesicles to a given extent. The values are still in the infinite phase separation limit for both 15% and 21% lipid (Figure 4.22). As there is no evidence of large domains from SANS interpretation, once again, it seems that pure liposomes are formed and lead to a global decrease of the FRET efficiency, as observed in the previous system.

Globally, SANS, TR-FRET and Cryo-TEM show that samples obtained from PEO_{12}-*b*-$PDMS_{43}$-*b*-PEO_{12}/DPPC mixtures are truly heterogeneous. The hybrid vesicles that are formed coexist with a significant amount of pure liposomes. This thus reduces the potential of those analyses to recover quantitative information. Compared to the PEO_8-*b*-$PDMS_{22}$-*b*-PEO_8/DPPC mixture, the fraction of pure vesicles seems to be larger, although we could not quantify it, and this could be ascribed to the higher hydrophobic mismatch between PEO_{12}-*b*-$PDMS_{43}$-*b*-PEO_{12} and DPPC.

4.2.3. Results for PEO_{17}-*b*-$PDMS_{67}$-*b*-PEO_{17}/lipid LHUVs

The same series of experiments were performed for mixtures of triblock copolymer PEO_{17}-*b*-$PDMS_{67}$-*b*-PEO_{17}. Since this polymer forms vesicles with very high membrane thickness, those samples are predicted to be strongly heterogeneous.

4.2.3.1. Small angle neutron scattering measurements

General features of scattering curves.

The SANS curves of mixtures with this largest molar mass triblock copolymer show a q^{-1} decrease characteristic of an elongated scattering object rather than a q^{-2} scaling law characteristic of vesicles (Figure 4.23).

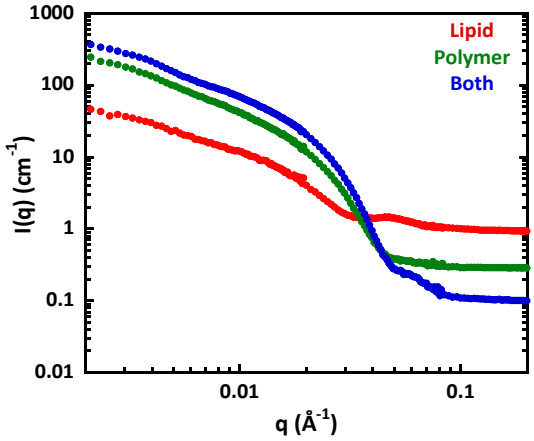

Figure 4.23. SANS curves recorded at 20°C for PEO_{17}-*b*-$PDMS_{67}$-*b*-PEO_{17}/DPPC-d_{62} mixture with lipid mass fraction f_d = 0.21 in three contrast conditions: lipid contrast (●), polymer contrast (●) and full contrast (●).

Moreover, unlike previous systems, the evolution with temperature in this mixture is almost negligible.

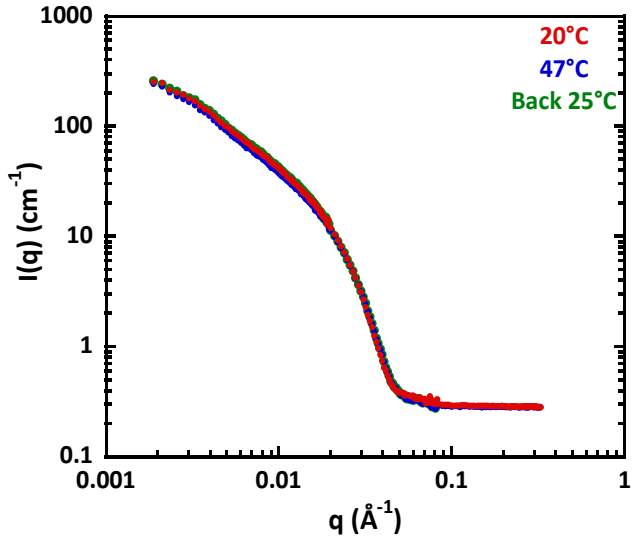

Figure 4.24. SANS curves recorded at different temperatures: 20°C (●), 47°C (●) and back to 25°C (●) for PEO_{17}-*b*-$PDMS_{67}$-*b*-PEO_{17}/DPPC-d_{62} mixture with lipid fraction f_d = 0.21 (weight fraction) in polymer contrast.

Quantitative analysis of the data

Due to the q^{-1} slope observed on the scattering curves, the data were fitted with a core-shell cylinder model. In polymer contrast, the fit works well with polymers forming the core of long cylinders with a core radius around 7 – 8 nm influenced neither by temperature nor by lipid fraction. Fit parameters are indicated in Table 4.8 and the typical curves are displayed in Figure 4.25. In lipid contrast, we observe at high *q* a clear and well-pronounced bump that does not arise from the scattering of the vesicle membrane but rather from a well-defined shell of core shell cylindrical scattering objects. However, at low *q*, the scattering intensity displays the oscillation characteristic of vesicle radii. These observations indicate clearly that a part of lipid is mixed somehow with the copolymer in cylindrical shaped objects, but another part forms vesicles probably of pure lipid. At large *q*, the data could be reasonably fitted with a core-shell cylinder model and the corresponding best fit parameters are also reported in Table 4.8.

In all mixtures, the shell thickness t_{shell} is 2 nm, about half of the membrane of pure lipid vesicles. Interestingly, there is a reasonable agreement between core radii found in polymer and lipid contrasts. From these fits, it seems that a large part of the nanostructure formed presents a core-shell cylindrical shape, with lipids forming the shell around the polymer core. This structure can be depicted as Figure 4.26.

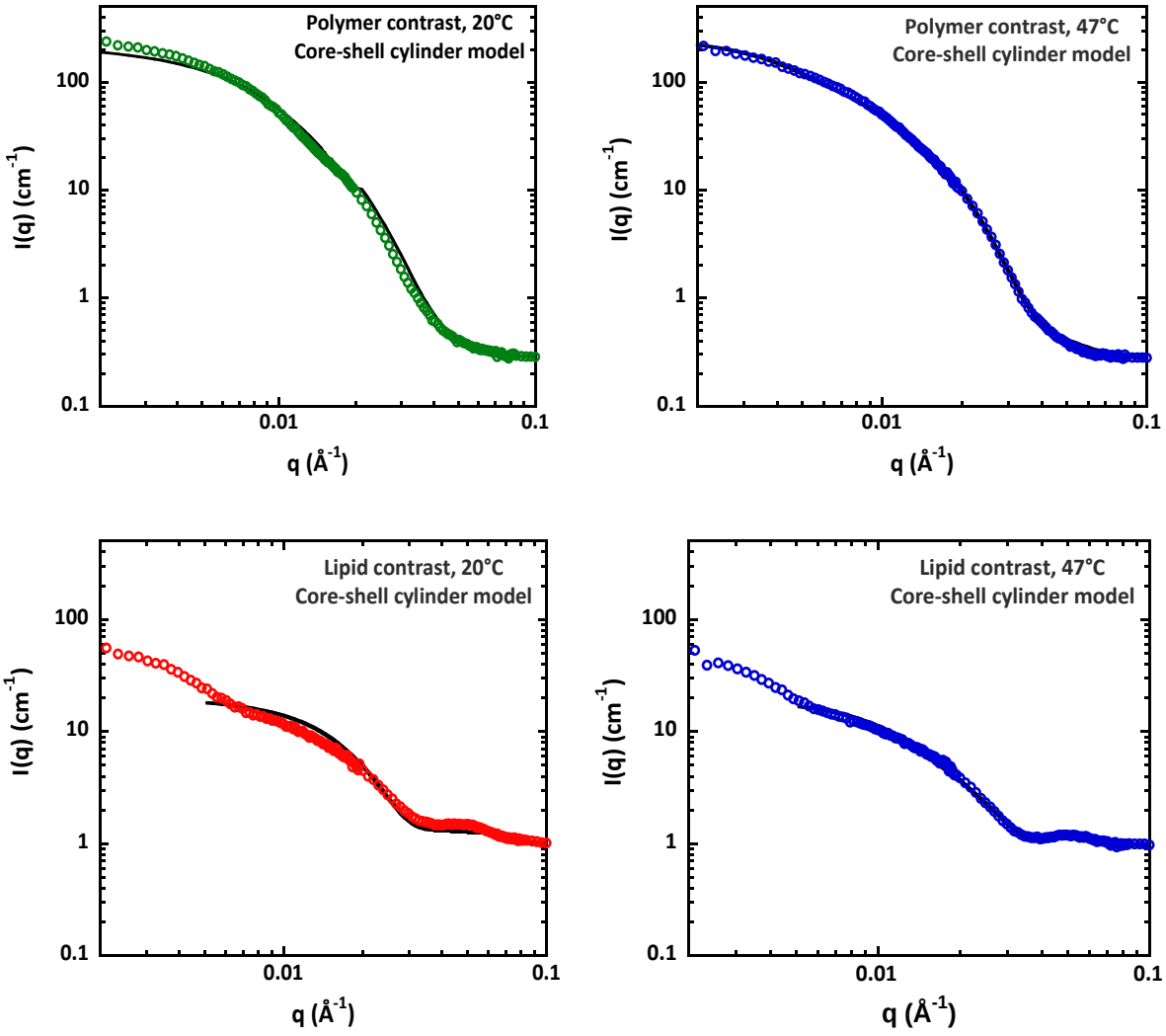

Figure 4.25. SANS curves obtained for mixtures of PEO_{17}-*b*-$PDMS_{67}$-*b*-PEO_{17}/DPPC at lipid fractions of f_d = 0.21 and best fit with the core-shell cylinder model (line). On the left: experiment at 20°C and on the right: experiment at 47°C.

Table 4.8. Fit parameters obtained from the core-shell cylinder model deduced from SANS curves of different PEO_{17}-b-$PDMS_{67}$-b-PEO_{17}/DPPC-d_{62} mixtures.

Lipid fraction f_d	T°C	Polymer contrast		Lipid contrast		
		Polymer filled cylinder		Core-shell cylinder model with lipid shell		
		R_{core} (nm)	$\sigma_{R_{core}}$	R_{core} (nm)	$\sigma_{R_{core}}$	t_{shell} (nm)
0.15	20°	7.7	0.16	6.3	0.15	2.1
	47°	7.4	0.17	5.9	0.14	2.0
0.21	20°	8.6	0.20	5.9	0.16	2.1
	47°	8.7	0.24	5.5	0.18	1.9
0.30	20°	6.8	0.20	5.4	0.18	2.1

47°	7.1	0.19	5.1	0.2	2.0

Such transverse phase separation in a vesicle bilayer driven by different spontaneous curvatures was predicted a long time ago for a binary mixture of membrane forming molecules [17]. However, it is rather counterintuitive here that the shortest chains (those of the lipids) form the outer shell, while the copolymer forms the inner core of the cylinder. Considering the complexity of these mixtures and the presence of pure vesicles not accounted in the fits, it is not possible to discuss the variations of the other parameters observed as a function of the lipid fraction or temperature.

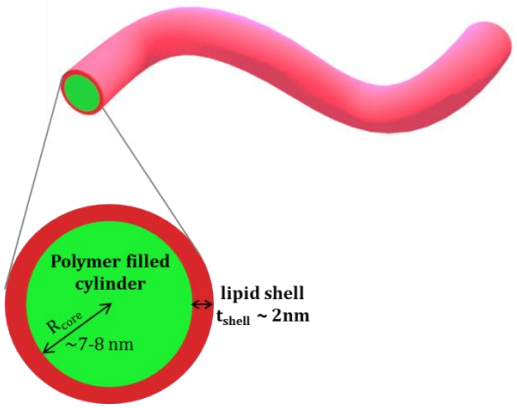

Figure 4.26. Scheme of the core-shell cylinder model with lipid shell and polymer core.

4.2.3.2 Cryo-TEM measurements

Cryo-TEM experiments indeed reveal the presence of multiple morphologies. Faceted vesicles with a relatively thin membrane (~6 nm) similar to those measured for pure DPPC vesicles are observed, as well as polymersomes with thick membrane (~12 nm). Worm-like micelles are also observed and represent ~ 50% of the population. Interestingly, some of these worm-like micelles present a “pan-like” shape, which corresponds to a worm-like micelle ending with a rounded disk. A statistic for those morphologies of PEO_{17}-b-$PDMS_{67}$-b-PEO_{17}/DPPC mixture containing 30% DPPC is displayed in Figure 4.27.

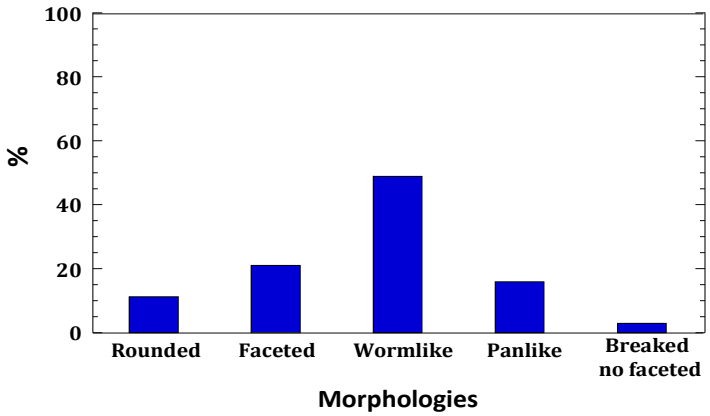

Figure 4.27. Morphologies reported in % for PEO_{17}-b-$PDMS_{67}$-b-PEO_{17}/DPPC mixture containing 30% DPPC.

Very interestingly, the Cryo-TEM signature of a flat DPPC lipid domain in a thick polymersome membrane is once again visible as illustrated in the inset of Figure 4.28. Although some vesicles could have hybrid character non-visible by Cryo-TEM, considering the amount of hybrid worm-like micelles and faceted DPPC vesicles, the number of LHUVs obtained with this high membrane thickness copolymer is probably limited. Worm-like micelles have been also observed very recently for mixtures composed of POPC and diblock copolymer PBd_{22}-*b*-PEO_{14} at 29% w/w lipid in hybrid vesicles, using classical rehydration/extrusion technique [18].

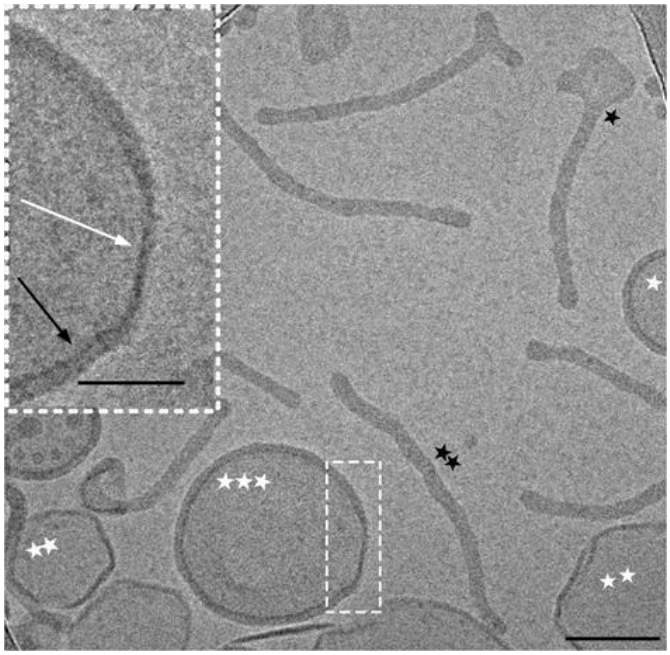

Figure 4.28. Cryo-TEM image of vesicles prepared from the 70/30 w/w ratio PEO_{17}-b-$PDMS_{67}$-b-PEO_{17}/DPPC mixture quenched from room temperature. The object pointed by a black star is called "pan-like" micelle. A worm-like micelle is indicated by two black stars. Vesicles can easily be identified by the thickness of their membrane; vesicle with one white star corresponds to a pure polymersome (membrane thickness is about 11.2 nm). The faceted vesicle with two white stars represents a typical pure DPPC vesicle with the thickness of 6.2

nm. The vesicle with 3 white stars is a hybrid vesicle. In the inset, the enlargement of a hybrid vesicle is shown. The white arrow points to the thinner membrane corresponding to the lipid membrane and the black arrow points to the thicker membrane corresponding to the polymer membrane. Scale bar length is 100 nm in the main image and 40 nm in the enlargement.

In summary, as predicted, due to strongly high hydrophobic mismatch, sample heterogeneity was also obtained for PEO_{17}-b-$PDMS_{67}$-b-PEO_{17}/DPPC mixtures. In addition to heterogeneity in terms of composition of vesicles (pure and hybrid), heterogeneity is also observed in terms of morphology, compared to previous triblocks. This render TR-FRET interpretation almost impossible with the proposed model and therefore FRET experiments were not carried out for those mixtures.

4.2.4. Results for $PDMS_{26}$-*g*-$(PEO_{12})_2$/lipid LHUVs

The same methodology was also done for mixtures made with a copolymer based on the same chemical nature (PDMS and PEG) but graft architecture $PDMS_{26}$-*g*-$(PEO_{12})_2$. This copolymer forms vesicular structure with a membrane thickness similar to vesicle formed by PEO_8-*b*-$PDMS_{22}$-*b*-PEO_8 triblock. Therefore, we can evaluate an architecture effect on the recovery of hybrid vesicles and membrane structuration.

4.2.4.1. Small angle neutron scattering measurements

General features of scattering curves

Figure 4.29 shows typical SANS curves of $PDMS_{26}$-*g*-$(PEO_{12})_2$/DPPC mixtures. All of them display the characteristic q^{-2} scaling law over a wide intermediate q range, corresponding to a vesicle structure. In this system, the whole vesicular structures are very polydisperse and almost no oscillation is visible on the SANS curves, unlike what was observed with PEO_8-*b*-$PDMS_{22}$-*b*-PEO_8 /DPPC mixtures.

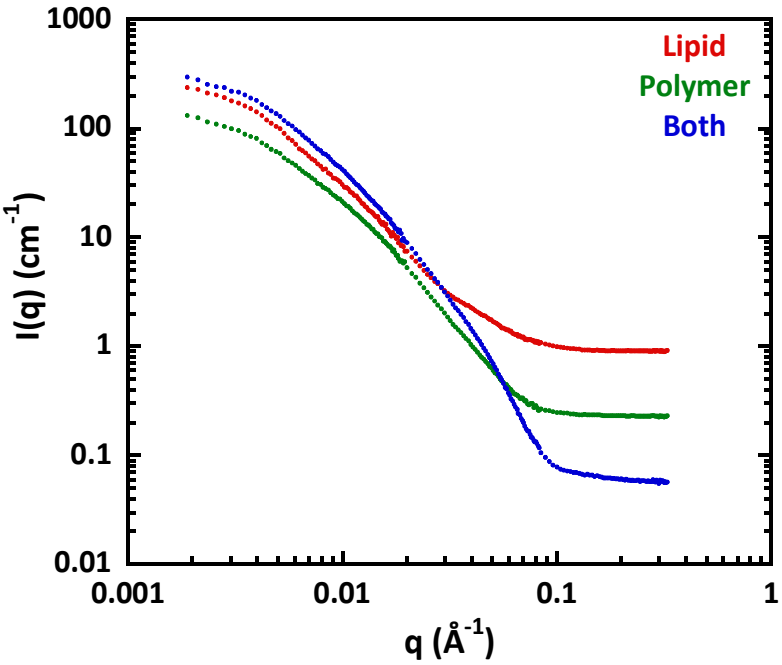

Figure 4.29. SANS curves recorded at 20°C for $PDMS_{26}$-*g*-$(PEO_{12})_2$/DPPC-d_{62} mixture with lipid weight fraction f_d = 0.21 in three different contrast conditions: lipid contrast (●), polymer contrast (●) and full contrast (●).

When the temperature increases, in polymer contrast, the curves are changing in the intermediate q range, as previously observed for PEO_8-*b*-$PDMS_{22}$-*b*-PEO_8 (Figure 4.30).

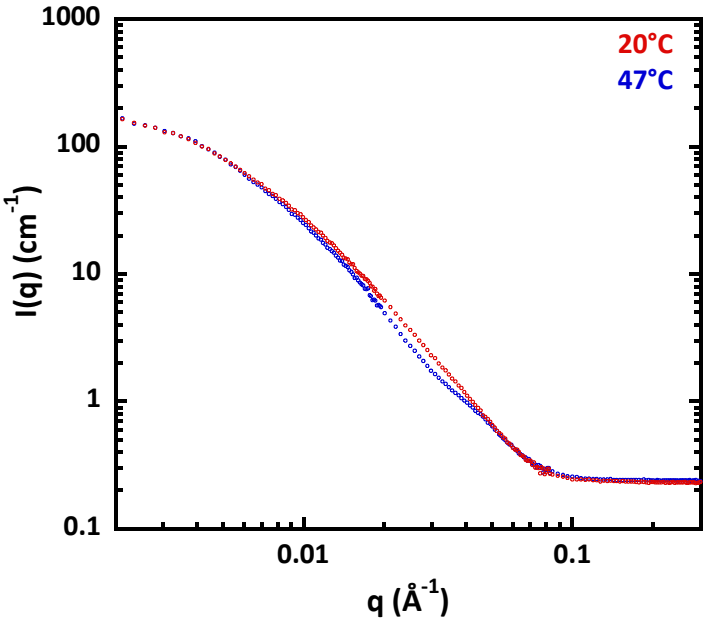

Figure 4.30. SANS curves recorded for $PDMS_{26}$-*g*-$(PEO_{12})_2$/DPPC-d_{62} mixture with lipid weight fraction f_d = 0.21in polymer contrast at different temperatures: 20°C (●), 47°C (●).

Quantitative analysis of the data

In polymer contrast, since changes upon temperature variation were observed in the same intermediate *q* range as for the previous triblock copolymer, the scattered intensity was also fitted with the hybrid vesicle model. The fits are shown in Figure 4.31 and the fit parameters reported in Table 4.9.

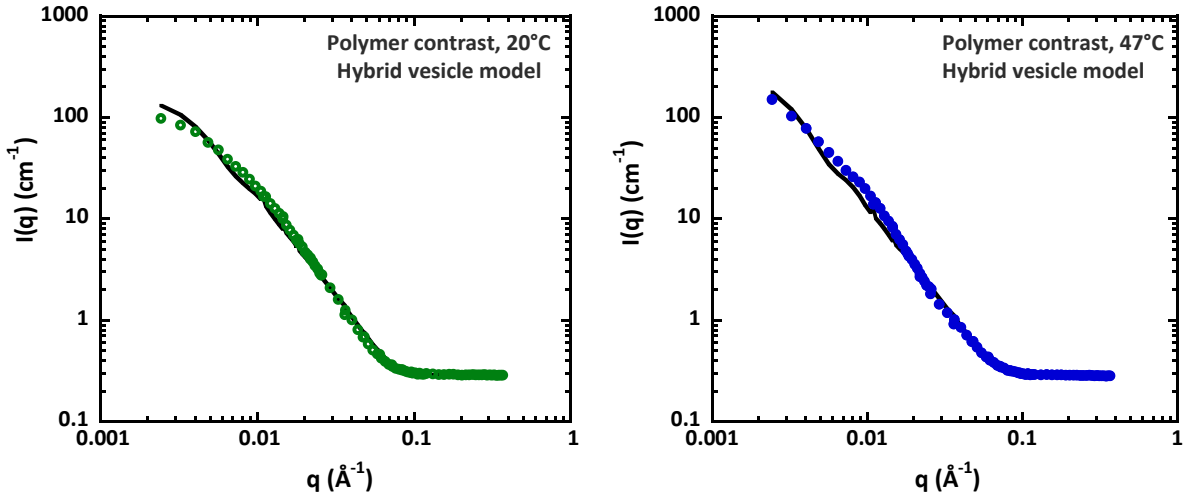

Figure 4.31. SANS curves obtained for mixture of $PDMS_{26}$-*g*-$(PEO_{12})_2$/DPPC-d_{62} at lipid fraction f_d = 0.21 and best fit with the hybrid vesicle model (line). On the left: experiment at 20°C and on the right: experiment at 47°C.

Despite the high polydispersity, the curves were reasonably fitted. Although the values obtained for the radius of the vesicles are meaningless, the fit accounted well any variation in the scattering curves upon temperature changes. On average, whatever the temperature or lipid fraction, we find about 4 – 6 disks of 6 – 14 nm diameter, very polydisperse in size. This suggests the formation of small domains of lipid in the polymer membrane. Interestingly, in lipid contrast, as for the previous triblock copolymer, data cannot be fitted with the simple vesicle ("spherical shell") form factor model, suggesting again that lipids are not simply homogeneously distributed within the polymer membrane.

Table 4.9. Best fit parameters obtained with hybrid vesicle model in polymer contrast: *: fixed parameters.

Lipid fraction f_d	T°C	Guinier	Hybrid vesicle model						
		R_g (nm)	R_ϑ (nm)	σ_{R_ϑ}	N_d	R_d (nm)	σ_{R_d}	δ_ϑ* (nm)	δ_d (nm)
0.15	20°C	32.5	8.5	1.2	5.7	2.9	3.1	5.6	4.3
	47°C	32.2	11.2	1.2	4.0	4.2	3.1	5.6	3.2
0.21	20°C	31.8	11.7	1.2	3.7	7.2	1.2	5.6	4.3
	47°C	31.ç	14.7	1.2	5.8	3.3	3.0	5.6	3.2

4.2.4.2. Cryo-TEM measurements

As for the previous copolymer PEO_8-b-$PDMS_{12}$-b-PEO_8, the membrane thickness of lipid membrane and polymer membrane are close, rendering the distinction of hybrid vesicle and visualisation of phase separation within membrane difficult. Representative electron microscopy image and morphology histograms are shown in Figure 4.32 and 4.33.

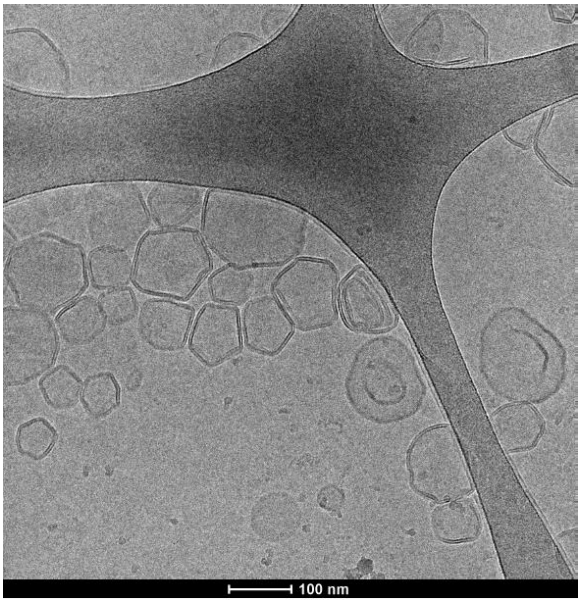

Figure 4.32. Cryo-TEM image of vesicles prepared from the 85/15 w/w ratio $PDMS_{26}$-*g*-$(PEO_{12})_2$/DPPC mixture quenched from room temperature.

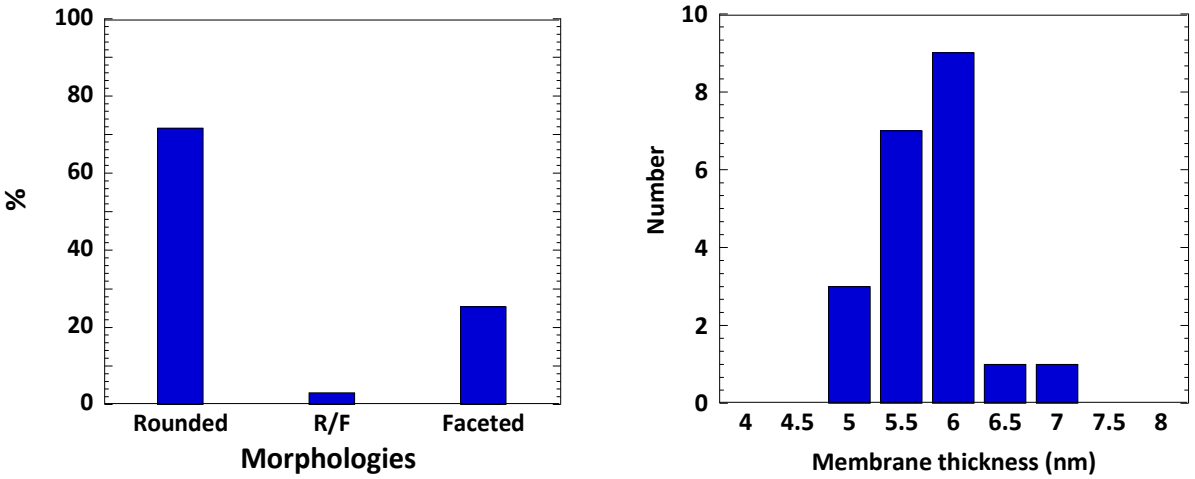

Figure 4.33. Distribution of morphology and membrane thickness of $PDMS_{26}$-*g*-$(PEO_{12})_2$/DPPC LHUVs containing 21% DPPC determined by Cryo-TEM observation; sample was frozen from 20°C.

4.2.4.3. Fluorescence spectroscopy measurements

To get more insight into putative $PDMS_{26}$-*g*-$(PEO_{12})_2$/DPPC phase separation, FRET measurements were also performed and compared to the prediction of homogeneous distribution of donor and acceptor probes within the membranes.

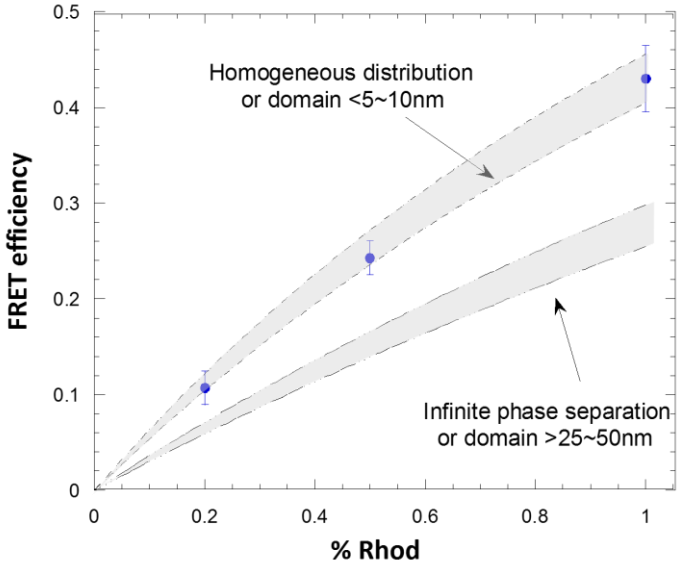

Figure 4.34. FRET efficiencies *vs* content of lipid labelled acceptor (molar %) for $PDMS_{26}$-*g*-$(PEO_{12})_2$/DPPC mixtures at 46°C with 15% lipid weight fraction. Theoretical expectation for the case of homogeneous distribution and infinite phase separation taking into account experimental uncertainty in the area per polymer chain determination are delimited by shaded areas.

In this case, experimental points fall in the range predicted for domains size below or close to the Förster radius of the donor-acceptor FRET pair considered here (5 nm). For domains presenting dimensions smaller than 5 nm, FRET efficiencies are expected to be almost identical to the expected values for a homogeneous distribution. Additionally, given the uncertainty in the area per copolymer molecule, it is difficult to determine with accuracy the presence of phase separation or the sizes of lipid domains in hybrid vesicles from the FRET data. In this context, the results of FRET are fully in line with the domain dimensions suggested by SANS (6 – 14 nm), as formation of these domains would produce only minor changes in FRET efficiency when compared to the expectation for a homogeneous distribution. In such systems, the association of the copolymer and lipid molecules within the same membrane is more efficient and the number of pure polymersomes and liposomes which inevitably perturb the SANS analysis and decreases the FRET efficiency, is considerably lower than for the previous considered copolymers, although still present, as illustrated by Cryo-TEM.

4.3. CONCLUSION

A systematic study on different hybrid polymer/lipid mixtures at nanoscale was performed and the significant differences between systems were seen, indicating the effect of different parameters. The film rehydration/extrusion technique for the production of hybrid polymer/lipid large unilamellar hybrid vesicles (LHUVs) appears as a non-ideal procedure, although commonly used in the literature [19-23]. Marrying of a single membrane triblock or diblock copolymer having high molar mass with phospholipids has already been achieved for GHUVs, although it has been reported that some mixtures did not give any vesicles [24] or led to the budding or eventual fission into separated liposomes and polymersomes [25]. In the case of LHUVs, the association seems driven by more subtle features. In summary, it is believed that a high line tension resulting from very significant differences in membrane thickness would lead to formation of separated liposomes and polymersomes, but other hybrid structures can be formed as illustrated by core-shell tubular (worm-like) or pan-like micelles obtained with PEO_{17}-*b*-$PDMS_{67}$-*b*-PEO_{17}/DPPC mixtures. Decreasing the molar mass of triblock copolymer results into the disappearance of these hybrid worm-like or pan-like micelles and to the formation at least to some extent, of hybrid vesicles. Their membrane structure cannot be characterized precisely because of the additional presence of pure liposomes and polymersomes. This heterogeneity seems to decrease when the molar mass of copolymer further decreases, leading to the formation of a more homogeneous vesicle population with membrane thicknesses close to that of liposomes (~ 5 nm). Interestingly, changing the copolymer architecture from triblock to grafted while maintaining the chemical nature, molar mass and membrane thickness unchanged, leads to a considerably more efficient mixing of the lipid and polymer molecules into the same membrane, generating hybrid vesicles presenting few lipid nanodomains of several nanometres (3 – 7 nm radius). This indicates that line tension at the lipid/polymer boundaries can be modulated through the architecture of the copolymer, in addition to the molar mass and chemical nature of the block. Although it is premature to generalize our results to all kind of copolymer/lipid assemblies, it is important to realize that association of copolymers and lipids that could be obtained on giant unilamellar hybrid vesicles (GHUVs) does not systematically reflect what happens at the nanoscale. In the case of LHUVs, higher curvature energy may add to the hydrophobic mismatch and chemical incompatibility between lipid tails and hydrophobic

copolymer blocks. Therefore, great attention has to be paid to the characterization of such structures before going further in the evaluation of their physical (e.g. membrane permeability, drug release, phase behaviour) or bio-functional (e.g. protein insertion, bio-recognition) properties. Techniques available in-lab such as Dynamic Light Scattering and Cryo-TEM commonly used to characterize classical LUVs may be insufficient to confirm the hybrid character of the vesicles. In addition, counting techniques such as Flow cytometry suffer from a lack of sensitivity at such vesicle size (100 nm). Beyond the issue of solving properly the hybrid character and membrane structure of such assemblies, it appears essential to think about other methods to marry block copolymers with high molecular weight and phospholipids into LHUVs in an efficient way, by playing either on molecular aspects (e.g. cholesterol addition) or by introducing new formulation processes.

ANNEX

A.4.1. SANS characterization for pure DPPC LUVs

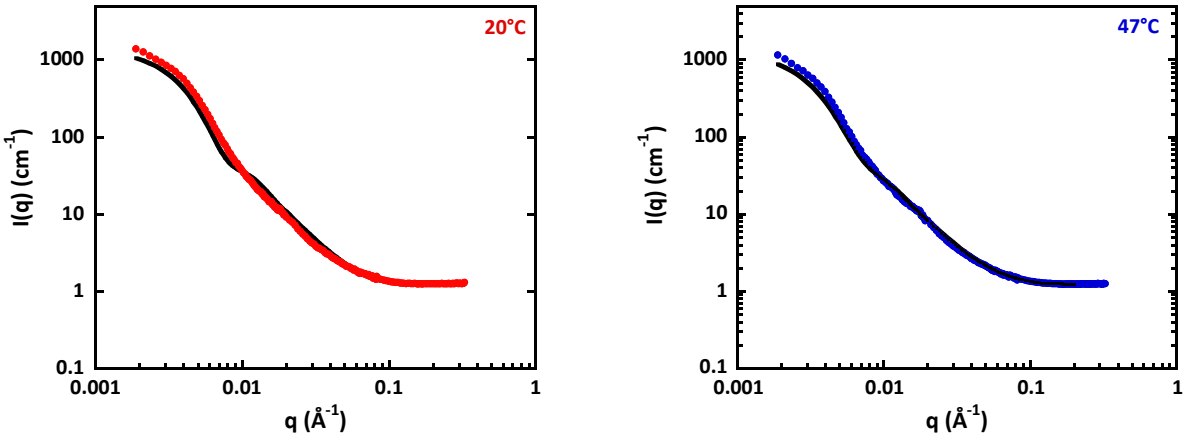

Figure A.4.1. SANS curves obtained for pure DPPC-d_{62} LUVs and best fit with the vesicle model (line). On the left: experiment at 20°C and on the right: experiment at 47°C.

Table A.4.1. Best fit parameters with vesicle model of SANS curves obtained from DPPC-d_{62} LUVs at 20°C and 47°C

T°C	Guinier plot	Vesicle form factor			
	R_g (nm)	R_ϑ (nm)	σ_{R_ϑ}	δ_ϑ (nm)	$\sigma_{\delta_\vartheta}$
20°C	45 ± 2	27	0.32	4.3	0.15
47°C	50 ± 2	31	0.31	3.1	0.15

A.4.2. Cryo-TEM for pure DPPC LUVs

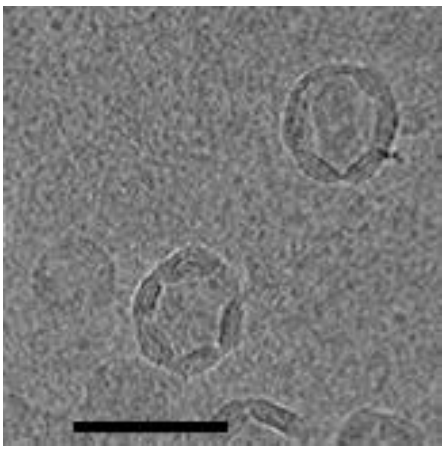

Figure A.4.2. Cryo-TEM image of pure DPPC LUVs quenched from room temperature. Scale bar length: 100 nm.

The membrane thicknesses of pure DPPC LUVs at 20°C and 47°C determined by Cryo-TEM are 6.2 ± 0.4 nm and 5.9 ± 0.6 nm respectively.

A.4.3. Guinier plots

Radii of gyration R_g were evaluated through the Guinier plots at low q regime. Some examples are given in Figures below.

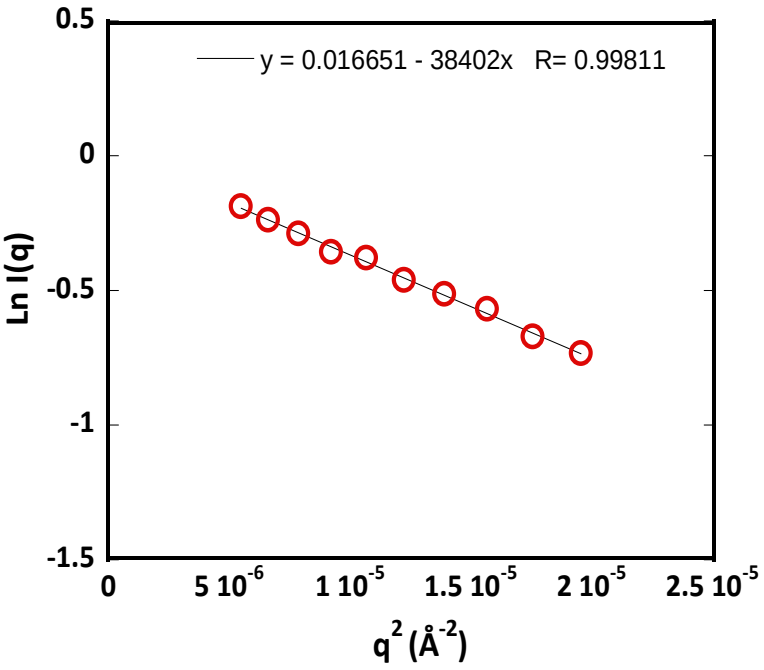

Figure A.4.3. Guinier plots of PEO_8-*b*-$PDMS_{22}$-*b*-PEO_8/DPPC-d_{62} mixture at 20°C (with lipid weight fraction f_d = 0.15) in polymer contrast. R_g was recovered from the slope of the linear fit.

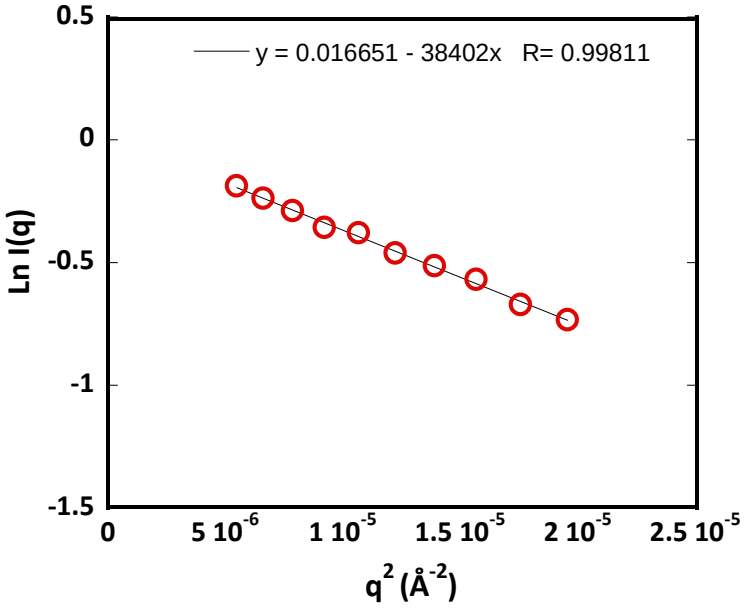

Figure A.4.4. Guinier plots of PEO_8-*b*-$PDMS_{22}$-*b*-PEO_8/DPPC-d_{62} mixture at 20°C (with lipid weight fraction f_d = 0.21) in lipid contrast. R_g was recovered from the slope of the linear fit.

REFERENCES

1. Pedersen, J.S., ed. *Neutron, X-rays and Light. Scattering Methods Applied to Soft Condensed Matter* 2002, (North-Holland Delta Series) Elsevier ed.; Elsevier; Amsterdam.
2. Bergström, L.M., et al., *Spontaneous Transformations between Surfactant Bilayers of Different Topologies Observed in Mixtures of Sodium Octyl Sulfate and Hexadecyltrimethylammonium Bromide.* Langmuir, 2014. **30**(14): p. 3928-3938.
3. Heberle, F.A., et al., *Hybrid and nonhybrid lipids exert common effects on membrane raft size and morphology.* Journal of the American Chemical Society, 2013. **135**(40): p. 14932-14935.
4. Anghel, V.N., et al., *Scattering from laterally heterogeneous vesicles. II. The form factor.* Journal of Applied Crystallography, 2007. **40**(3): p. 513-525.
5. Heberle, F.A., V.N. Anghel, and J. Katsaras, *Scattering from phase-separated vesicles. I. An analytical form factor for multiple static domains.* Journal of Applied Crystallography, 2015. **48**(5): p. 1391-1404.
6. Mildner, D.t. and J. Carpenter, *Optimization of the experimental resolution for small-angle scattering.* Journal of applied crystallography, 1984. **17**(4): p. 249-256.
7. Pedersen, J.S., D. Posselt, and K. Mortensen, *Analytical treatment of the resolution function for small-angle scattering.* Journal of Applied Crystallography, 1990. **23**(4): p. 321-333.
8. Davenport, L., et al., *Transverse location of the fluorescent probe 1,6-diphenyl-1,3,5-hexatriene in model lipid bilayer membrane systems by resonance excitation energy transfer.* Biochemistry, 1985. **24**(15): p. 4097-4108.
9. Loura, L.M.S., F. Fernandes, and M. Prieto, *Membrane microheterogeneity: Förster resonance energy transfer characterization of lateral membrane domains.* European Biophysics Journal, 2010. **39**(4): p. 589-607.
10. de Almeida, R.F.M., et al., *Complexity of Lipid Domains and Rafts in Giant Unilamellar Vesicles Revealed by Combining Imaging and Microscopic and Macroscopic Time-Resolved Fluorescence.* Biophysical Journal, 2007. **93**(2): p. 539-553.
11. Loura, L.M.S. and J.P.P. Ramalho, *Recent Developments in Molecular Dynamics Simulations of Fluorescent Membrane Probes.* Molecules, 2011. **16**(7): p. 5437.
12. Abrams, F.S. and E. London, *Extension of the parallax analysis of membrane penetration depth to the polar region of model membranes: Use of fluorescence quenching by a spin-label attached to the phospholipid polar headgroup.* Biochemistry, 1993. **32**(40): p. 10826-10831.
13. Mello-Vieira, J., et al., *Cytotoxic bile acids, but not cytoprotective species, inhibit the ordering effect of cholesterol in model membranes at physiologically active concentrations.* Biochimica et Biophysica Acta (BBA) - Biomembranes, 2013. **1828**(9): p. 2152-2163.
14. Nagle, J. and M. Wiener, *Structure of fully hydrated bilayer dispersions.* Biochimica et Biophysica Acta (BBA)-Biomembranes, 1988. **942**(1): p. 1-10.
15. Nagle, J.F. and S. Tristram-Nagle, *Structure of lipid bilayers.* Biochimica et Biophysica Acta (BBA)-Reviews on Biomembranes, 2000. **1469**(3): p. 159-195.

16. Andersson, M., L. Hammarstroem, and K. Edwards, *Effect of Bilayer Phase Transitions on Vesicle Structure, and its Influence on the Kinetics of Viologen Reduction.* The Journal of Physical Chemistry, 1995. **99**(39): p. 14531-14538.

17. Safran, S.A., et al., *Stability and phase behavior of mixed surfactant vesicles.* Physical Review A, 1991. **43**(2): p. 1071-1078.

18. Khan, S., et al., *Durable proteo-hybrid vesicles for the extended functional lifetime of membrane proteins in bionanotechnology.* Chemical Communications, 2016. **52**(73): p. 11020-11023.

19. Cheng, Z., et al., *Improved Tumor Targeting of Polymer-based Nanovesicles Using Polymer-Lipid Blends.* Bioconjugate Chemistry, 2011. **22**(10): p. 2021–2029.

20. Winzen, S., et al., *Submicron hybrid vesicles consisting of polymer-lipid and polymer-cholesterol blends.* Soft Matter, 2013. **9**(25): p. 5883-5890.

21. Lim, S., et al., *Hybrid, Nanoscale Phospholipid/Block Copolymer Vesicles.* Polymers, 2013. **5**(3): p. 1102.

22. Panneerselvam, K., et al., *Phospholipid-polymer amphiphile hybrid assemblies and their interaction with macrophages.* Biomicrofluidics, 2015. **9**(5).

23. Pippa, N., et al., *PEO-b-PCL-DPPC chimeric nanocarriers: self-assembly aspects in aqueous and biological media and drug incorporation.* Soft Matter, 2013. **9**(15): p. 4073-4082.

24. Nam, J., P.A. Beales, and T.K. Vanderlick, *Giant Phospholipid/Block Copolymer Hybrid Vesicles: Mixing Behavior and Domain Formation.* Langmuir, 2011. **27**(1): p. 1-6.

25. Schulz, M., et al., *Lateral surface engineering of hybrid lipid-BCP vesicles and selective nanoparticle embedding.* Soft Matter, 2014. **10**(6): p. 831-839.

CHAPTER 5

PHASE SEPARATION IN HYBRID POLYMER/LIPID GIANT UNILAMELLAR VESICLES

Table of Contents

OUTLINE

In this chapter, the phase separation in hybrid polymer/lipid vesicles at micron scale is discussed as a function of polymer/lipid composition, hydrophobic mismatch, lipid fluidity and copolymer architecture. In that purpose, we first report in section 5.1 a global view about phase separation *via* a systematic study on different giant hybrid vesicles. Briefly, the copolymers with same chemical nature but varying molar masses and architectures (grafted, triblock) were blended individually with phospholipid in fluid or gel state to formulate different GHUVs and their membrane structures were studied either at micron scale (formation of microdomains) or nanoscale. Domain stability driven by a balance between bending energy of the domain and line tension at the boundaries which can eventually lead to budding and/or fission phenomenon was also studied thoroughly.

Fluorescence confocal imaging was the main method to reveal information on the micrometric domains and particularly, an advanced microscopy methodology, FLIM-FRET (Förster Resonance Energy Transfer measurement through Fluorescence Lifetime Imaging Microscopy) was a complementary tool to detect nanodomains below the resolution of microscope. All the information on each hybrid system was summarized in an apparent phase diagram, and the different molecular parameters acting on the structuration of GHUVs are discussed in section 5.2.

5.1. DESCRIPTION OF PHASE SEPARATION IN DIFFERENT HYBRID GIANT SYSTEMS

5.1.1. Micron and nano scale fluid/fluid phase separation in GHUVs

In the following, the results for each copolymer will be shown in succession. As in Chapter 4, we start with the shortest triblock which self-assembles in vesicles with membrane thickness comparable to the membrane thickness of liposomes (a small hydrophobic mismatch is expected) and then go to systems which form a membrane significantly thicker (larger hydrophobic mismatch is expected). The effect of the architecture of copolymer, from previous results obtained by the team [1] using grafted copolymer $PDMS_{26}$-*g*-$(PEO_{12})_2$, and complementary experiments done in the framework of this thesis, will be discussed.

5.1.1.1. Case of PEO_8-*b*-$PDMS_{22}$-*b*-PEO_8/POPC mixtures

PEO_8-*b*-$PDMS_{22}$-*b*-PEO_8/POPC GHUVs were produced by the electroformation protocol as detailed in Chapter 2. They were generally within the 20 – 50 µm size range, unilamellar and stable at room temperature during at least three days. The preparation for all PEO_8-*b*-$PDMS_{22}$-*b*-PEO_8/lipid GHUVs in this section was always performed the day before analysis in order to study vesicles in an "equilibrium" state.

Micron scale phase separation

The phase separation in PEO_8-*b*-$PDMS_{22}$-*b*-PEO_8/POPC GHUVs was first characterized through confocal microscopy. The vesicles were loaded with both FITC labelled $PDMS_{26}$-*g*-$(PEO_{12})_2$ and Rhodamine labelled lipid DOPE, enabling the recognition of each phase. As seen in Figure 5.1, there is no difficulty to distinguish a mixed hybrid vesicle (A) where both of the probes are homogeneously distributed, from a demixed hybrid vesicle (B) where phase separation occurs leading to the formation of lipid rich fluid and polymer rich domains.

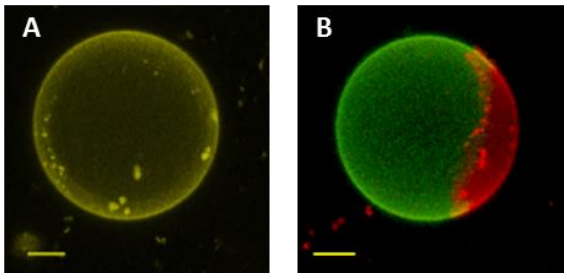

Figure 5.1. Overlay of maximum intensity 2D projection images taken for PEO_8-*b*-$PDMS_{22}$-*b*-PEO_8/POPC GHUVs loaded $PDMS_{26}$-*g*-$(PEO_{12})_2$-FITC (green channel) and DOPE-Rhod (red channel); A: mixed GHUV with homogeneous distribution of both signals; B: demixed GHUV with separated green signal (polymer-rich phase) and red signal (lipid-rich phase); scale bars: 5 µm.

In order to fully characterize the tendency for micrometric fluid-lipid domain formation in PEO_8-*b*-$PDMS_{22}$-*b*-PEO_8/POPC GHUVs, the GHUVs were monitored within the entire range of polymer/lipid weight fractions and at different temperatures, from room temperature (20°C) up to 55°C. First of all, no macroscopic domains were observed in GHUVs prepared from mixtures with less than 16% of POPC at room temperature. As shown in Figure 5.2, with 5% and 10% POPC, the membrane seemed to integrate ideally these low concentrations of lipid into the polymer-rich matrix, forming homogeneous hybrid vesicles at least at the micron scale. At higher POPC contents, formation of vesicles presenting fluid lipid-rich domains was detected and their number increases with the lipid content. Indeed, the phase coexistence was observed in more than 50% of hybrid vesicles prepared from mixtures containing more than 25% weight of lipid.

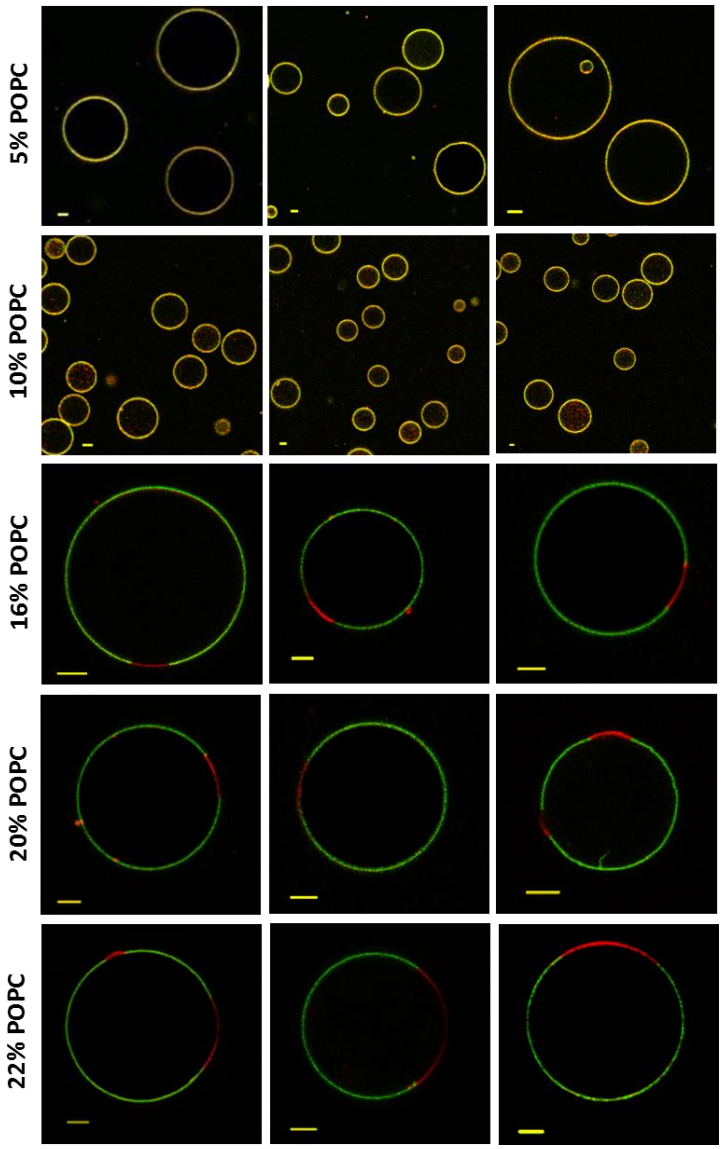

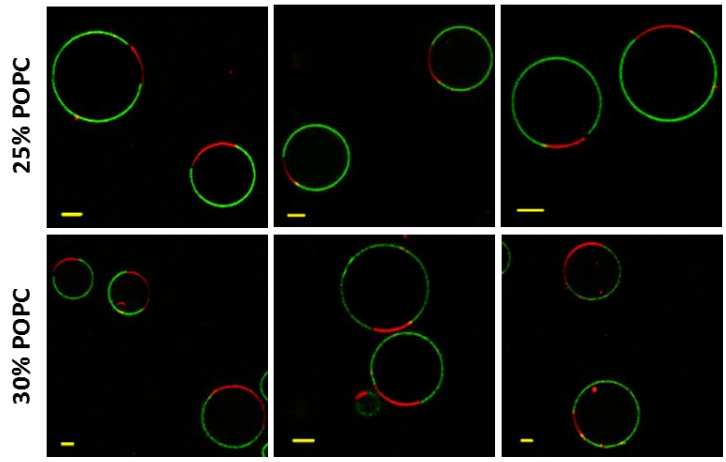

Figure 5.2. The equatorial slices of PEO_8-*b*-$PDMS_{22}$-*b*-PEO_8/POPC GHUVs labelled with $PDMS_{26}$-*g*-$(PEO_{12})_2$-FITC (green channel) and DOPE-Rhod (red channel) in the range of 5%, 10%, 16%, 20%, 22%, 25% and 30% POPC (% wt) measured by confocal fluorescence microscopy at room temperature; scale bars: 5 µm.

It is also important to notice that above 50% of POPC, domain budding occurs. Figure 5.3 shows a series of images taken over a broad range of 50% - 90% of POPC. It can be clearly seen that those budded domains could be either polymer or lipid phase. Interestingly, in many cases, they were stable at room temperature during at least two days after electroformation. This was not the case in $PDMS_{26}$-*g*-$(PEO_{12})_2$/POPC mixtures [1] where budding and fission phenomenon was seen, although not systematically, frequently observed for lipid fraction equal or above 22% w/w.

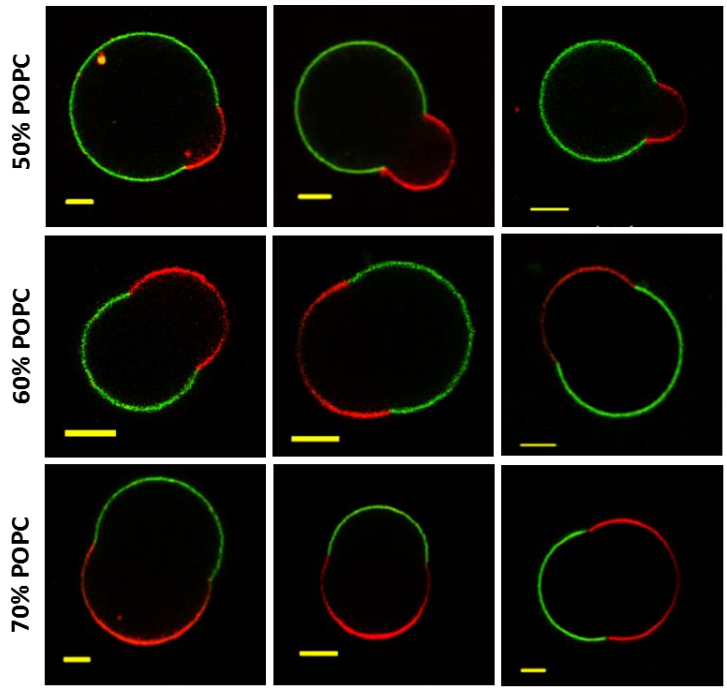

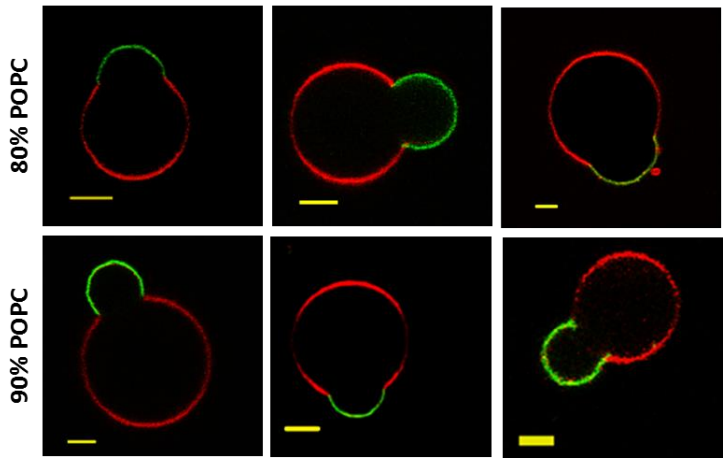

Figure 5.3. The equatorial slices of PEO_8-*b*-$PDMS_{22}$-*b*-PEO_8/POPC GHUVs containing 50%, 60%, 70%, 80% and 90% POPC (% wt) labelled with $PDMS_{26}$-*g*-$(PEO_{12})_2$-FITC (green channel) and DOPE-Rhod (red channel) measured by confocal fluorescence microscopy at room temperature; scale bars: 5 µm.

Interestingly, at higher temperatures, a minor change in the boundary of the phase coexistence region was observed. Indeed, in some cases, lipid domains in PEO_8-*b*-$PDMS_{22}$-*b*-PEO_8/POPC GHUVs with low POPC concentration (16%) at 20°C were no longer visible when temperature was increased. This was surprising since POPC is a low T_m phospholipid and is expected to be always in the fluid phase for range of temperature studied (20°C-55°C). Additionally, temperature is shown to be crucial for the stability of budded domains as at high POPC content (80%) and above 35°C, they were no longer visible and two GUV populations were now present with either polymer-rich phases or lipid-rich homogeneous phases. This suggests that fission of coexisting domains is significantly more efficient at higher temperatures. Figure 5.4 illustrates this fission event occurring with a budded lipid-domain (A) as well as budded polymer-domain (B).

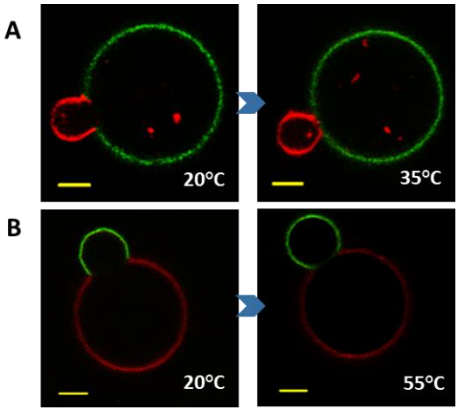

Figure 5.4. The equatorial slices of PEO_8-*b*-$PDMS_{22}$-*b*-PEO_8/POPC GHUVs at 90% POPC labelled with $PDMS_{26}$-*g*-$(PEO_{12})_2$-FITC (green channel) and DOPE-Rhod (red channel) measured by confocal fluorescence microscopy at different temperature. A: fission of budded lipid domain at 35°C and B: fission of budded polymer domains at 55°C; scale bars: 5 µm.

According to all observations described above, we present in Figure 5.5 an "apparent" phase diagram representative for PEO_8-*b*-$PDMS_{22}$-*b*-PEO_8/POPC hybrid system at micron scale, where the morphologies and membrane structure of vesicles obtained are represented at different temperature *versus* the initial polymer/lipid fractions. It is worth mentioning that the initial fractions do not reflect systematically the composition of each hybrid vesicles.

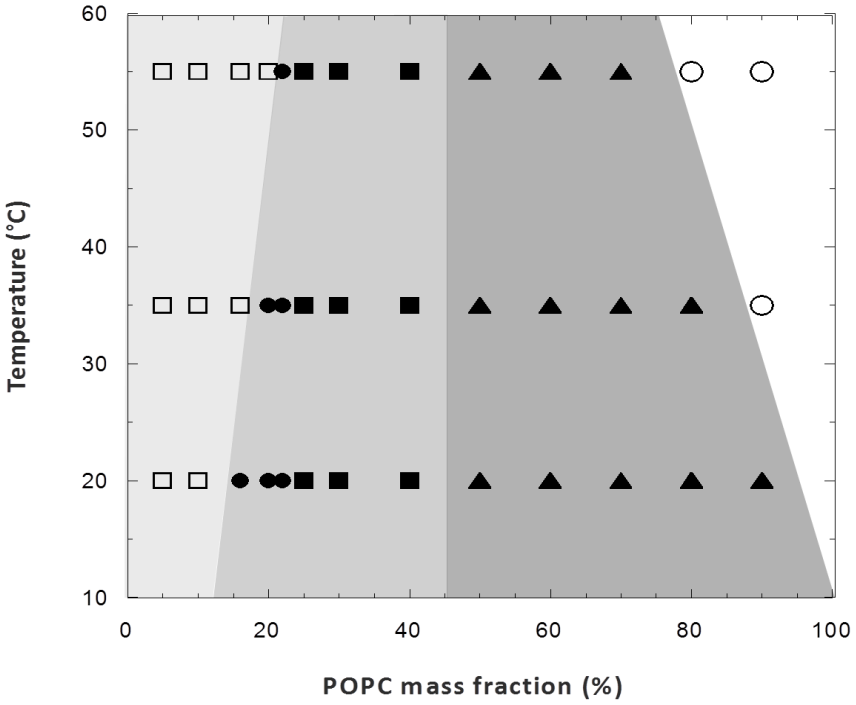

Figure 5.5. Outlined apparent phase diagram for PEO_8-*b*-$PDMS_{22}$-*b*-PEO_8/POPC binary system determined by confocal microscopy; symbols represent characteristic fractions and temperatures; shaded areas depict regions of the phase diagram with and without macroscopic phase separation, as well as the stability of coexisting domains. □: no macroscopic domains; ●: fraction of vesicle exhibiting phase separation lower than 50%; ■: fraction of vesicle exhibiting phase separation higher than 50%; ▲: stable domain budding; ○: fission of budded domains.

It is important to note that the results are quite different from the system $PDMS_{26}$-*g*-$(PEO_{12})_2$/POPC, already studied previously by the team [1]. The $PDMS_{26}$-*g*-$(PEO_{12})_2$ is a copolymer with similar molar mass compared to PEO_8-*b*-$PDMS_{22}$-*b*-PEO_8 and self-assembles into vesicles with the same membrane thickness (~ 5 nm) but different architecture (grafted instead of triblock). In this system, micron scale phase separation occurred in GHUVs with more than 50% molar of POPC (equivalent with 22% in weight). Particularly, it was illustrated that these biphasic vesicles only remain stable for few hours at room temperature. Indeed, a budding fission process occurred in most of the cases leading to the formation of separated polymersomes and liposomes.

Nanoscale phase separation

The apparent phase diagram shown in Figure 5.5 only describes the regions of microscale phase separation. In fact, confocal microscopy cannot probe the nanoscale phase separation since these heterogeneities occur below the spatial resolution provided by this technique. Consequently, in this part, we introduce the FLIM-FRET measurements performed on the GHUVs at for which no macroscopic domain was visible under confocal imaging. Theoretically, FRET efficiency between the polymer analogue ($PDMS_{26}$-*g*-$(PEO_{12})_2$-FITC: FRET donor) and phospholipid analogue (DOPE-Rhod: FRET acceptor) is extremely sensitive to phase separation in hybrid vesicles since the polymer analogue can only be incorporated in the polymer rich phase and the lipid analogue incorporates preferentially in lipid rich phases. As introduced in Chapter 4, the phase separation is expected to drive a decrease in FRET efficiencies as the average distance between donors and acceptors increases. For FLIM-FRET measurement in GHUVs, the polymer analogue $PDMS_{26}$-*g*-$(PEO_{12})_2$-FITC was used as FRET donor instead of $PDMS_{26}$-*g*-$(PEO_{12})_2$-NBD used for LHUVs, as FITC is more photostable than NBD, allowing sample observation under the microscope.

First of all, we examined the pure PEO_8-*b*-$PDMS_{22}$-*b*-PEO_8 polymersomes loaded only $PDMS_{26}$-*g*-$(PEO_{12})_2$-FITC for which the lifetime histogram presents a homogenous distribution centred at about 3 ns. When the acceptor probe is added, a large decrease of FITC fluorescence lifetime is observed as a consequence of a random distribution of the probes within the membrane, and therefore close proximity between donor and acceptor molecules (Figure 5.6).

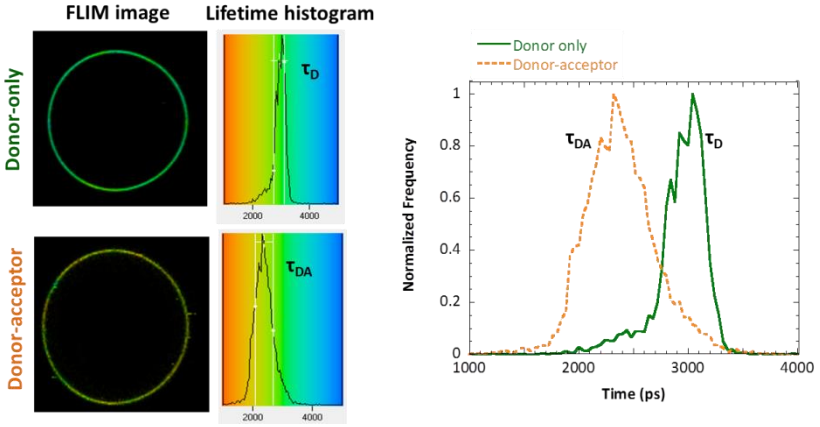

Figure 5.6. Equatorial z-section fluorescence lifetime images and their representative $PDMS_{26}$-*g*-$(PEO_{12})_2$-FITC fluorescence lifetime distribution histograms of pure PEO_8-*b*-$PDMS_{22}$-*b*-PEO_8 GUVs labelled with only $PDMS_{26}$-*g*-$(PEO_{12})_2$-FITC (1.5% molar) or with both $PDMS_{26}$-*g*-$(PEO_{12})_2$-FITC (1.5% molar) and DOPE-Rhod (0.5% molar). FRET between FITC and Rhod is responsible for the decrease in $PDMS_{26}$-*g*-$(PEO_{12})_2$-FITC fluorescence lifetimes.

Then we have studied PEO_8-*b*-$PDMS_{22}$-*b*-PEO_8/POPC GHUVs at different lipid content (typically 5%, 10% and 15% of POPC). Without acceptor (GHUVs loaded with only 1.5% molar of donor), $PDMS_{26}$-*g*-$(PEO_{12})_2$-FITC fluorescence lifetime images of those vesicles as well as their corresponding histogram are shown in Figure 5.7. When POPC was incorporated, the $PDMS_{26}$-*g*-$(PEO_{12})_2$-FITC lifetime distribution in those membranes became broader and slightly shifted to lower values. This dependence of $PDMS_{26}$-*g*-$(PEO_{12})_2$-FITC fluorescence lifetime with lipid content is likely the result of changes in polymer phase properties due to the insertion of lipid molecules, since no FRET takes place given the absence of acceptor molecules.

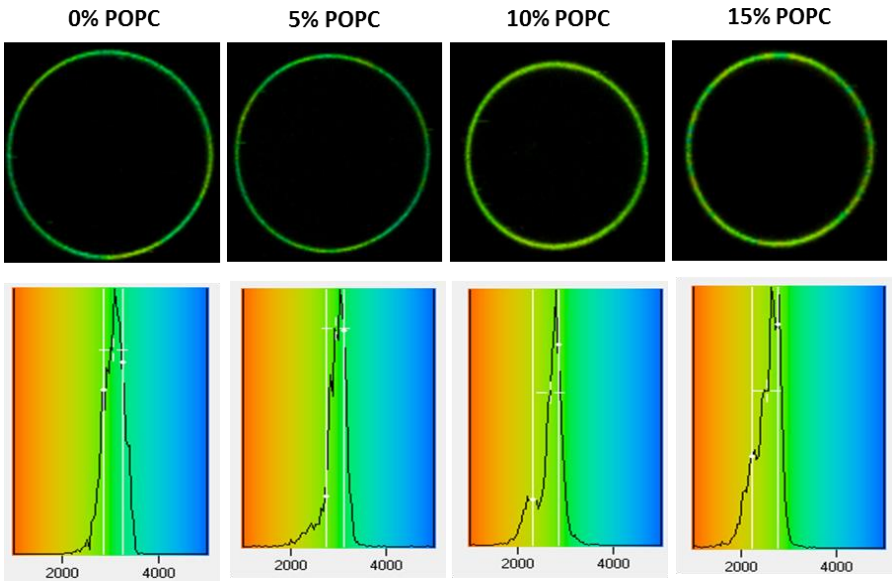

Figure 5.7. Equatorial z-section fluorescence lifetime images and its corresponding fluorescence lifetime distribution histogram of GHUVs prepared from different mixtures of PEO_8-*b*-$PDMS_{22}$-*b*-PEO_8/POPC GHUVs at room temperature, labelled with only $PDMS_{26}$-*g*-$(PEO_{12})_2$-FITC (1.5% molar).

GHUVs were then loaded with both FRET donor (1.5% molar) and FRET acceptor (0.5% molar) for each of the above described PEO_8-*b*-$PDMS_{22}$-*b*-PEO_8/POPC compositions. The fluorescence lifetime of $PDMS_{26}$-*g*-$(PEO_{12})_2$-FITC were recorded to assess FRET efficiencies. As seen in Figure 5.8, the decrease of the $PDMS_{26}$-*g*-$(PEO_{12})_2$-FITC fluorescence lifetime was not as pronounced as the one observed in pure polymersomes where a homogenous distribution was obviously expected, and a clear decrease of FRET was detected. In addition, the fluorescence single decays were also measured for about 10 – 15 individual vesicles in each sample and similar results were obtained (Table 5.1 lists the average lifetime values obtained). The clear decrease of FRET efficiencies with increasing POPC content was shown in Figure 5.9.

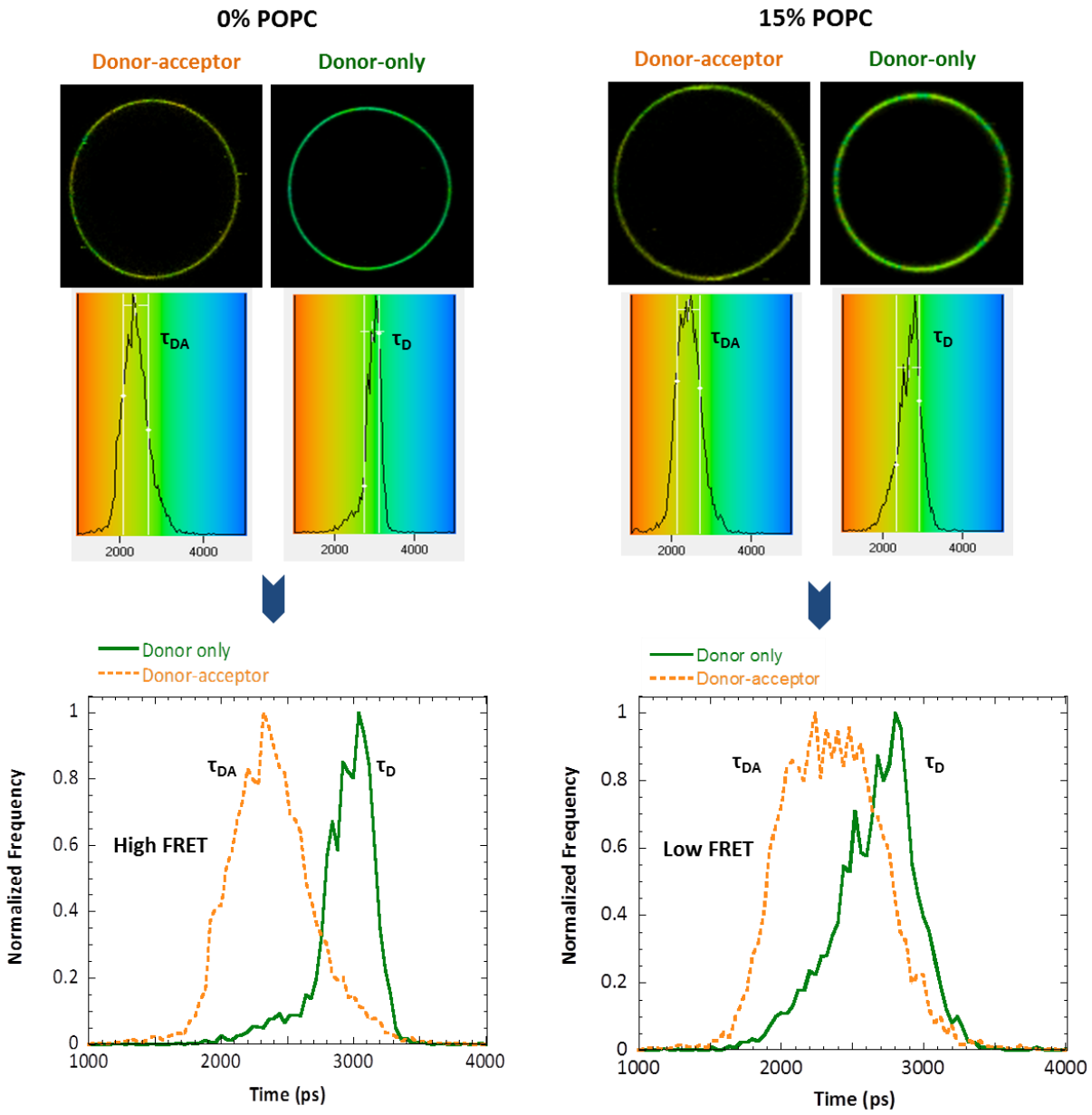

Figure 5.8. Equatorial z-section fluorescence lifetime images and their representative $PDMS_{26}$-*g*-$(PEO_{12})_2$-FITC fluorescence lifetime distribution histograms of pure PEO_8-*b*-$PDMS_{22}$-*b*-PEO_8 GUVs and GHUVs prepared from mixtures of 15% POPC labelled with only $PDMS_{26}$-*g*-$(PEO_{12})_2$-FITC (1.5% molar) or with both $PDMS_{26}$-*g*-$(PEO_{12})_2$-FITC (1.5% molar) and DOPE-Rhod (0.5% molar). FRET between FITC and Rhod is responsible for the decrease in $PDMS_{26}$-*g*-$(PEO_{12})_2$-FITC fluorescence lifetimes.

Since molecular areas are significantly smaller for POPC than for PEO_8-*b*-$PDMS_{22}$-*b*-PEO_8, an increase in POPC content is expected to decrease total membrane area and thus higher FRET efficiencies are expected (acceptor densities become larger) in case of homogeneous distributions of polymer and lipid. Therefore, the decrease in FRET efficiency detected here must be the result of nanoscale phase separation that increases the average distance between donor and acceptor probes in hybrid vesicles.

Table 5.1. The average fluorescence lifetime of $PDMS_{26}$-*g*-$(PEO_{12})_2$-FITC in different PEO_8-*b*-$PDMS_{22}$-*b*-PEO_8/POPC GHUVs obtained from fluorescence single decay measurements and corresponding FRET efficiency. ($\overline{\tau_D}$: average fluorescence lifetime in GHUVs loaded only 1.5% molar of $PDMS_{26}$-*g*-$(PEO_{12})_2$-FITC; $\overline{\tau_{DA}}$: average fluorescence lifetime in GHUVs loaded 1.5% molar of $PDMS_{26}$-*g*-$(PEO_{12})_2$-FITC and 0.5% molar of DOPE-Rhod).

% w/w POPC	$\overline{\tau_D}$ ± SD (ns)	$\overline{\tau_{DA}}$ ± SD (ns)	FRET efficiency
0%	3.102 ± 0.103	2.632 ± 0.047	0.152 ± 0.030
5%	3.065 ± 0.092	2.612 ± 0.046	0.148 ± 0.028
10%	2.931 ± 0.051	2.567 ± 0.042	0.124 ± 0.020
15%	2.890 ± 0.044	2.636 ± 0.036	0.088 ± 0.018

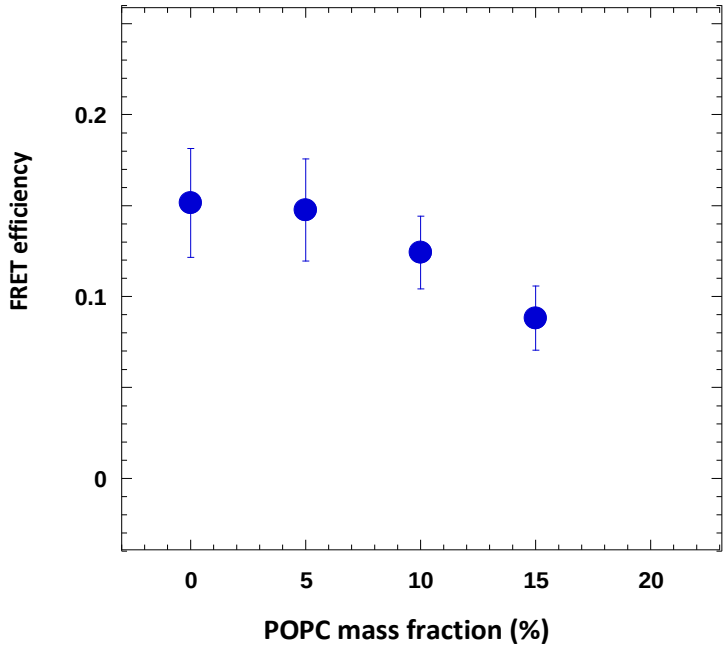

Figure 5.9. FRET efficiencies in PEO_8-*b*-$PDMS_{22}$-*b*-PEO_8/POPC GHUVs *vs* POPC content.

Alternatively, according to Monte Carlo simulations for membrane systems, a decrease in FRET efficiencies would only be noticeable if domain dimensions were larger than the Förster radius of the donor-acceptor FRET pair (in this case R_0 = 5 nm) [2, 3]. In this way, nanoscale phase separation into domains larger than 5 nm is evidenced in PEO_8-*b*-$PDMS_{22}$-*b*-PEO_8/POPC GHUVs at lipid content as low as 10%. At lower POPC concentrations, no FRET changes are observed, suggesting that either no phase separation takes place or that lipid domains are smaller than 5 nm.

The phase diagram for PEO_8-*b*-$PDMS_{22}$-*b*-PEO_8/POPC hybrid system is now represented in Figure 5.10 with additional information on nanoscale phase separation.

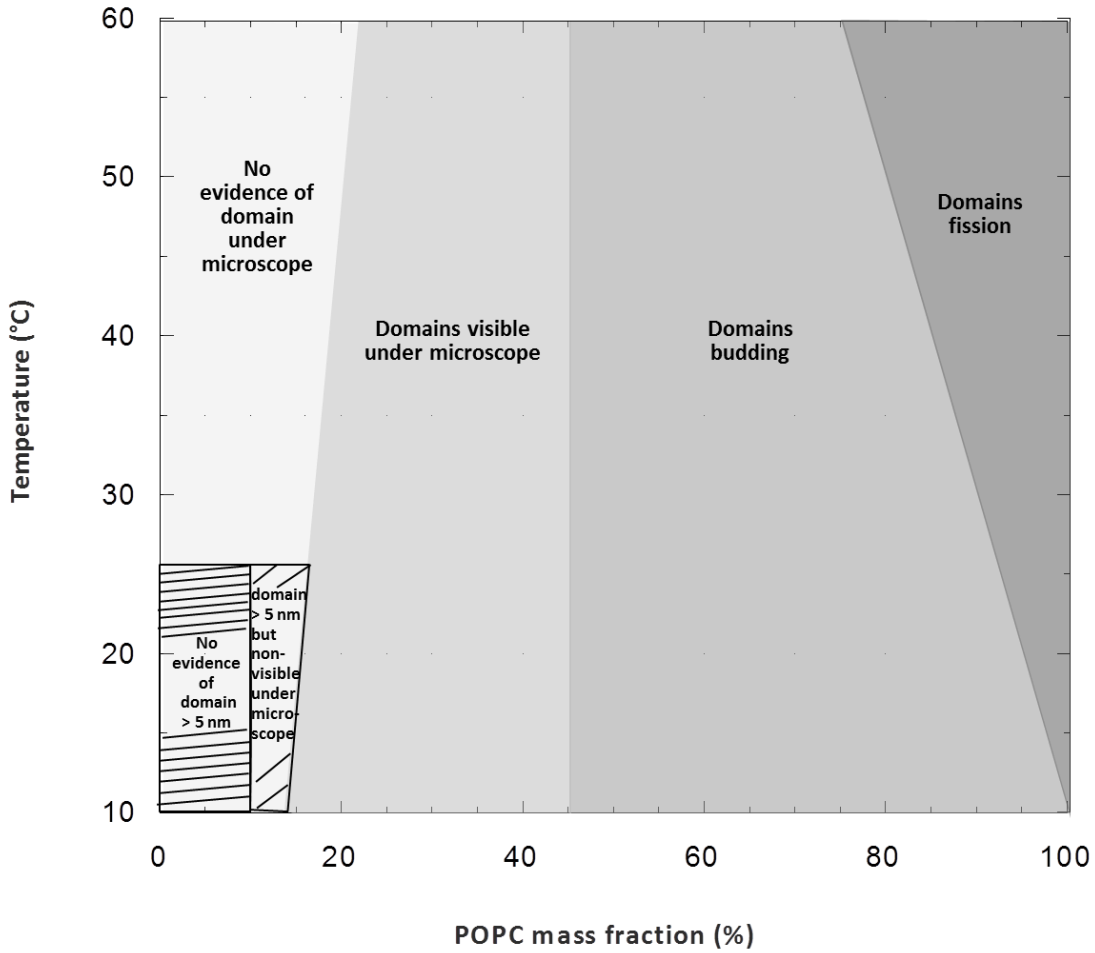

Figure 5.10. Outlined phase diagram for PEO_8-*b*-$PDMS_{22}$-*b*-PEO_8/POPC binary system determined by confocal microscopy and FLIM-FRET measurements on micron-size vesicles.

The same FLIM-FRET methodology was applied to the GHUVs of $PDMS_{26}$-*g*-(PEO_{12})/POPC. The phase separation in this mixture was already studied at micron scale [1] but not yet at nano scale. Interestingly, a decrease in FRET efficiency was also recorded when POPC was included in the mixture and it decreases gradually with increasing amount of POPC, again suggesting nanoscale phase separation. Data is detailed in Table 5.2.

Table 5.2. The average fluorescence lifetime of $PDMS_{26}$-*g*-$(PEO_{12})_2$-FITC in different $PDMS_{26}$-*g*-(PEO_{12})/POPC GHUVs obtained from fluorescence single decay measurements and corresponding FRET efficiency. ($\overline{\tau_D}$: average fluorescence lifetime in GHUVs loaded only 1.5% molar of $PDMS_{26}$-*g*-$(PEO_{12})_2$-FITC; $\overline{\tau_{DA}}$: average fluorescence lifetime in GHUVs loaded 1.5% molar of $PDMS_{26}$-*g*-$(PEO_{12})_2$-FITC and 0.5% molar of DOPE-Rhod).

% w/w POPC	$\overline{\tau_D}$ ± SD (ns)	$\overline{\tau_{DA}}$ ± SD (ns)	FRET efficiency
0%	3.025 ± 0.061	2.681 ± 0.044	0.114 ± 0.022
10%	2.903 ± 0.043	2.609 ± 0.029	0.101 ± 0.016
15%	2.737 ± 0.032	2.549 ± 0.035	0.069 ± 0.016

5.1.1.2. Case of PEO_{12}-*b*-$PDMS_{43}$-*b*-PEO_{12}/POPC mixtures

PEO_{12}-*b*-$PDMS_{43}$-*b*-PEO_{12} is the triblock copolymer which form vesicles with membrane thickness of 8.8 ± 0.5 nm, higher than those of liposomes, therefore high hydrophobic mismatch is expected at the lipid/polymer phase boundaries.

Micron scale phase separation

With such mixture, no vesicles with phase coexistence were observed for POPC concentration up to 40%: homogeneous yellow hybrid vesicles were observed on the overlay images due to the presence of both DOPE-Rhod and $PDMS_{26}$-*g*-$(PEO_{12})_2$-FITC fluorescence (Figure 5.11). In addition, the presence of pure liposomes was slightly more pronounced compared to PEO_8-*b*-$PDMS_{22}$-*b*-PEO_8. It represents for instance approximately 30% of the population for the initial mixture at 20 % w/w POPC, whereas it was only 4 – 5 % for the same composition for PEO_8-*b*-$PDMS_{22}$-*b*-PEO_8.

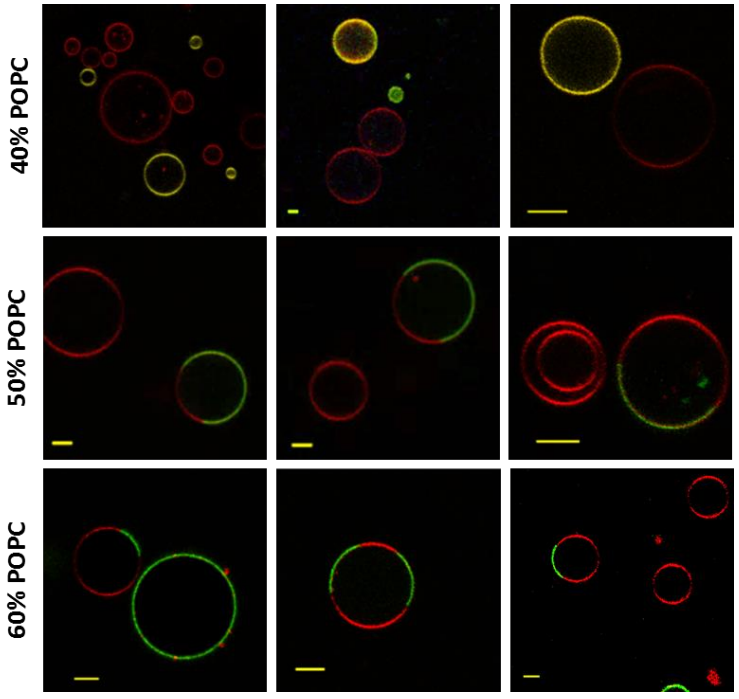

Figure 5.11. The equatorial slices of PEO_{12}-*b*-$PDMS_{43}$-*b*-PEO_{12}/POPC GHUVs containing 40%, 50% and 60% POPC (% wt) labelled with $PDMS_{26}$-*g*-$(PEO_{12})_2$-FITC (green channel) and DOPE-Rhod (red channel) measured by confocal fluorescence microscopy at room temperature; scale bars: 5 µm.

Particularly, budding of domains became more frequent for the whole range of fractions where phase coexistence was seen (> 50% POPC). Some representative images of each composition are displayed in Figure 5.12. Notice that unlike the mixture of PEO_8-*b*-$PDMS_{22}$-*b*-

PEO_8/POPC where the budded domains observed could be lipid phase or polymer-rich phase, all budded domains here are always the polymer-rich phase.

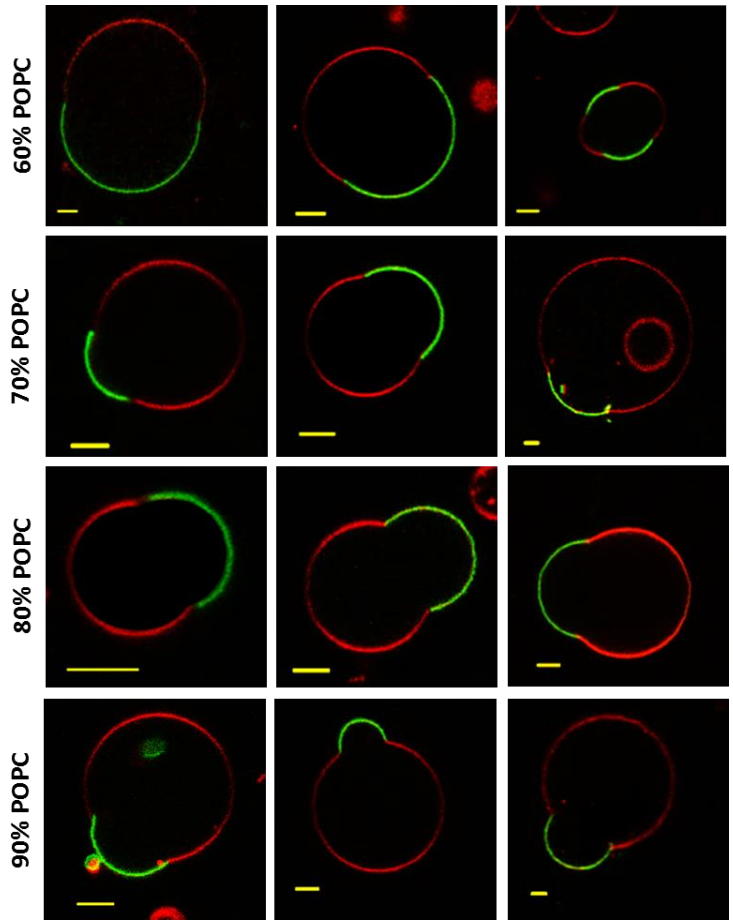

Figure 5.12. The equatorial slices of PEO_{12}-*b*-$PDMS_{43}$-*b*-PEO_{12}/POPC GHUVs labelled with $PDMS_{26}$-g-$(PEO_{12})_2$-FITC (green channel) and DOPE-Rhod (red channel) containing 60%, 70%, 80% and 90% POPC (% wt) measured by confocal fluorescence microscopy at room temperature; scale bars: 5 µm.

However, like PEO_8-*b*-$PDMS_{22}$-*b*-PEO_8/POPC GHUVs, they also exhibited fission into separated vesicles at high temperature as shown in Figure 5.13.

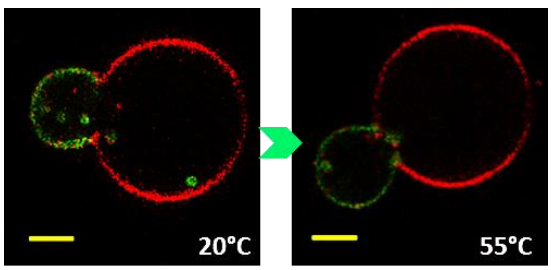

Figure 5.13. Illustration of fission of budded domains in PEO_{12}-*b*-$PDMS_{43}$-*b*-PEO_{12}/POPC GHUVs at high temperature, GHUVs were labelled with $PDMS_{26}$-*g*-$(PEO_{12})_2$-FITC (green channel) and DOPE-Rhod (red channel); scale bars: 5 µm.

All visualizations reported above were summarized into Figure 5.14 which is an outlined phase diagram for PEO_{12}-*b*-$PDMS_{43}$-*b*-PEO_{12}/POPC GHUVs.

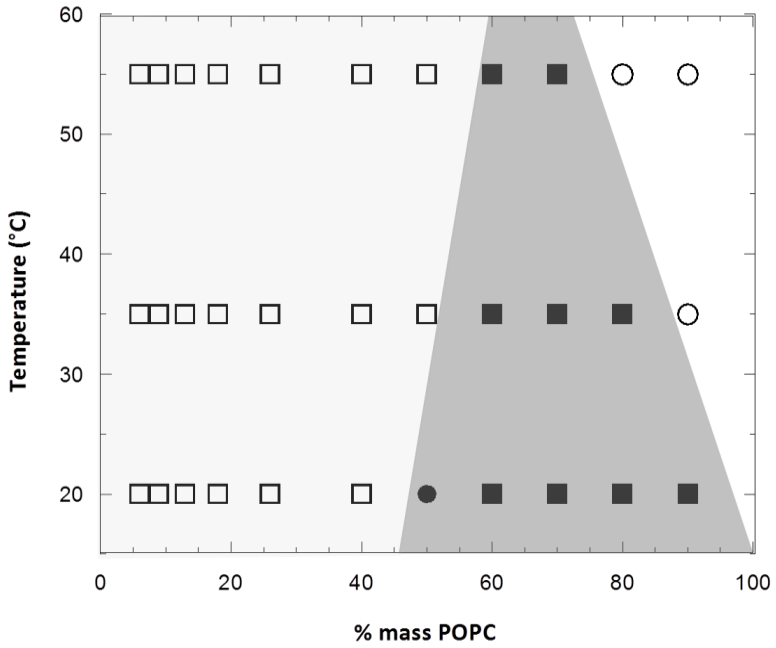

Figure 5.14. Outlined phase diagram for PEO_{12}-*b*-$PDMS_{43}$-*b*-PEO_{12}/POPC binary mixture determined by confocal microscopy. Symbols represent characterized compositions and temperatures. Shaded areas depict regions of the phase diagram with and without phase coexistence, as well as the stability of coexisting domains. □: no macroscopic domains; ●: vesicle exhibiting phase coexistence; ■: vesicle exhibiting phase coexistence with the stable budded domains; ○: fission of budded domains.

Nanoscale phase separation

The presence of nanoscale phase separation in PEO_{12}-*b*-$PDMS_{43}$-*b*-PEO_{12}/POPC GHUVs was also investigated through FLIM-FRET measurements following exactly the same methodology. Once again, a strong decrease of fluorescence lifetime distribution was observed for pure polymersomes when the acceptor probe was added to the membrane, reflecting the random distribution of probes within the membrane (Figure 5.15 A). In hybrid PEO_{12}-*b*-$PDMS_{43}$-*b*-PEO_{12}/POPC GHUVs, the decrease of lifetime was less pronounced in the presence of acceptor probe, compared to what was observed for pure polymersomes (Figure 5.15B), suggesting nanoscale phase separation. This hypothesis was also confirmed through fluorescence single decay measurements. According to data shown in Table 5.3 and Figure 5.16 below, the nanoscale phase separation in PEO_{12}-*b*-$PDMS_{43}$-*b*-PEO_{12}/POPC GHUVs was detected in hybrid vesicles of lipid content as low as 10% wt POPC. In Figure 5.16, we also recalled the values obtained from PEO_8-*b*-$PDMS_{22}$-*b*-PEO_8/POPC or $PDMS_{26}$-*g*-$(PEO_{12})_2$/POPC mixtures.

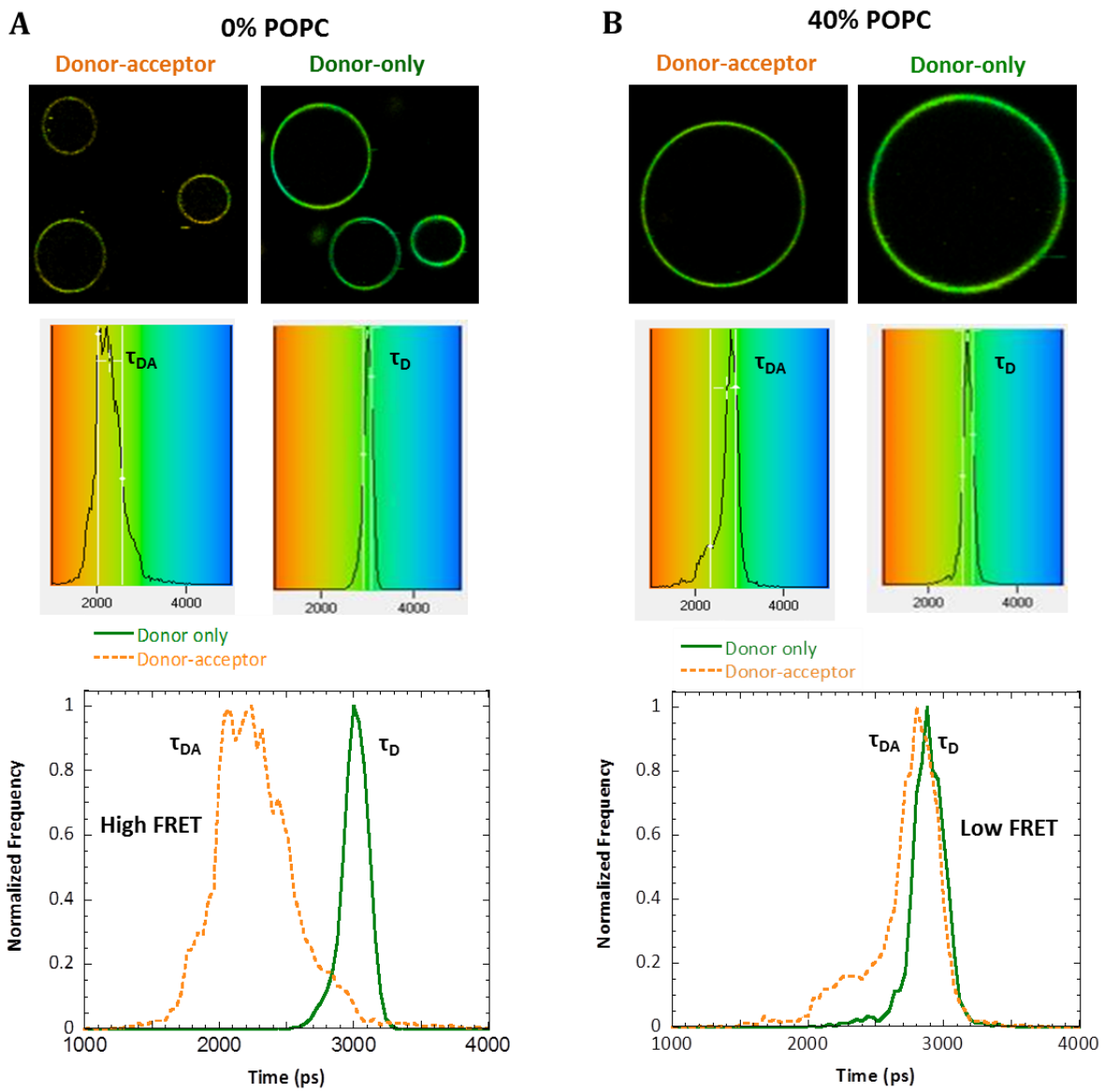

Figure 5.15. Equatorial z-section FLIM images and their representative PDMS$_{26}$-*g*-(PEO$_{12}$)$_2$-FITC fluorescence lifetime distribution histograms of pure PEO$_{12}$-*b*-PDMS$_{43}$-*b*-PEO$_{12}$ GUVs and GHUVs prepared from PEO$_{12}$-*b*-PDMS$_{43}$-*b*-PEO$_{12}$/POPC 60/40 (wt/wt) mixture labelled with only PDMS$_{26}$-*g*-(PEO$_{12}$)$_2$-FITC or with both PDMS$_{26}$-*g*-(PEO$_{12}$)$_2$-FITC and DOPE-Rhod. FRET between FITC and Rhod is responsible for the decrease in PDMS$_{26}$-*g*-(PEO$_{12}$)$_2$-FITC fluorescence lifetimes.

Table 5.3. The average fluorescence lifetime of PDMS$_{26}$-*g*-(PEO$_{12}$)$_2$-FITC in different PEO$_{12}$-*b*-PDMS$_{43}$-*b*-PEO$_{12}$/POPC GHUVs obtained from fluorescence single decay measurements and corresponding FRET efficiency. ($\overline{\tau_D}$: average fluorescence lifetime in GHUVs loaded only 1.5% molar of PDMS$_{26}$-*g*-(PEO$_{12}$)$_2$-FITC; $\overline{\tau_{DA}}$: average fluorescence lifetime in GHUVs loaded 1.5% molar of PDMS$_{26}$-*g*-(PEO$_{12}$)$_2$-FITC and 0.5% molar of DOPE-Rhod).

% POPC	$\overline{\tau_D}$ ± SD (ns)	$\overline{\tau_{DA}}$ ± SD (ns)	FRET efficiency
0%	3.034 ± 0.050	2.658 ± 0.070	0.124 ± 0.025
10%	2.824 ± 0.060	2.684 ± 0.057	0.049 ± 0.030
40%	2.795 ± 0.078	2.793 ± 0.053	0.005 ± 0.027

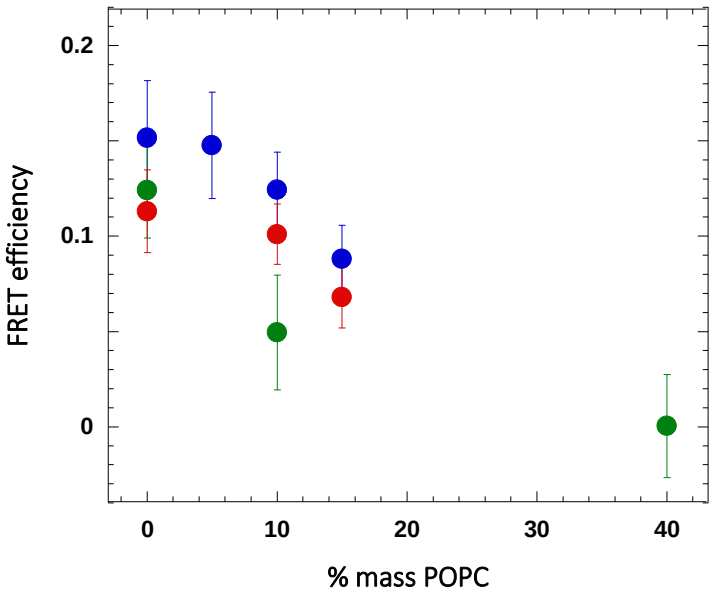

Figure 5.16. FRET efficiency in GHUVs of POPC with PEO_8-*b*-$PDMS_{22}$-*b*-PEO_8 (●);$PDMS_{26}$-*g*-$(PEO_{12})_2$ (●) and PEO_{12}-*b*-$PDMS_{43}$-*b*-PEO_{12} (●) measured by FRET-FLIM methodology.

At 40% POPC, the FRET was close to 0 with a large error bar. This result was unexpected because the acceptor DOPE-Rhod is still present in the polymer phases as already quantified through its partition coefficient in Chapter 4. However since the lipid composition was not perfectly controlled in each of the GHUVs, this may add to the uncertainty of the value (error bars are significant).

The very low FRET value obtained for PEO_{12}-*b*-$PDMS_{43}$-*b*-PEO_{12}/POPC mixtures with a POPC content of 40% suggest the presence of domains larger than the FRET infinite phase separation limit of 50 nm [4]. It should be stressed that in case phase separation resulted in domains larger than this limit or domain fission occurred, no additional changes in FRET efficiencies would be expected.

Very interestingly, another convincing evidence of the existence of such nanodomains in PEO_{12}-*b*-$PDMS_{43}$-*b*-PEO_{12}/POPC GHUVs was indicated *via* experiments manipulating their membrane tension. At first, we used micropipette aspiration technique to keep the vesicles at the stressed state. Micropipette fabrication and aspiration setup were done with the protocol used for mechanical properties measurements as described in Chapter 2 but the experiments were qualitatively recorded. As seen in Figure 5.17, under tension, an obvious change from visually homogeneous state to the phase separation with a lipid rich fluid phase where DOPE-Rhod incorporate preferentially and is recognizable as significantly brighter

phases. Notice that this phenomenon is irreversible, as those microdomains remain even when tension was gradually decreased. This demonstrates that the nanodomains evidenced by FLIM FRET experiments are in a metastable state. When the membrane tension increases, they probably coalesce into observable micrometer size domains. As suggested in literature, the lateral tension can increase the line tension between coexisting phases [5], therefore the coalescence of small domains into microdomain is promoted in order to minimize the interface energy. Some representative images are displayed in Figure 5.17.

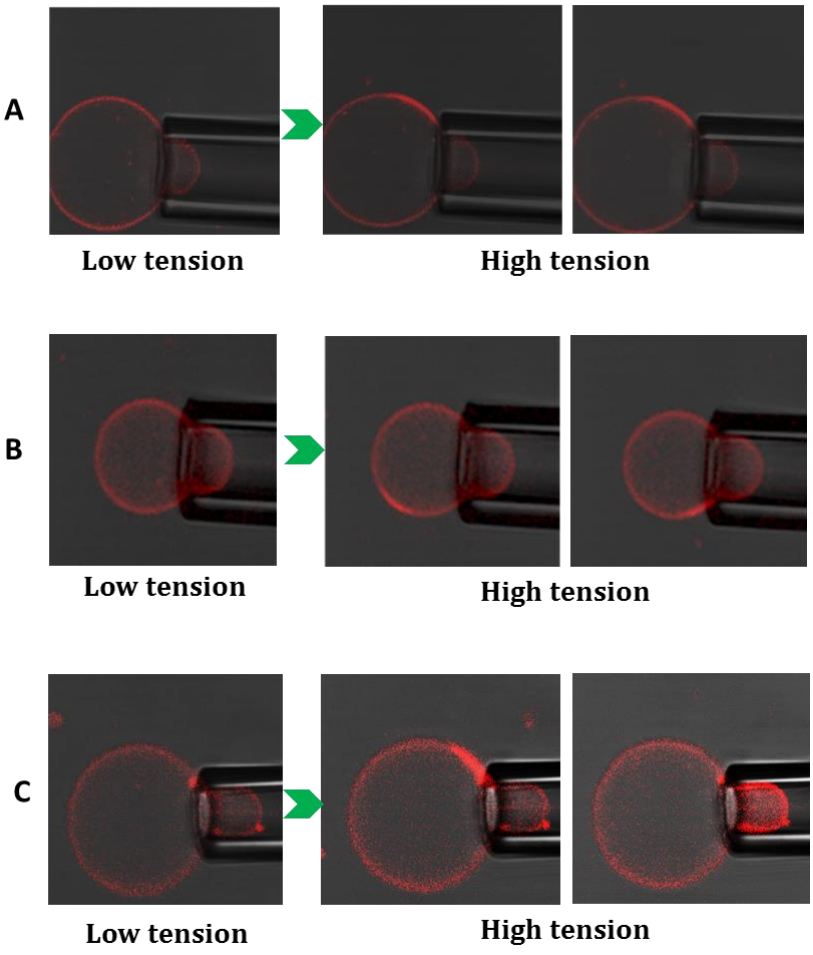

Figure 5.17. Appearance of visible micron domains in different PEO_{12}-*b*-$PDMS_{43}$-*b*-PEO_{12}/POPC GHUVs (30% wt POPC labelled 0.2 mol% DOPE-Rhod) under tensions produced by micropipette suction.

In addition, it is interesting that those lipid domains appeared mostly near the mouth of the pipette (i.e. Figure 5.17A). If it is not the case, the domain also moved quickly to reach this position (Figure 5.17B) and in some cases, they move on inside the pipette (Figure 5.17C).

Furthermore, instead of using suction pressure, we tried also to regulate membrane tension *via* osmotic pressure by modulating internal and external vesicle medium. Briefly, the vesicle suspension prepared in sucrose 0.1M (200 µL) was first transferred to a µ-Slide from Ibidi

(Munich, Germany) and observed for isosmotic condition. Small amounts of MiliQ water were then added gradually into this chamber and observed for hypotonic condition. Indeed, with this increasing tension, the coalescence of nanodomains towards macroscopic phase separation was once again confirmed as shown in Figure 5.18.

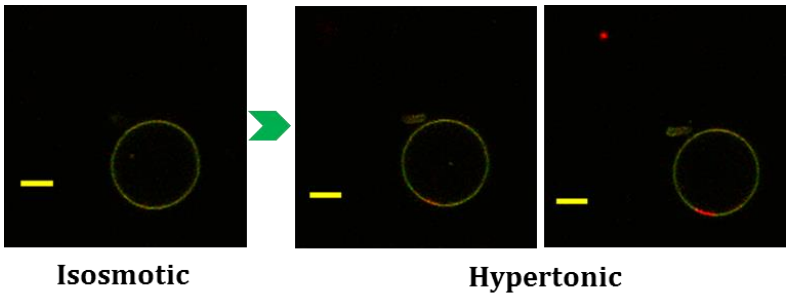

Figure 5.18. Appearance of microdomains in PEO_{12}-*b*-$PDMS_{43}$-*b*-PEO_{12}/POPC GHUVs (30% wt POPC labelled with 0.2 mol% DOPE-Rhod) under increased membrane tensions produced by osmotic pressure.

These preliminary tests were just qualitatively performed for the purpose of verifying the existence of nanodomains detected in PEO_{12}-*b*-$PDMS_{43}$-*b*-PEO_{12}/POPC mixtures. More quantitative experiments to study the effect of membrane tension on hybrid vesicles can be considered in further studies.

As nano phase separation occurred in PEO_{12}-*b*-$PDMS_{43}$-*b*-PEO_{12}/POPC GHUVs was confirmed thoroughly, the apparent phase diagram for this mixture is now displayed as Figure 5.19.

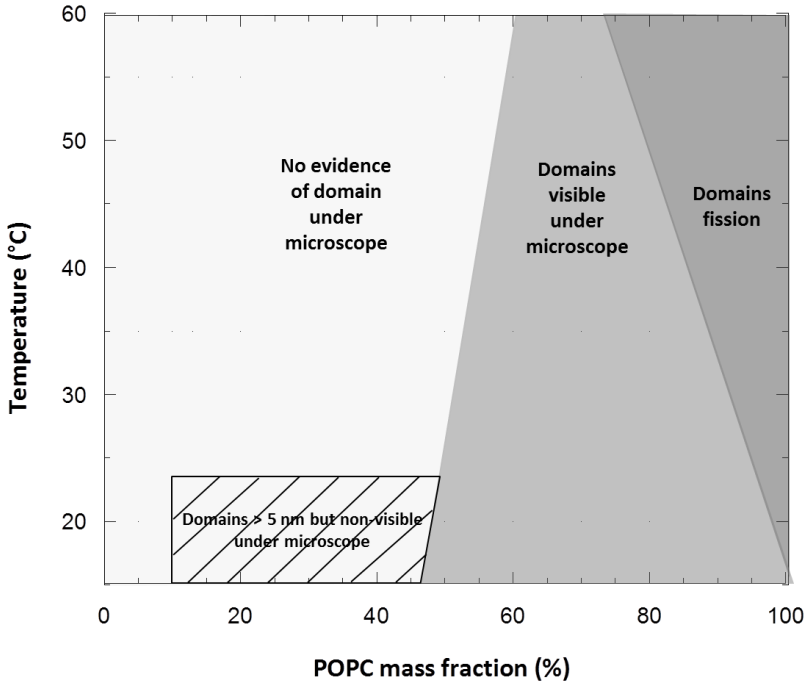

Figure 5.19. Outlined apparent phase diagram for PEO_{12}-*b*-$PDMS_{43}$-*b*-PEO_{12}/POPC binary system determined by confocal microscopy and FLIM-FRET measurements on micron-size vesicles.

5.1.1.3. Case of PEO_{17}-*b*-$PDMS_{67}$-*b*-PEO_{17}/POPC mixtures

The third triblock copolymer, PEO_{17}-*b*-$PDMS_{67}$-*b*-PEO_{17} self-assembles into vesicles with membrane thickness of 11.2 ± 1.2 nm. This value is about 2.5 times higher than the liposomal membrane; hence, the PEO_{17}-*b*-$PDMS_{67}$-*b*-PEO_{17}/lipid hybrid vesicles generally stand an extremely high hydrophobic mismatch. The electroformation protocol was used to prepare the PEO_{17}-*b*-$PDMS_{67}$-*b*-PEO_{17}/lipid GHUVs, nevertheless the GHUVs obtained were often in a smaller size range, typically 10 – 15 µm. FLIM-FRET experiments were not performed for this system and we studied the phase separation only at the microscale.

With such hydrophobic mismatch between PEO_{17}-*b*-$PDMS_{67}$-*b*-PEO_{17} chains and POPC, and considering the previous results obtained with the other block copolymers, we did not expect phase coexistence in PEO_{17}-*b*-$PDMS_{67}$-*b*-PEO_{17}/POPC GHUVs prepared from mixtures with low POPC concentration. Therefore, the measurements were performed with mixtures of 50% and 75% of POPC content. With this significantly larger polymer chain, no phase coexistence was observed and three populations of vesicles were always present: pure liposome, pure polymersome and a few homogeneous hybrid vesicles (Figure 5.20).

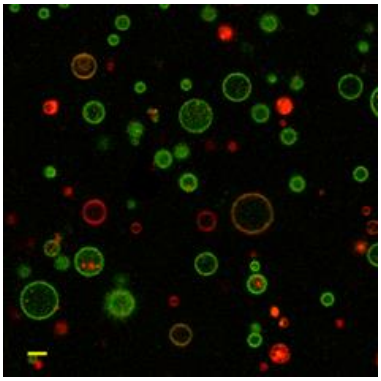

Figure 5.20. Confocal slice of PEO_{17}-*b*-$PDMS_{67}$-*b*-PEO_{17}/POPC GHUVs containing 75% POPC (% wt) labelled with $PDMS_{26}$-*g*-$(PEO_{12})_2$-FITC and DOPE-Rhod measured by confocal fluorescence microscopy at room temperature; scale bars: 5 µm.

These results suggest that the high hydrophobic mismatch may lead to very high line tension between PEO_{17}-*b*-$PDMS_{67}$-*b*-PEO_{17} chains and POPC, therefore the existence of stable micrometric lipid enriched domains is unlikely.

5.1.2. Micron scale fluid/gel phase separation in GHUVs

In order to explore the formation of gel-like domains in GHUVs, phase separation on GHUVs was also characterized on mixtures of the copolymers with DPPC as lipid. As the phase

transition of DPPC is about 41°C, measurements were carried out either below or above this temperature. In the case of GHUVs prepared at temperature above melting transition of the lipid and then cooled at room temperature, it has been shown in literature that cooling rate has an effect on the membrane tension as it induces a thermal contraction of both membrane and water, the contraction of membrane being faster than the aqueous core of the vesicle, inducing membrane stress which can go through a maximum. Indeed at high cooling rate, the rapid contraction of the membrane compared to the aqueous compartment abruptly reduces the surface-to-volume ratio and thus induces lateral tension in the membrane that can go above its lysis tension, inducing rupture and reseal phenomena during which water escapes from the vesicle, therefore relaxing tension. At low cooling rate, the membrane tension is continuously relaxed by natural diffusion of water through the membrane [6, 7]. The differences in membrane tension can then modulate the morphology of the DPPC domains (patches *versus* stripes). We have therefore tried to evaluate the effect of the hydrophobic length mismatch that is modulated through the molar mass of the block copolymer at different cooling rates, on the morphology and size of the domains obtained. Hybrid vesicles were electroformed at 50°C and cooled to 20°C at different rates, namely: 1°C/min, 5°C/min and 20°C/min. We also used a spontaneous cooling as it is the simplest procedure that can be used: it consists in cooling down naturally 1 mL of the vesicle suspension in a room thermostated at 22°C just after its electroformation at 50°C, in a closed Eppendorf tube. The decrease of temperature for this procedure was measured, is reproducible and is considered to be linear from 50°C until 35°C with a constant slope of 2.9°C/min (Figure 5.21).

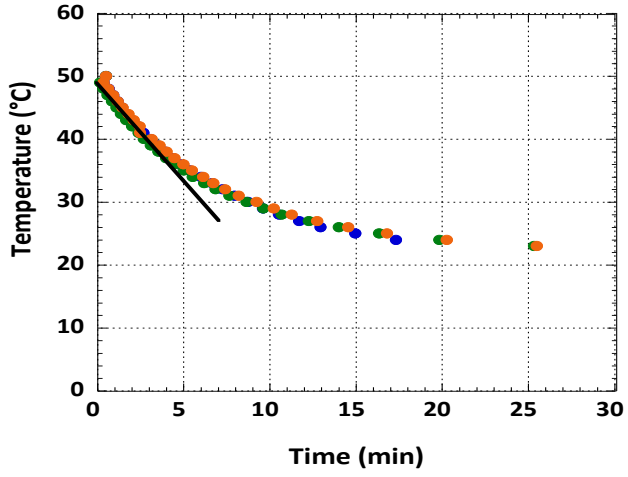

Figure 5.21. Evolution of temperature in the sample during the "natural" cooling process in room at 22°C. The different colours correspond to different experiments and attests to the repeatability of the measurements.

5.1.2.1. Case of PEO_8-b-$PDMS_{22}$-b-PEO_8/DPPC GHUVs

In brief, for this system, at room temperature, just 5% of DPPC is enough to drive phase separation in PEO_8-*b*-$PDMS_{22}$-*b*-PEO_8/DPPC GHUVs (Figure 5.22). It should be noted that DOPE-Rhod is excluded from the ordered phases, thus the DPPC-gel domains are now recognizable as dark domains, excluding both lipid and copolymer fluorescent analogues.

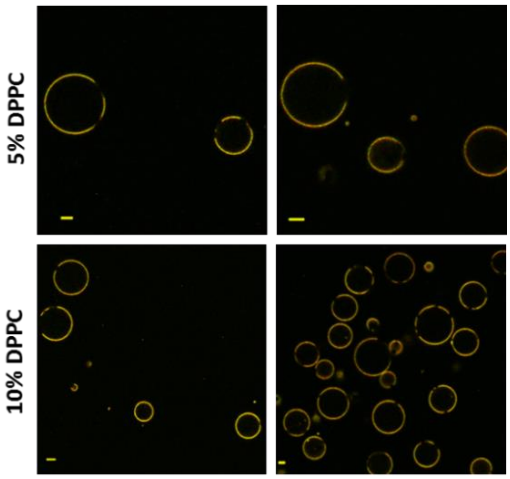

Figure 5.22. The equatorial slices of PEO_8-*b*-$PDMS_{22}$-*b*-PEO_8/DPPC GHUVs containing 5% and 10% DPPC (% wt) labelled with $PDMS_{26}$-*g*-$(PEO_{12})_2$-FITC and DOPE-Rhod measured by confocal fluorescence microscopy at room temperature. Both of the probes homogeneously distributed in polymer domains (yellow phase) while excluded in DPPC gel-domain (dark phase); scale bars: 5 µm.

While lipid fluid-domains normally present spherical shapes, these dark DPPC-gel domains exhibited various morphologies depending on cooling rate after electroformation at 50°C. Results are shown in Figure 5.23 with the representative domain shapes obtained at each cooling rate. Natural cooling rate resulted in the formation of stripped gel domains while a controlled slow rate generated large star-or flower- shaped domains and a controlled fast rate gave rise to many small patchy gel domains.

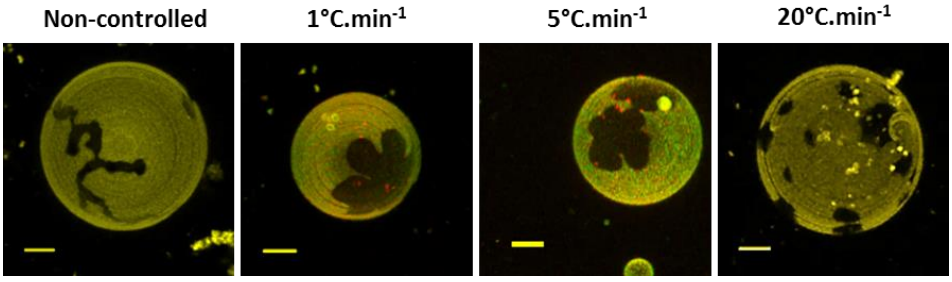

Figure 5.23. Overlay of maximum intensity 3D projection images taken for PEO_8-*b*-$PDMS_{22}$-*b*-PEO_8/DPPC GHUVs containing 20% DPPC (% wt) loaded with $PDMS_{26}$-*g*-$(PEO_{12})_2$-FITC and DOPE-Rhod. These vesicles were prepared according to the same electroformation method described previously, but cooled down to room temperature at different speeds; scale bars: 5 µm.

Furthermore, we have tried to characterize the copolymer/DPPC GHUV behaviour when submitted to gradual heating up to 50°C, well-above T_m of DPPC to obtain a lipid fluid phase and compare the results obtained with copolymer/POPC mixtures. Generally, no evidence of phase coexistence was probed for fractions below 15% of DPPC as it was observed for copolymer/POPC mixture at room temperature. For higher lipid content, separated DPPC-rich fluid phases and polymer-rich phases were observed. The large DPPC dark gel-domains observed at room temperature underwent a transition to circular red domains with DOPE-Rhod incorporated inside when samples were heated up to 50°C. This shape transition reflects the minimization of boundary line energy allowed by the fluid character of the lipid phase. It has to be noted that no budding/fission phenomenon occurred for any of the PEO_8-*b*-$PDMS_{22}$-*b*-PEO_8/DPPC GHUVs at 50°C. Results are shown in Figure 5.24.

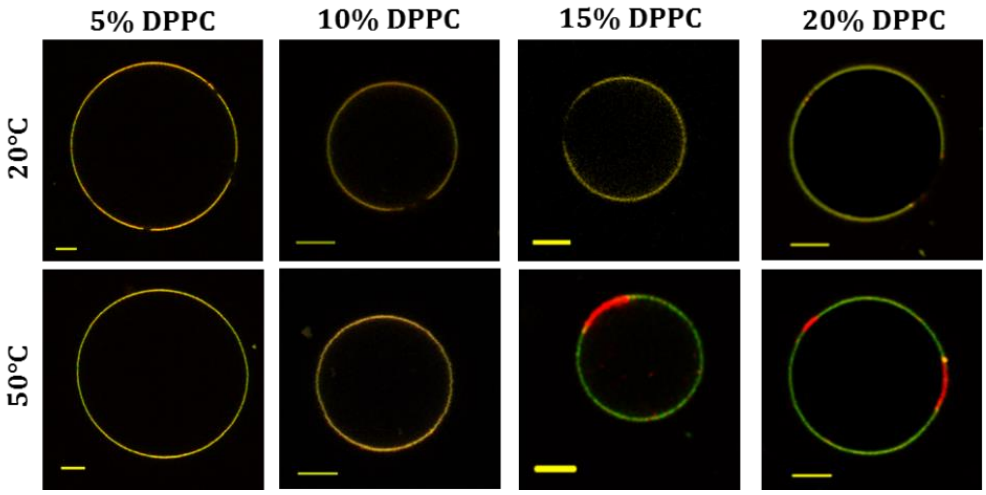

Figure 5.24. The equatorial slices of PEO_8-*b*-$PDMS_{22}$-*b*-PEO_8/DPPC GHUVs containing 5%, 10%, 15% and 20% DPPC (% wt) labelled with $PDMS_{26}$-*g*-$(PEO_{12})_2$-FITC and DOPE-Rhod measured by confocal fluorescence microscopy at 20°C and 50°C; scale bars: 5 µm.

Interestingly, the structuration of PEO_8-*b*-$PDMS_{22}$-*b*-PEO_8/DPPC GHUVs was also found to be reversible upon temperature. Indeed, in Figure 5.25, the cooling and heating cycles performed in one vesicle reproduced almost the same structuration.

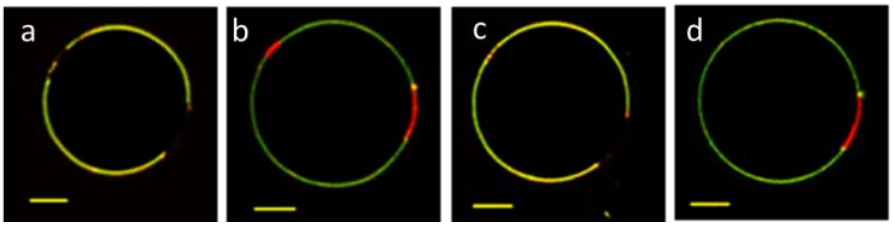

Figure 5.25. Reversible changes in phase separated GHUVs of PEO_8-*b*-$PDMS_{22}$-*b*-PEO_8/DPPC during cooling and heating cycles (a: 20°C; b: heated up at 50°C; c: back to 20°C and d: re-heated up at 50°C); scale bar: 10µm.

5.1.2.2. Case of $PDMS_{26}$-*g*-$(PEO_{12})_2$/DPPC GHUVs

As expected from a previous study of the team [1], we detected the micrometric gel-domain formation in $PDMS_{26}$-*g*-$(PEO_{12})_2$/DPPC GHUVs at DPPC content as low as 5%. Additionally, we performed the 3D projection images to investigate the morphology of DPPC gel-domains resulting from different cooling rates. The methodology was exactly the same as carried out for the other systems. Interestingly, the results are similar to those obtained with PEO_8-*b*-$PDMS_{22}$-*b*-PEO_8/DPPC GHUVs. Representative images are shown in Figure 5.26.

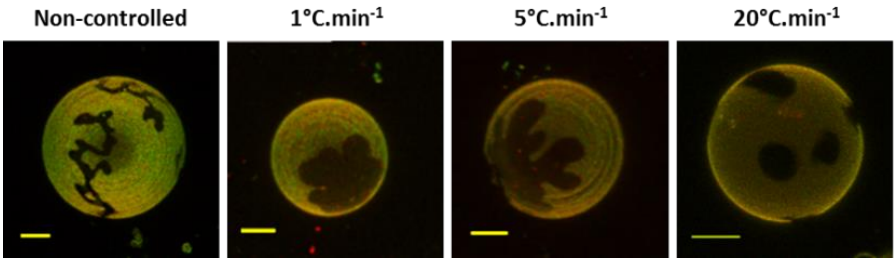

Figure 5.26. The impact of cooling rate on DPPC gel-domain morphology within phase separated $PDMS_{26}$-*g*-$(PEO_{12})_2$/DPPC GHUVs at 20% DPPC (% wt); scale bars: 5 µm.

Raising temperature above the T_m of DPPC, we could observe that GHUVs did not exhibit phase coexistence anymore at 50°C at 5% of DPPC, while GHUVs prepared from mixtures with 15% and 20% of DPPC exhibited red DPPC rich-fluid phases, as illustrated in Figure 5.27.

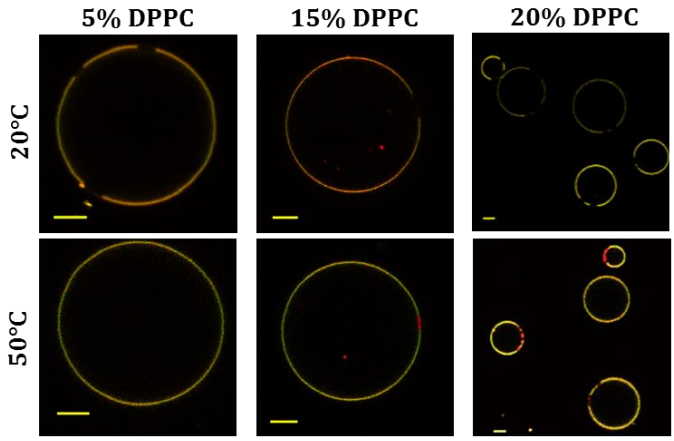

Figure 5.27. The equatorial slices of $PDMS_{26}$-*g*-$(PEO_{12})_2$/DPPC GHUVs containing 5%, 15% and 20% DPPC (% wt) labelled with $PDMS_{26}$-*g*-$(PEO_{12})_2$-FITC and DOPE-Rhod measured by confocal fluorescence microscopy at 20°C and 50°C; scale bars: 5 µm.

5.1.2.3. Case of PEO_{12}-*b*-$PDMS_{43}$-*b*-PEO_{12}/DPPC GHUVs

Phase separation occurred in PEO_{12}-*b*-$PDMS_{43}$-*b*-PEO_{12}/DPPC GHUVs at just 5% of DPPC as it was observed for $PDMS_{26}$-*g*-$(PEO_{12})_2$ and PEO_8-*b*-$PDMS_{22}$-*b*-PEO_8/DPPC mixtures and the morphology of DPPC gel-domains also varied with the cooling rate (Figure 5.28).

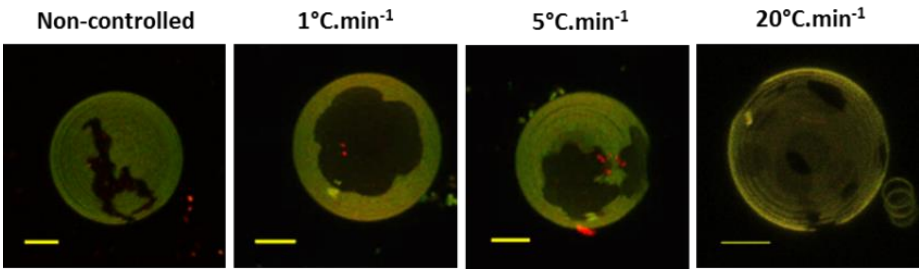

Figure 5.28. The impact of cooling rate on DPPC gel-domain morphology within phase separated PEO_{12}-*b*-$PDMS_{43}$-*b*-PEO_{12}/DPPC GHUVs (20/80 w/w); scale bars: 5 µm.

When DPPC was in the fluid phase, there were no visible signs of phase separation for samples with less than 50% DPPC content whereas phase coexistence was observed for samples with 50% and 60% of DPPC (Figure 5.29). In Figure 5.29, the small pure liposomes were found attached in PEO_{12}-*b*-$PDMS_{43}$-*b*-PEO_{12}/DPPC GHUVs 50% wt, perhaps due to the fission of DPPC-fluid phases at 50°C, but we were not able to directly observe budding and fission during the time-course of experiment.

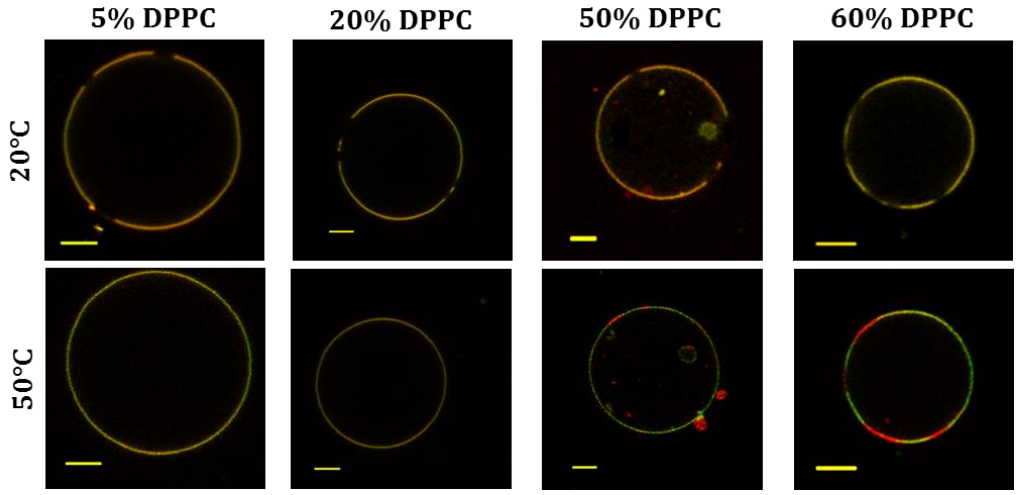

Figure 5.29. The equatorial slices of PEO_{12}-*b*-$PDMS_{43}$-*b*-PEO_{12}/DPPC GHUVs containing 5%, 20%, 50% and 20% DPPC (% wt) labelled with $PDMS_{26}$-*g*-$(PEO_{12})_2$-FITC and DOPE-Rhod measured by confocal fluorescence microscopy at 20°C and 55°C; scale bars: 5 µm.

5.1.2.4. Case of PEO_{17}-*b*-$PDMS_{67}$-*b*-PEO_{17}/DPPC GHUVs

As for previous systems, the formation of gel-like microdomains in GHUVs occurred at only 5% of DPPC. However, at different cooling speeds, while different morphologies were reported for all other copolymers, only one type of morphology was visible (patchy domains) in PEO_{17}-*b*-$PDMS_{67}$-*b*-PEO_{17}/DPPC system (Figure 5.30).

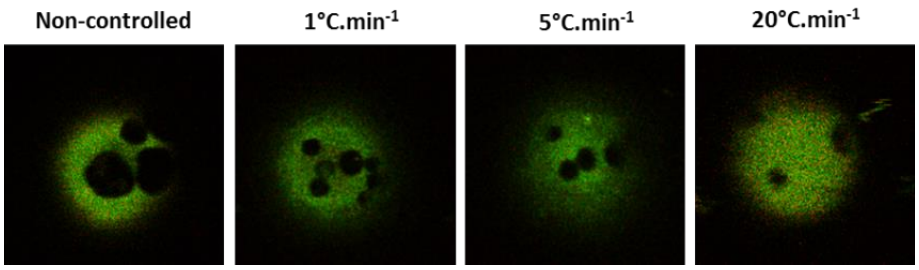

Figure 5.30. Top hemisphere of PEO_{17}-*b*-$PDMS_{67}$-*b*-PEO_{17}/DPPC GHUVs labelled with $PDMS_{26}$-*g*-$(PEO_{12})_2$-FITC and DOPE-Rhod measured by confocal fluorescence microscopy at room temperature; scale bars: 5 µm.

At a temperature well above the T_m of DPPC, no domains were observable over a broad range of polymer/lipid fraction. As shown in Figure 5.31, a heterogeneous phase separated hybrid vesicle at 20°C underwents a transition to homogeneous state when the temperature was raised to 55°C. The transition was perfectly reversible as illustrated in Figure 5.31.

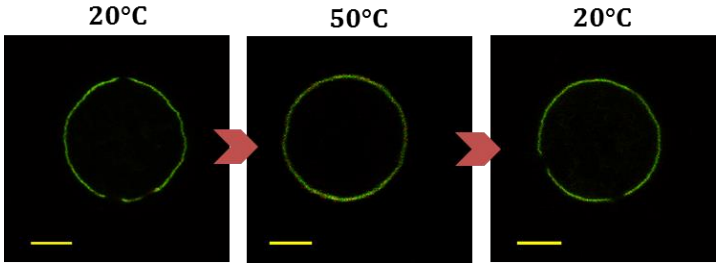

Figure 5.31. Reversible changes in PEO_{17}-*b*-$PDMS_{67}$-*b*-PEO_{17}/DPPC GHUVs at 75% DPPC (% wt) during cooling and heating cycles.

5.2. ANALYSIS AND DISCUSSION OF THE RESULTS

5.2.1. Hydrophobic mismatch

Phase separation properties in GHUVs formed from mixtures of POPC and triblock copolymers were highly dependent on the copolymer block molar masses. This point is evident through comparison of their phase diagrams presented in Section 4.1. Regarding the threshold of POPC weight content above which micronscale phase separation occurs, 16% was necessary for PEO_8-*b*-$PDMS_{22}$-*b*-PEO_8/POPC, 50% for PEO_{12}-*b*-$PDMS_{43}$-*b*-PEO_{12}/POPC and no phase coexistence was detected for PEO_{17}-*b*-$PDMS_{67}$-*b*-PEO_{17}/POPC. Nevertheless, submicron lipid domains were surprisingly detected for low lipid concentrations not only in PEO_8-*b*-$PDMS_{22}$-*b*-PEO_8/POPC GHUVs, but also in PEO_{12}-*b*-$PDMS_{43}$-*b*-PEO_{12}/POPC GHUVs. Since between PEO_8-*b*-$PDMS_{22}$-*b*-PEO_8 and PEO_{12}-*b*-$PDMS_{43}$-*b*-PEO_{12} copolymer, the line tension is expected to be higher in PEO_{12}-*b*-$PDMS_{43}$-*b*-PEO_{12}/POPC hybrid membranes, a larger tendency for domain coalescence and formation of larger domains was expected for

this mixture, as this allows for the minimization of the total boundary length. In case the energetic costs associated with line tension are too high, the length of the interface between domains can be further minimized through membrane curvature (budding), as predicted by theory, which can ultimately evolve towards fission. This was indeed confirmed through imaging immediately after electroformation of PEO_{12}-*b*-$PDMS_{43}$-*b*-PEO_{12}/POPC samples at lipid fraction range where homogeneous hybrid vesicles were predominantly observed the day after electroformation. As illustrated in the examples shown in Figure 5.32, PEO_{12}-*b*-$PDMS_{43}$-*b*-PEO_{12}/POPC GHUVs at 20% and 30% POPC shortly after electroformation displayed curved domains which evolved towards fission over time. This phenomenon also helps us explaining why a large number of pure liposomes were seen in samples prepared from mixtures of this copolymer and POPC.

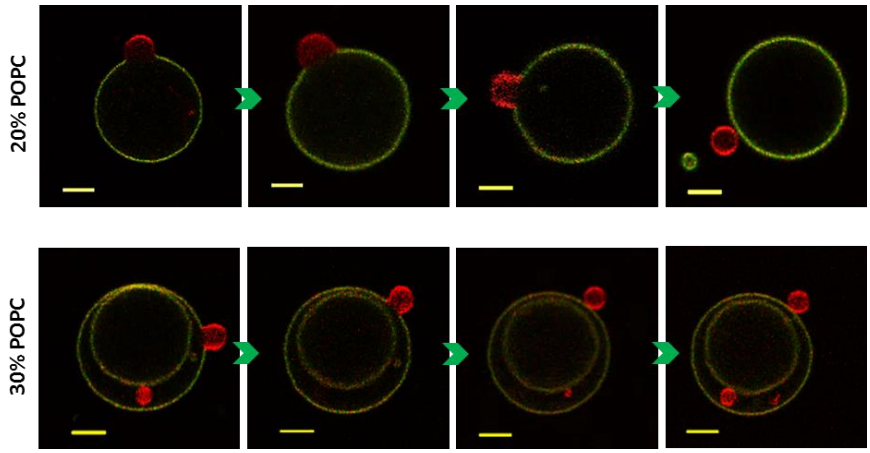

Figure 5.32. Typical behaviour for GHUVs of PEO_{12}-*b*-$PDMS_{12}$-*b*-PEO_{43}/POPC at low POPC concentrations: budding and fission of small lipid domains occurred shortly after electroformation (order: left to right); scale bars: 5 µm.

On the other hand, a great number of vesicles at POPC content higher than 50 % wt showed stable phase coexistence (after overnight incubation). This discrepancy between the stability of phase coexistence in PEO_{12}-*b*-$PDMS_{43}$-*b*-PEO_{12}/POPC mixtures with low and high lipid content may be explained by differences in curvature energies of lipid and polymer-rich domains. At high lipid content, the curvature of the polymer-rich membrane induced by the budding phenomenon is more pronounced and the bending energy associated with polymer domains is higher than the one associated with lipid domains. It should be noticed that bending rigidity of polymer domains is larger than that of lipid domains as it is quadratic with the bilayer thickness [8]. As such, equilibrium between line tension and bending energy costs is more easily achieved for small polymer-rich domains [9], while small lipid-rich domains

easily undergo large curvatures increases followed by membrane fission into separated vesicles.

Using the same rationalization, we believe that the curved domains in PEO_8-*b*-$PDMS_{22}$-*b*-PEO_8/POPC GHUVs are stable after days because the low hydrophobic mismatch between PEO_8-*b*-$PDMS_{22}$-*b*-PEO_8 and POPC leads to line tensions lower than the membrane bending energy required for fission. And conversely, for the case of PEO_{17}-*b*-$PDMS_{67}$-*b*-PEO_{17}, given the extremely high hydrophobic mismatch between polymer and lipid molecules, even if phase coexistence is present during electroformation, these domains are unstable and quickly disappear or evolve towards fission before their imaging is possible.

It is important to recall that even though budding and fission occurred, leading to the formation of separate liposomes and hybrid homogeneous vesicles, the presence of lipid nanodomains in these GHUVs was proven by FLIM/FRET experiments. The nanodomains are in a metastable state as illustrated by the micropipette suction experiments and may lead later to growth at a micrometer size observable by optical microscopy.

5.2.2. Fluidity of the components

In the studied POPC/copolymer mixtures, numerous differences have been observed between the different copolymers, explained by the modulation of hydrophobic length mismatch, line tension and bending rigidity of the membrane. With DPPC as lipid, the behaviours obtained looked similar: 5% of DPPC was enough to obtain stable lipid micron-sized domains in all studied mixtures. No budding phenomena was observed due to the solid character of the gel lipid phase. Interestingly, a lot of similarities with copolymer/POPC mixtures were observed for temperatures above the T_m of DPPC, with the exception of fission which was not observed, suggesting a slightly lower line tension at the lipid polymer boundaries compared to POPC.

Regarding the morphologies obtained at different cooling rates, some similarities were obtained with previous results of literature on PBut-*b*-PEO/DPPC mixtures observed at different cooling rates comparable to this study. Fast cooling favours the formation of multiple small patchy domains [10] as it reduces the free energy barrier for nucleation. Another aspect to consider is the membrane tension that can be modulated *via* the cooling rate as explained previously by difference of thermal dilatation coefficients between water and membranes [6]. High membrane tension would favour stripe-like morphology of DPPC

domains whereas low lateral tension would favour quasi-spherical patches. In our work, stripes were observed systematically for “natural” cooling evaluated at -2.9°C/min from 50°C to 35°C for all copolymers except for PEO_{17}-*b*-$PDMS_{67}$-*b*-PEO_{17}. Slightly slower or faster cooling gave rise to large flower-like domains, and small patchy domains were obtained at high cooling rate. In analogy with the work of Chen and Santore, it suggests that membrane tension goes to higher values for the “natural” cooling process. During slower cooling, the membrane stress can relax as water can diffuse across the membrane, whereas higher cooling rate generates tension that can overcome membrane lysis tension, leading to rupture and reseal processes (transient pores) during which water escapes from the vesicle and relaxes tension. However the modulation of domain morphologies has not been observed for the thickest PEO_{17}-*b*-$PDMS_{67}$-*b*-PEO_{17} copolymer. It is important to recall that line tension at the polymer/lipid boundary is higher for this system where the hydrophobic length mismatch is maximal. Moreover, membrane tension can lead to an increase of the line tension, as it will alter the deformation of the monolayer that occurs at the lipid/polymer interface to avoid hydrophobic exposure to water [5]. Therefore the formation of domains with striped morphology is unlikely as this would results in higher boundary line energies compared to patchy domains.

5.2.3. Architecture of copolymers

We analysed the impact of copolymer architecture on the GHUVs structuration by comparing the data obtained from PEO_8-*b*-$PDMS_{22}$-*b*-PEO_8/lipid GHUVs and $PDMS_{26}$-*g*-$(PEO_{12})_2$/lipid GHUVs. These two copolymers have identical chemical nature as well as hydrophobic membrane thickness, similar molar masses and only differ by their architecture: grafted for $PDMS_{26}$-*g*-$(PEO_{12})_2$ and triblock for PEO_8-*b*-$PDMS_{22}$-*b*-PEO_8. Therefore, the chain organization of the membrane is probably different. Regarding previous results obtained in our group and from literature, $PDMS_{26}$-*g*-$(PEO_{12})_2$ is probably organized as a bilayer in analogy to phospholipids [11], whereas hairpin or/and extended conformations can be found in the membrane for PEO_8-*b*-$PDMS_{22}$-*b*-PEO_8, but this has not been quantified yet. We found many similar behaviours between GHUVs prepared from mixtures of lipid and these copolymers but in the case of $PDMS_{26}$-*g*-$(PEO_{12})_2$, lipid micrometric domains were only visible starting from 22% (% wt) of POPC whereas only 16% of POPC fraction was enough to observe the phase coexistence in the case of PEO_8-*b*-$PDMS_{22}$-*b*-PEO_8. Moreover, $PDMS_{26}$-*g*-

(PEO_{12})$_2$/POPC mixtures displayed a clear instability of the domains (budding and fission) on the first few hours after electroformation, while the triblock PEO_8-*b*-$PDMS_{22}$-*b*-PEO_8 showed stable domains for several days. As the GHUVs were obtained in the same experimental conditions, such differences could be explained by different values of the line tension at the polymer/lipid boundaries and/or of the bending rigidity of the copolymer membrane. These parameters as well as the identification of chain conformation in these membranes need to be quantified in further studies.

5.3. SUMMARY AND CONCLUSION OF THE CHAPTER

We reported in this chapter a systematic study on different polymer/lipid GHUVs using copolymers with same chemical nature based on PDMS as hydrophobic block and PEO as hydrophilic block, but with different architectures (grafted *versus* triblock) and molar masses. They were blended with phosphocholine lipids at either gel or fluid lipid phase at room temperature. Using a combination of classical confocal microscopy imaging with an advanced fluorescence microscopy technique (FLIM-FRET), we were able to probe the membrane structure of giant hybrid membranes at both micro- and nano-scale. Based on all information detected, we found out the effect of different parameters including: lipid/polymer fraction, lipid fluidity, polymer architecture and polymer molar mass (hydrophobic mismatch). In particular, we brought a direct spectroscopic evidence of the presence of nano-domains in GHUVs which until now had only been suggested [10]. Globally, the study clearly shows the effect of the modulation of the line tension as well as bending rigidity of the polymer membrane on the GHUV morphology that could be obtained with a phospholipid in the fluid lipid phase at ambient temperature. The stabilization of fluid-state lipid micron-sized domains can occur in the membrane above a given threshold lipid fraction for copolymer presenting low molar mass and with a membrane thickness close to the bilayer of liposomes. Very interestingly, stable budded vesicles illustrating equilibrium between domain boundary energy and membrane curvature energy can be obtained, depending on the molar mass of the copolymer and on the lipid fraction. In addition, we showed that homogenous hybrid vesicles at the micronscale can only be observed below a given lipid fraction. This results from the budding and fission of lipid domains which occurs rapidly after electroformation for polymers and lipids with a high hydrophobic mismatch in the membrane. A fraction of the lipid remains in the polymer membrane including in

nanodomains which are in the metastable state as confirmed by micropipette suction experiments. Interestingly, the molar mass effect of the copolymer on membrane structuration can also be detected with lipid in the gel state at room temperature (DPPC), although less variation was observed compared to formulations with lipid in the fluid phase (POPC). Regarding the different morphologies obtained by modulation of the cooling rate and therefore induced membrane tension as interpreted by Chen and Santore [6], for the triblock copolymer having the highest molar mass, it seems that the very high hydrophobic length mismatch drives the morphology towards patchy domains whatever the cooling process used.

REFERENCES

1. Chemin, M., et al., *Hybrid polymer/lipid vesicles: fine control of the lipid and polymer distribution in the binary membrane.* Soft Matter, 2012. **8**(10): p. 2867-2874.
2. Šachl, R., et al., *Limitations of Electronic Energy Transfer in the Determination of Lipid Nanodomain Sizes.* Biophysical Journal, 2011. **101**(11): p. L60-L62.
3. Towles, K.B. and N. Dan, *Determination of Membrane Domain Size by Fluorescence Resonance Energy Transfer: Effects of Domain Polydispersity and Packing.* Langmuir, 2007. **23**(9): p. 4737-4739.
4. Loura, L.M.S., F. Fernandes, and M. Prieto, *Membrane microheterogeneity: Förster resonance energy transfer characterization of lateral membrane domains.* European Biophysics Journal, 2010. **39**(4): p. 589-607.
5. Akimov, S.A., et al., *Lateral tension increases the line tension between two domains in a lipid bilayer membrane.* Physical Review E, 2007. **75**(1): p. 011919.
6. Chen, D. and M.M. Santore, *Hybrid copolymer-phospholipid vesicles: phase separation resembling mixed phospholipid lamellae, but with mechanical stability and control.* Soft Matter, 2015. **11**(13): p. 2617-2626.
7. Chen, D. and M.M. Santore, *Large effect of membrane tension on the fluid–solid phase transitions of two-component phosphatidylcholine vesicles.* Proceedings of the National Academy of Sciences, 2014. **111**(1): p. 179-184.
8. Evans, E.A., *Bending Resistance and Chemically Induced Moments in Membrane Bilayers.* Biophysical Journal, 1974. **14**(12): p. 923-931.
9. Lipowsky, R., *Domain-induced budding of fluid membranes.* Biophysical Journal, 1993. **64**(4): p. 1133-1138.
10. Nam, J., T.K. Vanderlick, and P.A. Beales, *Formation and dissolution of phospholipid domains with varying textures in hybrid lipo-polymersomes.* Soft Matter, 2012. **8**(30): p. 7982-7988.
11. Salva, R., et al., *Polymersome Shape Transformation at the Nanoscale.* ACS Nano, 2013. **7**(10): p. 9298-9311.

CHAPTER 6

PHYSICAL PROPERTIES OF HYBRID POLYMER/LIPID MEMBRANES

Table of Contents

OUTLINE

This chapter focuses on the evaluation of the fluidity and mechanical properties of hybrid polymer/lipid membranes. These characteristics are of importance in many biological events (resistance of cells upon osmotic shock, cell fission and fusion, cell motility…) or even for drug delivery application in the case for instance of parenteral administration where nano vesicles must withstand in the high shear rate of blood circulation. To study our hybrid systems, we followed the same approaches often used in studies of pure liposomes and polymersomes [1-5]. As such, the translational fluidity was estimated *via* the lateral diffusion coefficient by Fluorescence Recovery After Photobleaching (FRAP) and the stretching elasticity (area compressibility modulus, lysis stress and strain) was evaluated by micropipette aspiration. All measurements were carried out on giant unilamellar vesicles.

The measurements of lateral diffusion of lipid or polymer chains in hybrid vesicles were performed on different mixtures composed of PEO_8-*b*-$PDMS_{22}$-*b*-PEO_8/POPC or PEO_{12}-*b*-$PDMS_{43}$-*b*-PEO_{12}/POPC at different mass percentages of POPC, using fluorescently labeled lipid or polymer as tracer molecules. Results are interpreted regarding the membrane structures and apparent phase diagrams (with or without nano-/micro domains) that have been determined in the previous chapter.

For mechanical properties studies, we decided to focus in the area of the apparent phase diagram where homogeneous hybrid vesicles were observed. As stretching elasticity is only affected by the chemical composition of the interface and so the interaction parameter χ that drives segregation and not by bilayer thickness [6], the study was carried out only on PEO_{12}-*b*-$PDMS_{43}$-*b*-PEO_{12}/POPC mixtures which offer a wide range of polymer/lipid fractions for which GHUVs do not present macroscopic domains. We have tried to evaluate the variation trend in area compressibility modulus of hybrid membrane with POPC content as well as the lysis stress and strain.

6.1. MEMBRANE DIFFUSION

Membrane fluidity or viscosity has an impact on both molecular rotational and translational diffusion rates. Translational diffusion rates can be described through a translational diffusion coefficient (D). In this section, the translational fluidity of the membrane is reported *via* Fluorescence recovery after photobleaching (FRAP) measurements. DOPE-Rhod was used as lipid dye analogue to study the mobility of phospholipids whereas FITC modified grafted copolymer $PDMS_{26}$-*g*-$(PEO_{12})_2$-FITC was used as polymer tracer to access the diffusion behavior of polymer chains. Investigations on both pure liposome and polymersome were performed in a first step in order to have references and validate all setting and experimental procedures.

6.1.1. Validation of methodology: measurements on single component membranes

6.1.1.1. Lateral diffusion in pure liposomes

Firstly, experiments were carried out on POPC GUVs labeled with 0.2 mol% of fluorescent dye DOPE-Rhod. The dynamic of this probe is assumed to be representative of the lateral mobility of POPC molecules and reflect the fluidity of POPC membranes. As described in Chapter 2, for FRAP experiments, the vesicles are immobilized on avidin coated glass slide through inclusion of biotynilated lipids (the biotynilated lipid: total lipid ratio is 1: 1.10^6). Immobilization efficiency of vesicles within the observation chamber is evidenced by the 2D maximum intensity projection images as illustrated in Figure 6.1. Such images are reconstructed from 113 slices and the acquisition took over 2 minutes, confirming their immobility necessary during FRAP data recording.

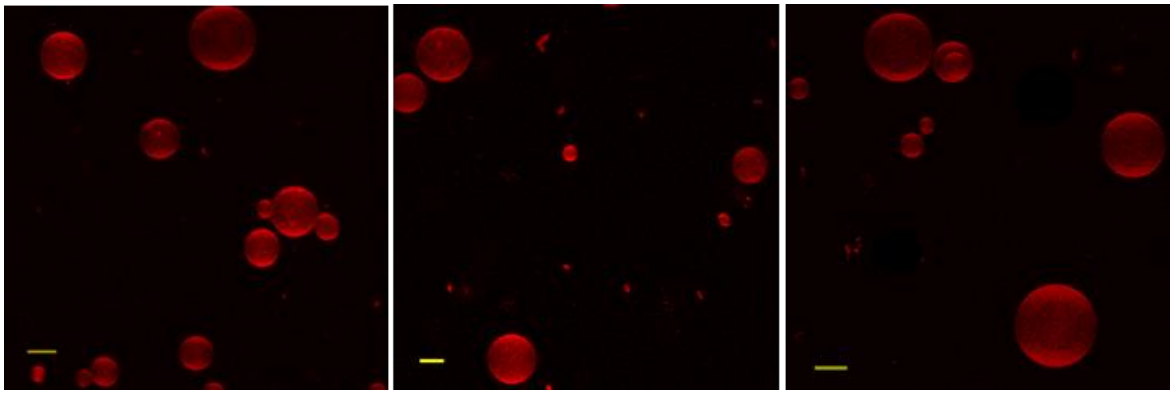

Figure 6.1. Maximum intensity projections of the POPC GUVs labeled with 0.2 mol% of DOPE-Rhod immobilized within the observation chamber, scale bars: 20 µm.

Generally, vesicles chosen to run FRAP experiments were in the size range of 25 – 40 µm diameter. Indeed, this allowed the top hemisphere where the measurement was performed to be significantly larger than the size of Region Of Interest (ROI) (5 µm). A typical FRAP measurement is illustrated in Figure 6.2 with the representative time-lapse images of the different measurement stages.

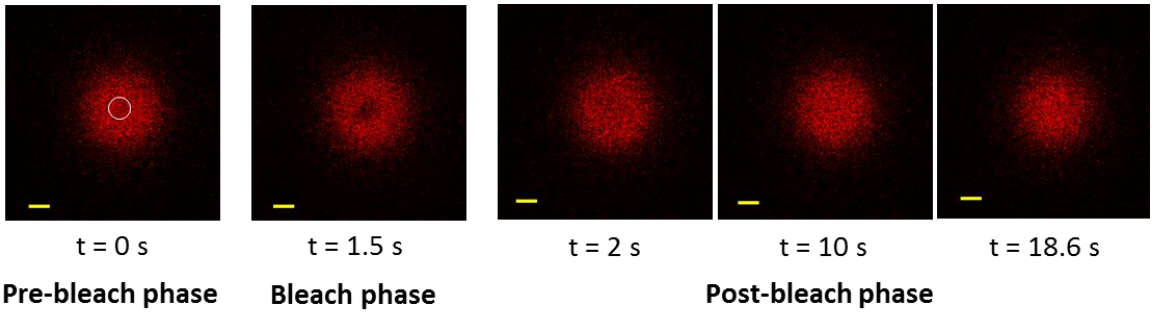

Figure 6.2. Representative time-lapse images recorded at different times of a typical FRAP measurement performed on the top hemisphere of a POPC GUV. The bleached ROI was centered on the top of the GUV (white circle); scale bars: 5 µm.

The mean fluorescence intensities are then extracted for each image and plotted as a function of the time, giving the corresponding FRAP curve as shown in Figure 6.3.

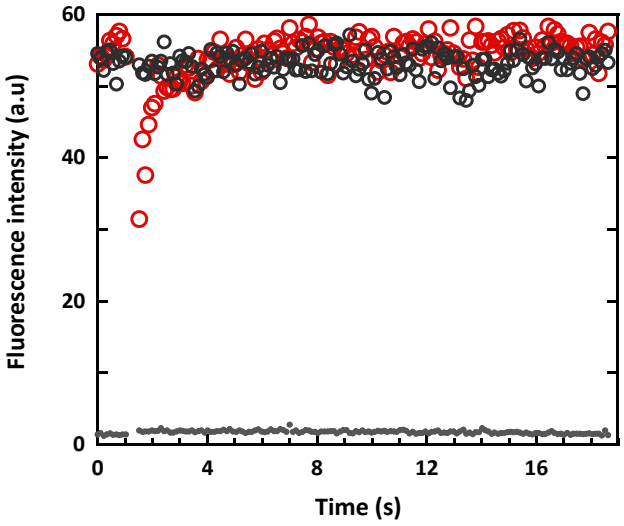

Figure 6.3. Mean fluorescence intensities plotted over time for signals from the ROI (●); from reference (●) and from background (●), in a FRAP measurement on a POPC GUV labeled with 0.2 mol% of DOPE-Rhod.

In this graph, the background and reference signals which are used to correct FRAP data are also displayed. At each point, the reference is the mean intensity extracted from an area on vesicle far enough of the ROI and background corresponds to the data collected in region outside of the vesicle. These two signals are used to correct for possible laser intensity

fluctuations and bleaching during image acquisition. As rhodamine is rather photostable, in Figure 6.3, there is no noticeable decrease in reference intensity during the recovery phase.

After background subtraction and normalization, the fluorescence recovery data are fitted (using formalisms described in Eq.2.30 Chapter 2), as seen in Figure 6.4. For the data shown in Figure 6.4, a diffusion coefficient value of D = 9.6 ± 2.1 $\mu m^2.s^{-1}$ (the error bar of value is the uncertainty of the fitting) and a mobile fraction M_f = 1 were recovered.

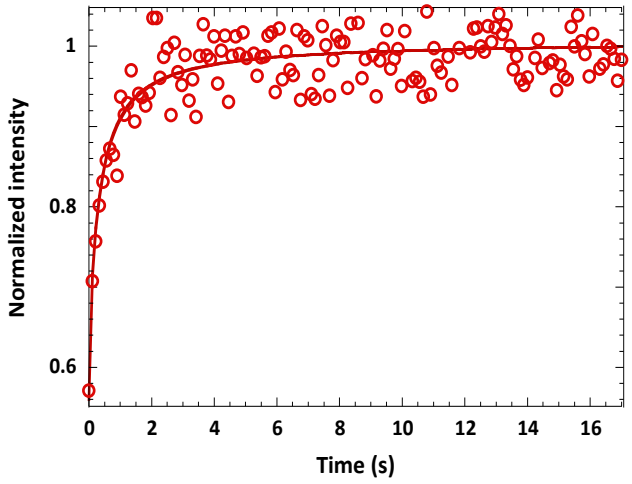

Figure 6.4. A representative normalized FRAP recovery curve obtained from a GUV composed of POPC with 0.2 mol% of DOPE-Rhod; the smooth line corresponds to the fit. The diffusion coefficient recovered for this dataset was D = 9.6 ± 2.1 $\mu m^2.s^{-1}$.

The measurements were repeated on different GUVs and results are represented by a histogram (Figure 6.5). The average diffusion coefficient of DOPE-Rhod in POPC GUVs over 10 measurements is $\overline{D}$ = 9.9 ± 1.6 $\mu m^2.s^{-1}$. This result is in agreement with many values reported previously in literature as summarized in Table 6.1.

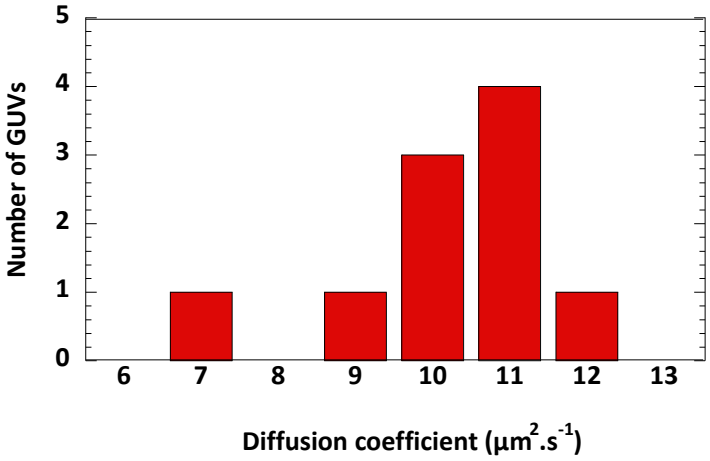

Figure 6.5. Distribution of diffusion coefficients recovered for DOPE-Rhod in POPC GUVs. Measurements were carried out in different vesicles (n = 10).

Table 6.1. Diffusion coefficients of pure lipid membranes that are reported in literature and in this work.

Reference	System	Probe	Technique	D ($\mu m^2.s^{-1}$)
This work	POPC GUVs	DOPE-Rhod	FRAP	9.9 ± 1.6
[7]	POPC GUVs	DHPE-Rhod	FRAP	9.8 ± 1.7
[8]	POPC GUVs	PE-NBD	FRAP	9.3 ± 1.6
[9]	Free-standing POPC bilayers	PE-NBD	FRAP	12.9 ± 1.2
[10]	POPC GUVs	PE-Rhod	z-scan FCS	12.5 ± 0.6
[11]	DOPC GUVs	DOPE-Atto647N	z-scan FCS	10.0 ± 0.7

6.1.1.2. Lateral diffusion in pure polymersomes

The translational fluidity of polymersomes was estimated *via* the measurement of lateral diffusion coefficients of the polymer tracer $PDMS_{26}$-*g*-$(PEO_{12})_2$-FITC inserted at 1.5% molar in GUVs. We characterized polymersomes made from self-assembly of different copolymers $PDMS_{26}$-*g*-$(PEO_{12})_2$, PEO_8-*b*-$PDMS_{22}$-*b*-PEO_8 and PEO_{12}-*b*-$PDMS_{43}$-*b*-PEO_{12}. Following exactly the same protocol described previously, Figure 6.6 represents a set of images acquired during measurement on a $PDMS_{26}$-*g*-$(PEO_{12})_2$ GUV and Figure 6.7 shows the corresponding raw FRAP curve. Although fluorescein is generally sensitive to photobleaching at high excitation irradiance, no fluorescence loss during image acquisition of recovery phase was observed at the laser excitation powers employed. A minor decrease in intensity of the reference signal immediately upon photobleaching in Figure 6.7 is probably the consequence of membrane fluctuations due to a local increase in temperature induced by the strong illumination of bleach phase [12].

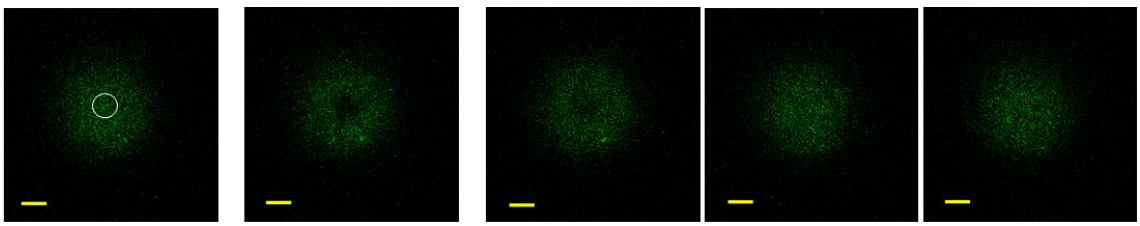

Figure 6.6. Representative time-lapse images recorded at different times of a typical FRAP measurement performed on the top hemisphere of a $PDMS_{26}$-*g*-$(PEO_{12})_2$ GUV containing 1.5 mol% of $PDMS_{26}$-*g*-$(PEO_{12})_2$-FITC. The bleached ROI was centered on the top of the GUV (white circle); scale bars: 5 µm.

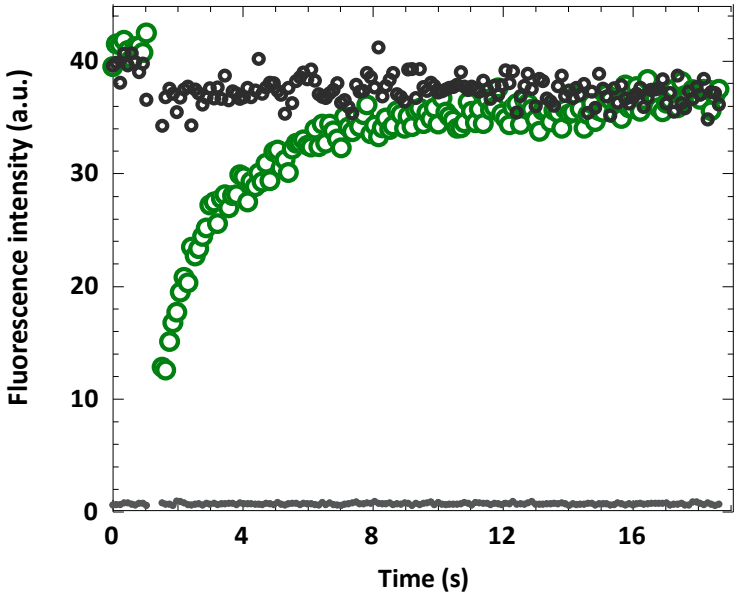

Figure 6.7. Mean fluorescence intensities plotted over time from the ROI (●), reference (●) and background (●) in a FRAP measurement on a $PDMS_{26}$-*g*-$(PEO_{12})_2$ GUV labeled with 1.5 mol% of $PDMS_{26}$-*g*-$(PEO_{12})_2$-FITC.

The slow recovery of fluorescence signal in comparison with POPC is illustrated in Figure 6.8. Interestingly, it can be clearly seen that a full recovery is obtained in both cases (mobile fraction $M_f = 1$).

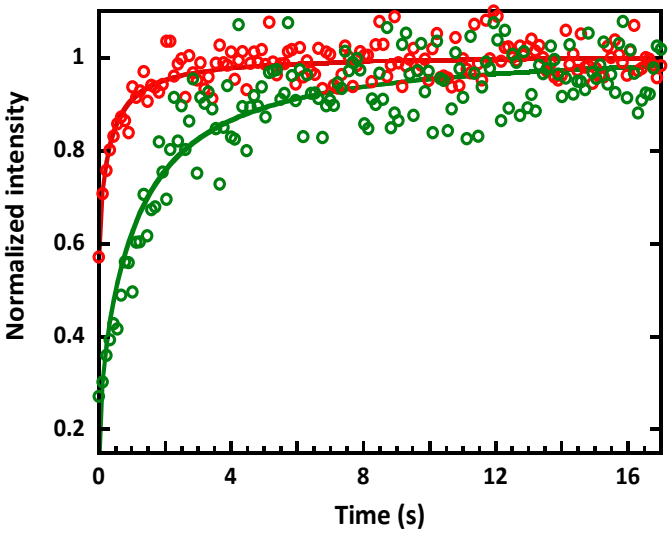

Figure 6.8. Representative FRAP curves and corresponding fits obtained for pure POPC GUV labeled DOPE-Rhod (red) and for pure polymersome $PDMS_{26}$-*g*-$(PEO_{12})_2$ labeled $PDMS_{26}$-*g*-$(PEO_{12})_2$-FITC (green).

The formalisms described in Chapter 2 were used to fit the data. A histogram of diffusion coefficients obtained from measurements on 15 vesicles is illustrated in Figure 6.9, giving an

average value $\overline{D}$ = 4.1 ± 0.9 µm².s^{-1}, about 2.5 times lower than diffusion of labeled lipids in POPC vesicles.

Figure 6.9. Distribution of diffusion coefficients recovered for PDMS$_{26}$-*g*-(PEO$_{12}$)$_2$-FITC in PDMS$_{26}$-*g*-(PEO$_{12}$)$_2$ GUVs. Measurements were carried out in 15 vesicles.

Using the same fluorescent copolymer as a tracer, measurements were also performed on GUVs made from the self-assembly of PEO$_8$-*b*-PDMS$_{22}$-*b*-PEO$_8$ and PEO$_{12}$-*b*-PDMS$_{43}$-*b*-PEO$_{12}$. Although the architecture and molar mass of the polymer tracer is now different from the triblock copolymers constituting the vesicle membrane, its motion is supposed to reflect the triblock copolymer mobility in the membrane, as the tracer is incorporated at a very low levels (1.5 mol%). The typical FRAP curves for all copolymers are represented in Figure 6.10. The FRAP curves obtained for PEO$_8$-*b*-PDMS$_{22}$-*b*-PEO$_8$ GUVs seems identical to FRAP curves from PDMS$_{26}$-*g*-(PEO$_{12}$)$_2$ GUVs and the recovery is slightly faster than those of PEO$_{12}$-*b*-PDMS$_{43}$-*b*-PEO$_{12}$. Quantitative analyses are shown in the histograms below (Figure 6.11). It should be noticed that all these membranes showed a full fluorescence recovery, typical of the absence of immobile fractions of fluorescence analogues.

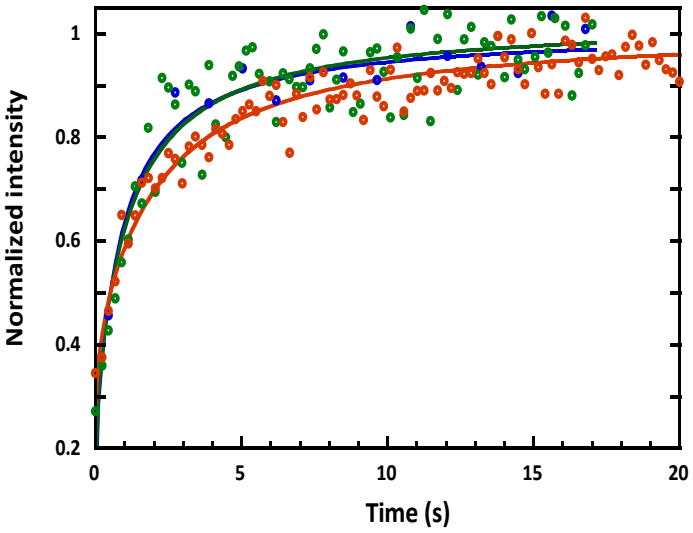

Figure 6.10. Representative FRAP data obtained from different polymersomes: (■): $PDMS_{26}$-*g*-$(PEO_{12})_2$, (■): PEO_8-*b*-$PDMS_{22}$-*b*-PEO_8; (■):PEO_{12}-*b*-$PDMS_{43}$-*b*-PEO_{12} containing 1.5 mol% of $PDMS_{26}$-*g*-$(PEO_{12})_2$-FITC. The smooth lines correspond to the fit following Eq.2.30 in Chapter 2.

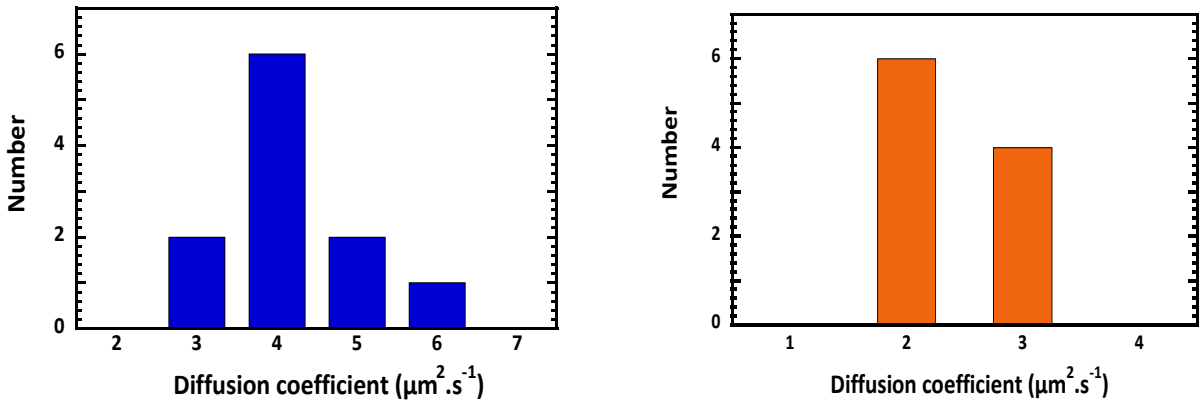

Figure 6.11. Histogram of diffusion coefficients obtained for PEO_8-*b*-$PDMS_{22}$-*b*-PEO_8 GUVs (left – blue) and PEO_{12}-*b*-$PDMS_{43}$-*b*-PEO_{12} GUVs (right – orange).

Following Saffman Delbück's continuum hydrodynamic model [13] describing lateral and rotational diffusion of cylindrical objects moving in a two dimension fluid (e.g. a lipid membrane), the lateral diffusion coefficient (D) can be expressed as:

$$D = \frac{k_b T}{4\pi\eta h}\left(\ln\left(\frac{\eta h}{\eta' R}\right) - \gamma\right) \qquad \text{(Eq. 6.1)}$$

where k_b is the Boltzmann constant, T is absolute temperature, h is the thickness of the bilayer, η is viscosity of the membrane, η' is viscosity of the outer liquid, R is the radius of the diffusing object and γ is Euler's constant. Using this equation, the membrane viscosities were calculated from our measurement of diffusion coefficient. The hydrophobic thicknesses d of the polymersomes measured by Cryo-TEM were used as the thickness of the bilayer h in

the calculation for polymersome membrane. R was approximated to be close of the radius of gyration $R_g = N^{\alpha}(b/6)$, where N is the number of siloxane units, b is the segments length (Si-O-Si) (= 0.311 nm) and α is the scaling exponent (= 0.66) found for membrane thickness of triblock copolymers in Chapter 3. Another approach is using the area/chain found in a vesicle to evaluate *R*. Table 6.2 summarizes the membrane characteristics obtained from the different copolymers. Typical values obtained for POPC membranes are also recalled.

The diffusion coefficient scales with hydrophobic block molar mass in a power law dependency ~ $M^{-1.3}$ as previously determined by Itel et al on diblock and triblock PDMS-*b*-PMOXA copolymers [10], illustrating the loss of fluidity of the membrane when molar mass increases. Using the formalism of Saffman Delbück's, copolymer membrane viscosities were found to be 2 to 3 times higher than POPC membrane viscosity and to increase with molecular weight. The viscosities found are well above the viscosity of PDMS bulk for such molar masses (between 0.036 and 0.052 Pa.s [14]) and could be explained by the extended conformation of the triblock chain through the membrane. In literature, membrane viscosities of PDMS-diblock copolymer bilayers have been found to be similar to PDMS bulk viscosity [10]. The higher viscosity observed also for grafted copolymer suggests that the degree of freedom of PDMS chain in the membrane is probably limited compared to a diblock copolymer with same molar mass.

Table 6.2. Characteristics of membranes obtained from different copolymers and phospholipid POPC (d: hydrophobic core thickness measured by Cryo-TEM, D: lateral diffusion coefficient, M_f: mobile fraction and η: viscosity of membrane with ^{a}: R from R_g, ^{b}: R from area/chain); * bilayer thickness of POPC Ref [15] ** with R = 0.45 nm [10].

Copolymer/Lipid	M_{PDMS} (g.mol^{-1})	*d* ± SD (nm)	D ± SD (µm².s^{-1})	M_f ± SD	η^a (Pa.s)	η^b (Pa.s)
$PDMS_{26}$-*g*-$(PEO_{12})_2$	1924	5.6 ± 0.6	4.1 ± 0.9	0.95 ± 0.07	0.094	0.077
PEO_8-*b*-$PDMS_{22}$-*b*-PEO_8	1628	5.4 ± 0.4	3.7 ± 0.8	1.00 ± 0.01	0.108	0.102
PEO_{12}-*b*-$PDMS_{43}$-*b*-PEO_{12}	3182	8.8 ± 0.5	1.9 ± 0.6	0.97 ± 0.04	0.130	0.132
POPC	-	4.0*	9.9 ± 1.6	1.00 ± 0.02	-	0.044**

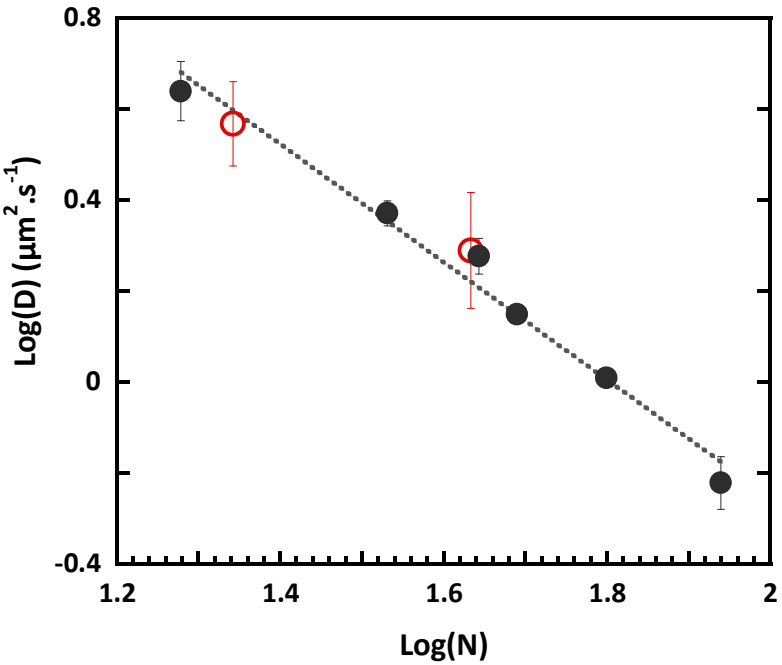

Figure 6.12. Log-log plot of diffusion coefficient D *vs* degree of polymerization (N) for PEO-*b*-PDMS-*b*-PEO GUVs (●) determined in this work and for PMOXA-*b*-PDMS-*b*-PMOXA (●) determined by Itel and col [10].

Our results being in good agreement with literature, our experimental settings for FRAP measurements can be reasonably validated. We therefore used these settings to study the more complex hybrid polymer/lipid membranes.

6.1.2. Evaluation on hybrid polymer/lipid membranes

The fluidity of hybrid membranes is evaluated through individual measurements of the translational diffusion of lipid molecules or copolymer chains.

6.1.2.1. Lateral diffusion of copolymer chains in hybrid membranes

In order to clarify the relationships between hybrid membrane fluidity and membrane structuration, measurements were carried out for GHUVs presenting homogenous and heterogeneous distribution of the component at micron scale. Briefly, for the PEO_8-*b*-$PDMS_{22}$-*b*-PEO_8/POPC mixture, GHUVs with a POPC content of 10%, 30% and 50% were analyzed. Based on the apparent phase diagram presented in previous chapter, GHUVs with 10% POPC are expected to present lipid nanodomains larger than 5 nm but non-visible under microscopy, whereas samples with 30% and 50% POPC show generally visible lipid microdomains. Hence, in FRAP measurements with only polymer fluorescent probe, GHUVs composed of 10% POPC were seen as homogenous as shown in Figure 6.13a whereas

"holes" were observed in GHUVs composed of 30% or 50% POPC (Figure 6.13b) since $PDMS_{26}$-*g*-$(PEO_{12})_2$-FITC does not incorporate in lipid domains. FRAP measurements in those samples were always performed in the polymer-rich phases.

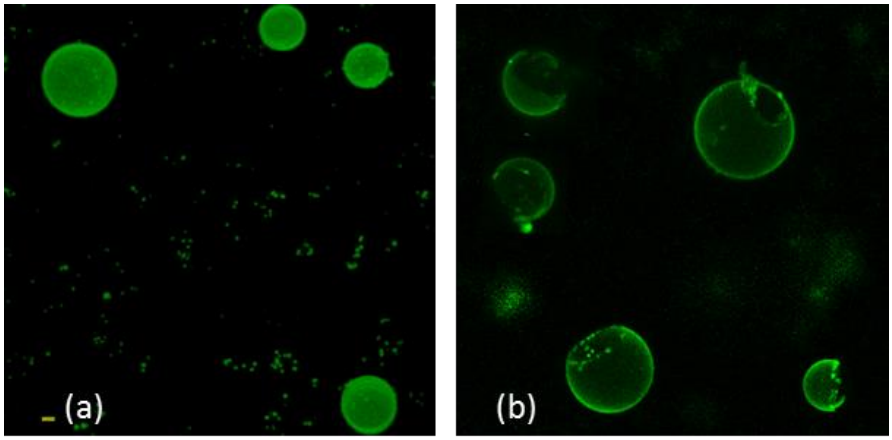

Figure 6.13. 2D maximum intensity projection images of PEO_8-*b*-$PDMS_{22}$-*b*-PEO_8/POPC GHUVs labeled with 1.5% $PDMS_{26}$-*g*-$(PEO_{12})_2$-FITC: (a): 10% POPC (no macroscopic domains) and (b): 50% POPC (macroscopic POPC domains appear as non-fluorescent phases); scale bars: 5 µm.

The typical FRAP curves for PEO_8-*b*-$PDMS_{22}$-*b*-PEO_8/POPC GHUVs at each aforementioned POPC fraction are presented in Figure 6.14. The effect of POPC on the mobility of copolymer chains can be qualitatively seen, particularly concerning the mobile fraction. The diffusion coefficients of copolymer chains values *versus* POPC concentration are represented in Figure 6.15 and all results are summarized in Table 6.3.

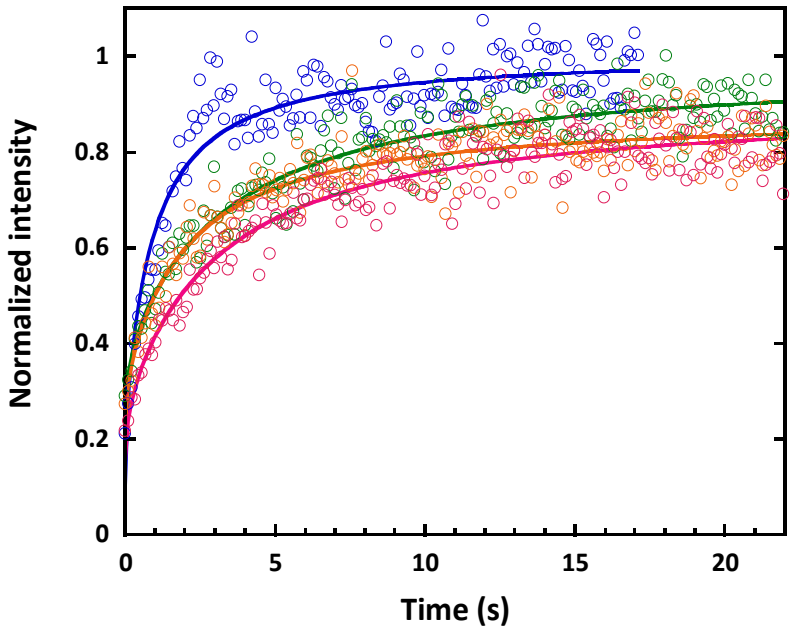

Figure 6.14. Representative FRAP data obtained from GHUVs with different PEO_8-*b*-$PDMS_{22}$-*b*-PEO_8/POPC compositions: (○):0% POPC; (○):10% POPC; (○):30% POPC and (○): 50% POPC containing 1.5% molar $PDMS_{26}$-*g*-$(PEO_{12})_2$-FITC. The smooth lines correspond to the fit using the formalisms described in Chapter 2.

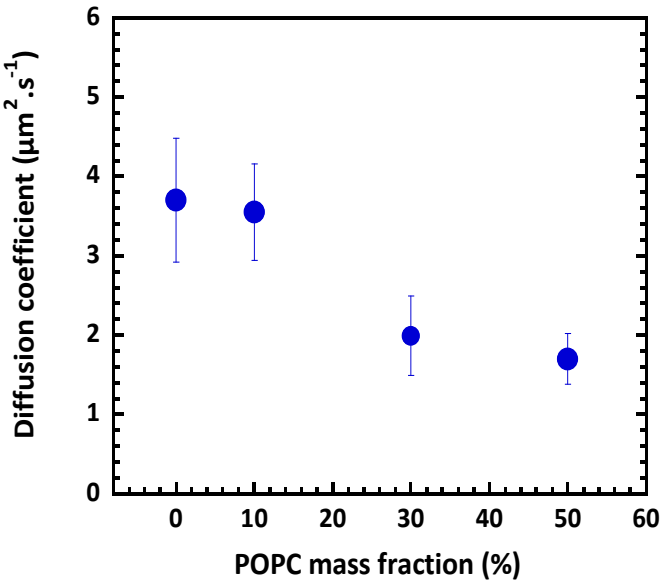

Figure 6.15. Illustration of recovered diffusion coefficients of fluorescent polymer probe in hybrid PEO_8-*b*-$PDMS_{22}$-*b*-PEO_8/POPC GHUVs as a function of POPC content.

Table 6.3. Lateral morphology and corresponding average lateral diffusion coefficients (D ± SD) and mobile fractions (M_f ± SD) of fluorescent polymer analogue in different hybrid PEO_8-*b*-$PDMS_{22}$-*b*-PEO_8/POPC membranes

POPC (%)	Membrane morphology	D ± SD (µm².s^{-1})	M_f ± SD
0%	-	3.70 ± 0.79	1.00 ± 0.01
10%	Nanodomains > 5 nm but invisible under microscope	3.55 ± 0.61	0.88 ± 0.05
30%	Microdomains visible under microscope	1.99 ± 0.50	0.82 ± 0.11
50%	Microdomains visible under microscope	1.70 ± 0.32	0.82 ± 0.11

Diffusion coefficients of polymer molecules in hybrid vesicles seem to be unmodified at low POPC fraction and then decreases when POPC fraction increases. The mobile fraction however is slightly modified even at low POPC content. This variation in diffusivity and mobile fraction is probably linked to the phase separation occurring in PEO_8-*b*-$PDMS_{22}$-*b*-PEO_8/POPC GHUVs. Polymer fluorescent marker $PDMS_{26}$-*g*-$(PEO_{12})_2$-FITC has been shown to be almost completely excluded from lipid phase as illustrated in Chapter 4. Therefore, the diffusion of copolymer chains is hindered due to the presence of those lipid domains. In this case, a small fraction of polymer fluorescent analogue would remain trapped by nanoscale lipid domains on the bleached ROI (FRAP was always carried out in fluorescent polymer-rich domains). With increasing POPC content, the diffusion coefficients decrease as a result of the presence of more lipid domain obstacles to diffusion.

Similar measurements were carried out for PEO_{12}-*b*-$PDMS_{43}$-*b*-PEO_{12}/POPC GHUVs. Interestingly, when POPC content increases, only a slight decrease of diffusion coefficient is observed in this system, as displayed in Figure 6.16 and Table 6.4, for GHUVs that do not present phase coexistence under microscope. In these lipid compositions for the previous block copolymer, variations were more pronounced. This may be due to the higher line tension observed in this system, which decreases the extent of formation of nanoscale lipid inclusions within polymer phases. In the PEO_{12}-*b*-$PDMS_{43}$-*b*-PEO_{12}/POPC mixture, the higher line tension promotes fission of lipid domains at significantly higher rates than the ones observed for PEO_8-*b*-$PDMS_{22}$-*b*-PEO_8/POPC GHUVs as discussed in Chapter 5. Interestingly, for samples showing microdomain coexistence under the confocal microscope (PEO_{12}-*b*-$PDMS_{43}$-*b*-PEO_{12}/POPC GHUVs composed of 50% POPC), there was no clear difference in both diffusion coefficient and mobile fraction values in comparison with pure polymersomes. This would suggest that there is no more lipid nanodomains in the polymer rich phase (but there is still some lipid incorporated in copolymer-rich phase, as Rhod DOPE signal is still detected in confocal images). The explanation of this is not obvious. May be this could be due to a probable high line tension at the polymer/lipid boundaries, which drives, above a critical threshold in lipid composition the existing nano scale lipid domains to coalesce rapidly into microdomains. In the previous system (PEO_8-*b*-$PDMS_{22}$-*b*-PEO_8/POPC) nanoscale lipid domains remain trapped within polymer-rich domains probably because of lower line tension.

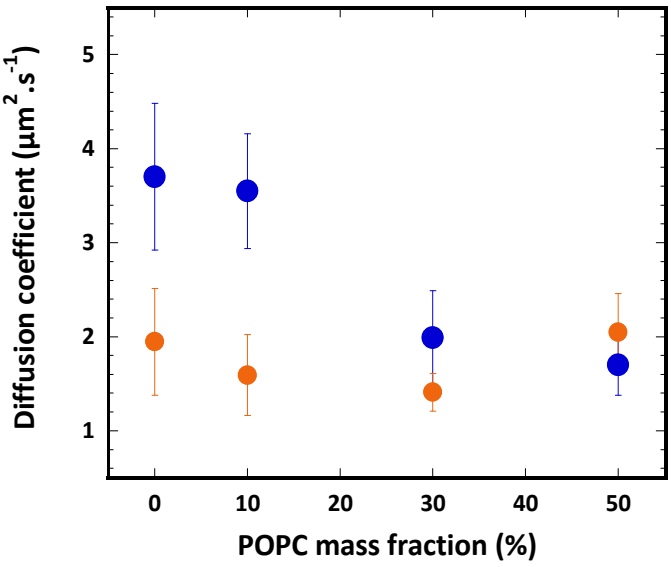

Figure 6.16. Diffusion coefficients of fluorescent polymer probe in PEO_{12}-*b*-$PDMS_{43}$-*b*-PEO_{12}/POPC GHUVs (●) and in PEO_8-*b*-$PDMS_{22}$-*b*-PEO_8/POPC GHUVs (●) as a function of POPC content.

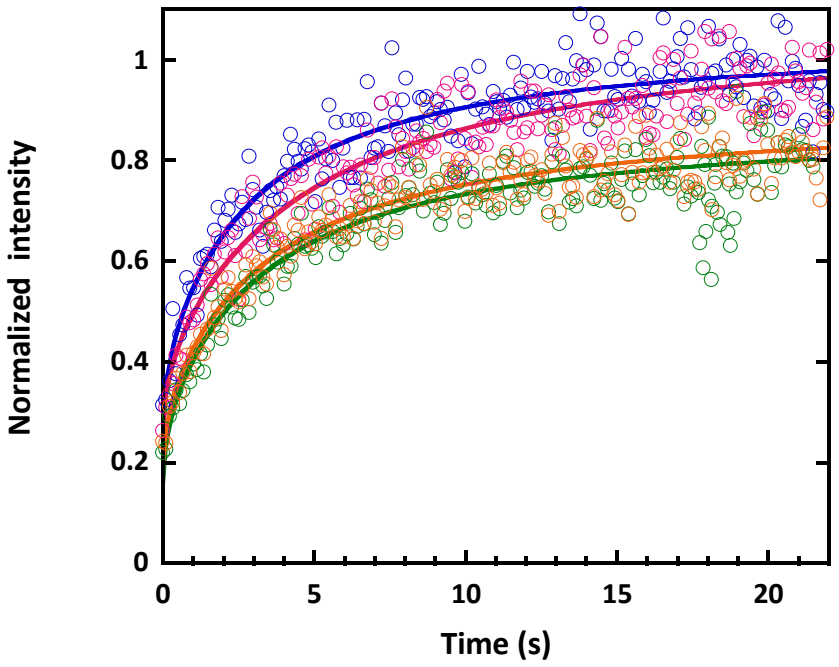

Figure 6.17. Representative FRAP data obtained from GHUVs with different PEO_{12}-*b*-$PDMS_{43}$-*b*-PEO_{12}/POPC compositions: (o):0% POPC; (o):10% POPC; (o):30% POPC and (o): 50% POPC containing 1.5% molar $PDMS_{26}$-*g*-$(PEO_{12})_2$-FITC. The smooth lines correspond to the fit using the formalisms described in Chapter 2.

Table 6.4. Lateral diffusion coefficient (D ± SD) and mobile fraction (M_f ± SD) of fluorescent polymer probe in different hybrid PEO_{12}-*b*-$PDMS_{43}$-*b*-PEO_{12}/POPC membranes.

POPC (%)	Lateral morphology	D ± SD ($\mu m^2.s^{-1}$)	M_f ± SD
0%	-	1.95 ± 0.57	1.00 ± 0.01
10%	Nanodomains > 5 nm but invisible under microscope	1.59 ± 0.43	0.81 ± 0.08
30%	Nanodomains > 5 nm but invisible under microscope	1.41 ± 0.20	0.82 ± 0.04
50%	Microdomains visible under microscope	2.05 ± 0.41	0.97 ± 0.07

6.1.2.2. Lateral diffusion of lipid molecules in hybrid membranes

The dynamic of lipid molecules in hybrid membranes was also studied through the diffusion coefficient of DOPE-Rhod. This probe partitions preferentially in lipid phase but not exclusively as shown in Chapter 4. Figure 6.18a and b present the typical images of PEO_8-*b*-$PDMS_{22}$-*b*-PEO_8/POPC GHUVs with 10% and 30% POPC (% wt) respectively. While DOPE-Rhod partitions homogeneously in all the GHUV at 10% POPC, it partition mostly into POPC microdomains in 30% POPC GHUVs (much brighter phases).

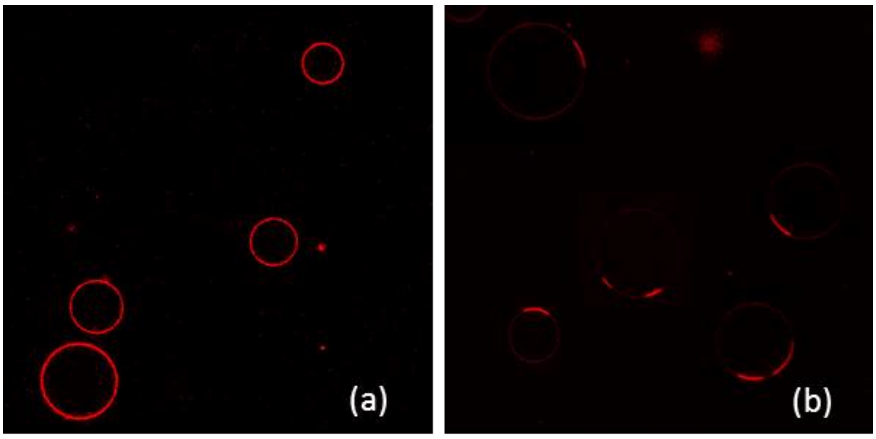

Figure 6.18. Equatorial images of PEO_8-*b*-$PDMS_{22}$-*b*-PEO_8/POPC GHUVs labeled with 0.2 mol% DOPE-Rhod and composed of (a): 10% POPC and (b): 30% POPC.

In phase separated GHUVs, the lipid fluorescent signal is too low in polymer-rich phases to perform FRAP measurements and the lipid-rich phases are rarely large enough to allow reliable measurements. Therefore, the study was only performed with GHUVs presenting homogeneous membrane structure at the micron scale. Based on the apparent phase diagram, measurements were carried out with PEO_8-*b*-$PDMS_{22}$-*b*-PEO_8/POPC GHUVs containing 10% and 15% of POPC. Results are shown in Figure 6.19 and the average values are summarized in Table 6.5.

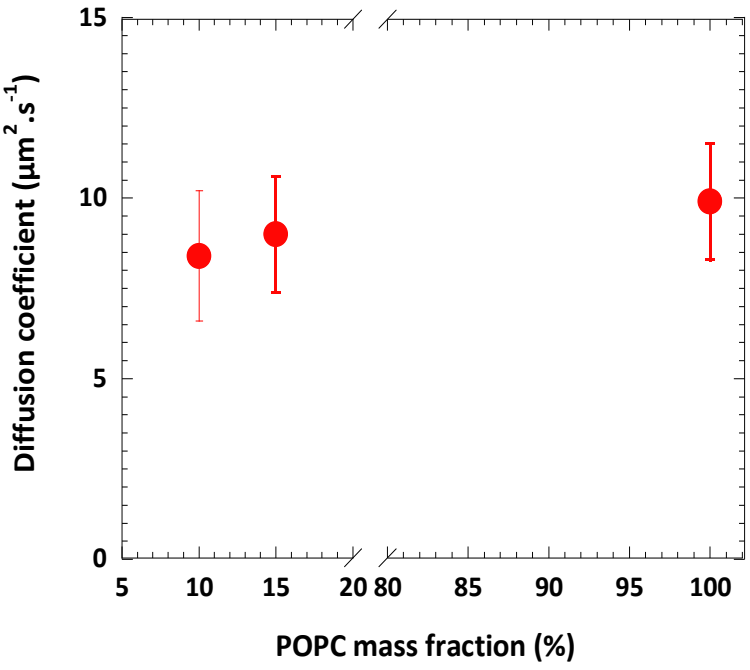

Figure 6.19. Diffusion coefficients of fluorescent lipid probe DOPE-Rhod in hybrid PEO_8-*b*-$PDMS_{22}$-*b*-PEO_8/POPC GHUVs as a function of POPC content.

Table 6.5. Lateral diffusion coefficient (D ± SD) and mobile fraction (M_f ± SD) of the fluorescent fluid lipid analogue DOPE-Rhod in hybrid PEO_8-*b*-$PDMS_{22}$-*b*-PEO_8/POPC GHUVs.

% POPC	D ± SD (µm².s^{-1})	M_f ± SD
10% POPC	8.4 ± 1.8	0.95 ± 0.09
15 % POPC	9.1 ± 1.8	0.98 ± 0.06
100% POPC	9.9 ± 1.6	1.00 ± 0.01

Lipid molecules diffuse about 2.5 times faster than polymer chains in the same host hybrid membrane ($D_{DOPE\text{-}Rhod}$ = 8.4 ± 1.8 vs $D_{PDMS_{26}-g-(PEO_{12})_2}$ = 3.55 ± 0.61 in PEO_8-*b*-$PDMS_{22}$-*b*-PEO_8/POPC GHUVs with 10% POPC). Considering the standard deviation of the measurement, there is no difference in diffusion coefficients of lipid in pure POPC and hybrid membranes composed of 10% and 15% of POPC. In this way, the diffusion of the lipid analogue is, unlike the copolymer analogue, not affected by nano scale phase separation. This suggests that FRAP reveal the lateral diffusion of lipid molecules (and not lipid nanodomains which obviously should have lower diffusion coefficient). The lipids dispersed in the polymer-rich phase can readily exchange with nano lipid domains and as such, these domains do not act as barriers for diffusion. This result also suggests that lipid diffusion in hybrid PEO_8-*b*-$PDMS_{22}$-*b*-PEO_8/POPC membrane is insensitive to either vesicle structuration or composition of hybrid vesicle. This result is different from the observation reported by Vanderlick and col [7] in which the lipid lateral diffusion coefficient in PBd_{46}-*b*-PEO_{30}/POPC GHUVs decreased gradually in proportion to the amount of incorporated polymer. However, since the copolymer used possesses a very low fluidity (D = 0.22 ± 0.06 µm².s^{-1} – 44 times lower than pure POPC), its influence on the lipid diffusion should be more pronounced.

6.2. MECHANICAL PROPERTIES

In this section, area compressibility moduli K_a, as well as rupture (lysis) stress and strain of different GUVs/GHUVs were evaluated by micropipette aspiration (MPA) method. Although developed a long time ago by Evan Evans [16] and widely used in literature to evaluate cell or synthetic membrane viscoelasticity [2, 17-21], (MPA) is a highly delicate and sensitive technique [22] which was set up in the lab in the framework of this thesis. The results obtained will be thoroughly discussed regarding the experimental procedures chosen to obtain reliable measurements.

As mentioned in the introduction of this section, if measurements were performed on different vesicles to evaluate the effect of the lipid/polymer composition on membrane properties, in parallel a number of test experiments on simple vesicles (liposome, polymersomes) were done in order to optimize the protocol, limit potential artifact and get reliable measurements. We particularly focused our attention on two aspects: Control of the osmotic pressure inside the sample and the coating of the micropipettes.

6.2.1. Control of the osmotic pressure, evaluation of area compressibility modulus

6.2.1.1. Pure vesicles

All GUVs are prepared in 0.1M sucrose solution to fix osmolarity, and decrease the eventual influence of slight variation of osmotic pressure in the environment. This was not sufficient in our experimental conditions for which evaporation of the water in the open chamber led to an increase of the concentration of sucrose outside vesicle and progressive deflation of the membrane. This obviously has an influence on the Area compressibility modulus measured. This has been evidenced on pure polymersome and hybrid vesicles, by performing experiments with the sample surrounded by oil (Brookfield, viscosity: 980 cP) to minimize water evaporation.

Micropipette aspiration measurements were performed on pure $PDMS_{26}$-*g*-$(PEO_{12})_2$ GUVs as a reference since its stretching modulus has been already reported in literature (K_a = 92 ± 5 $mN.m^{-1}$ [23] or ~ 95 $mN.m^{-1}$ [24] and for PEO_{12}-*b*-$PDMS_{43}$-*b*-PEO_{12} GUVs. Figure 6.20 represents an experiment performed on $PDMS_{26}$-*g*-$(PEO_{12})_2$ GUVs.

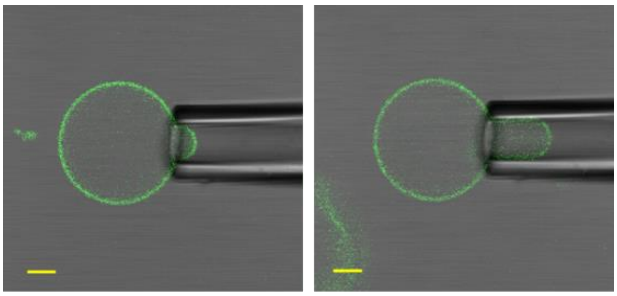

Figure 6.20. Representative images from a MPA experiment on $PDMS_{26}$-*g*-$(PEO_{12})_2$ GUV labeled 1.5 mol% $PDMS_{26}$-*g*-$(PEO_{12})_2$-FITC; scale bars: 5 µm.

Typical evolution of the membrane tension *versus* deformation of a sample surrounded by oil is illustrated in the following Figure 6.21.

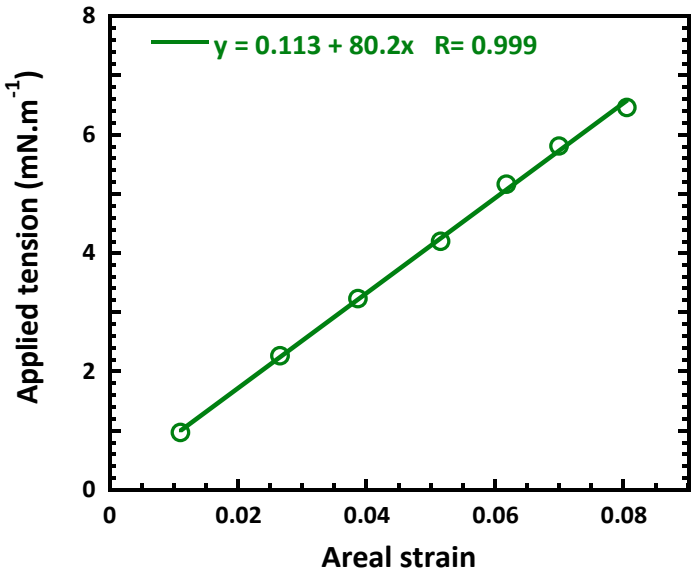

Figure 6.21. Representative stress-strain plots for $PDMS_{26}$-*g*-$(PEO_{12})_2$ vesicle in suspension surrounded by oil; line is the linear fit to the data points, returning K_a = 80.2 $mN.m^{-1}$.

The PEO_{12}-*b*-$PDMS_{43}$-*b*-PEO_{12} polymersomes were studied with and without presence of oil. A clear decrease of the stretching modulus is observed in absence of oil $\overline{K_a}$= 56 ± 8 $mN.m^{-1}$ (See Table 6.6) whereas in its presence, $\overline{K_a}$= 91 ± 11 $mN.m^{-1}$ stretching modulus is very close to the value obtained for $PDMS_{26}$-*g*-$(PEO_{12})_2$ $\overline{K_a}$ = 84 ± 12 $mN.m^{-1}$, which make sense as these copolymers have the same chemical nature area and compressibility modulus is only dependent of interfacial tension between the two blocks [6].

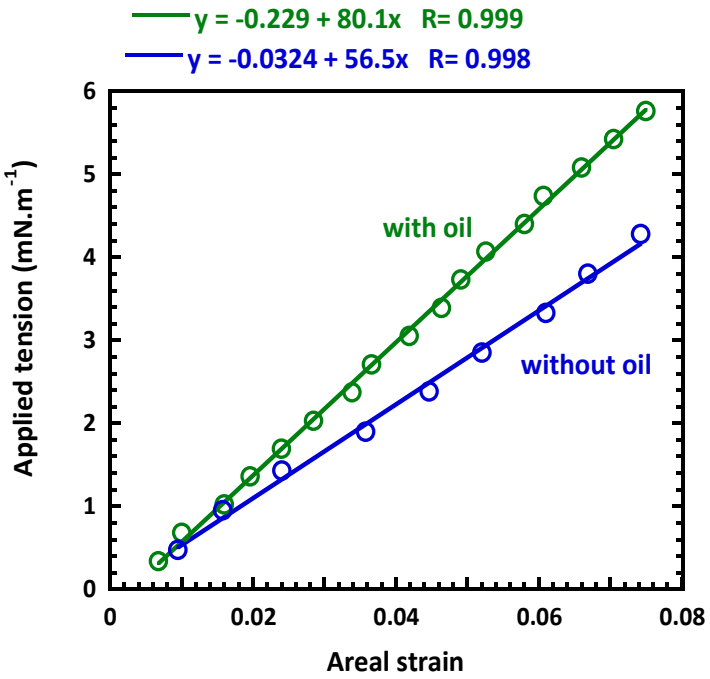

Figure 6.22. Representative stress-strain plots for PEO_{12}-*b*-$PDMS_{43}$-*b*-PEO_{12} vesicles in case using oil and no using oil.

Figure 6.23 represents the histogram of area compressibility modulus K_a obtained for pure polymersomes of $PDMS_{26}$-*g*-$(PEO_{12})_2$ GUVs. The average value $\overline{K_a}$ = 84 ± 12 $mN.m^{-1}$ is rather consistent with values reported in literature (Ka = 92 ± 5 $mN.m^{-1}$ [23] or ~ 95 $mN.m^{-1}$ [24]. This validates the protocol using oil to limit water evaporation during measurements.

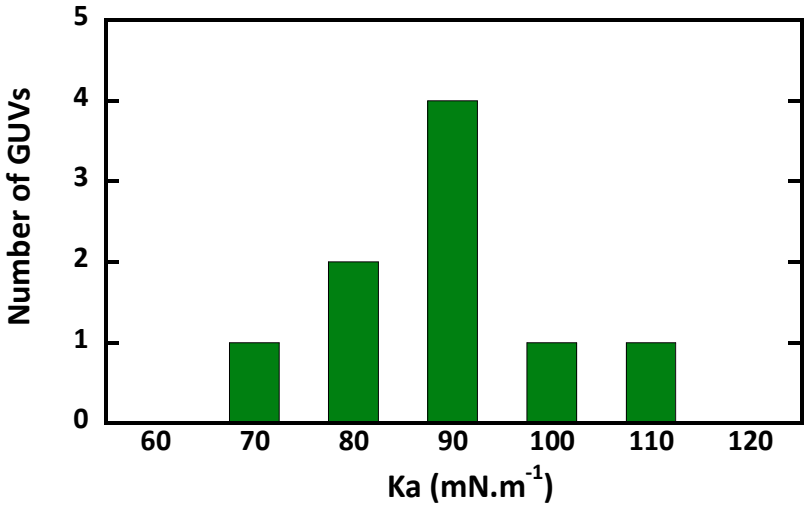

Figure 6.23. Distribution of area compressibility moduli measured for 9 individual $PDMS_{26}$-*g*-$(PEO_{12})_2$ GUVs with the usage of oil during experiment. The average value was $\overline{K_a}$ = 84.3 ± 12.2 $mN.m^{-1}$.

In Figure 6.24, histograms of area compressibility modulus K_a obtained from vesicles prepared in the same batch showed significantly different distribution of K_a with and without the use of oil.

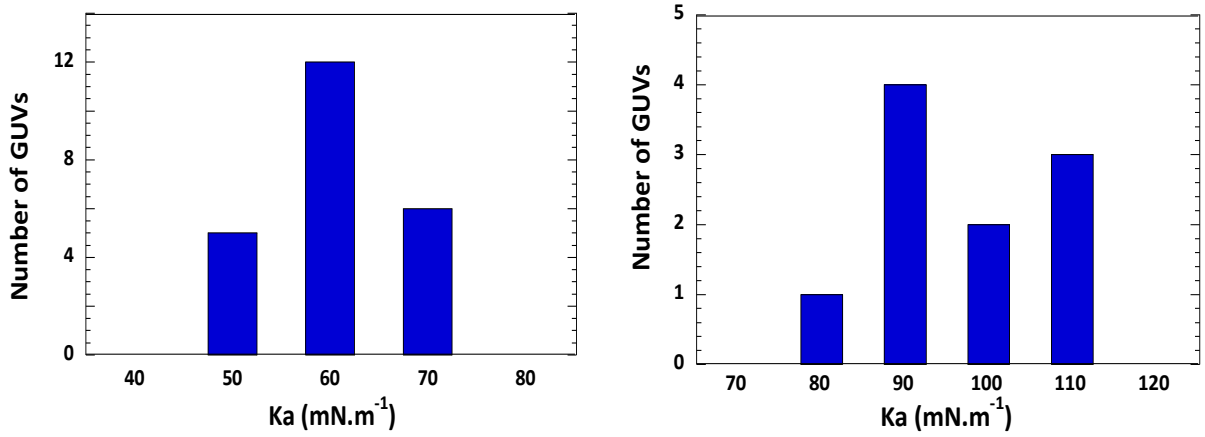

Figure 6.24 Evaluation of area compressibility modulus of pure PEO_{12}-*b*-$PDMS_{43}$-*b*-PEO_{12} GUVs in different conditions; left: Distribution of K_a determined without the usage of oil and right: Distribution of K_a determined using oil.

6.2.1.2. Hybrid vesicles

Micropipette aspiration measurements were then performed on different GHUVs prepared from PEO_{12}-*b*-$PDMS_{43}$-*b*-PEO_{12}/POPC in the POPC range of 5 – 20%, for which homogenous

distribution of components at the micron-scale was reported. As expected, the K_a of hybrid vesicles increase with increasing POPC content and all values are between values of pure polymersome ($\overline{K}_a$= 91 ± 11 mN.m^{-1}) and liposome ($\overline{K}_{a_{POPC}}$= 198 ± 8 mN.m^{-1} [25]). Values obtained from different measurements are shown in Figure 6.25.

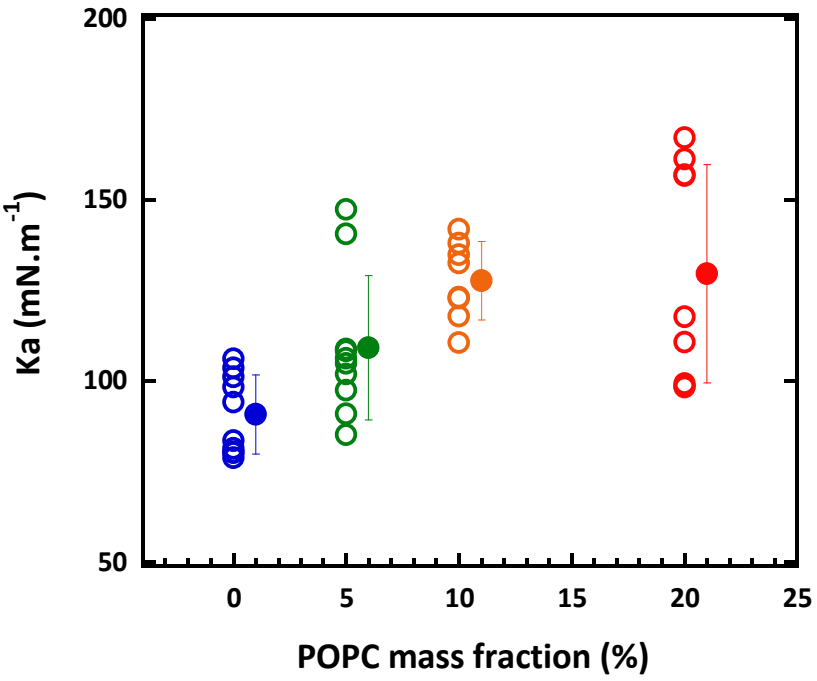

Figure 6.25. Variation of area compressibility modulus of hybrid PEO_{12}-*b*-$PDMS_{43}$-*b*-PEO_{12}/POPC GHUVs with POPC content: the open circles are experimental values obtained for individual GHUVs and the closed circular represents the corresponding averaged value with standard deviation (the symbol is slightly shifted to the right for clarity)

At 20% of POPC, there is no significant difference relative to the data obtained for samples at 10% POPC and the dispersity of measured values for K_a values is very high. Moreover, at 20% of POPC, it seems that two types of vesicles are present in the sample, one with a low K_a, slightly higher than the pure copolymer, and another with significantly higher K_a (~155 mN.m^{-1}). This probably reflects the heterogeneity in vesicle composition due to the fission events commonly observed with PEO_{12}-*b*-$PDMS_{43}$-*b*-PEO_{12}/POPC GHUVs. These events lead to the formation of GHUVs with considerably different membrane compositions.

In summary, the area compressibility moduli of hybrid polymer/lipid vesicles were successfully investigated and an increase with POPC fraction is observed. It is interesting to mention that for measurements made without the presence of oil, even if the K_a values were

underestimated, the variation trend of K_a with POPC content still remains as illustrated in Figure 6.26 and summarized in Table 6.6.

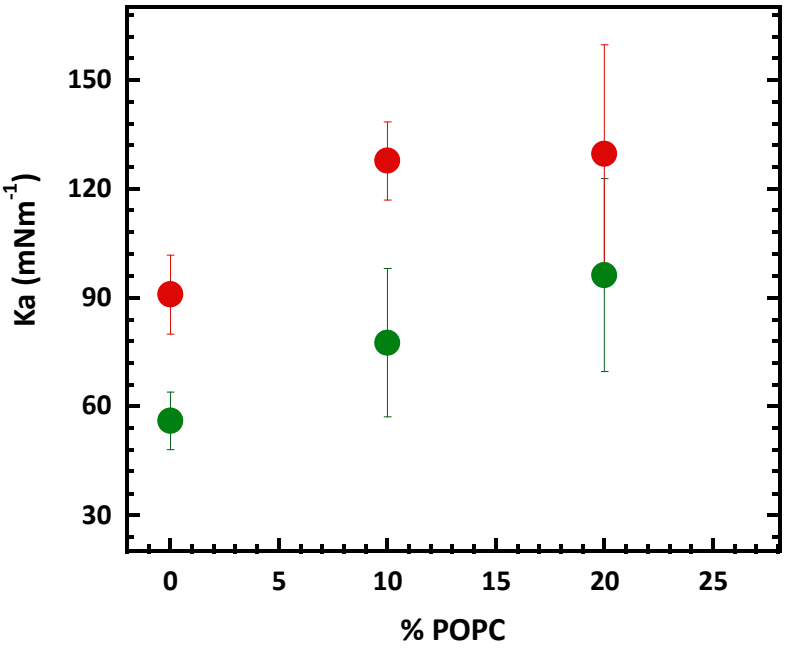

Figure 6.26. Variation of area compressibility modulus of hybrid PEO_{12}-*b*-$PDMS_{43}$-*b*-PEO_{12}/POPC GHUVs with POPC content (●): without the usage of oil and (●): using oil.

Table 6.6. Average area compressibility modulus values of different membranes determined in different conditions. Measurements were performed on 8 -10 vesicles for each composition.

Sample	K_a ± SD ($mN.m^{-1}$)	
	Without oil	With oil
$PDMS_{26}$-*g*-$(PEO_{12})_2$	-	84.3 ± 12.2
PEO_{12}-*b*-$PDMS_{43}$-*b*-PEO_{12}	56.0 ± 7.9	90.8 ± 10.9
PEO_{12}-*b*-$PDMS_{43}$-*b*-PEO_{12} /POPC 90/10	77.6 ± 20.5	127.7 ± 10.8
PEO_{12}-*b*-$PDMS_{43}$-*b*-PEO_{12} /POPC 80/20	96.2 ± 26.6	129.6 ± 30.1

6.2.2. Micropipette BSA coating, evaluation of lysis stress and strain

The evaluation of area compressibility modulus was achieved successfully, but the lysis stress and strain seems to be problematic from our results. For instance, Figure 6.27 shows the typical stress-strain curves for different GHUVs of PEO_{12}-*b*-$PDMS_{43}$-*b*-PEO_{12}/POPC. All lysis stress/strain of those GHUVs are very low, even lower than values reported for pure POPC GUVs (lysis stress τ_c = 7 $mN.m^{-1}$ and lysis strain α_c = 5% [7]).

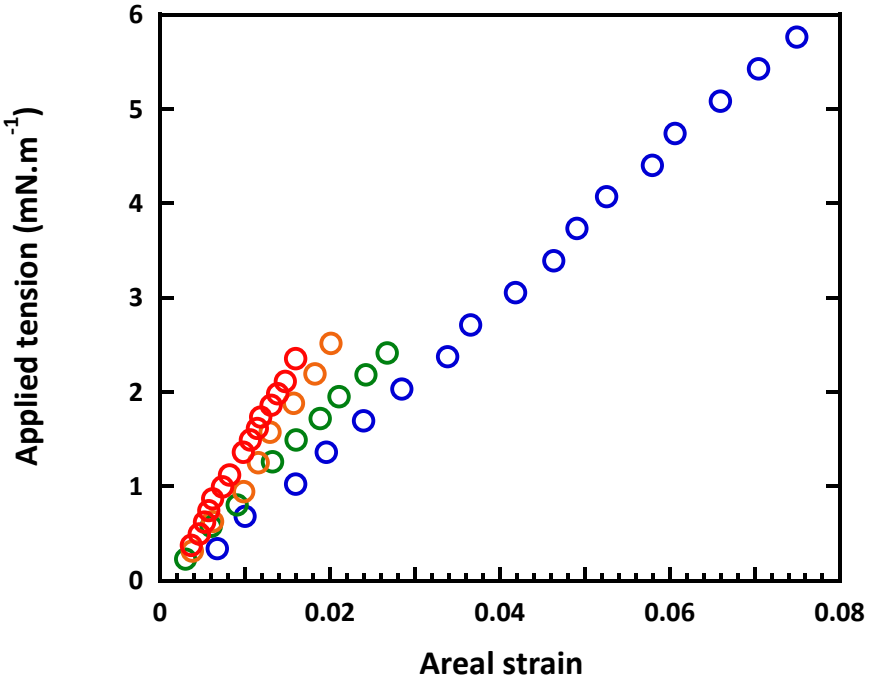

Figure 6.27. Representative stress – strain curves of PEO_{12}-*b*-$PDMS_{43}$-*b*-PEO_{12}/POPC GHUVs at different POPC content: (○): 0% POPC; (○): 5% POPC; (○): 10% POPC and (○): 20% POPC.

Variation in lysis tension under different rates of applied tension has been reported [1] but our protocol of increasing the suction pressure was unchanged (although the 1 cm step is done manually and not really controlled). Following different instructions and practical tips suggested in literature about coating of micropipettes to prevent vesicle adhesion and its possible influence on the lysis tension [1, 22], we decided to evaluate the effect of pipette treatment process (BSA coating) on $PDMS_{26}$-*g*-$(PEO_{12})_2$ GUVs as well as POPC (GUVs).

Briefly, micropipettes were left immersed in BSA solution to coat both inside and outside of the micropipette tip. This treatment was performed for different BSA concentrations and coating (immersion) times. First, for the coating time, using the same BSA concentration (0.01%), the immersion time was prolonged from 1-2h to the whole night. A minor improvement (Figure 6.28 and Table 6.7) was observed, suggesting that a longer time increase the levels of BSA adsorption. It should be notice that during the experiment, the pipettes tip is naturally washed and thus the actual BSA concentration is dramatically lowered. It is worth mentioning that excess of BSA should not be present in the GUV suspension as it may affect properties of the vesicles. This hypothesis is confirmed when we tried to increase BSA concentration up to 0.02%. Indeed both lysis stress and strain were

significantly higher and rather consistent with values reported in literature [23, 24]. Details of different examined conditions and corresponding results are summarized in Table 6.7.

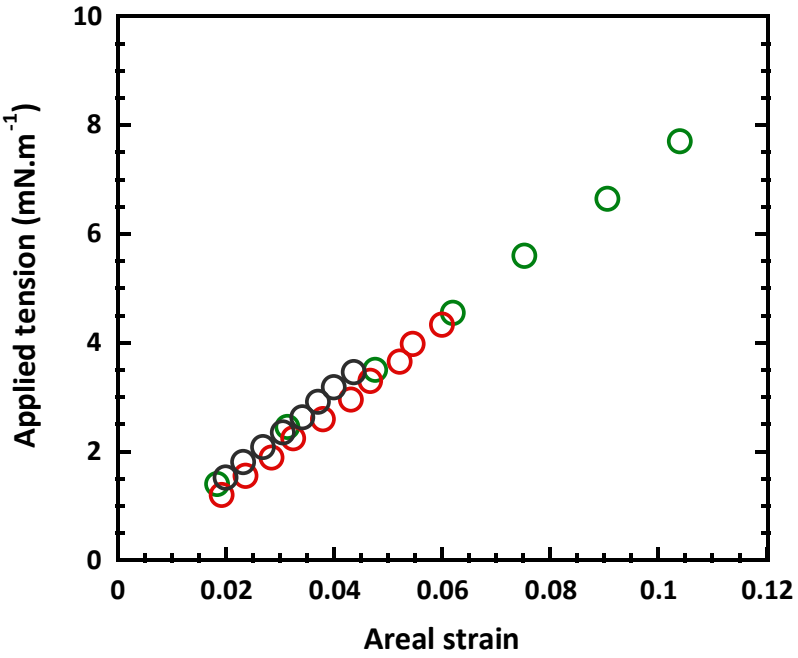

Figure 6.28. Representative stress-strain plots of $PDMS_{26}$-*g*-$(PEO_{12})_2$ GUVs obtained using micropipettes coated with BSA in different conditions: (○) BSA coating 0.01% during 1-2h; (○) BSA coating 0.01% during one night and (○): BSA coating 0.02% after one night.

Table 6.7. Average lysis tension (τ_c) and lysis strain (α_c) recovered from measurements on $PDMS_{26}$-*g*-$(PEO_{12})_2$ GUVs obtained using micropipettes coated with BSA in different conditions (9-11 vesicles were measured for each condition).

BSA coating procedure	τ_c ± SD (mN.m^{-1})	α_c ± SD (%)
BSA 0.01%, coating in 1 – 2 h	2.7 ± 0.8	3.8 ± 1.2
BSA 0.01%, coating overnight	3.8 ± 0.5	5.2 ± 0.8
BSA 0.02%, coating overnight	6.2 ± 0.5	8.1 ± 0.9
Ref: [23]	~ 7.5	~ 8

However, these coating procedures appeared to be insufficient for the study of pure POPC vesicles. Indeed low K_a (~ 150 mN.m^{-1}) as well as low lysis strain α_c (~ 2.5%) compared to typical value reported in literature (K_a ~ 200 mN.m^{-1}, α_c ~ 5%) was observed (Figure 6.29).

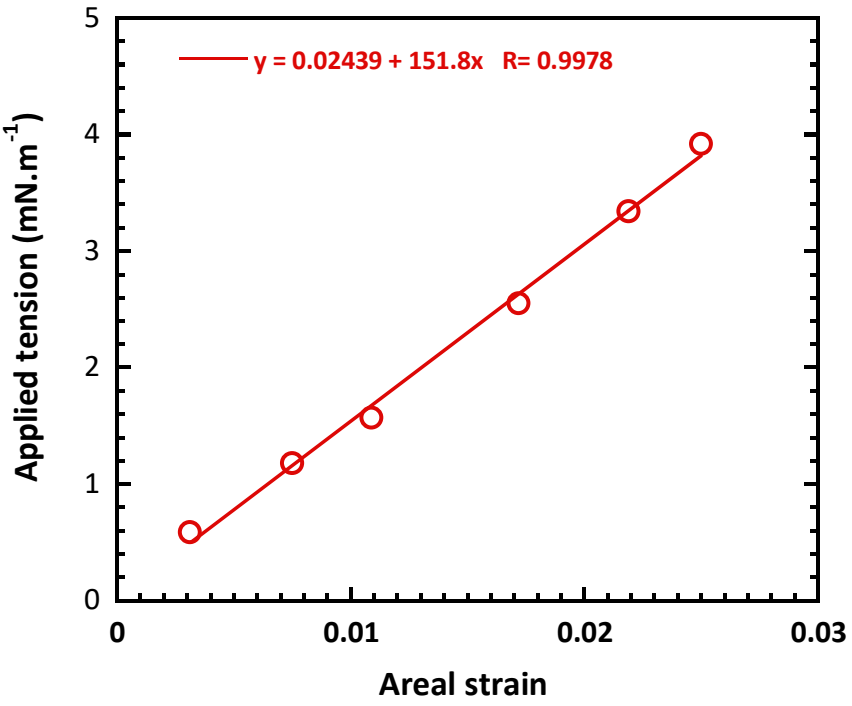

Figure 6.29. Representative stress-strain plots for POPC GUVs performed with the BSA coating procedure used to analyse $PDMS_{26}$-*g*-$(PEO_{12})_2$ GUVs (BSA 0.02%, coating overnight)

Therefore, we modified the BSA coating procedure with BSA solution at concentration 0.5 – 1%. Briefly, the pipet tip was immersed in vial containing BSA solution during 0.5 – 1h until the solution diffuse into the pipet by capillarity up to the region wherein the pipet tip begins to widen out. Afterward, the pipet tip was removed from this solution and entirely filled with sucrose solution 0.1M (the typical medium of vesicle suspensions) using a specific syringe with a very narrow flexible syringe needle. Then, after being connected with the water reservoir, the pipet was put in a vial containing sucrose 0.1M during 1h to remove all of BSA in excess. With such procedure, we observed the $\overline{K_a} = 171$ N.m^{-1} with lysis strain ~ 5%. A representative curve is shown in Figure 6.30.

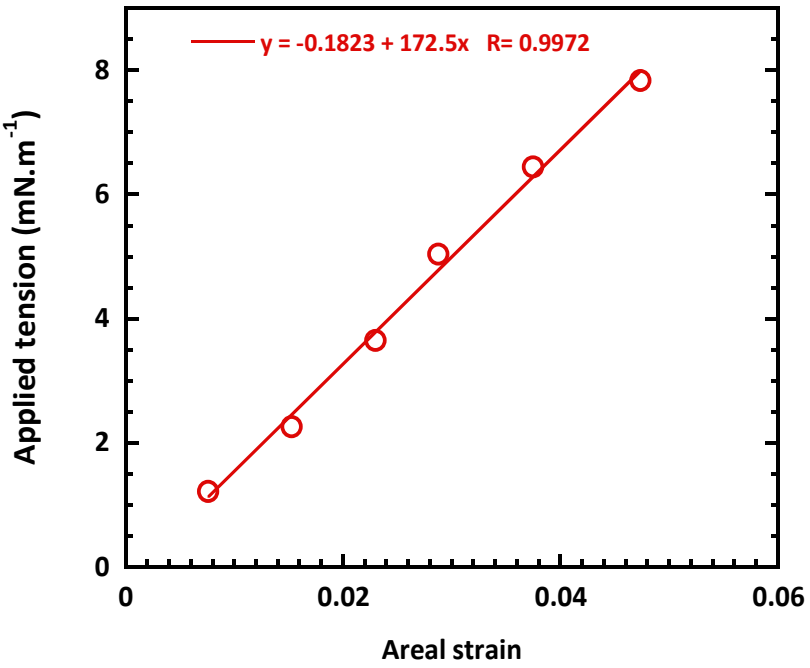

Figure 6.30. Representative stress-strain plots for POPC GUVs performed with the new BSA coating procedure.

6.3. CONCLUSION

In this chapter, the membrane fluidity of membranes in giant vesicles was estimated in terms of lateral diffusion for polymersomes based on PEO-*b*-PDMS-*b*-PEO triblock copolymers, liposomes based on POPC and hybrid polymer/lipid membranes made of both components. Diffusion coefficients obtained for pure lipid and copolymer vesicles were in agreement with literature, confirming the robustness of the methods employed here. Measurements on hybrid membranes clearly show that the incorporation of lipid together with polymer in a single membrane produces a strong effect on the dynamics of molecules, especially of polymer chains, which seems to be perturbed by the presence of lipid nanodomains.

Regarding the mechanical properties, the hybrid vesicles present area compressibility modulus that can be modulated between those of polymeric and lipidic membranes and gradually increases with lipid content. However, experimental protocols need to be optimized, especially regarding the accurate determination of lysis strain and stress values.

REFERENCES

1. Evans, E., et al., *Dynamic Tension Spectroscopy and Strength of Biomembranes.* Biophysical Journal, 2003. **85**(4): p. 2342-2350.
2. Discher, B.M., et al., *Polymersomes: Tough Vesicles Made from Diblock Copolymers.* Science, 1999. **284**(5417): p. 1143-1146.
3. Mullineaux, C.W. and H. Kirchhoff, *Using fluorescence recovery after photobleaching to measure lipid diffusion in membranes.* Methods in membrane lipids, 2007: p. 267-275.
4. Wu, E., K. Jacobson, and D. Papahadjopoulos, *Lateral diffusion in phospholipid multibilayers measured by fluorescence recovery after photobleaching.* Biochemistry, 1977. **16**(17): p. 3936-3941.
5. Pincet, F., et al., *FRAP to Characterize Molecular Diffusion and Interaction in Various Membrane Environments.* PLoS ONE, 2016. **11**(7): p. e0158457.
6. Bermudez, H., et al., *Molecular Weight Dependence of Polymersome Membrane Structure, Elasticity, and Stability.* Macromolecules, 2002. **35**(21): p. 8203-8208.
7. Nam, J., P.A. Beales, and T.K. Vanderlick, *Giant Phospholipid/Block Copolymer Hybrid Vesicles: Mixing Behavior and Domain Formation.* Langmuir, 2011. **27**(1): p. 1-6.
8. Lira, R.B., et al., *Posing for a picture: vesicle immobilization in agarose gel.* Scientific Reports, 2016. **6**: p. 25254.
9. Ladha, S., et al., *Lateral diffusion in planar lipid bilayers: a fluorescence recovery after photobleaching investigation of its modulation by lipid composition, cholesterol, or alamethicin content and divalent cations.* Biophysical Journal, 1996. **71**(3): p. 1364-1373.
10. Itel, F., et al., *Molecular organization and dynamics in polymersome membranes: A lateral diffusion study.* Macromolecules, 2014. **47**(21): p. 7588-7596.
11. Heinemann, F. and P. Schwille, *Preparation of Micrometer-Sized Free-Standing Membranes.* ChemPhysChem, 2011. **12**(14): p. 2568-2571.
12. Sezgin, E. and P. Schwille, *Fluorescence Techniques to Study Lipid Dynamics.* Cold Spring Harbor Perspectives in Biology, 2011. **3**(11): p. a009803.
13. Saffman, P.G. and M. Delbrück, *Brownian motion in biological membranes.* Proceedings of the National Academy of Sciences of the United States of America, 1975. **72**(8): p. 3111-3113.
14. Barry, A.J., *Viscometric Investigation of Dimethylsiloxane Polymers.* Journal of Applied Physics, 1946. **17**(12): p. 1020-1024.
15. Kučerka, N., M.-P. Nieh, and J. Katsaras, *Fluid phase lipid areas and bilayer thicknesses of commonly used phosphatidylcholines as a function of temperature.* Biochimica et Biophysica Acta (BBA) - Biomembranes, 2011. **1808**(11): p. 2761-2771.
16. Evans, E.A. and R.M. Hochmuth, *Membrane viscoelasticity.* Biophysical Journal, 1976. **16**(1): p. 1-11.
17. Hochmuth, R.M., *Micropipette aspiration of living cells.* Journal of Biomechanics, 2000. **33**(1): p. 15-22.
18. Tierney, K.J., D.E. Block, and M.L. Longo, *Elasticity and Phase Behavior of DPPC Membrane Modulated by Cholesterol, Ergosterol, and Ethanol.* Biophysical Journal, 2005. **89**(4): p. 2481-2493.

19. Needham, D. and R.S. Nunn, *Elastic deformation and failure of lipid bilayer membranes containing cholesterol.* Biophysical Journal, 1990. **58**(4): p. 997-1009.

20. Kwok, R. and E. Evans, *Thermoelasticity of large lecithin bilayer vesicles.* Biophysical Journal, 1981. **35**(3): p. 637-652.

21. Rawicz, W., et al., *Effect of chain length and unsaturation on elasticity of lipid bilayers.* Biophysical Journal, 2000. **79**(1): p. 328-339.

22. Longo, M.L. and H.V. Ly, *Micropipet Aspiration for Measuring Elastic Properties of Lipid Bilayers*, in *Methods in Membrane Lipids*, A.M. Dopico, Editor. 2007, Humana Press: Totowa, NJ. p. 421-437.

23. Nam, J. and M.M. Santore, *Adhesion Plaque Formation Dynamics between Polymer Vesicles in the Limit of Highly Concentrated Binding Sites.* Langmuir, 2007. **23**(13): p. 7216-7224.

24. Chen, D. and M.M. Santore, *Hybrid copolymer-phospholipid vesicles: phase separation resembling mixed phospholipid lamellae, but with mechanical stability and control.* Soft Matter, 2015. **11**(13): p. 2617-2626.

25. Shoemaker, S.D. and K.T. Vanderlick, *Material Studies of Lipid Vesicles in the La and La-Gel Coexistence Regimes.* Biophysical Journal, 2003. **84**.

GENERAL CONCLUSION AND OUTLOOK

General conclusion

In this thesis work, the formation and structuration (phase separation into domains) of hybrid polymer/lipid vesicles was investigated systematically at both micron and nano scale. For polymer component, different synthesized triblock copolymers based on the same chemical nature but in different molar masses were used: PEO_8-*b*-$PDMS_{22}$-*b*-PEO_8, PEO_{12}-*b*-$PDMS_{43}$-*b*-PEO_{12} and PEO_{17}-*b*-$PDMS_{67}$-*b*-PEO_{17}. These copolymers self-assemble into vesicles with different membrane thicknesses, from comparable to significantly thicker than liposomal membranes (from ~ 5.4 nm to ~ 11.2 nm), allowing to study the effect of hydrophobic length mismatch onto the formation of these hybrid vesicle and their membrane structuration. Using also a commercial grafted copolymer $PDMS_{26}$-*g*-$(PEO_{12})_2$ with molar mass and membrane thickness (~ 5nm) similar to the shortest triblock PEO_8-*b*-$PDMS_{22}$-*b*-PEO_8, we also investigated the effect of polymer architecture. For phospholipid component, either POPC (T_m = -2°C) or DPPC (T_m = 41°C) were used to evaluate the effect of phospholipid fluidity.

GHUVs formation were studied in the whole range of polymer/lipid fractions (from 0 to 100% w/w phospholipid and obtained by the classical electroformation process. LHUVs formation were studied up to 30% lipid weight content with the film rehydration/extrusion technique which is most commonly used in the literature for the preparation of LHUVs [1-5]. The association of different techniques (SANS, TR-FRET, Cryo-TEM) allowed us to show that LHUVs are formed in addition to non-negligible population of separated liposomes and polymersomes, it is not that easy when significant differences in membrane thickness of the lipid phase and polymer phase are considered. Even other morphologies (hybrid wormlike micelles can be obtained for the copolymer of the highest molar mass... Decreasing the molar mass or changing the copolymer architecture from triblock to grafted, resulted in a more efficient formation of hybrid vesicles. This suggests that if line tension at the polymer lipid boundaries is a parameter of importance it could be modulated not only by molar mass, but also the architecture of the copolymer.

Considering GHUVs, the study clearly shows that when lipid phase are in a fluid state, stable budded vesicles illustrating equilibrium between domain boundary energy and membrane curvature energy can be obtained depending on the molar mass of the copolymer. Briefly, we only observed the stabilization of fluid-state lipid micron-sized domains occurring in the vesicles of copolymer presenting low molar mass and with a membrane thickness close to the bilayer of liposomes (PEO_8-*b*-$PDMS_{22}$-*b*-PEO_8/POPC). With higher molar mass copolymers, the budding and fission of lipid domains occurred really rapidly after electroformation (PEO_{12}-*b*-$PDMS_{43}$-*b*-PEO_{12}/POPC). Globally in analogy with the study carried on LHUVS, the more the molar mass of the copolymer increases the more it is difficult to obtain in majority Hybrid GHUV vesicle. Very interestingly we were able to show that nanometric lipid domains GHUVs which appear as "homogenous" at microscale are present in the membrane using FLIM FRET methodology. The molar mass effect of the copolymer on the hybrid membrane structuration was illustrated also in study with lipid in the gel state (DPPC at room temperature) *via* domain morphology analyses. While the modulation of lipid-gel domains morphology into stripes or patchy can achieved with mixtures of PEO_8-*b*-$PDMS_{22}$-*b*-PEO_8/DPPC and PEO_{12}-*b*-$PDMS_{43}$-*b*-PEO_{12}/DPPC, it was impossible for the highest molar mass copolymer (PEO_{17}-*b*-$PDMS_{67}$-*b*-PEO_{17}) as only patchy domains were formed.

Concerning the architecture of copolymer, in addition to the facts that grafted copolymer lead to more efficient formation of hybrid vesicles at nano scale as mentioned above, at micron scale, a clear instability of domains (budding and fission) on the first few hours after electroformation was seen in hybrid vesicles with grafted polymer and not detected for triblock PEO_8-*b*-$PDMS_{22}$-*b*-PEO_8 for comparable polymer/lipid composition. This suggest that if similarities were observed for LHUV and GHUV studies, the behaviour observed in LHUV do not reflect systematically what happen for GHUV (and vice versa).

Also in this thesis, we have evaluated he modulation of the fluidity and stretching elasticity of the membrane. Diffusion of polymer chain in the hybrid membrane seems to be perturbed by presence of nanodomains, whereas diffusion of lipid molecules is similar to those of pure liposomes. In addition, the area compressibility modulus can be modulated between those of polymeric and lipidic membranes and gradually increases with lipid content.

Outlook

The information presented in this thesis is relevant regarding some aspects of hybrid vesicles but still several challenges need to be addressed. For instance, we intend to develop other preparation processes to obtain more efficiently the hybrid structure at the nanoscale. Afterward, it would be important to consider an approach to truly verify the hybrid character of the vesicles. Flow cytometry, cryo-TEM or scattering techniques were exploited during this PhD work, but the evidences from those approaches deserve further development.

On the other hand, the library of systems presented here may be used to quantify crucial parameters such as line tension at the lipid/polymer boundary, and the bending rigidity through the help of micropipette aspiration techniques. The outlook of this study will be to extend the qualitative interpretation in literature by more quantitative measurements of these two parameters: line tension and bending rigidity of the respectively lipid-rich and polymer-rich domains.

Finally, as the motivation of study on hybrid polymer/lipid formulation is generated from the expectation that it would incorporate in itself best characteristics of the two separate components for biomedical application, the further evaluations of several physical and bio-functional properties of those hybrid systems (such as membrane permeability, encapsulation and drug release, protein insertion, bio-recognition …) seems to be other important aspects for further fundamental and applied work.

REFERENCES

1. Cheng, Z., et al., *Improved Tumor Targeting of Polymer-based Nanovesicles Using Polymer-Lipid Blends.* Bioconjugate Chemistry, 2011. **22**(10): p. 2021–2029.
2. Winzen, S., et al., *Submicron hybrid vesicles consisting of polymer-lipid and polymer-cholesterol blends.* Soft Matter, 2013. **9**(25): p. 5883-5890.
3. Lim, S., et al., *Hybrid, Nanoscale Phospholipid/Block Copolymer Vesicles.* Polymers, 2013. **5**(3): p. 1102.
4. Panneerselvam, K., et al., *Phospholipid-polymer amphiphile hybrid assemblies and their interaction with macrophages.* Biomicrofluidics, 2015. **9**(5).
5. Pippa, N., et al., *PEO-b-PCL-DPPC chimeric nanocarriers: self-assembly aspects in aqueous and biological media and drug incorporation.* Soft Matter, 2013. **9**(15): p. 4073-4082.